

Search for the Decay $B^0 \rightarrow \eta\phi$
at the *BABAR* Experiment

D I S S E R T A T I O N

zur Erlangung des akademischen Grades

Doctor rerum naturalium
(Dr. rer. nat.)

vorgelegt

der Fakultät Mathematik und Naturwissenschaften
der Technischen Universität Dresden

von

Diplom-Physiker Stephan Otto
geboren am 29. November 1974 in Görlitz

Gutachter: Prof. Dr. Bernhard Spaan
Prof. Dr. Klaus R. Schubert
Prof. James G. Smith, Ph.D.

Eingereicht am: 29. November 2004

Abstract

Presented is a search for the rare hadronic B meson decay $B^0 \rightarrow \eta\phi$. It is based on 86×10^6 $B\bar{B}$ pairs recorded by the *BABAR* experiment at the Stanford Linear Accelerator Center between 1999 and 2002. ϕ mesons are reconstructed in the channel $\phi \rightarrow K^+K^-$. η mesons are reconstructed in the channels $\eta \rightarrow \gamma\gamma$ and $\eta \rightarrow \pi^+\pi^-\pi^0$. Signal events are identified by a candidate counting and a maximum-likelihood method. To ensure an unbiased measurement, the number of signal events is blinded throughout the analysis.

Although no significant signal is found by either method, the maximum-likelihood method obtains a smaller statistical uncertainty. In this method, the branching fraction of the decay $B^0 \rightarrow \eta\phi$ is determined by the upper limit $\mathcal{B}(B^0 \rightarrow \eta\phi) < 3.28 \times 10^{-6}$ (90%). This value includes a systematic uncertainty of 6.2%.

The cited upper limit is consistent with recent theoretical predictions. Therefore, this search gives no indication for particle interactions that are not described by the Standard Model of particle physics.

Kurzfassung

Vorgestellt wird eine Suche nach dem seltenen hadronischen B -Meson-Zerfall $B^0 \rightarrow \eta\phi$. Sie basiert auf 86×10^6 $B\bar{B}$ -Paaren, die zwischen 1999 und 2002 vom *BABAR*-Experiment am Stanford Linear Accelerator Center aufgezeichnet wurden. ϕ -Mesonen werden im Kanal $\phi \rightarrow K^+K^-$ rekonstruiert. η -Mesonen werden in den Kanälen $\eta \rightarrow \gamma\gamma$ und $\eta \rightarrow \pi^+\pi^-\pi^0$ rekonstruiert. Zur Identifikation von Signalereignissen wird eine Abzählmethode und eine Maximum-Likelihood-Methode verwendet. Um eine unvoreingenommene Messung zu gewährleisten, bleibt die Anzahl der Signalereignisse während der gesamten Analyse blind.

Durch keine der verwendeten Methoden wird ein signifikantes Signal nachgewiesen. Die Maximum-Likelihood-Methode liefert jedoch eine kleinere statistische Unsicherheit. In dieser Methode ist das Verzweigungsverhältnis des Zerfalls $B^0 \rightarrow \eta\phi$ durch die obere Grenze $\mathcal{B}(B^0 \rightarrow \eta\phi) < 3.28 \times 10^{-6}$ (90%) gegeben. Dieser Wert enthält eine systematische Unsicherheit von 6.2%.

Die angegebene obere Grenze ist mit aktuellen theoretischen Vorhersagen konsistent. Damit gibt diese Untersuchung keine Hinweise auf Wechselwirkungen, die nicht durch das Standardmodell der Elementarteilchenphysik beschrieben werden.

Man errs as long as he doth strive.

– Goethe

Contents

Introduction	15
1 The <i>BABAR</i> Experiment	17
1.1 Physical Motivation	17
1.1.1 Measurement of Quark Mixing	18
1.1.2 Measurement of <i>CP</i> Violation	19
1.1.3 Search for New Physics	21
1.2 The <i>BABAR</i> Detector	21
1.2.1 Interaction Point	21
1.2.2 Tracking System	22
1.2.3 Particle Identification	25
1.2.4 Electromagnetic Calorimeter	26
1.2.5 Instrumented Flux Return	28
1.2.6 Data Acquisition	30
1.3 Software Infrastructure	31
2 The Decay $B^0 \rightarrow \eta\phi$	33
2.1 Effective Theory	33
2.2 Decay Amplitude	37
2.3 Experimental Importance	39
2.4 Predictions and Measurements	39
3 Data Analysis	43
3.1 Analysis Strategy	43
3.1.1 Candidate Construction	43
3.1.2 Branching Fraction Calculation	44
3.1.3 Uncertainty Estimation	45
3.2 Data Samples	46

3.3	Event Variables	47
3.3.1	Kinematic Variables	47
3.3.2	Helicity Formalism	48
3.3.3	Momentum and Thrust	49
3.3.4	Momentum Flow	50
3.3.5	Fisher Discriminant	52
3.3.6	Helicity Angle	54
3.4	Event Reconstruction	55
3.4.1	Input	55
3.4.2	Tracks	55
3.4.3	Energy Clusters	56
3.4.4	π^0 Candidates	57
3.4.5	η Candidates	57
3.4.6	ϕ Candidates	57
3.4.7	B^0 Candidates	58
3.4.8	Output	58
3.5	Event Analysis	58
3.5.1	Number of Tracks	59
3.5.2	Kaon Identification	59
3.5.3	Photon Energy	59
3.5.4	B^0 Masses	61
	Signal Regions	64
	Sidebands	68
3.5.5	Resonance Masses	70
3.5.6	Fisher Discriminant	73
3.5.7	Helicity Angles	73
3.6	Candidate Counting Method	75
3.6.1	Background Subtraction	75
3.6.2	Selection Efficiencies	79
3.6.3	Signal Expectation	79
3.6.4	Background Expectation	79
3.6.5	Cut Optimization	80
3.6.6	Sideband Measurement	81
3.6.7	Systematic Uncertainties	81
3.7	Maximum-Likelihood Method	84

3.7.1	Likelihood Function	85
3.7.2	Selection Efficiencies	87
3.7.3	Selection Expectations	87
3.7.4	Fit Bias and Efficiency	87
3.7.5	Statistical Uncertainties	88
3.7.6	Systematic Uncertainties	90
3.8	Systematic Uncertainties	91
3.8.1	Efficiency Corrections	91
3.8.2	Method Summary	91
3.8.3	Peaking Backgrounds	92
3.9	Unblinded Results	93
3.9.1	Evaluation	94
3.9.2	Conclusion	97
	Summary	101
	References	103
	Acknowledgements	107
A	Resonance Masses	109
A.1	Channel $\eta \rightarrow \gamma\gamma$	110
A.2	Channel $\eta \rightarrow \pi^+\pi^-\pi^0$	113
B	Cut Optimization	119
B.1	Channel $\eta \rightarrow \gamma\gamma$	120
B.2	Channel $\eta \rightarrow \pi^+\pi^-\pi^0$	122
C	B^0 Masses	125
C.1	Channel $\eta \rightarrow \gamma\gamma$ Before Cuts	126
C.2	Channel $\eta \rightarrow \gamma\gamma$ After Optimized Cuts	127
C.3	Channel $\eta \rightarrow \pi^+\pi^-\pi^0$ Before Cuts	128
C.4	Channel $\eta \rightarrow \pi^+\pi^-\pi^0$ After Optimized Cuts	129
D	Probability Density Functions	131
D.1	Channel $\eta \rightarrow \gamma\gamma$	132
D.2	Channel $\eta \rightarrow \pi^+\pi^-\pi^0$	138

E Likelihood Projections	145
E.1 Channel $\eta \rightarrow \gamma\gamma$	146
E.2 Channel $\eta \rightarrow \pi^+\pi^-\pi^0$	149
F Yield Distributions	153
F.1 Channel $\eta \rightarrow \gamma\gamma$	154
F.2 Channel $\eta \rightarrow \pi^+\pi^-\pi^0$	155

List of Figures

1.1	Unitarity Triangle	19
1.2	Section of the <i>BABAR</i> detector	22
1.3	Section of the silicon vertex tracker	24
1.4	Section of the drift chamber	24
1.5	Energy loss per path length vs. momentum in the drift chamber	25
1.6	Section of the DIRC	26
1.7	Section of a crystal in the electromagnetic calorimeter	29
1.8	Section of a resistive plate chamber in the instrumented flux return	29
1.9	Map of the <i>BABAR</i> data acquisition system	30
2.1	QCD corrections to current-current operators	35
2.2	QCD corrections generating penguin operators	36
2.3	Feynman diagrams for the decay $B^0 \rightarrow \eta\phi$	38
3.1	Integrated luminosities	46
3.2	Helicity states	49
3.3	Constructed B candidate	50
3.4	Angular distributions of momentum and thrust momentum	51
3.5	Cones around the thrust momentum	51
3.6	Momentum flows in cones	52
3.7	Helicity angles of the η and the ϕ meson	54
3.8	Number of tracks	59
3.9	Kaon identification of the K^\pm candidates	60
3.10	Kaon identification of the π^\pm candidates	60
3.11	Energy of the photon candidates	61
3.12	Energy substituted mass in the $B\bar{B}$ Monte Carlo sample	62
3.13	Energy substituted mass in the off-peak data sample	62

3.14	Energy difference in the $B\bar{B}$ Monte Carlo sample	63
3.15	Energy difference in the off-peak data sample	63
3.16	Energy substituted mass in the signal Monte Carlo sample	65
3.17	Energy difference in the signal Monte Carlo sample	65
3.18	Energy substituted mass in the data sample	69
3.19	Energy difference in the data sample	69
3.20	Energy difference for best-mass selection in the data sample	70
3.21	Mass of the π^0 candidates	71
3.22	Mass of the η candidates	72
3.23	Mass of the ϕ candidates	72
3.24	Fisher discriminant	74
3.25	Helicity angle of the ϕ candidates	74
3.26	Helicity angle of the η candidates	75
3.27	Background ratios in the channel $\eta \rightarrow \gamma\gamma$	77
3.28	Background ratios in the channel $\eta \rightarrow \pi^+\pi^-\pi^0$	77
3.29	Fitted background ratios	78
3.30	Sideband expectations and measurements	83
3.31	Signal components of the mass of the η candidates	83
3.32	Signal components of the mass of the ϕ candidates	85
3.33	Signal yield of the maximum-likelihood fit	89
3.34	Variation of parameters in the maximum-likelihood fit	90
3.35	Negative logarithmic likelihoods for the signal yields	95
3.36	Likelihoods for the signal yields	96
3.37	Likelihood for the combined signal yield	96
3.38	Unblinded branching fractions $\mathcal{B}(B^0 \rightarrow \eta\phi)$	100
3.39	Unblinded upper limits on the branching fraction $\mathcal{B}(B^0 \rightarrow \eta\phi)$	100

List of Tables

2.1	Theoretical predictions for the branching fraction $\mathcal{B}(B^0 \rightarrow \eta\phi)$	40
3.1	Branching fractions of decay channels	44
3.2	Upper limits on the number of expected signal decays	47
3.3	Parameters of the Fisher discriminant	53
3.4	Parameters of energy substituted mass and energy difference	66
3.5	Counted and fitted numbers of signal candidates	67
3.6	Selection efficiencies and expected numbers of signal candidates	68
3.7	Parameters of energy substituted mass and energy difference (cont.) . . .	71
3.8	Background ratios	78
3.9	Expectations for signal optimized cuts	81
3.10	Fixed and no-signal optimized cuts	82
3.11	Expectations for no-signal optimized cuts	84
3.12	Sideband expectations and measurements	85
3.13	Systematic uncertainties due to shapes	86
3.14	Selection efficiencies and expectations of the maximum-likelihood fit . . .	88
3.15	Signal fit bias and signal fit efficiency of the maximum-likelihood fit . . .	89
3.16	Systematic uncertainties due to parameters	91
3.17	Statistical and systematic uncertainties for candidate counting	92
3.18	Statistical and systematic uncertainties for the maximum-likelihood fit . .	93
3.19	Common systematic uncertainties	93
3.20	Added systematic uncertainties	94
3.21	Peaking background decays	94
3.22	Unblinded results of candidate counting	98
3.23	Unblinded results of the maximum-likelihood fit	99

Introduction

Physics research has always been motivated by the demand for symmetries. A popular result, Einstein's Theory of Relativity, is based on the assumption that the laws of nature do not depend on the reference system from which they are observed.¹ In particle physics, symmetries are used to describe the internal structure of these laws. For instance, most particle interactions have the same strength as their mirror images. This defines a property called parity or "*P*" symmetry. The fact that not *all* processes obey this symmetry was proven in 1956 by Chien-Shiung Wu when she observed that electrons from radioactive cobalt-60 decays are aligned to the spins of the cobalt atoms. In our classification of interactions, this process is a "weak" decay. While the other known interactions — the electromagnetic and the "strong" interaction — obey parity, the weak interaction is apparently parity-violating.

The physical reason for parity violation in weak decays are the different "helicities" of neutrinos and anti-neutrinos: The former have left-handed spins, while the latter have right-handed spins. It follows that a replacement of all particles in a weak decay with their anti-particles temporarily restores parity. This replacement is called charge conjugation or "*C*" transformation. Hence, the transformed parity is a "*CP*" symmetry. The demand for *CP* symmetry leads to stringent constraints on the decays of neutral mesons. For instance, there should be one short-living K_S^0 meson decaying into two pions and one long-living K_L^0 meson decaying into three pions. In 1964, however, Cronin and Fitch discovered that a small fraction of the K_L^0 mesons also decay into two pions. Later, more evidence was found that the weak interaction is indeed *CP*-violating.

The property of *CP* violation unveils its full potential under inclusion of a third transformation called time reversal. This "*T*" transformation rewinds each process, making it run backward in time. The approval of relativity and quantum mechanics requires that *all* interactions obey "*CPT*" symmetry. Since the weak interaction is *CP*-violating, it must also violate time reversal. If it is proven not to, our understanding of relativity and quantum mechanics has to be reviewed. Another implication of *CP* violation is that shortly after the Big Bang matter and anti-matter were produced in unequal amounts. This, of course, is the very reason for our existence.

The Standard Model of particle physics describes *CP* violation by the different mixing of quarks and anti-quarks in the coupling to the Higgs boson. Unfortunately, the predictions of this mechanism do not explain the amount of matter observed in the universe. Moreover, the Higgs boson, which generates the masses of the fermions and gauge bosons, has not yet been discovered. The experimental limits placed on its mass,

¹Strictly speaking, this is *one* of the assumptions of *Special* Relativity.

however, impose a “gauge hierarchy problem”: In the renormalization dictated by the masses of the gauge bosons, the mass of the Higgs boson diverges. A variety of theories have been developed to solve these problems. Among the most promising are supersymmetry and string theory. Discussed are also extensions such as multiple Higgs bosons or additional fermion generations. All of these theories have their own strengths and weaknesses. More importantly, they predict different deviations from the Standard Model. The search for these deviations is the dominating task of modern particle physics.

The resolution achieved in particle experiments is proportional to the energy of the particles used. Therefore, precision tests of the Standard Model are the natural domain of High Energy Physics. With the energies available today, however, K mesons are no longer the most efficient system for the measurement of CP violation. Asymmetries larger by several orders of magnitude can be observed in the system of neutral B mesons. Established facilities for the production of these heavy mesons are large lepton colliders. The vastly studied physics of lepton collisions and the clean structure of the collision events allow measurements with the required efficiency and precision. Also needed are particle detectors with good spatial coverage, high momentum resolution, efficient particle identification and reliable photon detection. These considerations were the basis for the design and implementation of the *BABAR* experiment.

A characteristic of meson decays that makes them especially valuable for testing the Standard Model are the so-called “penguin” transitions. Their feature is a virtual quark loop that can interfere with other, potentially undiscovered particles. While penguin transitions contribute to most decays, they are usually suppressed by the more likely “tree” transitions. However, there is a rare class of B meson decays that does not permit tree transitions. One of the products of these “pure” penguin decays is the ϕ meson. It is used in the analysis presented in this thesis to search for penguin transitions in the B meson decays recorded by the *BABAR* experiment. The objective of this analysis is to find the most precise estimation for the branching fraction of the decay $B^0 \rightarrow \eta\phi$.

A detailed physical motivation for this analysis is given in Chapter 1 and 2. While Chapter 1 discusses the *BABAR* experiment and its general physical concepts, Chapter 2 specializes on the theoretical description of rare hadronic B meson decays. The experimental tools and methods used to identify the decay $B^0 \rightarrow \eta\phi$ are described in Chapter 3. A summary of results concludes this thesis.

Chapter 1

The *BABAR* Experiment

The *BABAR* experiment at the Stanford Linear Accelerator Center was launched in December 1993. Its primary goal is the measurement of CP -violating asymmetries in $B\bar{B}$ mesons systems. The high integrated luminosity and excellent reconstruction efficiency needed for this purpose, however, makes the *BABAR* experiment interesting for a wide range of physics studies. Important aspects of this rich research program are discussed in Sec. 1.1.

In the *BABAR* experiment, $B\bar{B}$ meson pairs are produced in e^+e^- collisions. Electrons and positrons are provided by the PEP-II storage ring [1] which was rebuilt by July 1998 to deliver a luminosity of $3\text{ nb}^{-1}\text{s}^{-1}$. The collisions take place in the *BABAR* detector, which is described in detail in Sec. 1.2. Since the beginning of data acquisition in November 1999, it has recorded more than 240 million $B\bar{B}$ meson pairs.

The task of the *BABAR* collaboration is to operate the detector and to analyze the recorded data. The distributed infrastructure deployed is addressed in Sec. 1.3. To assure a successful experiment, the *BABAR* collaborators work closely with accelerator operators, theorists and computing specialists. Up to the present day, approximately 600 physicists and engineers from ten different countries have joined the collaboration.

“Babar, the little elephant” [2] has been a popular cartoon figure since the 1930s. It lent its name to the *BABAR* experiment as tribute to the exciting world of physics in the $B\bar{B}$ system.

1.1 Physical Motivation

The *BABAR* experiment pursues an ambitious physics program. Its central target is the Standard Model [3] of particle physics. With the high volume and high quality of the recorded data, the predictions of this model can be tested with unequaled precision. Significant deviations from the predictions are a crucial indication for “new” and unknown physics. Small asymmetries are to be discovered, and the precision of many existing measurements is to be improved.

1.1.1 Measurement of Quark Mixing

In the Standard Model, elementary fermion fields are grouped by their chirality.¹ By demanding local gauge invariance, weak interactions are introduced as couplings of left-handed spinor doublets to the W boson vector triplet. By the same principle, particle masses are generated in the Higgs mechanism [4] by couplings of the left-handed doublets and the remaining right-handed singlets to a scalar doublet with spontaneously broken symmetry. In the quark sector, where all particles have non-vanishing masses, the Higgs mechanism produces two independent mass matrices $M_{\alpha\beta}^{(u)}$ and $M_{\alpha\beta}^{(d)}$. They generate the masses of the “up”-type and the “down”-type members of the quark doublets, respectively, in the three-family space $\alpha\beta$. The fact that up-type and down-type quarks are grouped in left-handed doublets implies that only one matrix $M_{\alpha\beta}$ can be diagonalized at a time. It follows that only one type of quarks can be turned into mass eigenstates. For the other type, mass eigenstates and chiral eigenstates are separated by a unitary transformation. By definition, the left-handed doublets

$$\begin{pmatrix} u \\ d' \end{pmatrix} \begin{pmatrix} c \\ s' \end{pmatrix} \begin{pmatrix} t \\ b' \end{pmatrix} \quad (1.1)$$

contain the mass eigenstates u, c, t ,² while the Cabibbo–Kobayashi–Maskawa (CKM) matrix [5] $V_{\alpha\beta}$ includes the mass eigenstates d, s, b ³ by the transformation

$$\begin{pmatrix} d' \\ s' \\ b' \end{pmatrix} = \begin{pmatrix} V_{ud} & V_{us} & V_{ub} \\ V_{cd} & V_{cs} & V_{cb} \\ V_{td} & V_{ts} & V_{tb} \end{pmatrix} \begin{pmatrix} d \\ s \\ b \end{pmatrix}. \quad (1.2)$$

If the quark generations are mixed by the matrix $V_{\alpha\beta}$, CPT invariance requires that the associated antiquark generations are mixed by the complex conjugated matrix $V_{\alpha\beta}^*$. Thus, complex phases in the CKM matrix are the origin of CP violation in the Standard Model. They are usually presented in the Wolfenstein parameterization [6]

$$V \approx \begin{pmatrix} 1 - \frac{1}{2}\lambda^2 & \lambda & A\lambda^3(\rho - i\eta) \\ -\lambda & 1 - \frac{1}{2}\lambda^2 & A\lambda^2 \\ A\lambda^3(1 - \rho - i\eta) & -A\lambda^2 & 1 \end{pmatrix} \quad (1.3)$$

with the expansion parameters $A = 0.81$ and $\lambda = 0.22$. The six unitarity conditions

$$\sum_{\alpha} V_{\alpha\beta} V_{\alpha\gamma}^* = 0 \quad (1.4)$$

for the elements of the CKM matrix correspond to triangles in the complex plane. The Unitarity Triangle with $\beta = d$ and $\gamma = b$ is shown in Fig. 1.1. Its angles

$$\alpha = \arg\left(-\frac{V_{td}V_{tb}^*}{V_{ud}V_{ub}^*}\right), \quad (1.5)$$

¹Although it is often used to denote *helicity*, this is the proper definition of “left-handed” and “right-handed”.

²These are the flavors “up”, “charm” and “top”.

³These are the flavors “down”, “strange” and “bottom”.

$$\beta = \arg \left(-\frac{V_{cd}V_{cb}^*}{V_{td}V_{tb}^*} \right), \quad (1.6)$$

$$\gamma = \arg \left(-\frac{V_{ud}V_{ub}^*}{V_{cd}V_{cb}^*} \right) \quad (1.7)$$

are gauge invariant⁴ combinations of six matrix elements. By measuring these matrix elements in weak interactions, the triangle can be overconstrained and the unitarity of the CKM matrix tested. This is a promising approach, since the largest matrix elements V_{tb} , V_{ud} and V_{cd} are already known to $\mathcal{O}(\lambda^4)$. In the *BABAR* experiment, V_{cb} can be measured in the semileptonic B meson decay $B \rightarrow D^*\ell\nu$, V_{ub} can be measured in the semileptonic decays $B \rightarrow \pi\ell\nu$ and $B \rightarrow \rho\ell\nu$, and the missing information on V_{td} can be obtained from $B^0\bar{B}^0$ mixing.

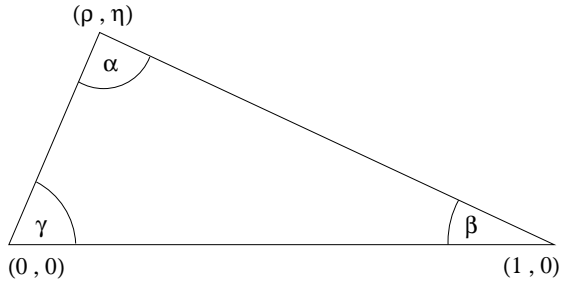


Figure 1.1 Unitarity Triangle of the unitarity condition $V_{ud}V_{ub}^* + V_{cd}V_{cb}^* + V_{td}V_{tb}^* = 0$ for the elements of the CKM matrix. The vertex coordinates follow from the Wolfenstein parameterization (Eq. 1.3) and the normalization to the basis.

1.1.2 Measurement of CP Violation

Composed from the quark mass eigenstates defined in Sec. 1.1.1, each hadron with fixed quark content is also a mass eigenstate. The quark content of neutral B mesons, however, is time-dependent. Due to $B^0\bar{B}^0$ mixing, a B meson produced as the quark state $|B^0\rangle = |\bar{d}b\rangle$ or $|\bar{B}^0\rangle = |\bar{b}d\rangle$ evolves into the combined state $a(t)|B^0\rangle + b(t)|\bar{B}^0\rangle$, while the two B meson mass eigenstates are the time-independent combinations

$$|B_H\rangle = p|B^0\rangle - q|\bar{B}^0\rangle, \quad (1.8)$$

$$|B_L\rangle = p|B^0\rangle + q|\bar{B}^0\rangle. \quad (1.9)$$

In the *BABAR* detector, $B^0\bar{B}^0$ meson pairs are produced in the coherent state

$$\frac{1}{\sqrt{2}} [|B_{\text{prod}}^0(t_1)\rangle |\bar{B}_{\text{prod}}^0(t_2)\rangle - |\bar{B}_{\text{prod}}^0(t_1)\rangle |B_{\text{prod}}^0(t_2)\rangle], \quad (1.10)$$

where $t_{1,2}$ are the proper times of both mesons. Measurements of CP violation depend on a “flavor tagging” decay that exposes the quark content of one of the mesons at $t_{1/2} = t_{\text{tag}}$. If the other meson decays into a CP eigenstate f at $t_{2/1} = t_{\text{CP}}$, the asymmetry in the decay rates

$$a_f(t) = \frac{\Gamma(B_{\text{prod}}^0(t) \rightarrow f) - \Gamma(\bar{B}_{\text{prod}}^0(t) \rightarrow f)}{\Gamma(B_{\text{prod}}^0(t) \rightarrow f) + \Gamma(\bar{B}_{\text{prod}}^0(t) \rightarrow f)} \quad (1.11)$$

depends on the time difference $t = t_{\text{CP}} - t_{\text{tag}}$ by

$$a_f(t) = \frac{(1 - |\lambda_f|^2) \cos(\Delta m t) - 2\Im \lambda_f \sin(\Delta m t)}{1 + |\lambda_f|^2}, \quad (1.12)$$

where Δm is mass difference between $|B_H\rangle$ and $|B_L\rangle$ [7]. Since $\hbar/\Delta m$ is of the same order of magnitude as the mean B meson life time [8], the time-dependence of this asymmetry can be experimentally observed. The gauge invariant⁴ product

$$\lambda_f = \frac{q}{p} \frac{\bar{A}_f}{A_f} \quad (1.13)$$

of the $B^0\bar{B}^0$ mixing amplitudes p, q (Eq. 1.8 and 1.9) and the decay amplitudes

$$A_f = \langle f | \mathcal{H} | B^0 \rangle, \quad (1.14)$$

$$\bar{A}_f = \langle f | \mathcal{H} | \bar{B}^0 \rangle \quad (1.15)$$

measures three types of CP violation:

CP violation in $B^0\bar{B}^0$ mixing

$$\left| \frac{q}{p} \right| \neq 1, \quad (1.16)$$

CP violation in the B^0 decay

$$\left| \frac{\bar{A}_f}{A_f} \right| \neq 1, \quad (1.17)$$

CP violation in the interference of $B^0\bar{B}^0$ mixing and the B^0 decay

$$\Im \left(\frac{q}{p} \frac{\bar{A}_f}{A_f} \right) \neq 0. \quad (1.18)$$

As discussed in Sec. 1.1.1, CP violation in the Standard Model depends on the presence of complex phases in quark mixing. $B^0\bar{B}^0$ mixing is a consequence of quark mixing and proceeds through intermediate up-type quarks of all three families. The mass dependence of the mixing amplitudes, however, suppresses all of the lighter quarks [9]. As a consequence, p and q only depend on the product of the CKM matrix elements V_{tb} and V_{td} . Since the magnitude of this product is constant under complex conjugation, there is no significant CP violation in $B^0\bar{B}^0$ mixing. In the case of the ‘‘golden channel’’ $B^0 \rightarrow J/\psi K_S^0$ which is governed by a tree-level W exchange, the decay amplitude $A_{J/\psi K_S^0}$ only depends on the product of V_{cs} and V_{cb} . Thus, there is no CP violation in this B^0 decay. Because $K^0\bar{K}^0$ mixing in the K_S^0 meson involves the product of V_{cd} and V_{cs} , the CP violation in the interference of $B^0\bar{B}^0$ mixing and this B^0 decay is given by

$$\lambda_{J/\psi K_S^0} = - \left(\frac{V_{tb}^* V_{td}}{V_{tb} V_{td}^*} \right) \left(\frac{V_{cs}^* V_{cb}}{V_{cs} V_{cb}^*} \right) \left(\frac{V_{cd}^* V_{cs}}{V_{cd} V_{cs}^*} \right). \quad (1.19)$$

⁴Only gauge invariant quantities are experimentally observable.

While $|\lambda_{J/\psi K_S^0}| = 1$, Eq. 1.3 and 1.5 imply that $\Im \lambda_{J/\psi K_S^0} = \sin 2\beta$, so that the time-dependent CP asymmetry (Eq. 1.12) simplifies to

$$a_{J/\psi K_S^0}(t) = -\sin 2\beta \sin(\Delta m t). \quad (1.20)$$

By comparison with the Unitarity Triangle (Fig. 1.1), the measurement of this asymmetry provides a powerful consistency check of the Standard Model. Similar, although more complicated, techniques exist for the angles α and γ .

1.1.3 Search for New Physics

Physics beyond the Standard Model are expected to strongly affect the CP violation observed in B meson decays. CP violation in both mixing and decay also occurs in systems of D mesons. The predicted asymmetries, however, are so small that any measured effect would be a proof for new physics. The large amount of charm quarks produced in e^+e^- collisions and B meson decays makes the *BABAR* experiment an ideal facility for such searches. The advanced vertex resolution and particle identification of the *BABAR* detector provide the needed experimental precision. Since charmed mesons decay through weak interactions of higher orders, they also reveal inconsistencies in the quark mixing mechanism.

Other systems with sizeable production cross sections in e^+e^- collisions on the $\Upsilon(4S)$ resonance are tau lepton and photon pairs. Tau leptons as representatives of the heaviest fermion family are most susceptible to undiscovered effects in mass generation. Since they even decay into hadrons, they provide a clean frame for poorly understood final state interactions caused by strong forces. The presence of different families of neutrinos in leptonic tau decays permits searches for the mass acquisition and family mixing effects known from the quark sector. Due to the high integrated luminosity, the *BABAR* experiment can also find exotic states produced by high energy photon pairs, like multiquarks, glueballs or meson molecules.

1.2 The *BABAR* Detector

The *BABAR* detector is a modern, multi-purpose particle detector. It combines high precision measurements with supreme reconstruction efficiency for all observable particles. Good angular coverage and a minimum of inactive material are common features of all detector systems. A schematic section of the detector is shown in Fig. 1.2. Each spatial dimension spans approximately 6 m. The longitudinal axis of the detector is the z axis of the right-handed coordinate system (x, y, z) . The origin of this system is the detector center. The entity of all detector systems covers the polar angle between 18° and 155° . The superconducting magnet coil that surrounds the central detector systems has an inner radius of 1.38 m and induces a magnetic field of approximately 1.5 T.

1.2.1 Interaction Point

In Fig. 1.2, the beam pipe runs horizontally through the detector middle. The electrons in the high energy beam, which enters from the left, have an energy of 9 GeV. The

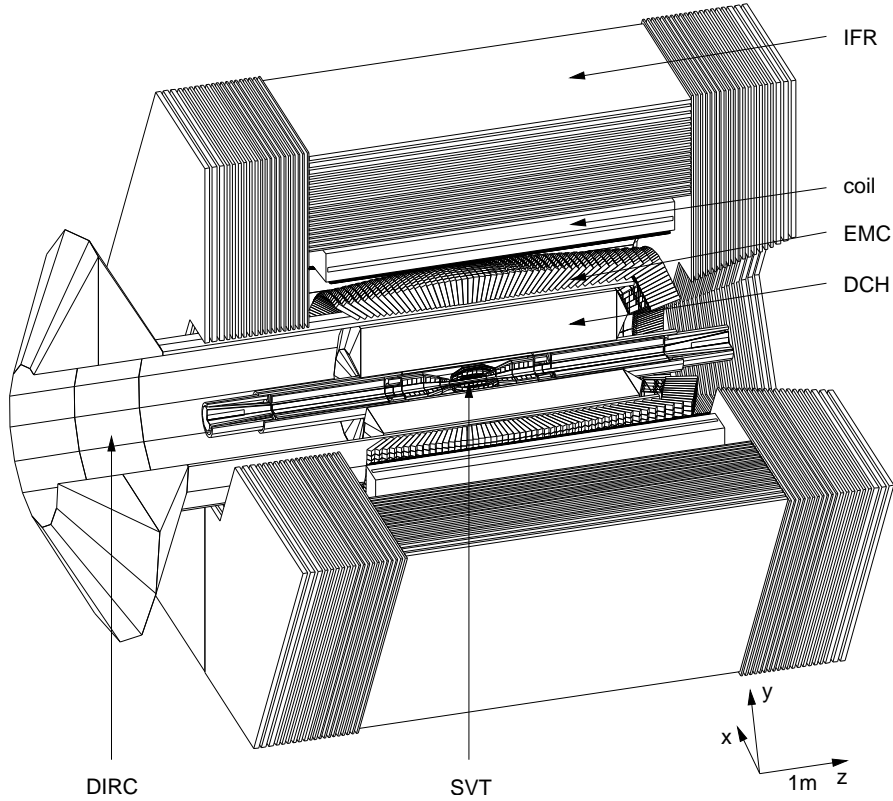


Figure 1.2 Schematic section of the *BABAR* detector with silicon vertex tracker (SVT), drift chamber (DCH), electromagnetic calorimeter (EMC), magnet coil, instrumented flux return (IFR) and detector of internally reflected Cherenkov light (DIRC) [10]. The longitudinal axis of the detector is the z axis of the right-handed coordinate system (x, y, z) .

positrons in the low energy beam, which enters from the right, have an energy of 3.1 GeV. The beams are brought to collision in the interaction point in the detector center.

In their center-of-mass system, the beams have an energy of 10.6 GeV, which is the mass of the $\Upsilon(4S)$ resonance of $b\bar{b}$ quark pairs. More than 96% of the quark pairs, which are produced at a cross section of 1.05 nb [7], decay into $B\bar{B}$ meson pairs. Due to their high masses [8], the B mesons are produced nearly at rest. In the detector coordinate system, they are boosted in the positive z direction, which becomes the “forward” direction of the detector, with $\beta\gamma = 0.56$. In its mean life time [8], each B meson passes a distance of $\Delta z \approx 260 \mu\text{m}$. The concept of the “asymmetric collider” allows the individual decay time of each B meson to be inferred from its measured decay vertex. It also dictates the asymmetric design of the detector systems.

1.2.2 Tracking System

In beam collisions and B meson decays a large number of charged particles are produced. Among those that escape the interaction point are electrons, muons, pions and kaons. While they pass through the surrounding matter, they lose part of their energy in

collisions⁵ with atomic electrons. The average energy loss per path length is described by the Bethe–Bloch formula [11]

$$-\frac{dE}{dx} = 2\pi N Z m_e c^2 r_e^2 \frac{1}{\beta^2} \left[\ln \left(\frac{2m_e c^2 \beta^2 \gamma^2 W_{\max}}{I^2} \right) - 2\beta^2 \right], \quad (1.21)$$

where N and Z are the atomic density and number, m_e and r_e are the electron mass and radius, W_{\max} is the maximum energy transfer and I is the mean excitation potential. If the transferred energy is sufficient to ionize the atoms, the track of the passing particle can be made visible. The *BABAR* detector implements this method in a two-stage tracking system which consists of an inner silicon vertex tracker and an outer drift chamber. Both stages are placed inside the magnetic field B which forces each single charged particle with transverse momentum p_t onto a circular path with radius $r = p_t/B$. The combined effects of energy loss and magnetic deflection render the tracks into helices.

The silicon vertex tracker (SVT) consists of 5 layers of silicon micro-strip detectors. These are 300 μm thick n-type silicon wafers with p⁺-type and n⁺-type readout strips on opposite sides.⁶ Charge carrier diffusion at the np⁺ junction creates a depletion⁷ zone which is expanded over the whole detector volume by an external voltage of 25–35 V. Ionization of the silicon atoms by charged particles creates new charge carriers that are transported in the electric field and collected in the strips. The strips on both sides of the wafers are placed orthogonally to each other, thus allowing a measurement of both the longitudinal distance z and the azimuthal angle φ . A total of 340 detectors and the readout electronics for approximately 150,000 channels are organized in 40–240 mm long modules and arranged azimuthally around the beam axis. The arrangement of all 52 modules is shown in Fig. 1.3. The whole SVT structure is fixed by a carbon fiber space frame and mounted inside the 20 cm inner radius of the support tube that also houses the beam pipe and several PEP-II magnets. This central placement and a strip pitch of 50–100 μm allow the inner silicon layers to reconstruct the primary decay vertices with a resolution of $\sigma_z = 55 \mu\text{m}$. The outer layers mainly serve for alignment with the drift chamber. The SVT is also the only system for reconstruction of tracks with a transverse momentum $p_t < 100 \text{ MeV}/c$.

The drift chamber (DCH) is used for the resolution of secondary vertices and the reconstruction of all tracks with a transversal momentum $p_t \geq 100 \text{ MeV}/c$. It consists of 40 concentric layers of aluminum wires that are spanned azimuthally around the beam axis in a gas mixture of 80% helium and 20% isobutane. Each layer consists of 96–256 hexagonal cells of field wires with one sense wire in the center of each cell. While the field wires are grounded, the sense wires are kept at a potential of 1–1.6 kV. Upon ionization of the gas atoms in a cell by passing charged particles, the freed electrons start drifting toward the sense wire. On their way they ionize more atoms, so that after a known drift time a cascade of $\mathcal{O}(10^4)$ electrons is collected. The actual gain is continuously updated from the analysis of collision events. The DCH layers are grouped into 10 superlayers, the first four of which are shown in Fig. 1.4. They alternate as indicated in their axial adjustment, allowing both the longitudinal and the azimuthal positions of tracks to be

⁵The term “collision” here stands for all excitation and ionization effects caused by Coulomb forces.

⁶A n⁽⁺⁾-type semiconductor is (heavily) doped with electron donors. A p⁽⁺⁾-type semiconductor is (heavily) doped with electron acceptors.

⁷“Depletion” means the absence of any charge carriers.

measured. The azimuthal resolution is $\sigma_\varphi = 1$ mrad. The collected charge measures the energy loss dE/dx with a resolution of 7.5%. The wires reach from $z = -102$ cm in backward direction to $z = 175$ cm in forward direction and are held by conical end plates. The backward end plate also holds the high voltage supplies and the readout electronics of the 7,104 channels. Both end plates and the inner and outer walls, which are mounted at radii of 22.5 cm and 80 cm, respectively, are made of carbon fiber. Fig. 1.5 shows the joint distribution of dE/dx and momentum measured in the DCH. Single particle species can be identified by the superimposed predictions of the Bethe–Bloch formula.

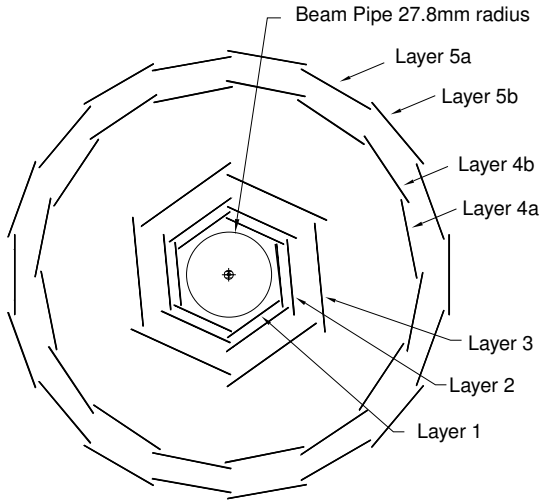


Figure 1.3 Transverse section of the silicon vertex tracker [12]. The inner layers (1–3) measure the vertex position. The outer layers (4, 5) serve for alignment with the drift chamber.

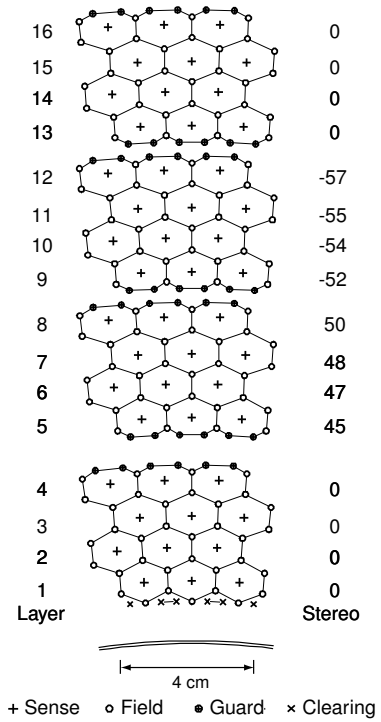


Figure 1.4 Transverse section of the innermost four superlayers of the drift chamber [12].

Tracks in the tracking system are parameterized by the vector $(d_0, \varphi_0, \omega, z_0, \tan \lambda)$ of the coordinates (d_0, φ_0, z_0) of the point of closest approach (POCA) to the z axis, the inverse transverse momentum $\omega = 1/p_t$ and the dip λ to the transverse plane at this point. The track parameters are fitted to the single position, time and energy measurements using a Kalman algorithm [13] which takes into account the distributions of the magnetic field and the detector material. The time-distance relation of the drift is calibrated with e^+e^- and $\mu^+\mu^-$ events. Two separate algorithms recover helices that end in the SVT or tracks that are scattered in the material between SVT and DCH. The POCA coordinates, which are mainly determined by the SVT measurements, achieve resolutions of $\sigma_{d_0} = 23 \mu\text{m}$, $\sigma_{\varphi_0} = 0.43$ mrad and $\sigma_{z_0} = 29 \mu\text{m}$. The dip resolution is $\sigma_{\tan \lambda} = 0.53 \times 10^{-3}$, and the transverse momentum resolution can be parameterized by

$$\frac{\sigma_{p_t}}{p_t} = 0.13\% \frac{p_t}{\text{GeV}/c} + 0.45\%. \quad (1.22)$$

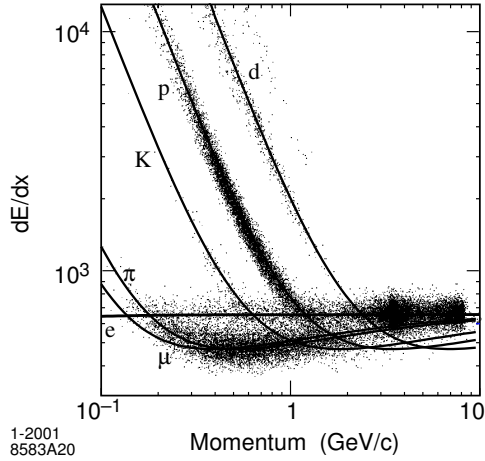


Figure 1.5 Joint distribution of energy loss per path length dE/dx and momentum measured in the drift chamber for electrons (e), muons (μ), pions (π), kaons (K), protons (p) and deuterons (d) [12]. Superimposed are the predictions of the Bethe–Bloch formula (Eq. 1.21). Muons and pions are indistinguishable. Pions and kaons can only be separated at momenta below $0.7 \text{ GeV}/c$.

1.2.3 Particle Identification

As seen in figure Fig. 1.5, pions and kaons can be separated by their energy loss dE/dx at momenta below $0.7 \text{ GeV}/c$. An efficient reconstruction of hadronic events, however, requires reliable particle identification over the full kinematic range. To provide for this, a novel device has been designed for use in the *BABAR* detector. It measures the velocity of charged particles by detection of internally reflected Cherenkov light (DIRC). Its overall layout is shown in Fig. 1.6. It consists of 144 bars of fused silica that are optically connected to a steel standoff box at the backward end of the detector. The 1.7 cm thick bars reach from $z = -315 \text{ cm}$ to $z = 175 \text{ cm}$ and are arranged in 12 planar sectors around the drift chamber. The sectors are separately sealed and mounted between two aluminum support cylinders. The energy deposited in the bar material by passing charged particles polarizes the molecules which emit photons in instant transitions to their ground states. The material is chosen such that the velocity of the emitted photons is smaller than the velocity of the passing particles. Hence these photons form a plane electromagnetic shock wave known as Cherenkov light.⁸ From geometrical considerations it is apparent that the Cherenkov angle ϑ_C between the path of the particle and the direction of the light depends on the particle velocity β as

$$\cos \vartheta_C = \frac{1}{\beta n}, \quad (1.23)$$

where the refraction index n of the material depends on the light frequency. The produced Cherenkov light is transported inside the bars by internal reflection. Light in forward direction is reflected by mirrors on the forward ends, and all light is transferred through a backward window into the standoff box. The standoff box is filled with purified water, which has a refraction similar to the silica and transports the light over a radius of 1.17 m to the outer wall, where it is detected by an array of 10,752 photomultiplier tubes (PMT's). The PMT's, which operate outside the magnetic field of the coil, use the photoelectric effect to convert photon radiation into an electric current and are read out from the outer side of the wall. The Cherenkov angle is preserved over the full light transfer and reconstructed from the detection time, the PMT position and the

⁸Cherenkov light is a “density correction” to the Bethe–Bloch formula (Eq. 1.21).

DCH track direction with a resolution of $\sigma_{\vartheta_C} = 2.5$ mrad. The DIRC identifies kaons with momenta up to 3.5 GeV/ c with an efficiency larger than 90% while misidentifying pions as kaons with a probability smaller than 12%.

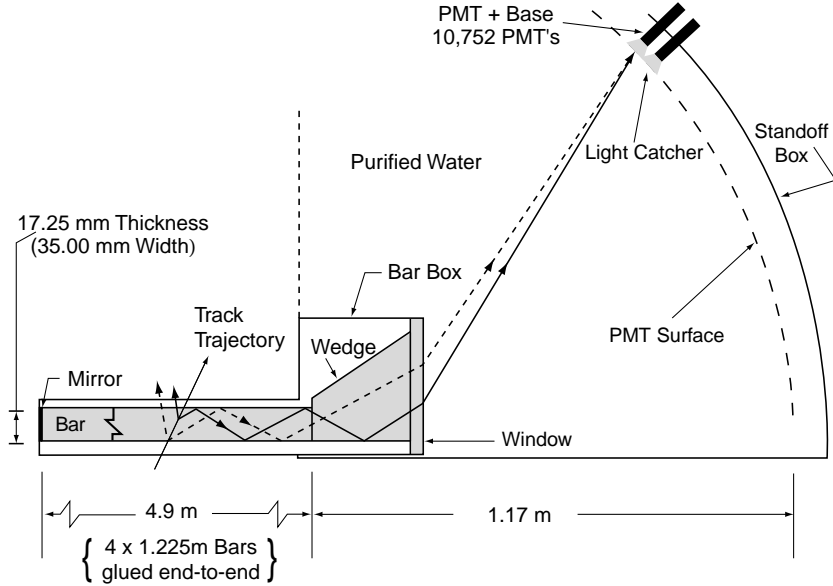


Figure 1.6 Longitudinal section of the DIRC (seen against the x axis) [12]. The Cherenkov light emitted along the track trajectory is transported inside the silica bars by internal reflection and detected by a PMT array outside the magnetic field.

1.2.4 Electromagnetic Calorimeter

While charged particles are detected by their energy loss in the tracking system, photons pass this system unobserved. The presence of π^0 and η mesons in B meson decays, however, leads to the production of equal amounts of charged particles and photons. For detection of the photons, an electromagnetic calorimeter (EMC) is installed in the space between the DIRC and the magnet coil. The EMC consists of 6580 thallium-doped cesium iodide (CsI(Tl)) crystals that are distributed over a cylindrical barrel and a conical forward end cap.

Two related processes provide for detection of the photons: pair production and bremsstrahlung.⁹ Pair production is the process in which a photon converts into an electron-positron pair. Bremsstrahlung is the process in which an electron loses part of its energy by emission of a photon. Both processes can only conserve energy and momentum by additional interactions with surrounding matter.¹⁰ In CsI, the mean path of a photon before pair production is $X_0 = 1.85$ cm. Over the next radiation length X_0 , both the electron and the positron produced emit on average one bremsstrahlung photon. The continuation of this cycle leads to an electromagnetic shower that consists of $N \approx 2^t$

⁹“Bremsstrahlung”, adopted from German, means “deceleration radiation”.

¹⁰In the Feynman picture, this is described by the exchange of virtual photons.

particles after t radiation lengths. If the original photon had the energy E_0 , the shower particles have energies $E \approx E_0/N$. The shower propagates until the electrons are slowed down to the critical energy E_c at which the energy loss in collisions, described by Eq. 1.21, becomes dominating. Since this energy loss rises with falling electron velocity, the shower ceases after $t_{\max} \approx \log_2(E_0/E_c)$. That means that a photon with the maximum energy of $E_0 = 6 \text{ GeV}$ is stopped in CsI, which has a critical energy of $E_c = 10 \text{ MeV}$, at $x_{\max} \approx 17 \text{ cm}$. To minimize energy leakage, the length of the EMC crystals ranges from 29.6 to 32.4 cm. The transverse dimension of the shower is described by the Moliere radius

$$R_M = X_0 \frac{E_s}{E_c} \quad (1.24)$$

and the multiple scattering energy $E_s = 21.2 \text{ MeV}$ [14]. More than 90% of the shower is contained within a distance of $2R_M$ from the longitudinal axis. The resulting Moliere radius for CsI is 3.8 cm. Since 50% of the photons from B meson decays have energies $E_0 < 200 \text{ MeV}$ and the energy deposited in each crystal must be separated from electronic noise, the transverse width of the crystals is chosen larger than R_M . Their trapezoidal cross section rises from $4.8 \times 4.7 \text{ cm}$ on the front face to $6.1 \times 6.0 \text{ cm}$ on the back face.

After the shower is absorbed into atomic excitations, the CsI acts as a scintillator: it reemits the absorbed energy as visible light. This light is detected by two silicon photodiodes glued to the crystal back face. In the depletion zone of these silicon detectors (see Sec. 1.2.2), photons create charge carriers by the photoelectric effect. The light response of each crystal is regularly calibrated at two distinct energies: Photons of 6.13 MeV are induced by a radioactive fluid that is circulated through aluminum pipes in front of the crystals. Between 3 and 9 GeV, the correlation between energy and polar angle of electrons in e^+e^- events is used. The response between these energies is interpolated logarithmically. For measurement of the readout linearity and for short-term monitoring, the EMC is equipped with a light pulser system that induces a set amount of light into each crystal. Two low-noise preamplifiers are integrated with the diodes in an aluminum frame. The analog signals from the preamplifiers include two fixed amplifications. They are combined with two further amplification steps and digitalized in the readout electronic boards on the backward end of the detector. The resulting energy ranges are 0–50 MeV, 50–400 MeV, 0.4–3.2 GeV and 3.2–13.0 GeV.

Each crystal is wrapped into a sequence of reflecting and insulating foils and fitted into a $300 \mu\text{m}$ strong carbon fiber compartment. The complete support and readout structure is shown in Fig. 1.7. In the barrel region, 21 compartments form a module, and each module is separately mounted to an external aluminum support structure. The barrel consists of 48 rings to 120 crystals. The barrel rings cover the polar angle between 27° and 141° . In the end cap, 41 compartments form a module, and a total of 20 modules makes up 8 rings. The end cap rings cover the polar angle between 16° and 27° . Each ring has a non-projectivity of 15–45 mrad to reduce the energy loss between the compartments. The whole EMC is surrounded by a double-layered aluminum Faraday shield and kept under a temperature controlled nitrogen atmosphere.

Electromagnetic showers in the EMC are produced by photons and by electrons. In addition, charged pions and kaons produce hadronic showers (see Sec. 1.2.5), which have electromagnetic components. The different shapes of these showers contribute to particle identification. Each shower deposits its energy into a cluster of neighboring

crystals. Each observed energy cluster, however, can originate from multiple showers. To find all showers, the clusters are split into “bumps”. Each bump represents a local maximum of the crystal energies. The bump energy

$$E_0 = \sum_{i=1}^{N_c} \epsilon_i E_i \quad (1.25)$$

is the fraction of the energies E_i of all N_c crystals in the cluster given by the weights ϵ_i . The bump centroid

$$\mathbf{r}_0 = \frac{\sum_{i=1}^{N_c} \rho_i \mathbf{r}_i}{\sum_{i=1}^{N_c} \rho_i} \quad (1.26)$$

is the center of gravity of the crystal coordinates \mathbf{r}_i calculated with the weights ρ_i . The weights ϵ_i and ρ_i for all N_b bumps are found by iteration of a two-step algorithm. In the first step, the centroids \mathbf{r}_0 are calculated from

$$\rho_i = 4 + \ln \left(\frac{\epsilon_i E_i}{E_0} \right), \quad (1.27)$$

where the energy weights are initialized by $\epsilon_i = 1$. In the second step, the energy weights are calculated from the crystal distances $R_i = |\mathbf{r}_i - \mathbf{r}_0|$ and the Moliere radius R_M by

$$\epsilon_i = \frac{E_i e \left(-2.5 \frac{R_i}{R_M} \right)}{\sum_{j=1}^{N_b} E_j e \left(-2.5 \frac{R_j}{R_M} \right)}. \quad (1.28)$$

The iteration ends when the centroids are stable within 1 mm. The achieved resolution in both angular coordinates depends on the energy E by

$$\sigma_\theta = \sigma_\phi = \frac{3.87 \text{ mrad}}{\sqrt{\frac{E}{\text{GeV}}}}. \quad (1.29)$$

The energy resolution can be expressed by the quadratic sum

$$\frac{\sigma_E}{E} = \frac{2.3\%}{\sqrt[4]{\frac{E}{\text{GeV}}}} \oplus 1.9\%. \quad (1.30)$$

By matching the bump centroids with track positions, showers from charged particles are identified. By evaluating the ratio of bump energy and track momentum, (pure) electromagnetic and hadronic showers are separated.

1.2.5 Instrumented Flux Return

Since muons and pions have almost the same mass, they are indistinguishable in the tracking system and the DIRC. In the EMC, muons only deposit collision energy, while

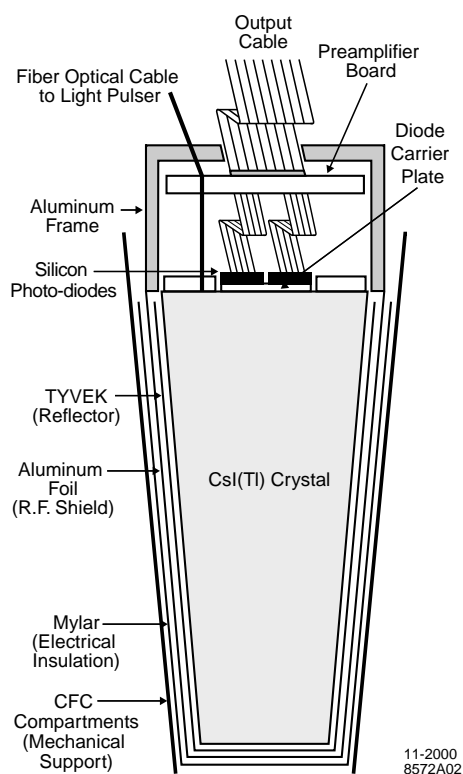


Figure 1.7 Longitudinal section of a thallium-doped cesium iodide (CsI(Tl)) crystal used in the electromagnetic calorimeter (EMC) [12]. The crystal is wrapped into insulating and reflecting foils and fitted into a carbon fiber compartment. Two photodiodes and preamplifiers for the light readout are integrated in an aluminum frame. An optical cable from the light pulser system induces a set amount of light.

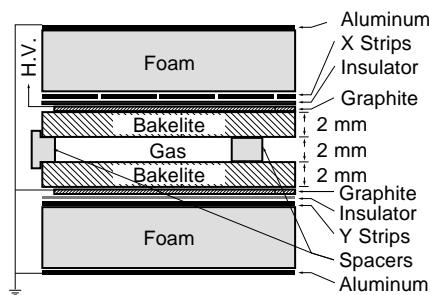


Figure 1.8 Cross section of a resistive plate chamber (RPC) used in the instrumented flux return (IFR) [12]. The active volume consists of a 2 mm wide gas gap under a voltage of approximately 8 kV.

pions start showering. The measured energy, however, is of the same order. Another unidentified species are K_L^0 mesons from B meson decays, which start showering in the EMC, but do not deposit all their energy. These ambiguities are resolved in interactions with the massive iron yoke that surrounds the magnet coil and returns the magnetic flux into the detector. All hadrons lose their energy in hadronic showers. Unlike electromagnetic showers, these showers are spawned by inelastic collisions with atomic nuclei. Most of the particles produced in these collisions are pions. Since on average one third of them is neutral and decays rapidly into photons, hadronic showers have sizeable electromagnetic components. While these components proceed until the electrons reach the critical energy (see Sec. 1.2.4), the hadronic propagation stops as soon as the energy of the hadrons sinks under the threshold for pion creation. The remaining energy of both components is lost in ionization.

Due to their hadronic showering, pions are stopped in the flux return measurably before the muons which do not take part in hadronic interactions. On the neutral side, isolated showers in the EMC that continue in the flux return are identified as K_L^0 mesons. Although the detectable energy in their hadronic showers fluctuates strongly, their momenta in the boosted B meson decays are sufficiently correlated to their polar angles. To uncover the paths of muons and hadrons, the hexagonal flux return is segmented into single layers that increase in width from 2 cm at the inside to 10 cm at the outside of the detector. The 3.2–3.5 cm wide gaps between these layers are instrumented with a total of 742 resistive plate chambers (RPC's). 19 RPC layers are installed in the central barrel, and 18 layers in each of the end caps. 64 more RPC's are arranged in two cylindrical layers around the magnet coil. The RPC's consist of two 2 mm strong bakelite sheets

that are kept at a distance of 2 mm by aluminum frames and polycarbonate spacers. The external surfaces of the sheets are coated with graphite and connected to a high voltage of approximately 8 kV against each other. The gaps between the sheets are filled with a gas mixture of 56.7% Argon, 38.8% Freon 143a and 4.5% isobutane that is continuously replaced. If the gas atoms are ionized, the strong electric field causes multiple electron cascades (see Sec. 1.2.2) that are eventually “quenched” by the Freon molecules. The charge signals are read out by aluminum strips that are capacitively coupled to the external surfaces of the sheets. The strips are arranged in two orthogonal directions and provide both longitudinal and azimuthal position measurements with angular resolutions of the order of 60 mrad. The strips are separated from the aluminum frame by two 4 mm thick foam sheets. They make a total of 38,500 channels with readout electronics installed in the iron gaps or just outside the detector. Fig. 1.8 shows the complete RPC layout. By the instrumented flux return (IFR) concept, muons are identified with an efficiency of 90%, while the probability for misidentifying hadrons as muons is smaller than 8%.

1.2.6 Data Acquisition

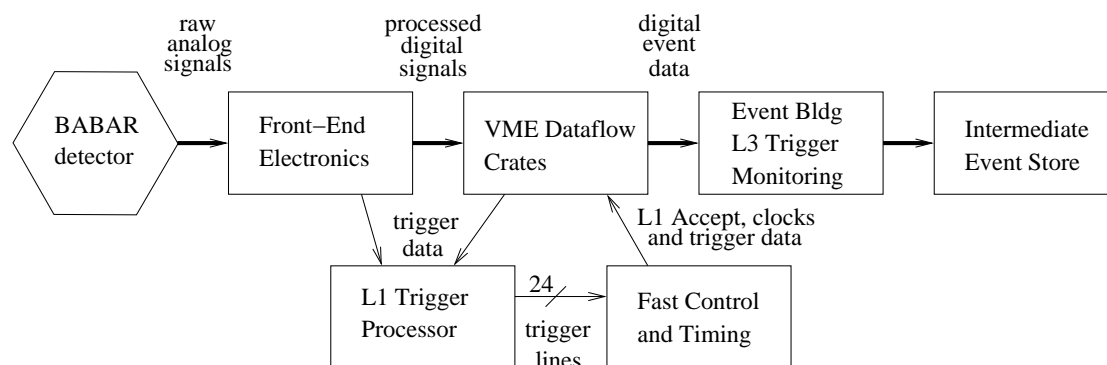


Figure 1.9 Map of the data acquisition system of the *BABAR* detector [12].

A map of the data acquisition (DAQ) system of the *BABAR* detector is shown in Fig. 1.9. The DAQ system is a federation of specialized subsystems that satisfies the needs for high precision and high volume data processing. The front-end electronics (FEE’s) of all detector systems are installed on the detector. They shape and digitalize the analog signals and send them at a rate of 1.2 Gbit/s via optical fibers to the external readout modules (ROM’s). The ROM’s are 157 Motorola *PowerPC*s running the real-time operating system *VxWorks*. They are distributed over 23 *VME* crates that constitute the online data flow (ODF) system. In the ROM’s, the detector data are compressed to their relevant “features” and buffered for event building. The first trigger level (Level 1) is hosted by 5 more *VME* crates. To assure redundancy and flexibility of data acquisition, the Level 1 trigger contains separate processors for DCH, EMC and IFR. The trigger processors receive hit patterns from the FEE’s and ROM’s and generate trigger signals on 24 trigger lines at a rate of 2 kHz. The trigger lines are linked to the fast control and timing system (FCTS) which consists of one *VME* crate and one dedicated module

in each ODF crate. The FCTS propagates each trigger “accept” signal to the ROM’s and initiates the event building cycle. This cycle proceeds in four nested steps the last of which is propagated to the online event processing (OEP) branch of an online computing farm. The computing farm consists of 32 Sun workstations running under the *Solaris* operating system and is connected to the ODF crates via a 100 Mbit/s Ethernet. The farm also hosts the second active trigger level (Level 3) that filters the events by physics content and reduces their rate to 120 Hz. The events are written to disk in an intermediate format and passed to the online prompt reconstruction (OPR) branch.

In OPR, the events are exposed to a first analysis and prepared for final storage. The immediate analysis of the physics content helps the detector operators assure a constant data quality. The final storage of the event data is organized in 5 categories.¹¹ While the first category contains the raw output of the OEP system, the second category contains the tracks (see Sec. 1.2.2) and energy clusters (see Sec. 1.2.4) found by OPR. The third and fourth category are compressed versions of the former two, commonly referred to as data summary tapes (DST’s). They serve as input to offline reconstruction and physics analysis. The fifth category collects various tags that are assigned to the events by defined selection criteria. All categories of event data are stored in an object-oriented database. A separate such database contains the associated running conditions of the detector.

1.3 Software Infrastructure

The *BABAR* experiment provides a uniform software infrastructure. It is distributed over all collaborating institutes and supports both commercial and free (*Linux*) implementations of the *UNIX* operating platform. To enforce stability and flexibility, all developed code uses an object-oriented standard. The programming language of choice is *C++* [15]. Its modular design uses code classes as abstractions of hardware objects (e.g. single detector components) or physical objects (e.g. tracks or energy clusters). Specialized classes (e.g. particles of a certain species associated with a combination of tracks and energy clusters) are conveniently derived by the system of class inheritance. Established routines traditionally programmed in *Fortran* can be easily accessed via object-oriented interfaces.

The *BABAR* software infrastructure extends to real-time, online and offline applications. The separate software modules are pooled in approximately 1,600 software packages. While the code development is distributed over large parts of the collaboration, individual assignments of packages ensure code convergence and maintenance. Package evolution is managed by the commonly used versioning system *CVS*. Central package repositories are accessible via the network file system *AFS*. The network connection between different institutes is based on the Internet.¹²

Software packages for data analysis are issued in dedicated releases. While development releases are updated daily, extensively tested “production” releases persist over several

¹¹There is an additional category for Monte Carlo generated information.

¹²Interestingly, the Internet was initiated in 1969 with a network connection between the University of California, L. A., and the Stanford Research Institute. 22 years later, the Stanford Linear Accelerator Center hosted the first web page outside Europe.

years. As user interface, all releases contain an application framework. The framework processes all modules used in an application in predefined sequences. A configuration of modules and sequences in the script language *Tcl* is possible in both interactive and batch processing. All releases provide generic sequences for access to the databases, reconstruction of elementary physical objects and storage of individual results in a variety of formats. All application modules are derived from the class `AppModule` and implement the methods

```
AppResult beginJob(AbsEvent *);
AppResult beginRun(AbsEvent *);
AppResult event(AbsEvent *);
AppResult endRun(AbsEvent *);
AppResult endJob(AbsEvent *);
```

that are called by the framework for each new application, detector run or data event, respectively. The `AbsEvent` object referenced in the method arguments contains lists of all objects created by preceding modules. A global `AbsEnv` object provides access to running conditions and geometrical constants of the detector. The returned `AppResult` object notifies the framework about the processing success.

Chapter 2

The Decay $B^0 \rightarrow \eta\phi$

The decay $B^0 \rightarrow \eta\phi$ is a rare hadronic decay of the B meson. Its branching fraction is of the order of one in one million, which makes its analysis a challenging task. Nevertheless, the study of rare meson decays provides a unique insight into the basic structure of matter. Since such decays proceed through a variety of internal states, they expose the properties of highly virtual particles as well as possibly undiscovered interaction mechanisms.

The fundamental difficulty of a description of rare hadronic decays is the close relationship of weak and strong interactions. While the former can be conventionally treated by the means of perturbation theory, the latter reveal a scale dependence that makes this powerful procedure unreliable. As a consequence, theoretical predictions for the branching fractions of rare hadronic decays exhibit large uncertainties and pronounced model dependences.

This chapter reviews a common approach to accommodate this contrary situation. Sec. 2.1 introduces a five-quark effective theory that describes the essential properties of weak and strong interactions in a state-independent way. Sec. 2.2 shows the application and evaluation of this theory for the investigated B meson decay. Thereafter, Sec. 2.4 gives a summary of recently made predictions and measurements.

2.1 Effective Theory

The most basic description of a B meson decay is a tree-level W exchange between two left-handed quark currents (see Sec. 1.1.1)

$$J_{q_2 q_1} = \bar{q}_2 \gamma_\mu (1 - \gamma_5) q_1. \quad (2.1)$$

The amplitude

$$A = i \frac{G_F}{\sqrt{2}} V_{qb}^* V_{qd} \frac{M_W^2}{p^2 - M_W^2} J_{dq} J_{qb} \quad (2.2)$$

of the transition $b \rightarrow q\bar{q}d$, for instance, is given for $q = u, c$ in first order perturbation theory by the Fermi constant G_F [3], the CKM matrix elements V_{qb} and V_{qd} (see Sec.

¹Since $\bar{q}_2 \gamma_\mu q_1$ is a vector, while $\bar{q}_2 \gamma_\mu \gamma_5 q_1$ is an axial vector [3], J is called a “ $V - A$ ” current.

1.1.1), the mass M_W of the W boson and the momentum transfer p . Since the mass m_b of the b quark sets $p^2 = \mathcal{O}(m_b^2)$, but $M_W \gg m_b$, the W propagator in Eq. 2.2 can be expanded into

$$\frac{M_W^2}{p^2 - M_W^2} = - \sum_{n=0}^{\infty} \left(\frac{p^2}{M_W^2} \right)^n, \quad (2.3)$$

yielding in leading order the amplitude

$$A = -i \frac{G_F}{\sqrt{2}} V_{qb}^* V_{qd} J_{dq} J_{qb}. \quad (2.4)$$

It is natural to relate this amplitude to an effective Hamiltonian

$$\mathcal{H}_{\text{eff}} = \frac{G_F}{\sqrt{2}} \sum_{q=u,c} \xi_q O^{(q)} \quad (2.5)$$

built from CKM factors

$$\xi_q = V_{qb}^* V_{qd} \quad (2.6)$$

and local² current-current operators

$$O^{(q)} = J_{dq} J_{qb}. \quad (2.7)$$

The expression of the Hamiltonian in terms of local operators is known as operator product expansion [16]. In a generalized form, it states

$$\mathcal{H}_{\text{eff}} = \frac{G_F}{\sqrt{2}} \sum_i C_i \sum_{q_i} \xi_{q_i} O_i^{(q)}, \quad (2.8)$$

introducing the Wilson coefficients C_i . The benefit of this parameterization is that the Wilson coefficients do not depend on the external states and can absorb quantum corrections to the transition amplitude. The most sizable corrections come from quantum chromo-dynamics (QCD), i.e. the strong interactions between the quarks. To determine all relevant C_i , the effective amplitude (Eq. 2.4) is “matched” to the full amplitude (Eq. 2.2) in first order perturbation theory including the QCD corrections sketched in Fig. 2.1. The presence of gluon links between the quark currents in Eq. 2.7 distinguishes the color structures of the operators

$$O_1^{(q)} = \sum_{ij} J_{d_i q_j} J_{q_j b_i}, \quad (2.9)$$

$$O_2^{(q)} = \sum_{ij} J_{d_i q_i} J_{q_j b_j}, \quad (2.10)$$

where $i, j = r, g, b$ are color indices.

Since the application of perturbation theory involves an expansion in the strong coupling constant α_s , it is only justified for $\alpha_s \ll 1$. Due to the property of asymptotic freedom [3], this condition is satisfied for strong interactions at short distances. While the energy scale m_b gives the W boson a virtuality so high that the weak interaction of

²The term “local” refers to the absence of the propagator.

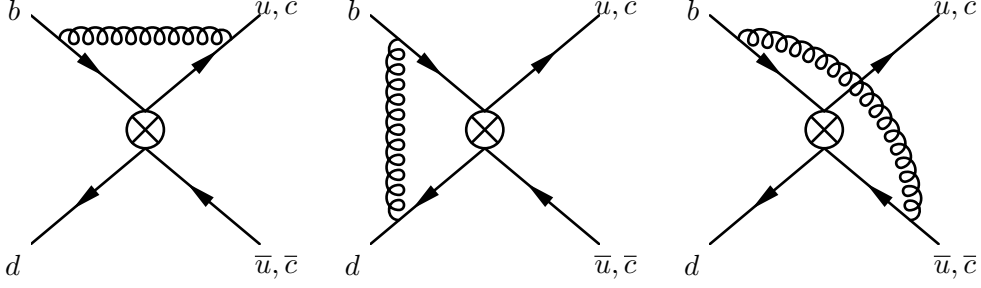


Figure 2.1 First order QCD corrections to the current-current operators $O^{(u)}$ and $O^{(c)}$ (Eq. 2.7). The crossed circles represent effective vertices. Gluon links between the currents distinguish the color structures of the operators O_1 and O_2 (Eq. 2.9 and 2.10).

the quarks becomes local, the corresponding virtualities of the gluons are much smaller, and the strong interactions have a finite distance. Since even lower scales drive $\alpha_s > 1$, it is desirable to restrict the Wilson coefficients to *short*-distance QCD corrections, while including *long*-distance QCD effects in the matrix elements of the local operators. Formally, the removal of the W boson from the full amplitude (Eq. 2.2) constitutes an integration over a (virtual) momentum p' , where the splitting

$$\int_{-p^2}^{M_W^2} \frac{dp'^2}{p'^2} = \int_{\mu^2}^{M_W^2} \frac{dp'^2}{p'^2} + \int_{-p^2}^{\mu^2} \frac{dp'^2}{p'^2} \quad (2.11)$$

$$\ln \frac{M_W^2}{-p^2} = \ln \frac{M_W^2}{\mu^2} + \ln \frac{\mu^2}{-p^2} \quad (2.12)$$

at $\mu^2 = \mathcal{O}(m_b^2)$ separates the energy scales $m_b \dots M_W$ and $0 \dots m_b$. The factorization of Eq. 2.8 is achieved at first order in α_s by [17]

$$1 + G \alpha_s \ln \frac{M_W^2}{-p^2} = \left(1 + G \alpha_s \ln \frac{M_W^2}{\mu^2} \right) \left(1 + G \alpha_s \ln \frac{\mu^2}{-p^2} \right), \quad (2.13)$$

where G is an appropriate compound term. Apparently, both the Wilson coefficients and the local operators depend on the splitting scale μ . Since μ is also the proper renormalization scale, but the perturbation theory applied is renormalized at the scale M_W , the Wilson coefficients have to be readjusted. On the contrary, the adjusted expansion parameter $\alpha_s(\mu) \ln(M_W/\mu) \approx 1$ spoils the perturbation series. It turns out that both problems can be solved by the renormalization group. First it resums all orders n of perturbation theory to order m of the improved expansion parameter

$$\alpha_s^m \sum_{n=0}^{\infty} \left(\alpha_s \ln \frac{M_W}{\mu} \right)^n, \quad (2.14)$$

then it evolves the Wilson coefficients by a matrix equation

$$C_i(\mu) = \sum_j U_{ij} C_j(M_W) \quad (2.15)$$

of the desired “logarithmic” order [17].³

So far, the effective Hamiltonian (Eq. 2.8) includes two current-current operators (Eq. 2.9 and 2.10) with renormalization group improved Wilson coefficients. However, first order QCD corrections generate additional operators, as shown in Fig. 2.2. These operators are characterized by an internal quark loop, which due to the mass dependence of the transition amplitudes [9] is dominated by a (virtual) top quark. Inspired by its shape, Fig. 2.2(a) is called a “penguin diagram”.⁴ The “penguin operators” have the standard representations

$$O_3^{(t)} = \sum_{q=u,d,s,c,b} \sum_{ij} J_{d_i b_i} J_{q_j q_j}, \quad (2.16)$$

$$O_4^{(t)} = \sum_{q=u,d,s,c,b} \sum_{ij} J_{d_i b_j} J_{q_j q_i}, \quad (2.17)$$

$$O_5^{(t)} = \sum_{q=u,d,s,c,b} \sum_{ij} J_{d_i b_i} J'_{q_j q_j}, \quad (2.18)$$

$$O_6^{(t)} = \sum_{q=u,d,s,c,b} \sum_{ij} J_{d_i b_j} J'_{q_j q_i}, \quad (2.19)$$

where $i, j = r, g, b$ are again color indices and

$$J'_{q_2 q_1} = \bar{q}_2 \gamma_\mu (1 + \gamma_5) q_1 \quad (2.20)$$

is a right-handed quark current.⁵ In Fig. 2.2(b) the top quark with a mass $m_t \gg m_b$ is removed by the operator product expansion (Eq. 2.3), leaving a five-quark effective theory.

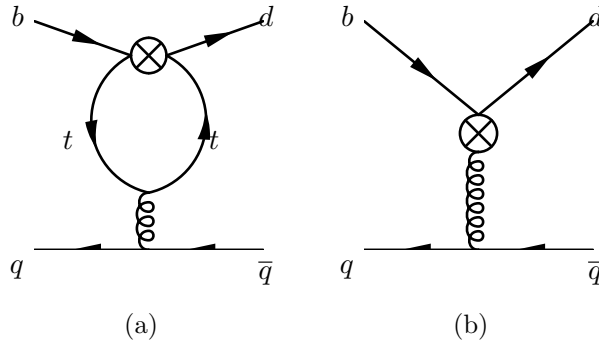


Figure 2.2 First order QCD correction generating the penguin operators O_3 to O_6 (Eq. 2.16 to 2.19) before (a) and after (b) integrating out the top quark. The crossed circles represent effective vertices.

³Representations of U_{ij} and Wilson coefficients for the leading and next-to-leading logarithmic order can be found in [17].

⁴The name “penguin diagram” was first used by J. R. Ellis on page 12 of [18]. After he had “smoked some illegal substance”, he found the diagram appropriate to redeem a dart bet by using the word “penguin” in one of his publications [19].

⁵Since q does not couple to the W boson, its current has a left-handed (“ $V-A$ ”) and a right-handed (“ $V+A$ ”) component (see also footnote 1 on page 33).

2.2 Decay Amplitude

Neutral B mesons are formed from b and d quarks in the states

$$|B^0\rangle = |d\bar{b}\rangle, \quad (2.21)$$

$$|\bar{B}^0\rangle = |b\bar{d}\rangle. \quad (2.22)$$

This analysis searches for the decay of $|B^0\rangle$ or $|\bar{B}^0\rangle$ into the state $|\eta\phi\rangle$, where

$$|\eta\rangle = \frac{1}{\sqrt{6}} (|u\bar{u}\rangle + |d\bar{d}\rangle - 2|s\bar{s}\rangle) \quad (2.23)$$

is part of the nonet of pseudoscalar mesons and

$$|\phi\rangle = |s\bar{s}\rangle \quad (2.24)$$

is part of the nonet of vector mesons formed from u , d and s quarks [3]. This decay is described in lowest order perturbation theory by the three Feynman diagrams shown in Fig. 2.3. In the five-quark effective theory outlined in Sec. 2.1, these diagrams exclusively generate penguin operators (Eq. 2.16 to 2.19), and $B^0 \rightarrow \eta\phi$ is a “pure penguin decay”. Note, however, that a minimum of three gluons is needed in Fig. 2.3(c) to produce the $|s\bar{s}\rangle$ state as a color singlet with spin $j = 1$ [3]. Since these gluons also carry the full momentum of the ϕ meson, their coupling is suppressed by the OZI rule [3]. In Fig. 2.3(a) and (b), the gluons are replaced by either a photon or a Z^0 boson. In a coarse comparison of the strong coupling $\mathcal{O}(\alpha_s^3)$ at the b quark mass with the electroweak coupling $\mathcal{O}(\alpha)$ these diagrams contribute 10–50% to the transition amplitude. Hence, additional “electroweak penguin operators” $O_7 - O_{10}$ have to be considered in the effective Hamiltonian (Eq. 2.8). Because Eq. 2.15 “mixes” the structures of all addends, these operators are up to a factor 3/2 identical to the operators $O_3 - O_6$ (Eq. 2.16–2.19).

A determination of the decay amplitude

$$A = -i \langle \phi\eta | \mathcal{H}_{\text{eff}} | B^0 \rangle \quad (2.25)$$

requires the evaluation of the matrix elements

$$M_i = \langle \phi\eta | O_i^{(t)} | B^0 \rangle \quad (2.26)$$

of the local operators $i = 3 \dots 10$. However, this is simplified by exploiting relations between them. Firstly, the “color-mismatched” matrix elements M_4, M_6, M_8, M_{10} are suppressed by the number of colors N_c with respect to the “color-matched” matrix elements M_3, M_5, M_7, M_9 . Secondly, the “ $V - A$ ” currents J_{ss} in M_3, M_4, M_9, M_{10} and the “ $V + A$ ” currents J'_{ss} in M_5, M_6, M_7, M_8 contribute equal amounts. Hence, the amplitude can be expressed as

$$A = -i \frac{G_F}{\sqrt{2}} V_{tb}^* V_{td} \left(a_4 + a_6 + \frac{3}{2} a_8 + \frac{3}{2} a_{10} \right) M_3, \quad (2.27)$$

where

$$a_{2i} \equiv C_{2i-1} + \frac{1}{N_c} C_{2i} \quad (2.28)$$

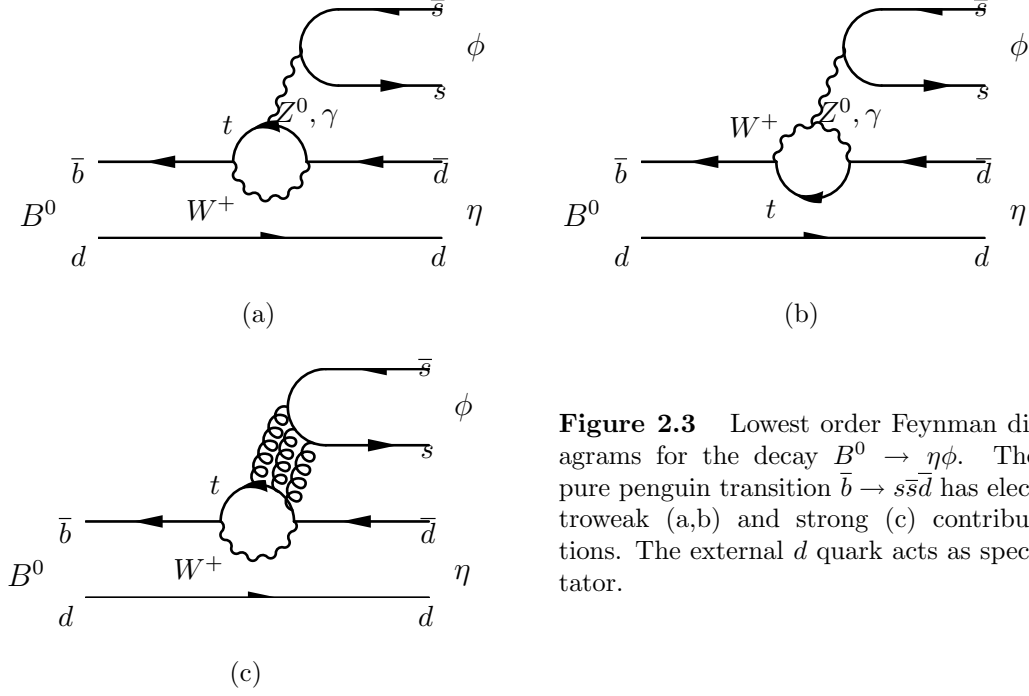


Figure 2.3 Lowest order Feynman diagrams for the decay $B^0 \rightarrow \eta\phi$. The pure penguin transition $\bar{b} \rightarrow s\bar{s}d$ has electroweak (a,b) and strong (c) contributions. The external d quark acts as spectator.

and

$$M_3 = \sum_{i=1}^{N_c} \sum_{j=1}^{N_c} \langle \phi\eta | J_{d_i b_i} J_{s_j s_j} | B^0 \rangle. \quad (2.29)$$

Since the matrix elements, which describe the long-distance strong interactions of the quarks, cannot be expanded in the strong coupling constant α_s (see Sec. 2.1), the usual approach is to expand them in the inverse number of colors $1/N_c$ and drop all non-leading terms. This, of course, is an approximation that has to be justified by measurements. Indeed, a comparison of hadronic and semileptonic B meson decays [20] suggests a value $N_c \rightarrow \infty$. In the theory of the $1/N_c$ expansion [21], this has important implications:

- Decays of mesons containing a heavy and a light quark are only determined by the heavy “valence quark”. The light quark acts as external “spectator”.
- The decay matrix elements factorize into simple single-current matrix elements.
- All interactions between the final states vanish.

As a consequence, the matrix element M_3 (Eq. 2.29) factorizes as

$$\langle \phi\eta | J_{db} J_{ss} | B^0 \rangle = \langle \phi | J_{ss} | 0 \rangle \langle \eta | J_{db} | B^0 \rangle. \quad (2.30)$$

The remaining single-current matrix elements are further decomposed into form factors that have to be calculated in a chosen physics model.

2.3 Experimental Importance

The study of pure penguin decays is essential to the physics program of the *BABAR* experiment. As outlined in Sec. 1.1.3, the search for new physics is an important part of this program. Penguin transitions are especially sensitive to undiscovered particles because highly virtual particles can even occur in the internal loop. Popular candidates for such particles come from additional fermion families, extended Higgs fields or supersymmetry partners [7]. While penguin transitions contribute to most decays, they are usually suppressed by coupling constants and CKM matrix elements. In pure penguin decays, however, even smallest effects of new physics become visible.

Conclusions about penguin amplitudes also benefit the understanding of decays with penguin contributions. An especially interesting aspect is the interference of “weak” phases φ_i from CKM matrix elements and “strong” phases δ_i from the matrix elements of “magnetic” penguin operators [17]. For i participating transition amplitudes, the decay amplitude takes the form

$$A = \sum_i A_i e^{i(\varphi_i + \delta_i)}. \quad (2.31)$$

Since the weak phases change their sign under CP conjugation, while the strong phases remain unchanged, the CP conjugate amplitude \bar{A} generally differs by

$$|A|^2 - |\bar{A}|^2 = -2 \sum_{ij} A_i A_j \sin(\varphi_i - \varphi_j) \sin(\delta_i - \delta_j). \quad (2.32)$$

In the classification given in Sec. 1.1.2, penguin amplitudes are a source of CP violation in B meson decays. This fact was proven by the observation of CP violation in the decay $B^0 \rightarrow K^+\pi^-$ at the *BABAR* experiment [22].

Finally, CP violation in the interference of $B^0\bar{B}^0$ mixing and B^0 decays is also influenced by penguin amplitudes. The time-dependent CP asymmetry (Eq. 1.11 and 1.12) of the decays $B^0 \rightarrow \pi\pi$ and $B^0 \rightarrow \rho\rho$, for instance, measures the angle α (Eq. 1.5) of the Unitarity Triangle. The penguin and tree amplitudes of these decays compete because the involved CKM matrix elements V_{ub} and V_{td} (Eq. 1.2 and 1.3) are of the same order of magnitude. Since only the tree amplitudes are color-matched in the charged channels $B^0 \rightarrow \pi^+\pi^-$ and $B^0 \rightarrow \rho^+\rho^-$, while only the penguin amplitudes are color-matched in the neutral channels $B^0 \rightarrow \pi^0\pi^0$ and $B^0 \rightarrow \rho^0\rho^0$, a comparison of the decay rates in these channels helps estimate the “penguin pollution” of a measurement of α . The *BABAR* collaboration has refined this estimate by the observation of the decay $B^0 \rightarrow \rho^+\rho^-$ [23] and the reduction of the uncertainty on the unobserved decay $B^0 \rightarrow \rho^0\rho^0$ [24]. While these results hint on a rather small penguin amplitude, the *BABAR* collaboration has observed an unexpectedly large rate for the decay $B^0 \rightarrow \pi^0\pi^0$ [25]. This puzzle is proof for the utility of studying penguin amplitudes under the clean conditions of pure penguin decays.

2.4 Predictions and Measurements

The theoretical predictions for the branching fraction $\mathcal{B}(B^0 \rightarrow \eta\phi)$ presented here are based on the effective Hamiltonian for b quark transitions developed in [26]. The

renormalization group improved Wilson coefficients (Eq. 2.15) are calculated in next-to-leading logarithmic order so as to

- test the validity of the perturbation theory applied,
- make the renormalization scale and scheme dependences explicit and
- gain sensitivity for the mass of the (virtual) top quark.

As an additional feature, the two-loop QCD applied yields non-vanishing values for the Wilson coefficients of the color-matched penguin operators O_3 and O_5 (Eq. 2.16 and 2.18). This was first reported in 1993 by Du and Xing [27] who called Fig. 2.3 the “hairpin diagram”. For evaluation of the matrix element M_3 (Eq. 2.29) these authors use the form factors calculated by Bauer, Stech and Wirbel [28] from relativistic oscillator potentials. They cite branching fractions for $N_c = 3$ and $N_c = \infty$, which are listed in Tab. 2.1.

A different set of form factors for M_3 was used by Deandrea *et al.* in 1994 [29]. It had previously been derived by the same authors from heavy quark spin-flavor symmetry, chiral symmetry and the hidden symmetry approach for light vector resonances [30]. The authors point out that the factorization approximation carries large uncertainties and give the branching fractions for $N_c = 2$, $N_c = 3$ and $N_c = \infty$ listed in Tab. 2.1. After electroweak penguin operators had been included in the effective Hamiltonian [31], they were first applied to B meson decays by Du and Guo in 1997 [32]. Relying again on the form factors from Bauer, Stech and Wirbel, they find electroweak contributions to the transition amplitude of -33% for $N_c = 2$ and $+18\%$ for $N_c = \infty$, leading to the branching fractions listed in Tab. 2.1.

	$\mathcal{B}(B^0 \rightarrow \eta\phi)$		
	$N_c = 2$	$N_c = 3$	$N_c = \infty$
Du, Xing (1993)		1.5×10^{-11}	1.0×10^{-7}
Deandrea <i>et al.</i> (1994)	1.30×10^{-8}	8.55×10^{-12}	4.8×10^{-8}
Du, Guo (1997)	6.11×10^{-9}		7.73×10^{-8}

Table 2.1 Theoretical predictions for the branching fraction $\mathcal{B}(B^0 \rightarrow \eta\phi)$.

Although theoretical uncertainties are difficult to estimate, there are a number of uncertain parameters that enter the calculations. Beyond the effective number of colors N_c , large contributions come from the scale dependence of the Wilson coefficients and the uncertainties on the quark masses. It should also be kept in mind that the factorization approximation itself, including the valence quark approximation and the neglect of final state interactions, depends on the value of N_c . Finally, there are “annihilation” diagrams of leading order in $1/N_c$ which are neglected in the calculations because of a suppression by the B meson mass [21].

In a recent measurement [33], the CLEO collaboration gives an upper limit of $\mathcal{B}(B^0 \rightarrow \eta\phi) < 9 \times 10^{-6}$ (90%). Although this result is consistent with all theoretical predictions in Tab. 2.1, it is desirable to reduce the experimental uncertainty with the increased integrated luminosity and the improved experimental opportunities of the *BABAR* experiment.

Chapter 3

Data Analysis

This chapter explains the analysis in which the data acquired in the first two years of the *BABAR* experiment are examined for the decay $B^0 \rightarrow \eta\phi$. The successful identification of this rare decay requires a thorough investigation of its experimental signature and an efficient technique for its reconstruction. It has been shown in previous chapters that the *BABAR* experiment provides an excellent environment for meeting these requirements.

The overall strategy of the analysis is outlined in Sec. 3.1, while Sec. 3.2 describes the individual data samples and Sec. 3.3 introduces all analysis specific variables. Sec. 3.4 covers the event reconstruction in the *BABAR* software infrastructure, before Sec. 3.5 takes a first look at the obtained physics content. In Sec. 3.6 and 3.7, two different methods of separating signal events from background contributions are discussed. Sec. 3.8 summarizes the systematic uncertainties, and Sec. 3.9 presents the final results.

An elementary feature of the presented analysis is the blinding of the measurements until the calibration of the employed methods is completed. This procedure assures that no statistical degrees of freedom can be used to impose an experimenter's bias. As a consequence, it is only at the very end of this chapter that the actual “unblinded” results are shown.

3.1 Analysis Strategy

In order to identify instances of the considered decay $B^0 \rightarrow \eta\phi$, the *BABAR* data are examined for its detectable products. Special care is taken for a proper separation of detected decays from the products of similar background processes. A set of basic formulae is then used to translate the observations into decay branching fractions with well-defined uncertainties.

3.1.1 Candidate Construction

This analysis uses $B\bar{B}$ meson pairs produced at the $\Upsilon(4S)$ resonance and follows the convention $\mathcal{B}(\Upsilon(4S) \rightarrow B^0\bar{B}^0)/\mathcal{B}(\Upsilon(4S) \rightarrow B^+B^-) = 0.5$ for the branching ratio of $B^0\bar{B}^0$ and B^+B^- production. The detected products of the B meson decays are combined

to “candidates” for the resonances in the “signal” decay $B^0 \rightarrow \eta\phi$. η candidates are reconstructed in the two channels $\eta \rightarrow \gamma\gamma$ and $\eta \rightarrow \pi^+\pi^-\pi^0$, with the branching fraction $\mathcal{B}(\pi^0 \rightarrow \gamma\gamma) = 1$ assumed for the π^0 meson decay, while ϕ candidates are reconstructed in the channel $\phi \rightarrow K^+K^-$. The branching fractions of the η and ϕ meson decays are provided by the Particle Data Group [8] and summarized in Tab. 3.1.

	\mathcal{B}
$\eta \rightarrow \gamma\gamma$	0.3943 ± 0.0026
$\eta \rightarrow \pi^+\pi^-\pi^0$	0.226 ± 0.004
$\phi \rightarrow K^+K^-$	0.492 ± 0.007

Table 3.1 Branching fractions \mathcal{B} of decay channels.

There are two different types of “background” in the reconstructed B^0 decays:

$B\bar{B}$ Background B^0 candidates made from the products of non-signal B decays in $B\bar{B}$ events and

$q\bar{q}$ Background B^0 candidates made from the products of quark fragmentation in continuum $q\bar{q}$ events.

In addition, the η candidates include “background” photons from interactions of natural, beam or event generated particles with the detector material.

3.1.2 Branching Fraction Calculation

The branching fraction

$$\mathcal{B}(B^0 \rightarrow \eta\phi) = \frac{S}{\varepsilon_S \mathcal{B}_{\text{ch}} N_{B^0}} \quad (3.1)$$

is calculated from the measured number of signal B^0 candidates S , the signal selection efficiency ε_S , the number of processed B^0 mesons N_{B^0} and the channel branching fractions \mathcal{B}_{ch} , which evaluate to

$$\mathcal{B}_{\text{ch}} = \mathcal{B}(\phi \rightarrow K^+K^-) \mathcal{B}(\eta \rightarrow \gamma\gamma) \quad (3.2)$$

in the channel $\eta \rightarrow \gamma\gamma$ and

$$\mathcal{B}_{\text{ch}} = \mathcal{B}(\phi \rightarrow K^+K^-) \mathcal{B}(\eta \rightarrow \pi^+\pi^-\pi^0) \quad (3.3)$$

in the channel $\eta \rightarrow \pi^+\pi^-\pi^0$. S is measured in two different ways:

Candidate Counting Selective cuts are applied on kinematic and topological variables, and the remaining B^0 candidates are counted.

Maximum Likelihood Signal and background components are separated by a global maximum-likelihood fit to the distributions of these variables.

S is called a “significant” signal if it excludes 0 with five standard deviations σ_S . If no significant signal is found, an upper limit $\mathcal{B}_\varepsilon(B^0 \rightarrow \eta\phi)$ on the branching fraction is calculated from the upper limit \bar{S}_ε on the mean value of S . Relying on Bayesian statistics [34],

$$1 - \varepsilon = \int_0^{\bar{S}_\varepsilon} f_{\bar{S}}(\bar{S}|S) d\bar{S} \quad (3.4)$$

is the probability for \bar{S} with the conditional probability density $f_{\bar{S}}(\bar{S}|S)$ to lie between 0 and \bar{S}_ε . It can be calculated from the known conditional probability density $f_S(S|\bar{S})$ and Bayes’ theorem by [35]

$$1 - \varepsilon = \frac{\int_0^{\bar{S}_\varepsilon} f_S(S|\bar{S}) d\bar{S}}{\int_0^\infty f_S(S|\bar{S}) d\bar{S}}. \quad (3.5)$$

In this picture, using Eq. 3.1 with the requirement

$$1 - \varepsilon = \int_0^{\mathcal{B}_\varepsilon} f_{\mathcal{B}}(\mathcal{B}|S) d\mathcal{B} \quad (3.6)$$

for the conditional probability density $f_{\mathcal{B}}(\mathcal{B}|S)$ of the branching fraction $\mathcal{B}(B^0 \rightarrow \eta\phi)$ gives the upper limit

$$\mathcal{B}_\varepsilon(B^0 \rightarrow \eta\phi) = \frac{\bar{S}_\varepsilon}{\varepsilon_S \mathcal{B}_{\text{ch}} N_{B^0}}. \quad (3.7)$$

In the concurrent frequentist interpretation [34], ε is the fraction of identical experiments that would measure a value greater than S if the mean value was \bar{S}_ε . The frequentist limits follow from construction, as published by Feldman and Cousins in [36]. In this analysis, \mathcal{B}_{Bay} denotes branching fractions under the Bayesian limit, and \mathcal{B}_{FC} denotes branching fractions under the Feldman–Cousins limit. All limits are cited at a confidence level (c.l.) of $1 - \varepsilon = 90\%$.

3.1.3 Uncertainty Estimation

Systematic uncertainties are derived from the deviation of two measurements beyond their statistical uncertainties. If the measurements n_1 and n_2 have the statistical uncertainties σ_{n_1} and σ_{n_2} , the level of confidence (c.l.) that both measurements follow the same distribution of n is approximated by the Gaussian integral

$$1 - \varepsilon = e^{-\frac{(n_1 - n_2)^2}{2(\sigma_{n_1}^2 + \sigma_{n_2}^2)}}. \quad (3.8)$$

If $1 - \varepsilon$ is smaller than the desired level $1 - \varepsilon'$, the systematic uncertainty on all measurements of n is estimated by

$$\Delta n = \sqrt{-\frac{(n_1 - n_2)^2}{2 \log(1 - \varepsilon')} - (\sigma_{n_1}^2 + \sigma_{n_2}^2)}. \quad (3.9)$$

All systematic uncertainties are cited for $1 - \varepsilon' = 32\%$.

3.2 Data Samples

This analysis is based on data collected by *BABAR* between November 1999 and July 2002. An integrated luminosity of $(81.62 \pm 0.98) \text{ fb}^{-1}$ recorded “on peak” of the $\Upsilon(4S)$ resonance delivers $(85.7 \pm 1.0) \times 10^6 B\bar{B}$ events at a cross section of 1.05 nb [7] and $(276.7 \pm 3.3) \times 10^6 q\bar{q}$ events at a cross section of 3.39 nb [7]. Another $(9.61 \pm 0.12) \text{ fb}^{-1}$ recorded approximately 40 MeV “off peak” deliver $(32.58 \pm 0.39) \times 10^6 q\bar{q}$ events at the same cross section. These samples contain all events marked `isPhysics` in the detector runs 1 and 2. For comparison, the integrated luminosities recorded until November 2004 are shown in Fig. 3.1.

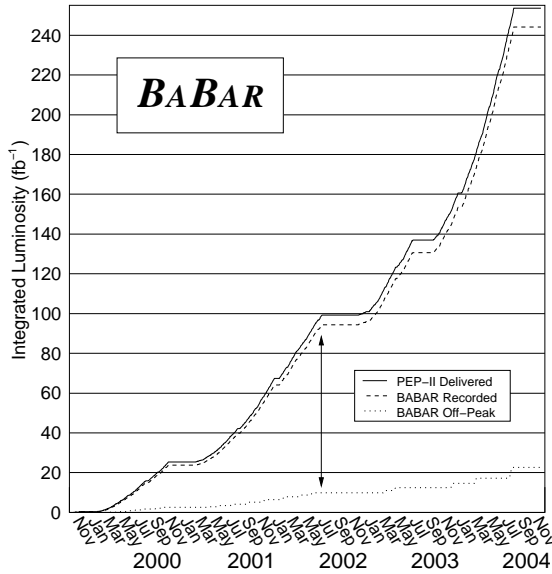


Figure 3.1 Integrated luminosity delivered by PEP-II, recorded by *BABAR* and recorded by *BABAR* off-peak. This analysis uses data collected between November 1999 and July 2002.

Simulated data events come from the *BABAR* Monte Carlo [35] simulation production 4. They include $39 \times 10^3 B^0\bar{B}^0$ events with signal B^0 decays in the channel $\eta \rightarrow \gamma\gamma$, $37 \times 10^3 B^0\bar{B}^0$ events with signal B^0 decays in the channel $\eta \rightarrow \pi^+\pi^-\pi^0$ and $109 \times 10^6 B\bar{B}$ events with generic B decays. While the $B\bar{B}$ Monte Carlo sample simulates $B\bar{B}$ background, the off-peak data sample entirely contains $q\bar{q}$ background. Although the off-peak energy shift entails systematic uncertainties, the use of collected data is generally more reliable than the use of Monte Carlo samples.

With the “ $B\bar{B}$ counting” from an inclusive analysis of hadronic $B\bar{B}$ events [37], the expected number of $B\bar{B}$ events in the data sample is $(88.58 \pm 0.98) \times 10^6$. Assuming the CLEO upper limit on the branching fraction $\mathcal{B}(B^0 \rightarrow \eta\phi)$ [33], the expected number of signal B^0 decays in the data sample

$$\hat{N}_{B^0}(B^0 \rightarrow \eta\phi) = N_{B\bar{B}} \mathcal{B}(B^0 \rightarrow \eta\phi)^1 \quad (3.10)$$

is limited to $\hat{N}_{B^0}(B^0 \rightarrow \eta\phi) < 797.2 \pm 8.8$ (90%). Scaling by the channel branching fractions in Tab. 3.1 gives the upper limits in each channel listed in Tab. 3.2.

	$\hat{N}_{B^0}(B^0 \rightarrow \eta\phi)$
$\eta \rightarrow \gamma\gamma$	$< 154.6 \pm 3.0$
$\eta \rightarrow \pi^+\pi^-\pi^0$	$< 88.6 \pm 2.2$

Table 3.2 Upper limits on the number of expected signal B^0 decays $\hat{N}_{B^0}(B^0 \rightarrow \eta\phi)$ in the channels $\eta \rightarrow \gamma\gamma$ and $\eta \rightarrow \pi^+\pi^-\pi^0$ at 90% c.l.

3.3 Event Variables

To separate signal B^0 decays from background processes, two classes of event variables are employed. “Kinematic” variables are evaluated from the measured energies and momenta and describe the masses of the constructed candidates. The variables for the mass of the B^0 candidates used in this analysis are defined in Sec. 3.3.1. Other variables that exploit the different topologies² of signal and background processes include the angular distributions in production and decay of B mesons. These “topological” variables are discussed in Sec. 3.3.2 to 3.3.6.

3.3.1 Kinematic Variables

$B\bar{B}$ events in beam collisions are described in this analysis by the decorrelated variables m_{ES} and ΔE [38]. These variables exploit the kinematic information of both the reconstructed and the recoil B meson by constraining their masses with event parameters.

The energy difference

$$\Delta E = E_B^* - \frac{1}{2}E_0^* \quad (3.11)$$

measures the difference between the masses of both B mesons. It is calculated in the center-of-mass system of the beams from the beam energy E_0^* and the energy E_B^* of the reconstructed meson. For correctly reconstructed B mesons, ΔE only deviates from 0 by the B meson mass resolution. For reconstructed background processes, however, the deviation is arbitrary.

The energy substituted mass

$$m_{\text{ES}} = \sqrt{\left(\frac{1}{2}E_0^*\right)^2 - p_B^{*2}} \quad (3.12)$$

measures the mass of both B mesons under the assumption $\Delta E = 0$. It is calculated in the center-of-mass system of the beams from the beam energy E_0^* and the momentum

¹In this calculation, the assumed branching ratio $\mathcal{B}(\Upsilon(4S) \rightarrow B^0\bar{B}^0)/\mathcal{B}(\Upsilon(4S) \rightarrow B^+B^-)$ and the $B^0\bar{B}^0$ multiplicity cancel to 1.

²This is synonymous with “event shape”.

\mathbf{p}_B^* of the reconstructed meson. To avoid boosting the measured momentum \mathbf{p}_B into the center-of-mass system of the beams, the modified expression

$$m_{\text{ES}} = \sqrt{\frac{(\frac{1}{2}E_0^{*2} + \mathbf{p}_0 \cdot \mathbf{p}_B)^2}{E_0^2} - p_B^2} \quad (3.13)$$

is used for computation. It is evaluated in the laboratory system using the beam energy E_0 and the beam momentum \mathbf{p}_0 . For correctly reconstructed B mesons, m_{ES} varies within the B meson mass resolution, while for reconstructed background processes it is free below E_0^* . To compensate the energy shift in off-peak data, m_{ES} is increased by the difference of the $\mathcal{T}(4S)$ resonance mass and E_0^* .

3.3.2 Helicity Formalism

In the following, transition amplitudes are evaluated in the helicity basis [39]. The “helicity”

$$\lambda = \frac{\mathbf{s} \cdot \mathbf{p}}{|\mathbf{p}|} \quad (3.14)$$

of a particle is the component of its spin \mathbf{s} along its momentum \mathbf{p} . Since the orbital angular momentum $\mathbf{l} = \mathbf{r} \times \mathbf{p}$ is perpendicular to the momentum, any two-particle state with total angular momentum j quantized along the momentum \mathbf{p}_1 is defined in its center-of-mass system by the two helicities λ_1 and λ_2 .³ Denoting this state $|j(\lambda_1 - \lambda_2)\rangle$, it may result from the spin state $|jm\rangle$, which is quantized along the z axis. Fig. 3.2 illustrates both states. The amplitude for the transition from $|jm\rangle$ to $|j(\lambda_1 - \lambda_2)\rangle$ is given by [39]

$$A_{m,\lambda_1\lambda_2}(\Omega) = \sqrt{\frac{2j+1}{4\pi}} A_{\lambda_1\lambda_2} D_{m,\lambda_1-\lambda_2}^{j*}(\Omega), \quad (3.15)$$

where $A_{\lambda_1\lambda_2}$ is the helicity amplitude for this process and $D_{m,\lambda_1-\lambda_2}^{j*}(\Omega)$ constitutes a rotation by $\Omega = (\vartheta, \varphi)$. For the definition of Ω see Fig. 3.2. By squaring Eq. 3.15 and choosing the representation

$$D_{m,m'}^j(\Omega) = e^{-i\varphi m} d_{m,m'}^j(\vartheta) e^{i\varphi m'} \quad (3.16)$$

by the tabulated [8] real-valued “ d ” function $d_{m,m'}^j(\vartheta)$, the differential rate for this transition in the angle element $d\Omega = d\cos\vartheta d\varphi$ and the remaining phase-space element $d\Phi$ is found to be

$$d\Gamma_{m,\lambda_1\lambda_2}(\Omega, \Phi) = \frac{2j+1}{4\pi} |A_{\lambda_1\lambda_2}|^2 \left| d_{m,\lambda_1-\lambda_2}^j(\vartheta) \right|^2 d\Omega d\Phi. \quad (3.17)$$

Integrating over Φ and φ and summing over all helicities $\lambda_1\lambda_2$ gives the angular distribution

$$\frac{1}{\Gamma_m} \frac{d\Gamma_m(\vartheta)}{d\cos\vartheta} = \frac{\Phi}{\Gamma_m} \frac{2j+1}{2} \sum_{\lambda_1\lambda_2} |A_{\lambda_1\lambda_2}|^2 \left| d_{m,\lambda_1-\lambda_2}^j(\vartheta) \right|^2 \quad (3.18)$$

of the final state with respect to z .

³ j and m are quantum numbers. In this context λ is also used as a quantum number.

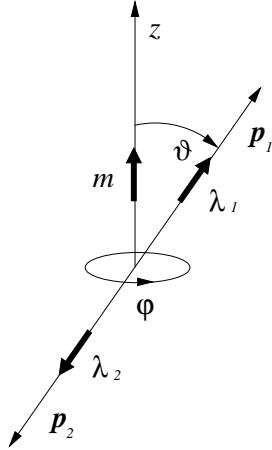


Figure 3.2 States $|jm\rangle$ (quantized along z) and $|j(\lambda_1-\lambda_2)\rangle$ (quantized along \mathbf{p}_1) in their common center-of-mass system. The transition from $|jm\rangle$ to $|j(\lambda_1-\lambda_2)\rangle$ constitutes a rotation from z to \mathbf{p}_1 .

3.3.3 Momentum and Thrust

The beams are polarized to produce intermediate bosons in the spin state $|jm\rangle = |11\rangle$ with respect to the beam axis. Since B mesons are spin states $|j_s\lambda\rangle = |00\rangle$, the only helicity amplitude for $B\bar{B}$ pair production is A_{00} . According to Eq. 3.18, the angular distribution of the B momentum has the shape

$$|d_{1,0}^1(\vartheta)|^2 = \frac{1 - \cos^2 \vartheta}{2}. \quad (3.19)$$

Non- b quark pairs produced in the continuum involve two spins $|j_s\lambda\rangle = |\frac{1}{2} \pm \frac{1}{2}\rangle$ and four possible helicity amplitudes $A_{++}, A_{+-}, A_{-+}, A_{--}$. Evaluating the electroweak vertex with the quark mass m_q and the center-of-mass energy E_0 , one finds that the amplitudes A_{++} and A_{--} are proportional to m_q , while A_{+-} and A_{-+} are proportional to $E_0 + \mathcal{O}(m_q^2/E_0^2)$ [40]. Since $E_0 \gg m_q$, continuum quark pair production is dominated by A_{++} and A_{--} , and Eq. 3.18 gives the shape of the angular distribution of the quark momentum by

$$|d_{1,1}^1(\vartheta)|^2 + |d_{1,-1}^1(\vartheta)|^2 = \frac{1 + \cos^2 \vartheta}{2}. \quad (3.20)$$

The condition $E_0 \gg m_q$ also implies that the continuum quarks have high momenta that boost all subsequent processes into isolated jets. This stands in contrast to B mesons, which are produced close to rest at $E_0 \approx 2m_B$ and decay spherically. However, continuum quark events contain no B mesons, and all B candidates must be (artificially) constructed from the jets. A jet event with a constructed B candidate is illustrated in Fig. 3.3.

Let \mathbf{p}_1 and \mathbf{p}_2 be momenta in the jets. Given by the angle between \mathbf{p}_1 and \mathbf{p}_2 , the momentum

$$\mathbf{p}_0 = \mathbf{p}_1 + \mathbf{p}_2 \quad (3.21)$$

of the B candidate has an arbitrary direction. To recover the direction of the original quark momenta, we follow the procedure proposed in [41]: For every unit vector \mathbf{e}_t ,

$$t = \sum_{i=1,2} |\mathbf{p}_i \cdot \mathbf{e}_t| \quad (3.22)$$

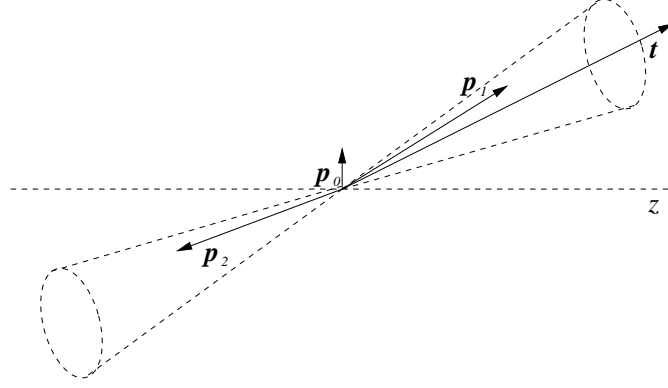


Figure 3.3 Continuum $q\bar{q}$ event with a constructed B candidate. \mathbf{p}_1 and \mathbf{p}_2 are momenta in the jets. \mathbf{p}_0 is the momentum, and \mathbf{t} is the thrust momentum of the B candidate. z is the beam axis.

is the sum of magnitudes of all projections $\mathbf{p}_i \cdot \mathbf{e}_t$. The “thrust momentum” is then defined by the vector $\mathbf{t} = t \mathbf{e}_t$ for which

$$t \rightarrow \max . \quad (3.23)$$

With \mathbf{p}_+ being the sum of all momenta with positive projections, Eq. 3.22 implies that $t = (2\mathbf{p}_+ - \mathbf{p}_0) \cdot \mathbf{e}_t$. To satisfy Eq. 3.23, we adjust \mathbf{e}_t parallel to $2\mathbf{p}_+ - \mathbf{p}_0$ and obtain the thrust momentum

$$\mathbf{t} = 2\mathbf{p}_+ - \mathbf{p}_0 .^4 \quad (3.24)$$

If \mathbf{p}_1 and \mathbf{p}_2 enclose an angle $\alpha < \frac{\pi}{2}$, both will have positive projections, and Eq. 3.24 becomes

$$\mathbf{t}(\alpha < \frac{\pi}{2}) = \mathbf{p}_1 + \mathbf{p}_2 . \quad (3.25)$$

If \mathbf{p}_1 and \mathbf{p}_2 enclose an angle $\alpha \geq \frac{\pi}{2}$, only one will have a positive projection, and for $|\mathbf{p}_1| > |\mathbf{p}_2|$ Eq. 3.24 becomes

$$\mathbf{t}(\alpha \geq \frac{\pi}{2}) = \mathbf{p}_1 - \mathbf{p}_2 . \quad (3.26)$$

While in continuum quark events the thrust momentum is aligned to the momenta of the originally produced quarks, in $B\bar{B}$ events it is aligned to the momenta of the B decay products, which have arbitrary directions. The angular distributions of the momentum and the thrust momentum of the B^0 candidates in the signal Monte Carlo, the $B\bar{B}$ Monte Carlo and the off-peak data sample for the channel $\eta \rightarrow \gamma\gamma$ are shown in Fig. 3.4. The distributions from Eq. 3.19 and 3.20 are found for the momentum in the signal Monte Carlo and for the thrust momentum in the off-peak data sample. The thrust momentum generally disappears at small angles due to the limited detector acceptance.

3.3.4 Momentum Flow

Utilizing the newly defined thrust momentum, the space around it is divided into nine cones, each of which covers an angle $\Delta\vartheta = \frac{\pi}{18}$. The first three of these cones are shown

⁴ [41] assumes $\mathbf{p}_0 = 0$ and calls \mathbf{p}_+ the “principal momentum”.

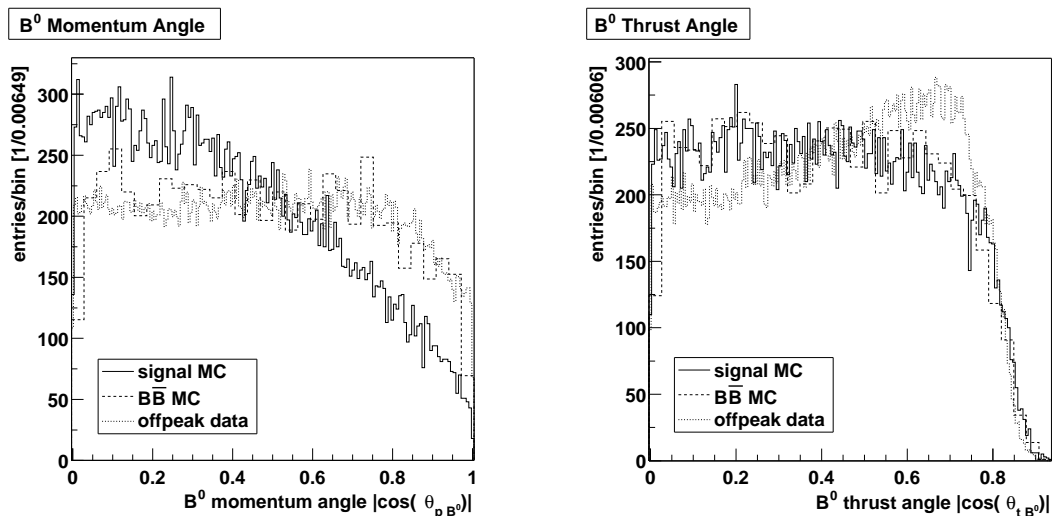


Figure 3.4 Angular distributions of the momentum (left) and the thrust momentum (right) of the B^0 candidates in the signal Monte Carlo, $B\bar{B}$ Monte Carlo and off-peak data sample for the channel $\eta \rightarrow \gamma\gamma$. All frequencies are scaled against the signal Monte Carlo sample.

in Fig. 3.5. All nine cones cover $\Delta\vartheta = \frac{\pi}{2}$, with the space beyond being mirrored into them. The momentum flow

$$p_i = \sum_j |\mathbf{p}_{ij}| \quad (3.27)$$

is defined as the scalar sum of all momenta \mathbf{p}_{ij} found inside the i th cone. Fig. 3.6 shows the distributions of the momentum flows p_1 , p_5 and p_9 in the signal Monte Carlo and the off-peak data sample for the channel $\eta \rightarrow \gamma\gamma$. While in the spherical B decays all cones have similar momentum flows, in jet events the momentum flows decrease as the cones move away from the jet axis.

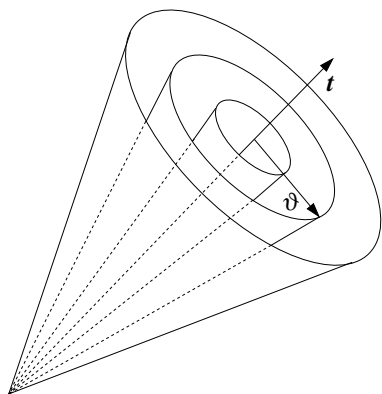


Figure 3.5 First three cones around the thrust momentum \mathbf{t} . Each cone covers an angle $\Delta\vartheta = \frac{\pi}{18}$.

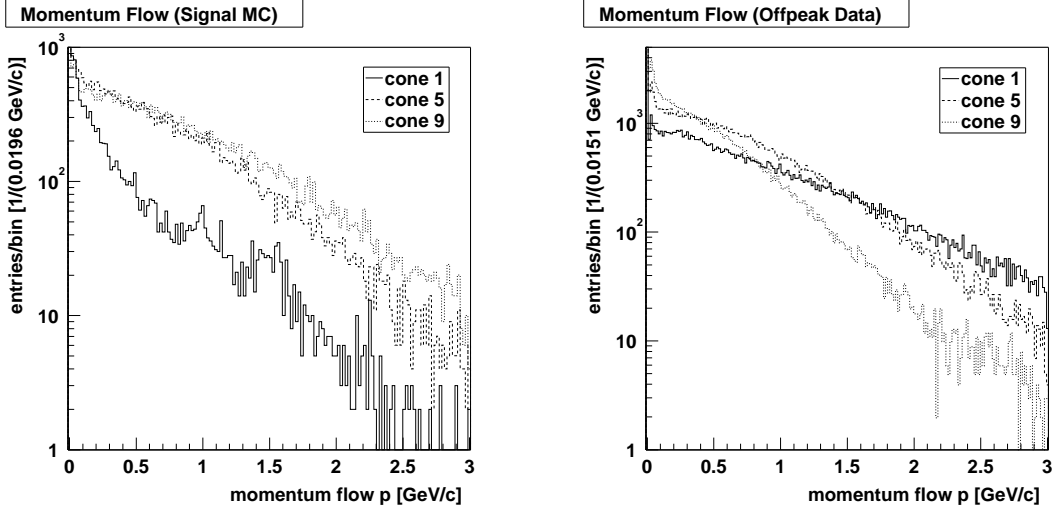


Figure 3.6 Distributions of momentum flows in cone 1, 5, and 9 in the signal Monte Carlo (left) and the off-peak data (right) sample for the channel $\eta \rightarrow \gamma\gamma$. The ordinate is logarithmic.

3.3.5 Fisher Discriminant

Since the variables discussed in Sec. 3.3.3 and 3.3.4 are partially correlated, they are used in combinations. The linear combination

$$\mathcal{F} = \mathbf{c} \cdot \mathbf{x} \quad (3.28)$$

of all variables \mathbf{x} that maximizes the separation between two categories of events is called the Fisher discriminant [42]. The separation is expressed in terms of the difference \mathcal{D} between the values in the categories 1, 2. With the mean value

$$\overline{\mathcal{D}} = \overline{\mathcal{F}}_1 - \overline{\mathcal{F}}_2 \quad (3.29)$$

and the variance

$$s_{\mathcal{D}} = s_{\mathcal{F}_1} + s_{\mathcal{F}_2}, \quad (3.30)$$

the separation is given by $\overline{\mathcal{D}}/\sigma_{\mathcal{D}}$. The criterion for maximum separation is

$$\frac{\overline{\mathcal{D}}^2}{s_{\mathcal{D}}} \rightarrow \max, \quad (3.31)$$

which leads to the condition

$$\frac{\overline{\mathcal{D}}}{s_{\mathcal{D}}^2} \left[2 s_{\mathcal{D}} \frac{\partial \overline{\mathcal{D}}}{\partial \mathbf{c}} - \overline{\mathcal{D}} \frac{\partial s_{\mathcal{D}}}{\partial \mathbf{c}} \right] = 0. \quad (3.32)$$

Since

$$\overline{\mathcal{D}} = \mathbf{c} \cdot (\overline{\mathbf{x}}_1 - \overline{\mathbf{x}}_2) \quad (3.33)$$

and

$$s_{\mathcal{D}} = \mathbf{c} (\mathbf{S}_1 + \mathbf{S}_2) \mathbf{c}, \quad (3.34)$$

with $\mathbf{S}_{1,2}$ being the covariance matrices in both categories, the sought coefficients \mathbf{c} must be proportional to those in

$$\bar{\mathbf{x}}_1 - \bar{\mathbf{x}}_2 = (\mathbf{S}_1 + \mathbf{S}_2) \mathbf{c}. \quad (3.35)$$

Hence, they are given by

$$\mathbf{c} \sim (\mathbf{S}_1 + \mathbf{S}_2)^{-1} (\bar{\mathbf{x}}_1 - \bar{\mathbf{x}}_2). \quad (3.36)$$

Following the spirit of the CLEO experiment [43], we form a Fisher discriminant from

- the magnitude of the cosine of the angle of the B^0 momentum,
- the magnitude of the cosine of the angle of the B^0 thrust momentum and
- the nine momentum flows around the B^0 thrust momentum,

calculated in the center-of-mass system of the beams with respect to the beam axis.

Two different sets of Fisher coefficients are considered. Set \mathbf{c}_1 was optimized in [44] for separation between $B^+ \rightarrow \omega K^+$ Monte Carlo and off-peak data events. Set \mathbf{c}_2 is optimized for separation between $B^0 \rightarrow \eta\phi$ Monte Carlo and off-peak data events in each of the channels $\eta \rightarrow \gamma\gamma$ and $\eta \rightarrow \pi^+\pi^-\pi^0$. Both sets are computed with the **Cornelius++** package [45, 46] from 1000–3000 events in each category. The resulting parameters of the discriminant in the $B^0 \rightarrow \eta\phi$ Monte Carlo and the off-peak data sample and the achieved separations are listed in Tab. 3.3. It is evident that the optimization for the $B^0 \rightarrow \eta\phi$ Monte Carlo sample does not improve the separation. An equivalent behavior was already observed in [43]. As a consequence, this analysis uses the coefficient set \mathbf{c}_1 .

		$\eta \rightarrow \gamma\gamma$		$\eta \rightarrow \pi^+\pi^-\pi^0$	
		\mathbf{c}_1	\mathbf{c}_2	\mathbf{c}_1	\mathbf{c}_2
signal	$\bar{\mathcal{F}}$	-0.354 ± 0.011	-0.413 ± 0.007	-0.325 ± 0.011	-0.561 ± 0.009
	$\sigma_{\mathcal{F}}$	0.575 ± 0.011	0.390 ± 0.007	0.642 ± 0.011	0.522 ± 0.009
$q\bar{q}$	$\bar{\mathcal{F}}$	0.596 ± 0.014	0.099 ± 0.008	0.655 ± 0.013	0.139 ± 0.010
	$\sigma_{\mathcal{F}}$	0.715 ± 0.014	0.418 ± 0.008	0.739 ± 0.013	0.566 ± 0.010
	$\bar{\mathcal{D}}/\sigma_{\mathcal{D}}$	1.036 ± 0.019	0.895 ± 0.019	1.002 ± 0.017	0.908 ± 0.017

Table 3.3 Mean values $\bar{\mathcal{F}}$, standard deviations $\sigma_{\mathcal{F}}$ and separations $\bar{\mathcal{D}}/\sigma_{\mathcal{D}}$ of the Fisher discriminant in the $B^0 \rightarrow \eta\phi$ (signal) Monte Carlo and off-peak ($q\bar{q}$) data sample for the channels $\eta \rightarrow \gamma\gamma$ and $\eta \rightarrow \pi^+\pi^-\pi^0$ for coefficient sets \mathbf{c}_1 (optimized for $B^+ \rightarrow \omega K^+$) and \mathbf{c}_2 (optimized for $B^0 \rightarrow \eta\phi$).

3.3.6 Helicity Angle

Finally, the helicity formalism is used to calculate the decay angles of the intermediate B^0 decay products. The starting point is the rest frame of the B^0 meson, where the total angular momentum $j = 0$. While η mesons are spin states $|j_s\lambda\rangle = |00\rangle$, ϕ mesons occur in the states $|j_s\lambda\rangle = |1-1\rangle, |10\rangle, |1+1\rangle$. However, the orbital angular momentum of the η and the ϕ meson, which must compensate the spin of the ϕ meson, is perpendicular to the momenta of both mesons. Thus, the ϕ meson must occur in the state $|j_s\lambda\rangle = |10\rangle$,⁵ with its spin perpendicular to its momentum. If we choose its momentum as quantization axis and move into its rest frame, the decay of the ϕ meson is described by the two kaon spin states $|j_s\lambda\rangle = |00\rangle$. The angle of the kaon momentum is now measured between the kaon momentum in the ϕ meson rest frame and the ϕ meson momentum in the B^0 meson rest frame. This angle, shown in Fig. 3.7, is called the ‘‘helicity angle’’ ϑ_λ . Eq. 3.18 demands that its distribution has the shape

$$|d_{0,0}^1(\vartheta)|^2 = \cos^2 \vartheta. \quad (3.37)$$

Again, this shape is expected for correctly reconstructed B^0 mesons, whereas B^0 candidates from background processes do not correspond to real mesons.

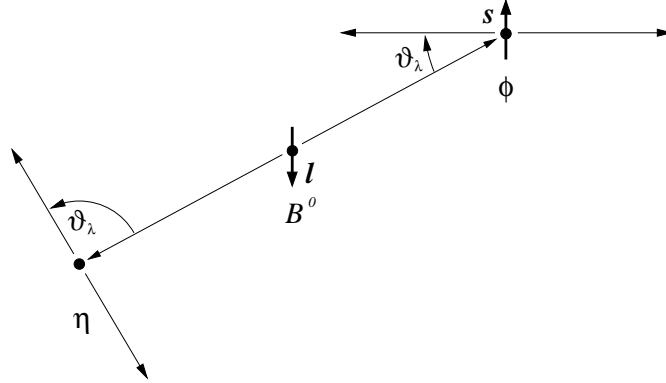


Figure 3.7 Helicity angles ϑ_λ of the η and the ϕ meson in the decay $B^0 \rightarrow \eta\phi$. The η meson decays into two photons, and the ϕ meson decays into two kaons. The η helicity angle is measured between the η momentum in the B^0 rest frame and the photon momentum in the η rest frame. The ϕ helicity angle is measured between the ϕ momentum in the B^0 rest frame and the kaon momentum in the ϕ rest frame. Because the orbital angular momentum l of the η and the ϕ meson is perpendicular to both their momenta, the spin s of the ϕ meson is perpendicular to its momentum.

In the fundamental case of the decay of a spin state $|j_s\lambda\rangle = |00\rangle$ we expect the angular distribution of the decay products to be flat. This applies to both the η and the π^0 meson. However, here the decay products are hard photons, while background photons are typically soft. If one photon candidate corresponding to a decay photon and one photon candidate corresponding to a background photon are combined, their center-of-mass system will be strongly aligned to the harder photon. Hence, the distribution of

⁵This is referred to as spin alignment.

the helicity angles of η and π^0 candidates from background processes will rise towards $|\cos(\vartheta_{\lambda\eta})| = 1$.

3.4 Event Reconstruction

All data samples are processed with *BABAR* software release analysis-13b, updated to

- `CompositionSequences` fdl051003,
- `CompositionUtils` fdl-061401-ana13,
- `BetaMicro` yumiceva-06Aug02-ana13,
- `BetaPid` V00-01-42-01,
- `BetaSequences` V00-10-09-01,
- `BetaTools` yumiceva-06Aug02-ana13 and
- `BtaMicroSequences` V00-01-03-02.

The application is provided by the `BetaUser` package [45]. Tracks and energy clusters are taken from the `BtaGoodTrackSequence`. While their construction has been explained in Sec. 1.2.2 and 1.2.4, their parameters are given in Sec. 3.4.2 and 3.4.3, respectively. π^0 candidates come from the `CompPi0Sequence`, and η and ϕ candidates from the `CompMicroSequence`. The parameters of these candidates are given in Sec. 3.4.4 to 3.4.6. The `CompositionTools` package [45] is used to build B^0 candidates. Particle identification is performed in the `PidMicroSequence`. Data samples are processed at the Forschungszentrum Karlsruhe, and Monte Carlo samples at the Rutherford Appleton Laboratory.

3.4.1 Input

All data and Monte Carlo events are fetched from the `Kanga` [47] event store. Control files for the input module are generated separately at every site by the `skimData` tool. For data reconstruction, a private skim of events containing at least one ϕ candidate is produced from the `AllEventsKanga` stream. This is accomplished by inserting a filter module, followed by a `RooModules` output module, into the reconstruction sequence. Monte Carlo events are read directly from the `SPKanga` stream. A filter module added in this case removes signal events from the $B\bar{B}$ modes.

3.4.2 Tracks

Tracks of charged particles in the vertex tracker or the drift chamber (see Sec. 1.2.2) are added to the `GoodTracksVeryLoose` list if they have

- a momentum $p \leq 10 \text{ GeV}/c$ and

- a distance of closest approach to the beam spot
 - $d_t \leq 1.5$ cm transversal to the beam axis and
 - $d_l \leq 10$ cm along the beam axis.

They are added to the `GoodTracksLoose` list if they also have

- a momentum $p_t \geq 0.1$ GeV/ c transversal to the beam axis and
- at least 12 hits in the drift chamber.

By default, tracks are identified as pions. To separate π^\pm from K^\pm candidates, the kaon identification performed by the `PidKaonSMSSelector` [48] is used. This selector combines

- the energy losses per path length in the silicon vertex tracker and the drift chamber (see Sec. 1.2.2) and
- the number and the angle of the Cherenkov photons in the DIRC (see Sec. 1.2.3)

into likelihoods for pions, kaons and protons. The energy losses are described by Gaussian distributions with mean values from the Bethe–Bloch formula (Eq. 1.21) and measured resolutions. The Cherenkov angle is described by a Gaussian distribution with a parameterized mean value and a measured resolution, and the number of Cherenkov photons is described by a Poisson distribution with tabulated mean values.

To assure their consistency with data, Monte Carlo events are assigned a tracking efficiency correction from the tables provided by the Tracking Efficiency Task Force [49]. For the same reason, the kaon selector is replaced by the efficiency tables provided by the PID Tools Group [50].

3.4.3 Energy Clusters

Energy clusters are energy depositions in contiguous crystals of the electromagnetic calorimeter (see Sec. 1.2.4) that are not associated with tracks. The lateral moment of a cluster of N crystals with distances r_i from the cluster centroid and energy depositions E_i is defined as

$$M_{\text{lat}} = \frac{E_{\text{lat}}}{E_{\text{lat}} + 25(E_0 + E_1)}, \quad (3.38)$$

where

$$E_{\text{lat}} = \sum_{i=2}^N r_i^2 E_i \quad (3.39)$$

and E_0 and E_1 are the two largest energy depositions.

By default, clusters are identified as photons. Photon candidates are added to the `GoodPhotonLoose` list if they have

- an energy $E \geq 0.03$ GeV and

- a lateral moment $M_{\text{lat}} \leq 0.8$.

In Monte Carlo events, the photon energies are smeared with the dilution factors provided by the Neutrals Analysis Working Group (AWG) [51].

3.4.4 π^0 Candidates

Composite π^0 candidates are made from two `GoodPhotonLoose` candidates by the `Pi0-ToGG_LooseMass` module. They have

- an invariant mass $0.10 \leq m_{\gamma\gamma} \leq 0.16 \text{ GeV}/c^2$ and
- an energy $E_{\pi^0} \geq 0.2 \text{ GeV}$.

The composite vertex is taken to be the event vertex, the composite mass is set to the π^0 meson mass, and the photon momenta are refitted.

Merged π^0 candidates are single energy clusters that are consistent in shape with an incident π^0 meson [52] and not contained in any composite π^0 candidate. Their frequencies in the signal Monte Carlo and the data sample for the channel $\eta \rightarrow \pi^+\pi^-\pi^0$ are 1.7% with a relative statistical uncertainty below 5% and a consistency above 32% c.l. They are therefore ignored in this analysis.

In Monte Carlo events, a certain, but randomly chosen fraction of π^0 candidates is discarded according to the correction factors provided by the Neutrals AWG [51].

3.4.5 η Candidates

η candidates in the channel $\eta \rightarrow \gamma\gamma$ are composed from two `GoodPhotonLoose` candidates by the `EtaToGG_DefaultMass` module. They have

- photon energies $E_\gamma \geq 0.05 \text{ GeV}$,
- an invariant mass $0.47 \leq m_{\gamma\gamma} \leq 0.62 \text{ GeV}/c^2$ and
- a momentum $p_{\pi^0} \geq 0.2 \text{ GeV}/c$.

The composite vertex is taken to be the event vertex, the composite mass is set to the η meson mass, and the photon momenta are refitted.

η candidates in the channel $\eta \rightarrow \pi^+\pi^-\pi^0$ are composed from two `GoodTracksLoose` tracks and one π^0 candidate by the `EtaToPiPiPi0_Default` module. They have

- a composite mass $0.515 \leq m_\eta \leq 0.575 \text{ GeV}/c^2$.

3.4.6 ϕ Candidates

ϕ candidates are composed from one `GoodTracksVeryLoose` and one `GoodTracksLoose` track by the `PhiToKK_Default` module. They have

- a composite mass $0.989 \leq m_\phi \leq 1.049 \text{ GeV}/c^2$.

3.4.7 B^0 Candidates

B^0 candidates are composed from one η and one ϕ candidate by a `CompB0Selector` requiring

- a composite mass $4.5 \leq m_{B^0} \leq 6.0 \text{ GeV}/c^2$ and
- an energy difference $|\Delta E| \leq 0.05 \text{ GeV}$.

3.4.8 Output

All variables of the reconstructed events are stored in *ROOT* [53] n-tuples. The tuple format is managed by the `Q2BUser` package [45]. Evaluation of `PidMicroSequence` particle identification is added to the `Q2BUserAnalysis` module. Events without B^0 candidates are omitted. The stored variables include

- the number of `GoodTracksVeryLoose` tracks N_{track} ,
- the kaon identification i_{K^\pm} of the π^\pm and K^\pm candidates,
- the energy E_γ of the photon candidates,
- the energy substituted mass m_{ES} and the energy difference ΔE defined in Sec. 3.3.1,
- the invariant mass $m_{\gamma\gamma}$ of the π^0 candidates in the channel $\eta \rightarrow \pi^+\pi^-\pi^0$ and the η candidates in the channel $\eta \rightarrow \gamma\gamma$,
- the composite masses m_η of the η candidates in the channel $\eta \rightarrow \pi^+\pi^-\pi^0$ and m_ϕ of the ϕ candidates and
- the Fisher discriminant \mathcal{F} and the helicity angles ϑ_λ defined in Sec. 3.3.5 and 3.3.6.

3.5 Event Analysis

The n-tuples defined in Sec. 3.4 are analyzed in a separate *ROOT* [53] 3.02.07 application. First, the `Q2BUser` n-tuples are converted to a format containing all required variables in scalar columns and one B^0 candidate per row. Events with multiple B^0 candidates are treated according to the different approaches discussed in Sec. 3.5.4. At the same time all cuts on kinematic and topological variables are applied. Next, the distributions of the variables are extracted. They motivate the range of cuts considered for candidate counting. To fit probability density functions (p.d.f.), a `RooFitCore` V00-00-16 and `RooFitModels` V00-00-10 package [45, 54] is integrated. Fits of a given number of parameters are limited to samples that contain at least the same number of candidates. Values are chosen at maximum likelihood, with prior 100-fold binning applied to samples containing at least 10000 candidates. The complete set of p.d.f.'s for the global maximum-likelihood fit is given in App. D.

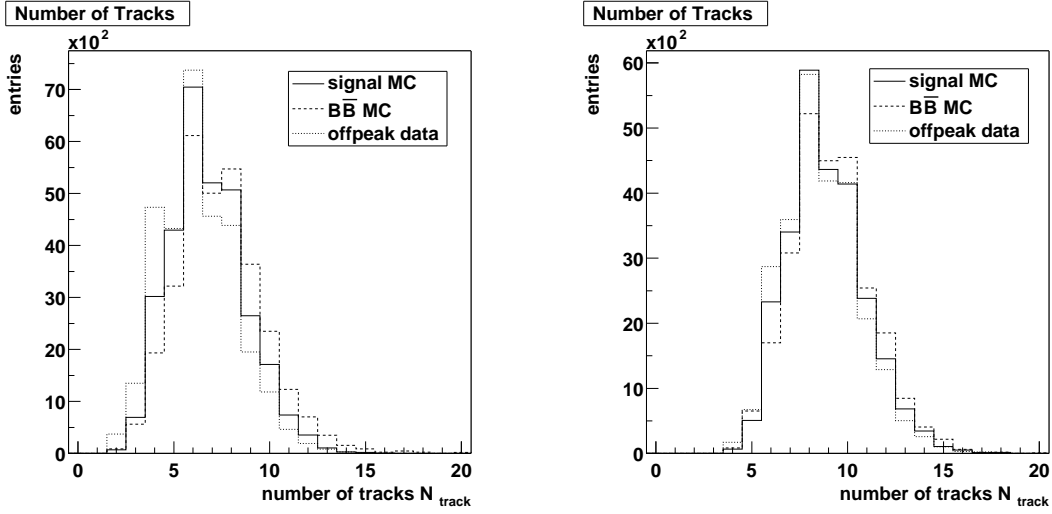


Figure 3.8 Distributions of the number of tracks in the signal Monte Carlo, $B\bar{B}$ Monte Carlo and off-peak data sample for the channels $\eta \rightarrow \gamma\gamma$ (left) and $\eta \rightarrow \pi^+\pi^-\pi^0$ (right). All frequencies are scaled against the signal Monte Carlo sample.

3.5.1 Number of Tracks

The distributions of the number of tracks N_{track} are shown in Fig. 3.8. Since the distributions in the different samples are widely identical, the fixed cuts $N_{\text{track}} \geq 3$ in the channel $\eta \rightarrow \gamma\gamma$ and $N_{\text{track}} \geq 5$ in the channel $\eta \rightarrow \pi^+\pi^-\pi^0$ are applied for all methods.

3.5.2 Kaon Identification

The distributions of the kaon identification i_{K^\pm} of the K^\pm candidates are shown in Fig. 3.9. The distributions of the kaon identification $i_{K^\pm\pi^\pm}$ of the π^\pm candidates are shown in Fig. 3.10. The bins labeled 0 contain unidentified candidates, while the bins labeled 1, 2, 3, 4 contain candidates identified in the categories **VeryLoose**, **Loose**, **Tight**, **VeryTight** [48]. The accumulation of signal and background samples at opposite ends of this scale suggests cuts in between. Since their correlations are not known, separate cuts $i_{K^\pm} \geq 0 \dots 4$ and $i_{K^\pm\pi^\pm} \leq 0 \dots 4$ are implemented for both tracks contributing to a ϕ and an η candidate, respectively. These cuts are optimized for candidate counting and subsequently used in the global maximum-likelihood fit.

3.5.3 Photon Energy

The distributions of the energies E_γ of the photon candidates are shown in Fig. 3.11. To suppress soft background photons in candidate counting, cuts in the ranges $E_\gamma \geq 0.0 \dots 1.0$ GeV in the channel $\eta \rightarrow \gamma\gamma$ and $E_\gamma \geq 0.0 \dots 0.5$ GeV in the channel $\eta \rightarrow \pi^+\pi^-\pi^0$ are considered.

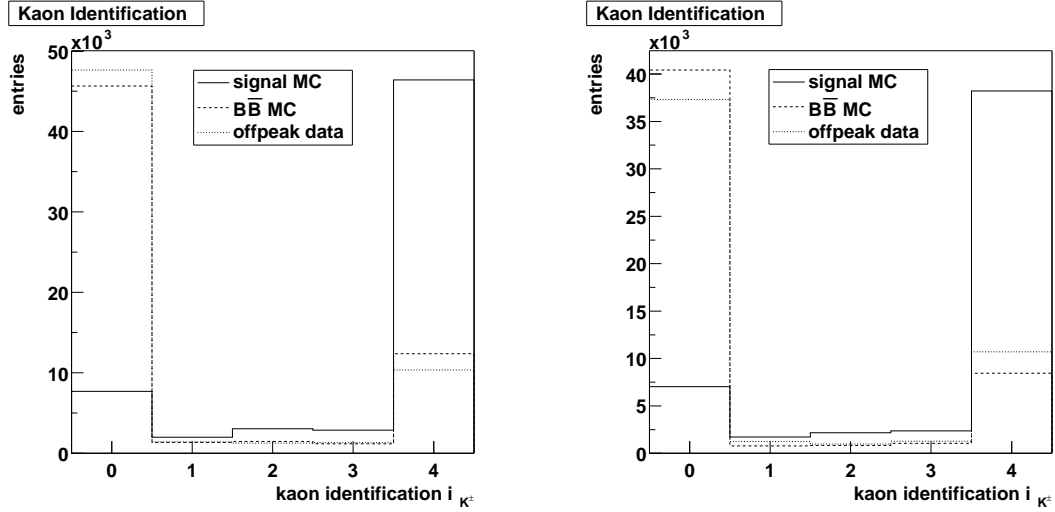


Figure 3.9 Distributions of the kaon identification of the K^\pm candidates in the signal Monte Carlo, $B\bar{B}$ Monte Carlo and off-peak data sample for the channels $\eta \rightarrow \gamma\gamma$ (left) and $\eta \rightarrow \pi^+\pi^-\pi^0$ (right). All frequencies are scaled against the signal Monte Carlo sample. Bin 0 contains unidentified candidates. Bins 1...4 contain VeryLoose...VeryTight candidates.

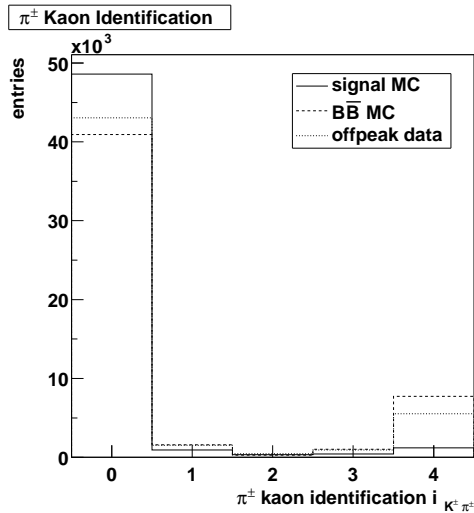


Figure 3.10 Distributions of the kaon identification of the π^\pm candidates in the signal Monte Carlo, $B\bar{B}$ Monte Carlo and off-peak data sample for the channel $\eta \rightarrow \pi^+\pi^-\pi^0$. All frequencies are scaled against the signal Monte Carlo sample. Bin 0 contains unidentified candidates. Bins 1...4 contain VeryLoose...VeryTight candidates.

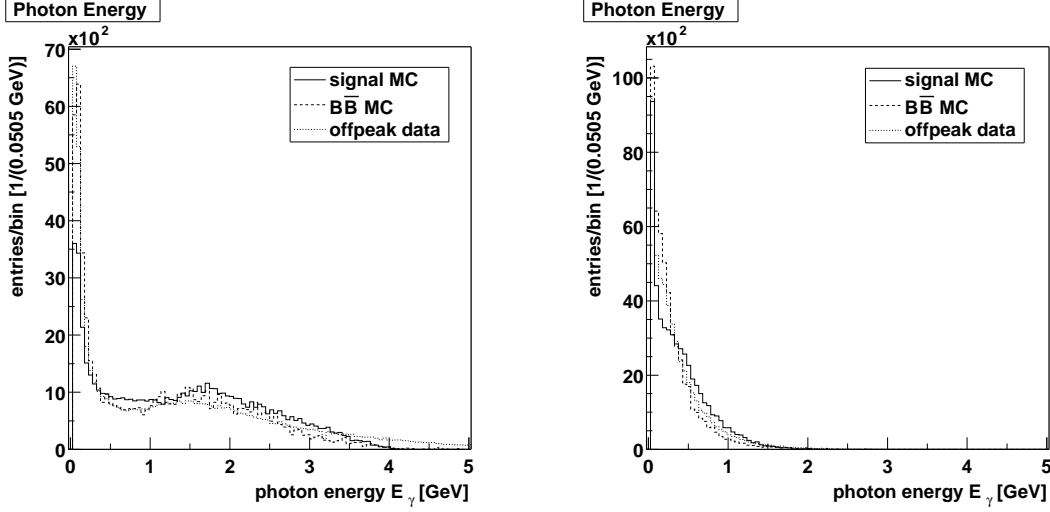


Figure 3.11 Distributions of the energy of the photon candidates in the signal Monte Carlo, $B\bar{B}$ Monte Carlo and off-peak data sample for the channels $\eta \rightarrow \gamma\gamma$ (left) and $\eta \rightarrow \pi^+\pi^-\pi^0$ (right). All frequencies are scaled against the signal Monte Carlo sample.

3.5.4 B^0 Masses

The distributions of the masses m_{ES} and ΔE of the B^0 candidates in the $B\bar{B}$ Monte Carlo and the off-peak data sample are shown in Fig. 3.12 to 3.15. The distribution of m_{ES} depends on the distribution of the momenta p_B^* of the B^0 candidates the center-of-mass system of the beams through Eq. 3.12 as

$$\frac{dN}{dm_{ES}} = \frac{m_{ES}}{p_B^*} \frac{dN}{dp_B^*}. \quad (3.40)$$

Since the distribution of p_B^* is expected to be proportional to p_B^{*2} in the two-body phase space, the distribution of m_{ES} is expected to be proportional to $m_{ES} \sqrt{1 - (m_{ES}/m_0)^2}$, where $m_0 = \frac{1}{2}E_0^*$ is half the the beam energy in the center-of-mass system of the beams. This shape was first proposed by the ARGUS collaboration in [55]. Allowing for deviations from this expectation, the final ‘‘ARGUS’’ function fitted to the distributions of m_{ES} is

$$f_{\text{arg}}(x) \propto x \sqrt{1 - x^2} e^{p(1-x)} \Theta(1-x), \quad (3.41)$$

where $x = m_{ES}/m_0$, p is a free parameter, and $\Theta(1-x)$ is the Heaviside function for the limit $m_{ES} \leq m_0$.

The distributions of ΔE are fitted by second degree polynomials

$$f_{\text{cheb}}(x) \propto T^0(x) + c_1 T^1(x) + c_2 T^2(x). \quad (3.42)$$

The transformation

$$x = -1 + 2 \frac{\Delta E - \Delta E_1}{\Delta E_2 - \Delta E_1} \quad (3.43)$$

maps the fit range $\Delta E_1 \leq \Delta E \leq \Delta E_2$ onto the interval $-1 \leq x \leq +1$ where the Chebychev polynomials⁶ T^i are orthogonal [34].

⁶These are, strictly speaking, Chebychev polynomials of the first kind.

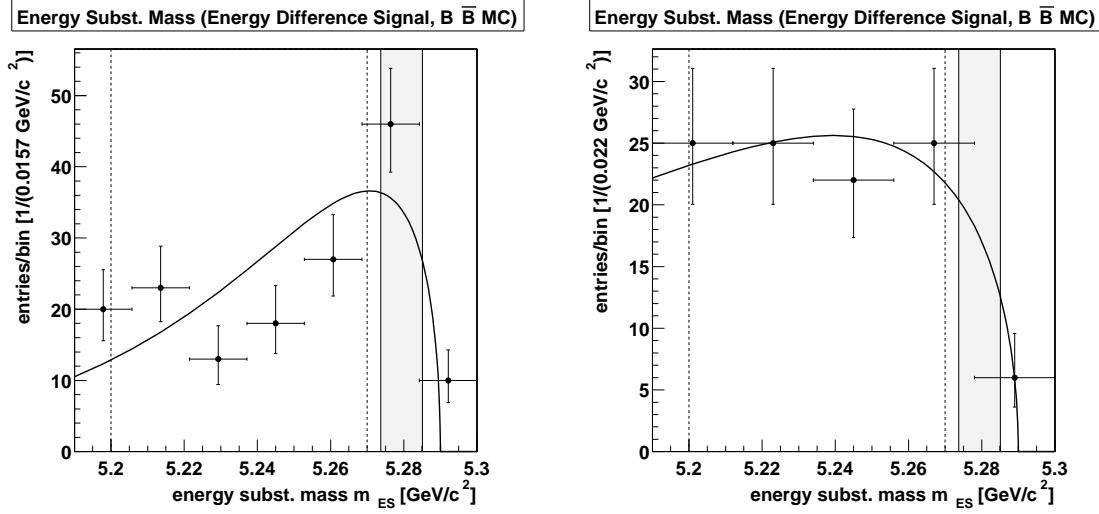


Figure 3.12 Distributions of the energy substituted mass of the B^0 candidates (in the signal region of the energy difference) in the $B\bar{B}$ Monte Carlo sample for the channels $\eta \rightarrow \gamma\gamma$ (left) and $\eta \rightarrow \pi^+\pi^-\pi^0$ (right). Solid curves show fitted p.d.f.'s. Solid lines border the signal regions, and dashed lines border the sidebands.

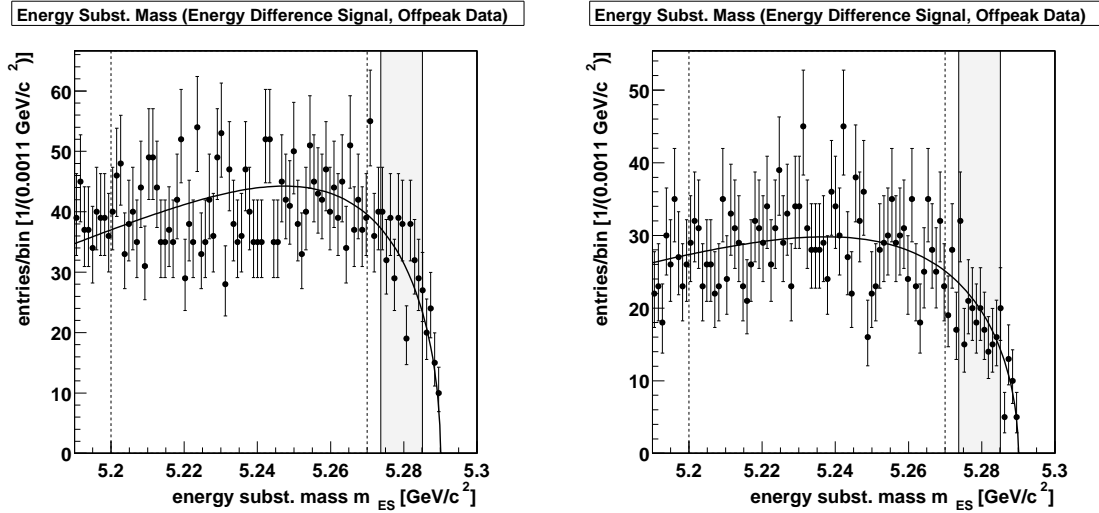


Figure 3.13 Distributions of the energy substituted mass of the B^0 candidates (in the signal region of the energy difference) in the off-peak data sample for the channels $\eta \rightarrow \gamma\gamma$ (left) and $\eta \rightarrow \pi^+\pi^-\pi^0$ (right). Solid curves show fitted p.d.f.'s. Solid lines border the signal regions, and dashed lines border the sidebands.

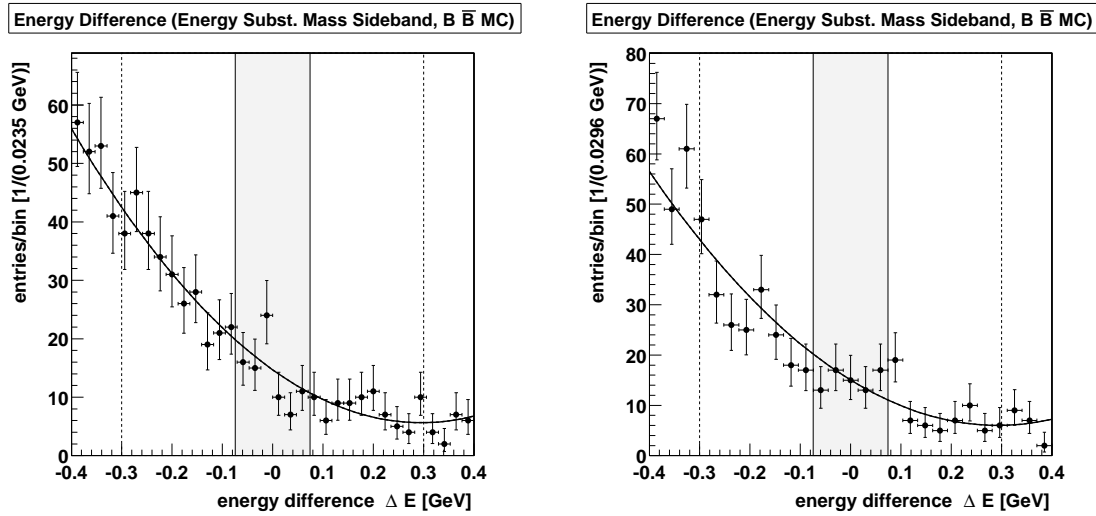


Figure 3.14 Distributions of the energy difference of the B^0 candidates (in the sideband of the energy substituted mass) in the $B\bar{B}$ Monte Carlo sample for the channels $\eta \rightarrow \gamma\gamma$ (left) and $\eta \rightarrow \pi^+\pi^-\pi^0$ (right). Solid curves show fitted p.d.f.'s. Solid lines border the signal regions, and dashed lines border the sidebands.

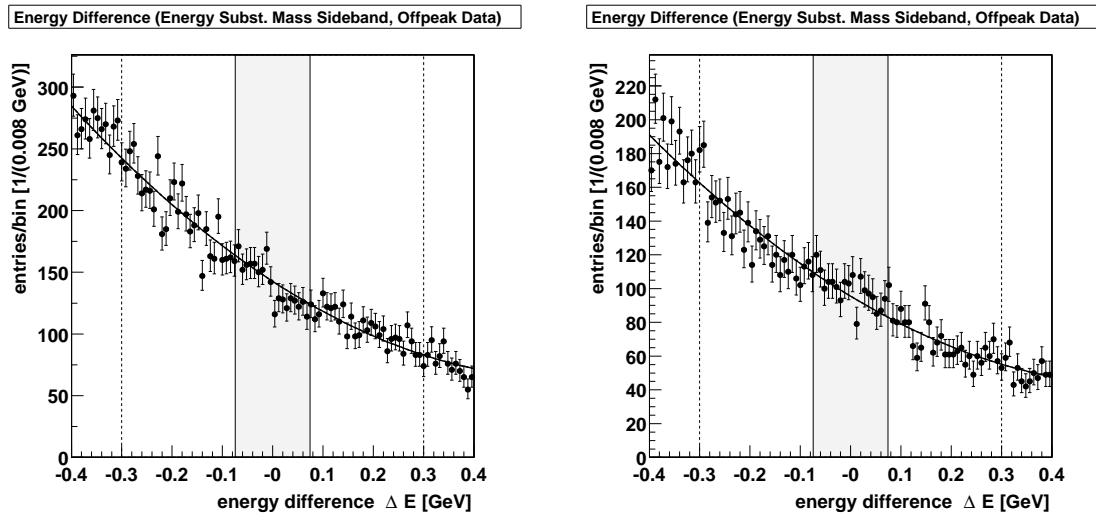


Figure 3.15 Distributions of the energy difference of the B^0 candidates (in the sideband of the energy substituted mass) in the off-peak data sample for the channels $\eta \rightarrow \gamma\gamma$ (left) and $\eta \rightarrow \pi^+\pi^-\pi^0$ (right). Solid curves show fitted p.d.f.'s. Solid lines border the signal regions, and dashed lines border the sidebands.

The distributions of m_{ES} and ΔE in the signal Monte Carlo samples are shown in Fig. 3.16 and 3.17. As expected in Sec. 3.3.1, m_{ES} peaks at the B meson mass, and ΔE peaks at 0. Due to leakage effects in the deposition of photon energy in the electromagnetic calorimeter, the distributions cease into “radiative” tails. They are fitted by so-called Crystal Ball functions [56]

$$f_{\text{CB}}(x) = \begin{cases} e^{-\frac{(x-\mu)^2}{2\sigma^2}} & , \quad x \geq \mu - \alpha\sigma \\ \frac{\left(\frac{r}{\alpha}\right)^r e^{-\frac{\alpha^2}{2}}}{\left(\frac{\mu-x}{\sigma} + \frac{r}{\alpha} - \alpha\right)^r} & , \quad x < \mu - \alpha\sigma \end{cases}, \quad (3.44)$$

consisting of a Gaussian p.d.f. and an r th power law tail attached at $x = \mu - \alpha\sigma$. While Eq. 3.12 allows for left and right side tails in m_{ES} , Eq. 3.11 only accommodates a left side tail in ΔE . However, the right side tail of m_{ES} gets cut off at the limit $m_{\text{ES}} \leq m_0$, while ΔE shows a small right side tail, as well. Consequently, a left side tail p.d.f. with $\alpha > 0$ is used for m_{ES} , and a joint p.d.f.

$$f(x) = \begin{cases} f_{\text{CB}1}(x), & x < \mu \\ f_{\text{CB}2}(x), & x \geq \mu \end{cases} \quad (3.45)$$

with a left side tail $\alpha_1 > 0$ and a right side tail $\alpha_2 < 0$ is used for ΔE . The tail powers r , r_1 and r_2 are fixed in the fits and adjusted to yield maximum χ^2 [35] values. To account for combinatoric background, the corresponding background p.d.f.’s f_{arg} or f_{cheb} are added.

The parameters of the p.d.f.’s fitted to the distributions in Fig. 3.12 to 3.15 are listed in Tab. 3.4. The joint distributions of m_{ES} and ΔE in the signal Monte Carlo, $B\bar{B}$ Monte Carlo, off-peak data and data sample are shown in App. C. (*This appendix contains unblinded results.*)

Signal Regions

A signal box is defined to cover two standard deviations of the Gaussian components of the signal distributions, which correspond to $|m_{\text{ES}} - m_{B^0}| \leq 0.00568 \text{ GeV}/c^2$ and $|\Delta E| \leq 0.0743 \text{ GeV}$. Only B^0 candidates inside these regions are considered signal candidates. However, the signal box also contains candidates from the background distributions. Since these contributions rise concurrently, the signal regions do *not* follow the signal asymmetries. To be blind for the signal, the regions $5.27 \leq m_{\text{ES}} \leq 5.29 \text{ GeV}/c^2$ and $|\Delta E| \leq 0.2 \text{ GeV}$ over the signal box are covered in the data sample.

The number of signal B^0 candidates can be obtained by either counting the signal box or integrating one of the p.d.f.’s fitted in the signal regions. The statistical uncertainty of a counted number N is given by the standard deviation $\sigma_n = \sqrt{N}$ of a Poisson distribution with mean value $\bar{n} = N$. The statistical uncertainty of an integral of a fitted p.d.f. is estimated by the (calculated) standard deviation of the distribution of 5000 integrals obtained while varying the p.d.f. parameters within their fit uncertainties. While it is assured that this distribution is approximately Gaussian, the calculation preserves the correlations in an integral ratio. Tab. 3.5 lists the resulting numbers of signal candidates in the signal Monte Carlo, the $B\bar{B}$ Monte Carlo and the off-peak data sample.

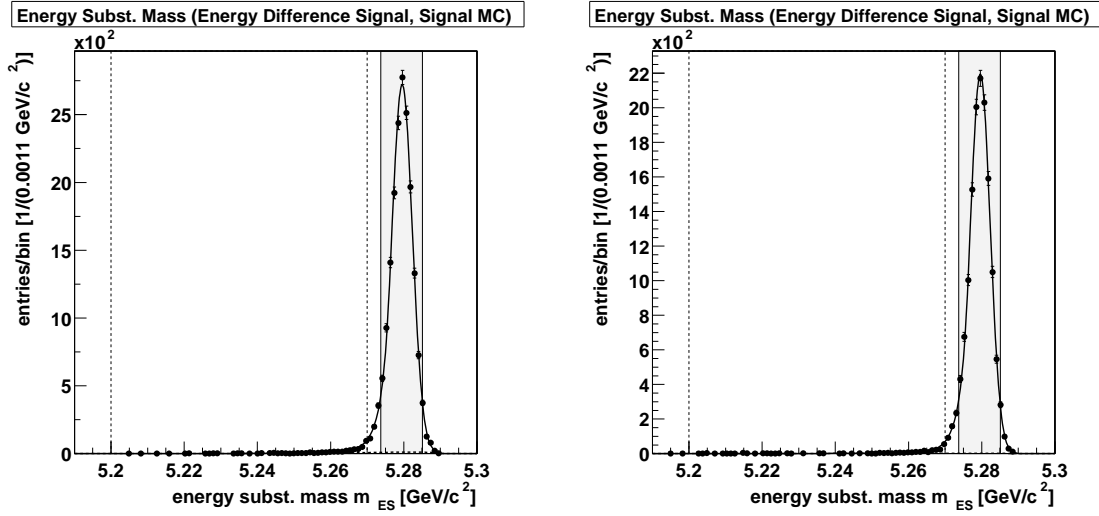


Figure 3.16 Distributions of the energy substituted mass of the B^0 candidates (in the signal region of the energy difference) in the signal Monte Carlo sample for the channels $\eta \rightarrow \gamma\gamma$ (left) and $\eta \rightarrow \pi^+\pi^-\pi^0$ (right). Solid curves show fitted p.d.f.'s. Solid lines border the signal regions, and dashed lines border the sidebands.

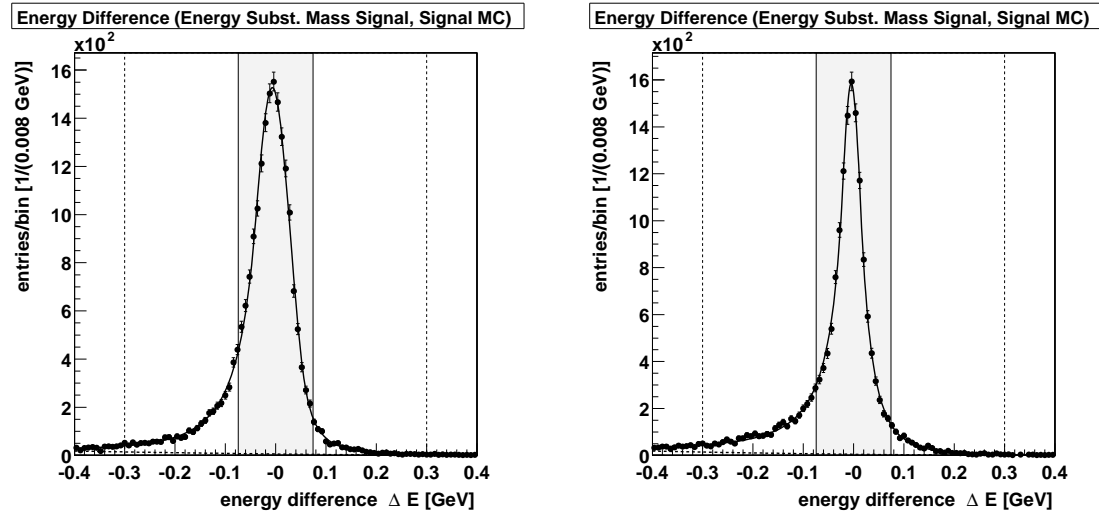


Figure 3.17 Distributions of the energy difference of the B^0 candidates (in the signal region of the energy substituted mass) in the signal Monte Carlo sample for the channels $\eta \rightarrow \gamma\gamma$ (left) and $\eta \rightarrow \pi^+\pi^-\pi^0$ (right). Solid curves show fitted p.d.f.'s. Solid lines border the signal regions, and dashed lines border the sidebands.

		m_{ES}	ΔE
$\eta \rightarrow \gamma\gamma$	signal	$S = 0.9822 \pm 0.0029$ $\mu = (5.279563 \pm 0.000031) \text{ GeV}/c^2$ $\sigma = (2.773 \pm 0.026) \text{ MeV}/c^2$ $r = 10$ $\alpha = 1.329 \pm 0.036$ $p = -173 \pm 15$	$S = 0.9673 \pm 0.0047$ $\mu = -(6.56 \pm 0.43) \text{ MeV}$ $\sigma = (35.17 \pm 0.42) \text{ MeV}$ $r_1 = 3$ $r_2 = 3$ $\alpha_1 = 0.963 \pm 0.019$ $\alpha_2 = -1.691 \pm 0.030$ $c_1 = -1.199 \pm 0.019$ $c_2 = -1.691 \pm 0.030$
	$B\bar{B}$	$p = -68.0 \pm 8.2$	$c_1 = -1.068 \pm 0.043$ $c_2 = 0.362 \pm 0.043$
	$q\bar{q}$	$p = -30.6 \pm 1.7$	$c_1 = -0.663 \pm 0.012$ $c_2 = 0.111 \pm 0.012$
$\eta \rightarrow \pi^+\pi^-\pi^0$	signal	$S = 0.9923 \pm 0.0014$ $\mu = (5.279624 \pm 0.000027) \text{ GeV}/c^2$ $\sigma = (2.687 \pm 0.021) \text{ MeV}/c^2$ $r = 10$ $\alpha = 1.311 \pm 0.024$ $p = -74 \pm 16$	$S = 0.9640 \pm 0.0052$ $\mu = -(4.73 \pm 0.29) \text{ MeV}$ $\sigma = (20.88 \pm 0.36) \text{ MeV}$ $r_1 = 2$ $r_2 = 4$ $\alpha_1 = 0.775 \pm 0.014$ $\alpha_2 = -0.949 \pm 0.019$ $c_1 = -1.324 \pm 0.088$ $c_2 = 0.31 \pm 0.11$
	$B\bar{B}$	$p = -25.7 \pm 9.8$	$c_1 = -1.051 \pm 0.048$ $c_2 = 0.359 \pm 0.049$
	$q\bar{q}$	$p = -24.7 \pm 2.0$	$c_1 = -0.667 \pm 0.015$ $c_2 = 0.111 \pm 0.015$

Table 3.4 Signal fractions S and p.d.f. parameters of the energy substituted mass m_{ES} (Eq. 3.41 and 3.44) and the energy difference ΔE (Eq. 3.42 and 3.45) in the signal Monte Carlo (Fig. 3.16 and 3.17), $B\bar{B}$ Monte Carlo (Fig. 3.12 and 3.14) and off-peak ($q\bar{q}$) data (Fig. 3.13 and 3.15) sample for the channels $\eta \rightarrow \gamma\gamma$ and $\eta \rightarrow \pi^+\pi^-\pi^0$.

		N_{sig}		
		count	m_{ES} fit	ΔE fit
$\eta \rightarrow \gamma\gamma$	signal	16702 ± 129	16542 ± 129	16548 ± 131
	$B\bar{B}$	36 ± 6	24 ± 3	
	$q\bar{q}$	348 ± 19	326 ± 10	
$\eta \rightarrow \pi^+\pi^-\pi^0$	signal	13138 ± 115	13077 ± 113	13125 ± 116
	$B\bar{B}$	7 ± 3	9 ± 2	
	$q\bar{q}$	198 ± 14	203 ± 8	

Table 3.5 Number of signal B^0 candidates N_{sig} obtained by counting the signal box or fitting the distributions of energy substituted mass m_{ES} or energy difference ΔE in the signal regions of the signal Monte Carlo, $B\bar{B}$ Monte Carlo and off-peak ($q\bar{q}$) data sample for the channels $\eta \rightarrow \gamma\gamma$ and $\eta \rightarrow \pi^+\pi^-\pi^0$.

The integrals of the p.d.f.'s fitted to the distributions in the signal Monte Carlo sample only contain the signal components. Although the counted numbers additionally contain combinatoric contributions, they agree statistically with the fitted numbers. Since they also have competitive statistical uncertainties, counted numbers are used in this analysis. The fitted numbers in the background samples have smaller statistical uncertainties due to the inclusion of a larger range in m_{ES} . To use this range for counting, sidebands are defined below.

The selection efficiency ε_{sig} for Monte Carlo signal B^0 decays is defined as the ratio of the number of signal B^0 candidates N_{sig} and the number of signal B^0 decays $N_{B^0}^0(B^0 \rightarrow \eta\phi)$ in the Monte Carlo sample. Since every signal Monte Carlo event contains one signal B^0 decay, $N_{B^0}^0(B^0 \rightarrow \eta\phi)$ is substituted with the number of signal Monte Carlo events $N_{B^0\bar{B}^0}^0(B^0 \rightarrow \eta\phi)$. The selection efficiency for Monte Carlo background B decays is defined as the ratio of the number of signal B^0 candidates and the number of background B decays $N_B^0(B^0 \rightarrow \eta\phi)$ in the Monte Carlo sample. Since every $B\bar{B}$ Monte Carlo event contains two background B decays, $N_B^0(B^0 \rightarrow \eta\phi)$ is substituted by twice the number of $B\bar{B}$ Monte Carlo events $N_{B\bar{B}}^0(B^0 \rightarrow \eta\phi)$. For the off-peak data sample, an estimation of ε_{sig} is based on twice the number of $q\bar{q}$ events assumed in Sec. 3.2.

Derived from the selection efficiencies are the expected numbers of signal B^0 candidates \hat{N}_{sig} in the data sample. Upper limits on the contributions from signal B^0 decays are obtained from the upper limits on the numbers of signal B^0 decays given in Tab. 3.2. Contributions from background B decays are estimated using the number of $B\bar{B}$ events from $B\bar{B}$ counting. Again, for $q\bar{q}$ background, the assumptions in Sec. 3.2 are used.

The resulting efficiencies and expected numbers of signal candidates are listed in Tab. 3.6. The estimates show clearly that the $q\bar{q}$ background contribution dominates the number of signal B^0 candidates. Its suppression is the primary motivation for applying further cuts. Although the selection efficiency for background B decays is at least one order of magnitude smaller, the expected number of signal B^0 candidates from background

B decays is still in the same order of magnitude as the expected upper limit on the number of signal candidates from signal B^0 decays. Hence, the $B\bar{B}$ background has to be considered as a systematic uncertainty. However, the selection efficiency for background B decays is also at least one order of magnitude smaller than the number of signal B^0 decays in the signal Monte Carlo sample, so that no signal B^0 candidates from background B decays are expected in this sample. Indeed, the signal B^0 candidates in the signal Monte Carlo sample that are not associated with signal B^0 decays predominantly contain one ϕ candidate and one photon candidate associated with constituents of a signal decay and one photon candidate associated with a background photon.

		ε_{sig}	\hat{N}_{sig}
$\eta \rightarrow \gamma\gamma$	signal	0.4283 ± 0.0033	$< 66.2 \pm 1.4$
	$B\bar{B}$	$(0.166 \pm 0.028) \times 10^{-6}$	29.4 ± 4.9
	$q\bar{q}$	$(0.534 \pm 0.029) \times 10^{-5}$	2956 ± 166
$\eta \rightarrow \pi^+\pi^-\pi^0$	signal	0.3551 ± 0.0031	$< 31.46 \pm 0.83$
	$B\bar{B}$	$(0.32 \pm 0.12) \times 10^{-7}$	5.7 ± 2.2
	$q\bar{q}$	$(0.304 \pm 0.022) \times 10^{-5}$	1682 ± 123

Table 3.6 Selection efficiencies ε_{sig} and expected numbers of signal B^0 candidates \hat{N}_{sig} in the data sample from signal B^0 decays, $B\bar{B}$ background decays and $q\bar{q}$ events in the channels $\eta \rightarrow \gamma\gamma$ and $\eta \rightarrow \pi^+\pi^-\pi^0$. Limits are given at 90% c.l.

Sidebands

Sidebands are regions in which only background events are expected. They are therefore separated from the signal box and chosen to cover as much statistics as available. Sidebands are defined for this analysis in the regions $5.20 \leq m_{\text{ES}} \leq 5.27 \text{ GeV}/c^2$ and $|\Delta E| \leq 0.3 \text{ GeV}$. Fig. 3.12 to 3.15 show m_{ES} in the ΔE signal region and ΔE in the m_{ES} sideband. Fig. 3.16 and 3.17 show m_{ES} in the ΔE signal region and ΔE in the m_{ES} signal region.

The sideband distributions of m_{ES} in the ΔE signal region and the distributions of ΔE in the m_{ES} sideband in the data sample are shown in Fig. 3.18 and 3.19. Although the signal region of m_{ES} is blinded, the p.d.f.'s fitted in the sidebands are extrapolated into the full m_{ES} range. This allows a comparison with the off-peak data sample which is discussed in detail in Sec. 3.6. As expected from Tab. 3.6, the distributions in the data sample are generally best described by those in the off-peak data sample.

The high statistics of the data sample also reveal the effects of different approaches for the treatment of events with multiple B^0 candidates. Fig. 3.20 shows the distributions of ΔE for the candidates with the smallest deviation from the B meson mass. The exclusive selection of these candidates enhances the frequency in the signal region. The resulting signal shape is well modeled by a joint Crystal Ball signal p.d.f. An inspection of

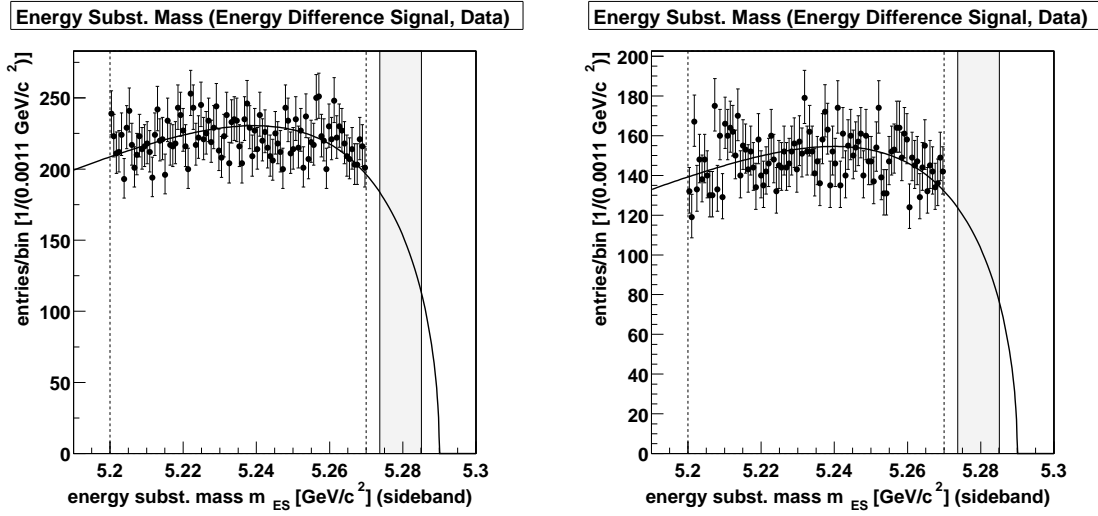


Figure 3.18 Sideband distributions of the energy substituted mass of the B^0 candidates (in the signal region of the energy difference) in the data sample for the channels $\eta \rightarrow \gamma\gamma$ (left) and $\eta \rightarrow \pi^+\pi^-\pi^0$ (right). Solid curves show fitted p.d.f.'s. Solid lines border the signal regions, and dashed lines border the sidebands.

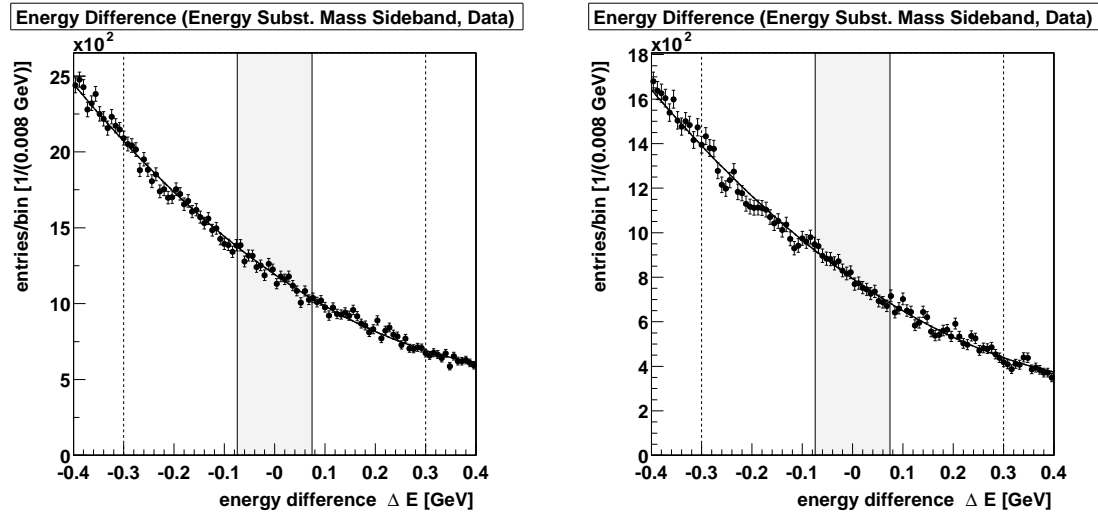


Figure 3.19 Distributions of the energy difference of *all* B^0 candidates (in the sideband of the energy substituted mass) in the data sample for the channels $\eta \rightarrow \gamma\gamma$ (left) and $\eta \rightarrow \pi^+\pi^-\pi^0$ (right). Solid curves show fitted p.d.f.'s. Solid lines border the signal regions, and dashed lines border the sidebands.

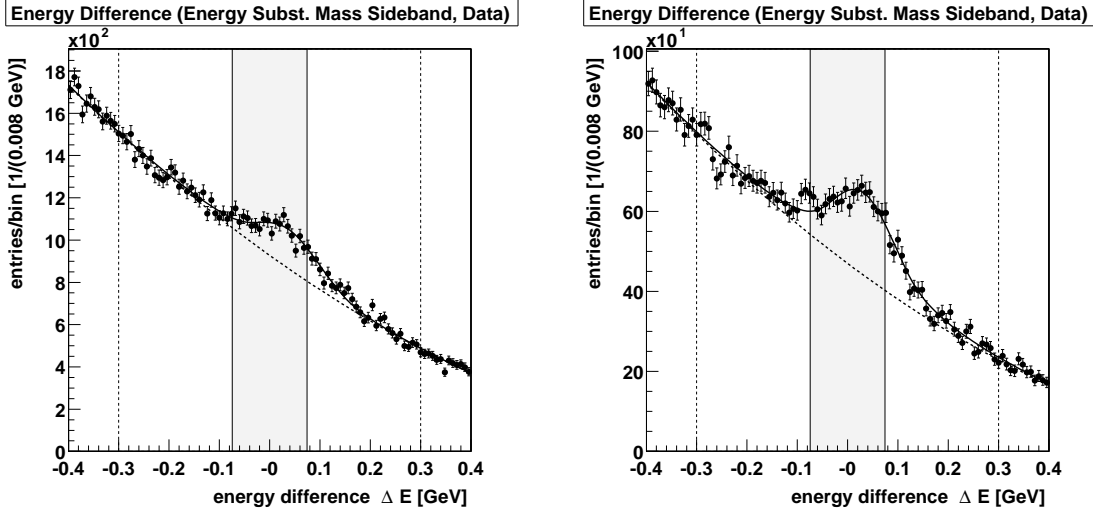


Figure 3.20 Distributions of the energy difference of the B^0 candidates with the smallest deviation from the B meson mass (in the sideband of the energy substituted mass) in the data sample for the channels $\eta \rightarrow \gamma\gamma$ (left) and $\eta \rightarrow \pi^+\pi^-\pi^0$ (right). Solid curves show fitted p.d.f.'s. Solid lines border the signal regions, and dashed lines border the sidebands.

continuum Monte Carlo samples shows that many B^0 candidates in this region contain a ϕ candidate correctly reconstructed from a ϕ meson that is combined with an η candidate made from a random combination of background photons. Given the large number of background photons in the absence of a vertex constraint, a B^0 candidate with a mass close to the B meson mass is thus easily constructed. The distribution of the masses of *all* constructed B^0 candidates, however, is still arbitrary. For the benefit of a smoothly shaped background, all B^0 candidates in each event are accepted throughout this analysis. The mean multiplicities in the data samples are 1.4 in the channel $\eta \rightarrow \gamma\gamma$ and 1.7 in the channel $\eta \rightarrow \pi^+\pi^-\pi^0$, measured with statistical uncertainties of approximately 1%. Although multiple signal B^0 candidates are also found for signal B^0 decays, the term selection *efficiency* is used, since it is always smaller than 1. The parameters of the p.d.f.'s fitted to the distributions in Fig. 3.18 to 3.20 are listed in Tab. 3.7.

3.5.5 Resonance Masses

The distributions of the invariant mass $m_{\gamma\gamma}$ of the π^0 candidates in the channel $\eta \rightarrow \pi^+\pi^-\pi^0$ are shown in Fig. 3.21. The distributions of the invariant mass $m_{\gamma\gamma}$ of the η candidates in the channel $\eta \rightarrow \gamma\gamma$ and the composite mass m_η of the η candidates in the channel $\eta \rightarrow \pi^+\pi^-\pi^0$ are shown in Fig. 3.22. The distributions of the composite mass m_ϕ of the ϕ candidates are shown in Fig. 3.23.

The signal components of the $m_{\gamma\gamma}$ distributions in the channel $\eta \rightarrow \gamma\gamma$ show radiative left side tails and are fitted by single Crystal Ball functions. Their background components are fitted by (ordinary) first degree polynomials. The signal components of the $m_{\gamma\gamma}$ and m_η distributions in the channel $\eta \rightarrow \pi^+\pi^-\pi^0$ show radiative left side and also smaller

		m_{ES}	ΔE
$\eta \rightarrow \gamma\gamma$	all	$p = -25.74 \pm 0.90$	$c_1 = -0.6756 \pm 0.0041$ $c_2 = 0.1237 \pm 0.0041$
	m_{B^0}		$S = 0.0402 \pm 0.0030$ $\mu = (37.5 \pm 3.6) \text{ MeV}$ $\sigma = (62.7 \pm 3.0) \text{ MeV}$ $r_1 = 3$ $r_2 = 3$ $\alpha_1 = 1.238$ $\alpha_2 = -1.967$ $c_1 = -0.6877 \pm 0.0041$ $c_2 = 0.0622 \pm 0.0068$
$\eta \rightarrow \pi^+\pi^-\pi^0$	all	$p = -26.1 \pm 1.1$	$c_1 = -0.7036 \pm 0.0050$ $c_2 = 0.1187 \pm 0.0050$
	m_{B^0}		$S = 0.0880 \pm 0.0073$ $\mu = (31.96081 \pm 0.00056) \text{ MeV}$ $\sigma = (64.3 \pm 3.9) \text{ MeV}$ $r_1 = 3$ $r_2 = 3$ $\alpha_1 = 1.293$ $\alpha_2 = -1.378$ $c_1 = -0.7433 \pm 0.0086$ $c_2 = 0.073 \pm 0.013$

Table 3.7 Signal fractions S and p.d.f. parameters of the energy substituted mass m_{ES} (Eq. 3.41) and the energy difference ΔE (Eq. 3.42 and 3.45) of *all* B^0 candidates (Fig. 3.18 and 3.19) and the candidates with the best composite mass m_{B^0} (Fig. 3.20) in the data sample for the channels $\eta \rightarrow \gamma\gamma$ and $\eta \rightarrow \pi^+\pi^-\pi^0$.

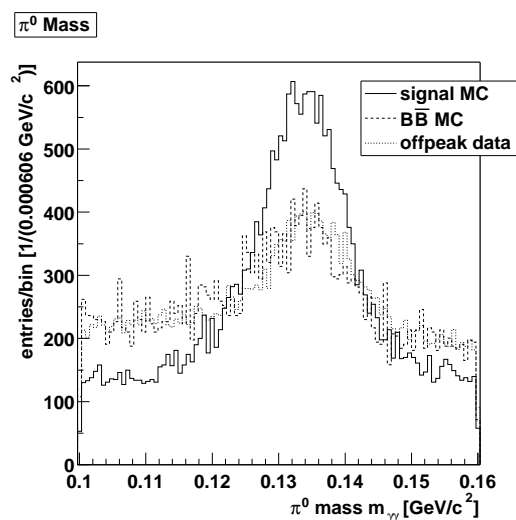


Figure 3.21 Distributions of the invariant mass of the π^0 candidates in the signal Monte Carlo, $B\bar{B}$ Monte Carlo and off-peak data sample for the channel $\eta \rightarrow \pi^+\pi^-\pi^0$. All frequencies are scaled against the signal Monte Carlo sample.

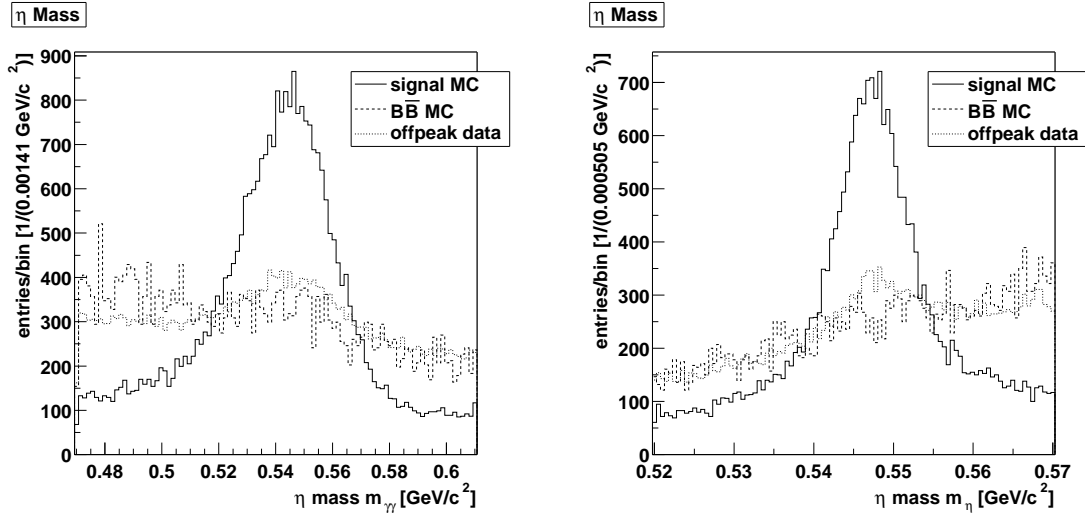


Figure 3.22 Distributions of the invariant mass and the composite mass, respectively, of the η candidates in the signal Monte Carlo, $B\bar{B}$ Monte Carlo and off-peak data sample for the channels $\eta \rightarrow \gamma\gamma$ (left) and $\eta \rightarrow \pi^+\pi^-\pi^0$ (right). All frequencies are scaled against the signal Monte Carlo sample.

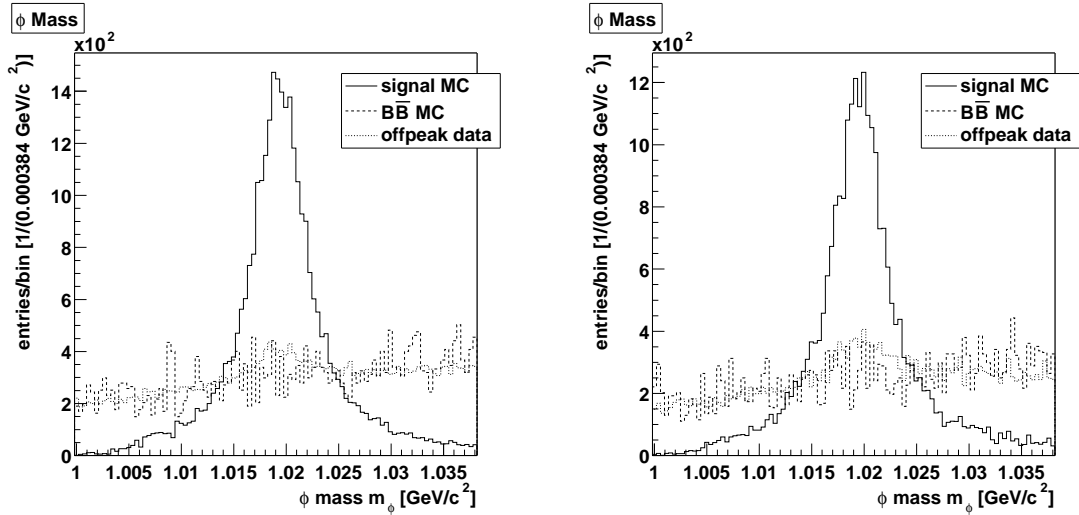


Figure 3.23 Distributions of the composite mass of the ϕ candidates in the signal Monte Carlo, $B\bar{B}$ Monte Carlo and off-peak data sample for the channels $\eta \rightarrow \gamma\gamma$ (left) and $\eta \rightarrow \pi^+\pi^-\pi^0$ (right). All frequencies are scaled against the signal Monte Carlo sample.

right side tails and are therefore fitted by joint Crystal Ball functions. Their background components are fitted by second degree polynomials. The m_ϕ distributions are fitted by convolutions of a Breit–Wigner decay function

$$f_{\text{dec}}(x) \propto \frac{1}{(x - \mu)^2 + (\frac{1}{2}\Gamma)^2} \quad (3.46)$$

and a Gaussian resolution function

$$f_{\text{res}}(x) \propto e^{-\frac{(x-\mu)^2}{2\sigma^2}} \quad (3.47)$$

with the common mean value μ . Their background components are fitted by second degree polynomials. The Breit–Wigner decay widths Γ and the transition parameters α , α_1 and α_2 of the Crystal Ball functions are fixed in all samples to the values fitted to the signal Monte Carlo sample.

The distributions of the masses of the resonance candidates in the data sample can be fitted by the signal and the background p.d.f.’s found in the signal Monte Carlo and the off-peak data sample. The p.d.f.’s fitted to the distributions of the masses of the π^0 , η and ϕ candidates in the signal Monte Carlo, the off-peak data and the data sample are compared in App. A. The general agreement of the signal components in Monte Carlo and data events suggests that the Monte Carlo simulation is reliable. Systematic effects in this comparison are discussed in Sec. 3.6. The close match of signal *and* background components in off-peak and on-peak data events supports the conclusion that the $q\bar{q}$ background is dominating.

To suppress background contributions in candidate counting, cuts are applied around the meson masses \bar{m}_{π^0} , \bar{m}_η and \bar{m}_ϕ [8]. In the channel $\eta \rightarrow \gamma\gamma$, cuts in the range $|m_\eta - \bar{m}_\eta| \leq 0.010 \dots 0.070 \text{ GeV}/c^2$ and $|m_\phi - \bar{m}_\phi| \leq 0.001 \dots 0.020 \text{ GeV}/c^2$ are considered. In the channel $\eta \rightarrow \pi^+\pi^-\pi^0$, cuts in the ranges $|m_{\pi^0} - \bar{m}_{\pi^0}| \leq 0.005 \dots 0.025 \text{ GeV}/c^2$, $|m_\eta - \bar{m}_\eta| \leq 0.005 \dots 0.025 \text{ GeV}/c^2$ and $|m_\phi - \bar{m}_\phi| \leq 0.001 \dots 0.020 \text{ GeV}/c^2$ are considered.

3.5.6 Fisher Discriminant

The distributions of the Fisher discriminant \mathcal{F} are shown in Fig. 3.24. They are fitted by the sum of three independent Gaussian p.d.f.’s. To optimize separation in candidate counting, cuts in the range $\mathcal{F} \leq -0.5 \dots 1.0$ are considered.

3.5.7 Helicity Angles

The distributions of the magnitudes of the cosines of the helicity angles $|\cos(\vartheta_{\lambda\phi})|$ of the ϕ candidates are shown in Fig. 3.25. The distributions in the signal Monte Carlo sample follow the expectation of Sec. 3.3.2 and are fitted by parabolas. The distributions in the $B\bar{B}$ Monte Carlo and the off-peak data sample are generally flat, but show accumulations toward $|\cos(\vartheta_{\lambda\phi})| = 1$. They are therefore fitted by third degree polynomials. Strong background suppression in candidate counting is expected from cuts in the range $|\cos(\vartheta_{\lambda\phi})| \geq 0.1 \dots 0.6$.

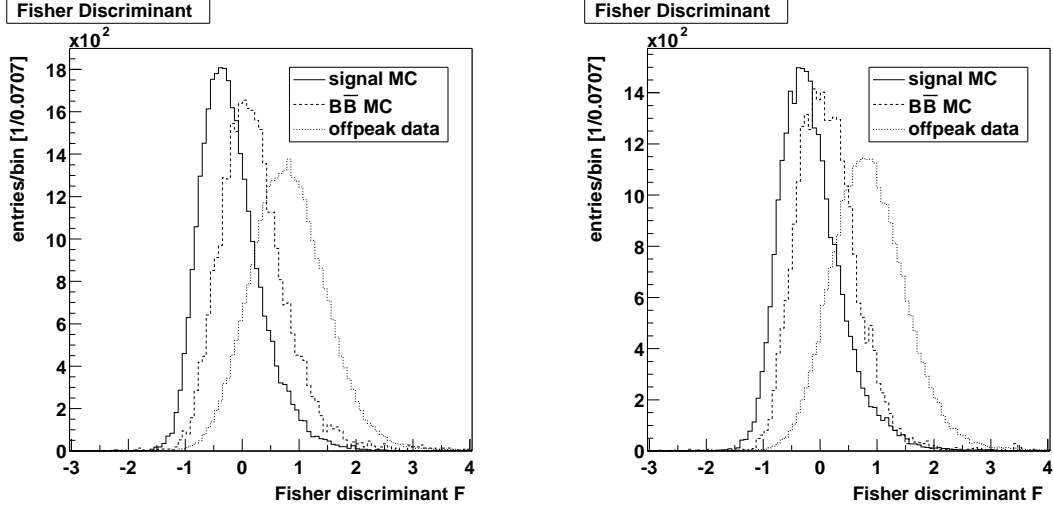


Figure 3.24 Distributions of the Fisher discriminant in the signal Monte Carlo, $B\bar{B}$ Monte Carlo and off-peak data sample for the channels $\eta \rightarrow \gamma\gamma$ (left) and $\eta \rightarrow \pi^+\pi^-\pi^0$ (right). All frequencies are scaled against the signal Monte Carlo sample.

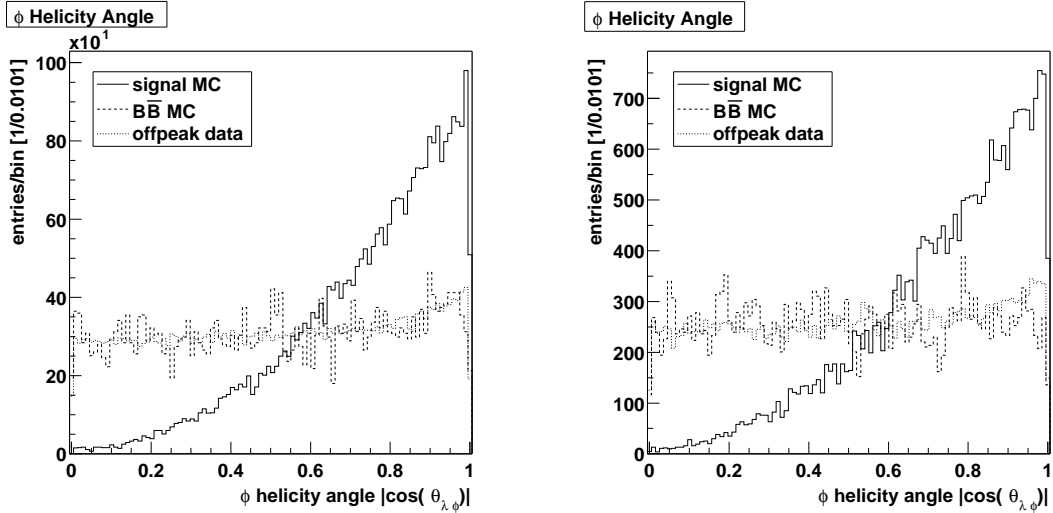


Figure 3.25 Distributions of the magnitude of the cosine of the helicity angle of the ϕ candidates in the signal Monte Carlo, $B\bar{B}$ Monte Carlo and off-peak data sample for the channels $\eta \rightarrow \gamma\gamma$ (left) and $\eta \rightarrow \pi^+\pi^-\pi^0$ (right). All frequencies are scaled against the signal Monte Carlo sample.

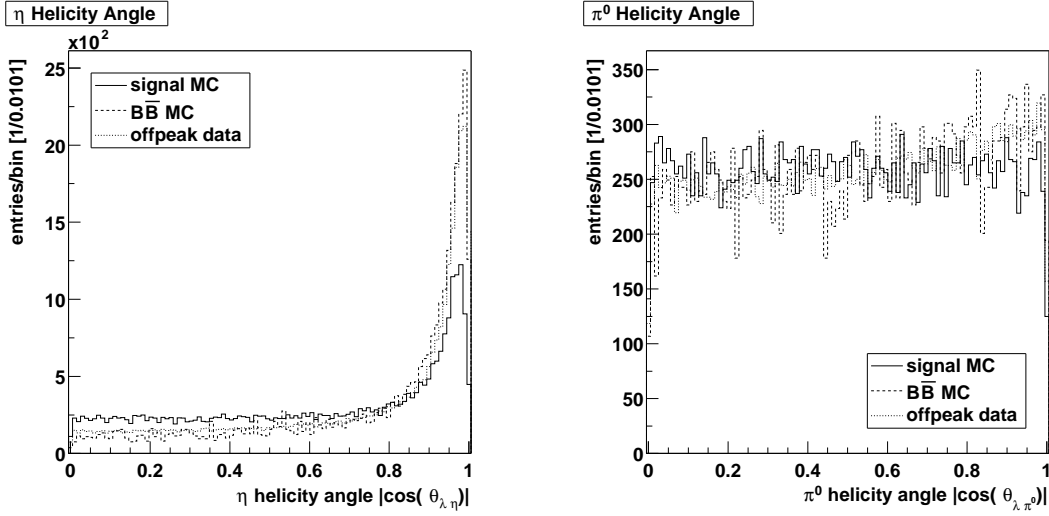


Figure 3.26 Distributions of the magnitude of the cosine of the helicity angle of the η candidates and the π^0 candidates, respectively, in the signal Monte Carlo, $B\bar{B}$ Monte Carlo and off-peak data sample for the channels $\eta \rightarrow \gamma\gamma$ (left) and $\eta \rightarrow \pi^+\pi^-\pi^0$ (right). All frequencies are scaled against the signal Monte Carlo sample.

The distributions of the magnitudes of the cosines of the helicity angles $|\cos(\vartheta_{\lambda\eta})|$ of the η candidates in the channel $\eta \rightarrow \gamma\gamma$ and $|\cos(\vartheta_{\lambda\pi^0})|$ of the π^0 candidates in the channel $\eta \rightarrow \pi^+\pi^-\pi^0$ are shown in Fig. 3.26. Since the expected rise of the distribution of $|\cos(\vartheta_{\lambda\eta})|$ in the background samples at $|\cos(\vartheta_{\lambda\eta})| = 1$ is very strong, cuts are considered for candidate counting in the range $|\cos(\vartheta_{\lambda\eta})| \leq 0.6 \dots 1.0$. Since the same effect in the distribution of $|\cos(\vartheta_{\lambda\pi^0})|$ is much smaller, which can be explained by the lower mass of the π^0 meson, the fixed cut $|\cos(\vartheta_{\lambda\pi^0})| \leq 0.9$ is applied.

3.6 Candidate Counting Method

The candidate counting method obtains the number of signal B^0 candidates in the data sample from counting the entries in the signal box. In order to use the signal Monte Carlo sample to determine the signal selection efficiency, the background contributions in the signal box need to be subtracted. This is accomplished by means of the sidebands. To achieve high signal and low background selection, all cuts on kinematic and topological variables considered in Sec. 3.5 are optimized.

3.6.1 Background Subtraction

After application of all cuts, the (background subtracted) signal number

$$S = N_{\text{sig}} - B \quad (3.48)$$

is calculated from the number of B^0 candidates in the signal box N_{sig} and the background number B , where

$$B = R N_{\text{SB}} \quad (3.49)$$

is obtained from the number of B^0 candidates in the sideband N_{SB} and the background ratio R . If R is small and the Poisson distributed N_{sig} and N_{SB} are large enough to estimate their standard deviations by $\sigma_{N_{\text{sig}}} = \sqrt{N_{\text{sig}}}$ and $\sigma_{N_{\text{SB}}} = \sqrt{N_{\text{SB}}}$, the standard deviation

$$\sigma_S = \sqrt{N_{\text{sig}} + R^2 N_{\text{SB}}} \quad (3.50)$$

of S simply becomes

$$\sigma_S = \sqrt{S + B}. \quad (3.51)$$

The background ratios are found by evaluating

$$R = \frac{N_{\text{sig}}}{N_{\text{SB}}} \quad (3.52)$$

in the $B\bar{B}$ Monte Carlo and the off-peak data sample while successively applying cuts in the ranges considered in Sec. 3.5 in the order

1. mass of the η candidates
2. mass of the ϕ candidates
3. mass of the π^0 candidates ⁷
4. kaon identification of the first K^\pm candidate
5. kaon identification of the second K^\pm candidate
6. kaon identification of the first π^\pm candidate ⁷
7. kaon identification of the second π^\pm candidate ⁷
8. Fisher discriminant
9. helicity angle of the η candidates ⁸
10. helicity angle of the ϕ candidates
11. helicity angle of the π^0 candidates ⁷
12. energy of the photon candidates
13. number of tracks.

The resulting evolutions of the ratios are shown in Fig. 3.27 and 3.28. To estimate the ratios at the final number of cuts, these evolutions are fitted by constants. Since the statistical uncertainties rise for subsequent values, the constants inherit the uncertainties of the initial ratios, while deviations from the constants at 32% c.l. are averaged as systematic uncertainties. The resulting constants are given in Tab. 3.8.

⁷Only in the channel $\eta \rightarrow \pi^+\pi^-\pi^0$.

⁸Only in the channel $\eta \rightarrow \gamma\gamma$.

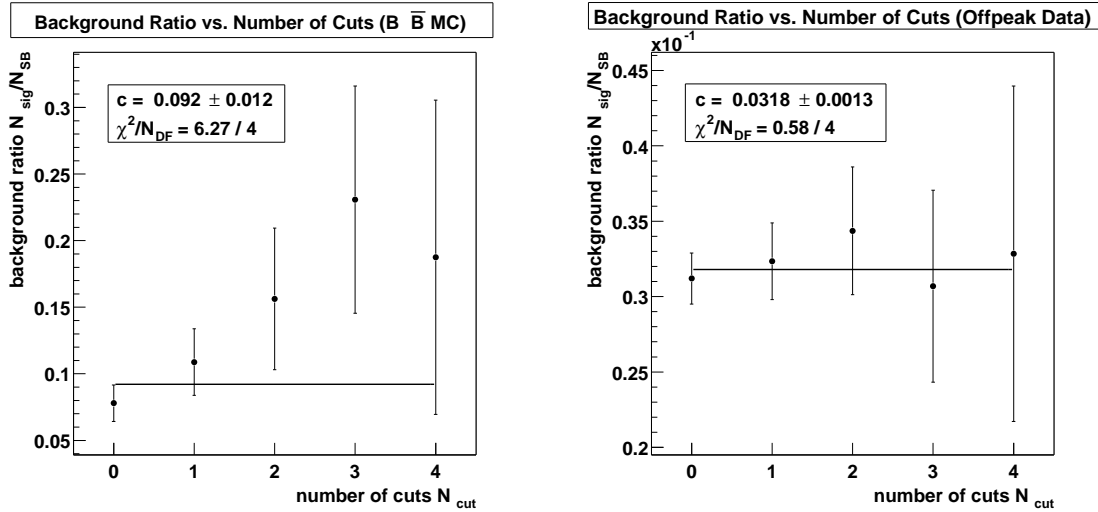


Figure 3.27 Background ratios R in the $B\bar{B}$ Monte Carlo (left) and the off-peak data (right) sample for the channel $\eta \rightarrow \gamma\gamma$ vs. number of cuts. Solid lines show fitted constants.

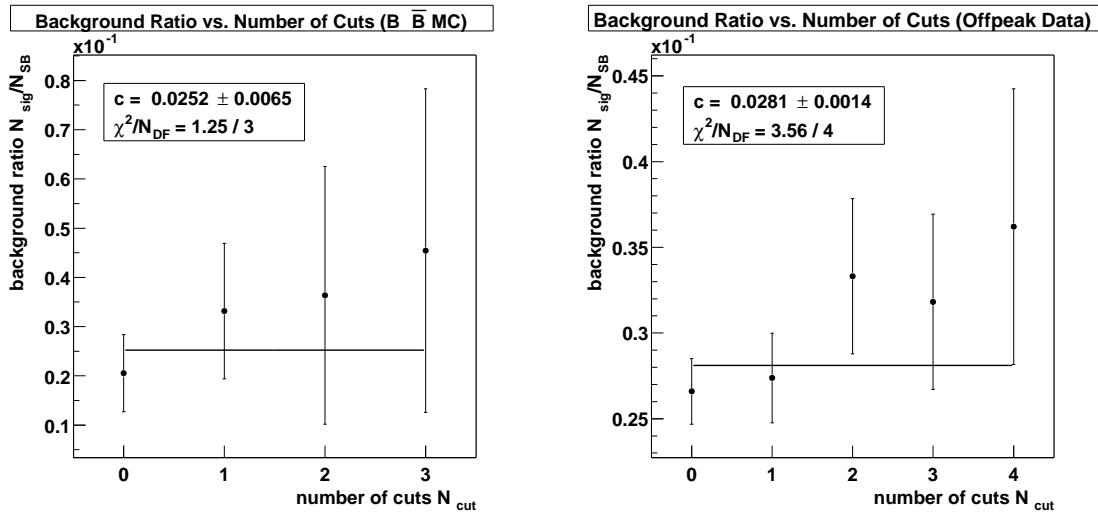


Figure 3.28 Background ratios R in the $B\bar{B}$ Monte Carlo (left) and the off-peak data (right) sample for the channel $\eta \rightarrow \pi^+\pi^-\pi^0$ vs. number of cuts. Solid lines show fitted constants.

	$\eta \rightarrow \gamma\gamma$	$\eta \rightarrow \pi^+\pi^-\pi^0$
$R_{B\bar{B}}$	0.0921 ± 0.0179	0.0252 ± 0.0065
$R_{q\bar{q}}$	0.0318 ± 0.0013	0.0281 ± 0.0014

Table 3.8 (Counted) background ratios $R_{B\bar{B}}$ and $R_{q\bar{q}}$ in the channels $\eta \rightarrow \gamma\gamma$ and $\eta \rightarrow \pi^+\pi^-\pi^0$.

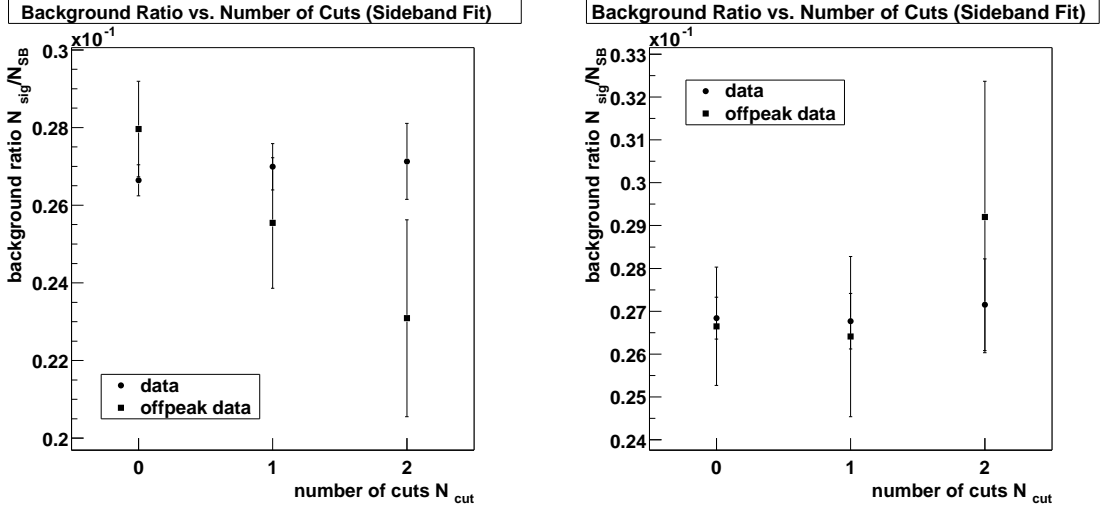


Figure 3.29 Background ratios R fitted to the sidebands in the on-peak and the off-peak data sample for the channels $\eta \rightarrow \gamma\gamma$ (left) and $\eta \rightarrow \pi^+\pi^-\pi^0$ (right) vs. number of cuts.

Alternatively,

$$R = \frac{\int_{\text{sig}} f_{\text{arg}}(m_{\text{ES}}) dm_{\text{ES}} \int f_{\text{cheb}}(\Delta E) d\Delta E}{\int_{\text{SB}} f_{\text{arg}}(m_{\text{ES}}) dm_{\text{ES}} \int_{\text{SB}} f_{\text{cheb}}(\Delta E) d\Delta E} \quad (3.53)$$

is calculated from the p.d.f.'s f_{arg} and f_{cheb} fitted to the distributions of m_{ES} and ΔE , respectively, in Fig. 3.12 to 3.15 by integrating them in the signal regions (“sig”) and sidebands (“SB”). The advantage of this method is that it is even applicable to the data sample if the f_{arg} fit is limited to the m_{ES} sideband and afterward extrapolated to the m_{ES} signal region. The comparison of these sideband extrapolated ratios in the on-peak and the off-peak data sample is shown in Fig. 3.29. They are consistent within their statistical uncertainties. A systematic uncertainty of 4.9% in the channel $\eta \rightarrow \gamma\gamma$ and 5.5% in the channel $\eta \rightarrow \pi^+\pi^-\pi^0$ for using $R_{q\bar{q}}$ in the data sample is estimated from the statistical uncertainties of the initial ratios.

3.6.2 Selection Efficiencies

The selection efficiencies for signal and background B decays have been defined in Sec. 3.5.4. The signal selection efficiency ε_S is obtained by evaluating

$$\varepsilon_S = \varepsilon_{\text{MC}} \frac{N_{\text{sig}}}{N_{B^0\bar{B}^0}^0} \quad (3.54)$$

in signal Monte Carlo sample, where $N_{B^0\bar{B}^0}^0$ is the number of events and ε_{MC} is the mean value of the products of the tracking efficiency corrections for all tracks contributing to one B^0 candidate. The $B\bar{B}$ background selection efficiency $\varepsilon_{B\bar{B}}$ is obtained by evaluating

$$\varepsilon_{B\bar{B}} = \varepsilon_{\text{MC}} \frac{N_{\text{SB}}}{2N_{B\bar{B}}^0} \quad (3.55)$$

in the $B\bar{B}$ Monte Carlo sample, with $N_{B\bar{B}}^0$ being the number of events.

The effect of signal B^0 decays that were removed from the $B\bar{B}$ Monte Carlo sample *after* $N_{B\bar{B}}^0$ was counted is negligible, since the relative deviation of the selection efficiency depends on the signal branching fraction \mathcal{B} by

$$\frac{\Delta\varepsilon_{B\bar{B}}}{\varepsilon_{B\bar{B}}} \approx -2\mathcal{B} \quad (3.56)$$

for $\mathcal{B} \ll 1$. On the other hand, the selected background B decays have to be subtracted from N_{sig} in Eq. 3.54. The relative deviation of the signal selection efficiency, however, is

$$\frac{\Delta\varepsilon_S}{\varepsilon_S} = \frac{R_{B\bar{B}}\varepsilon_{B\bar{B}}}{\varepsilon_S}, \quad (3.57)$$

which is negligible with regard to $\varepsilon_{\text{sig}} = R_{B\bar{B}}\varepsilon_{B\bar{B}}$ in Tab. 3.6.

3.6.3 Signal Expectation

The expected signal number \hat{S} is determined for a given set of cuts from the signal selection efficiency ε_S and the expected number of signal B^0 decays in the data sample $\hat{N}_{B^0\bar{B}^0}^0(B^0 \rightarrow \eta\phi)$ by

$$\hat{S} = \varepsilon_S \hat{N}_{B^0\bar{B}^0}^0(B^0 \rightarrow \eta\phi). \quad (3.58)$$

Assuming a significant signal, an upper limit on $\hat{N}_{B^0\bar{B}^0}^0(B^0 \rightarrow \eta\phi)$ is calculated from the CLEO upper limit on $\mathcal{B}(B^0 \rightarrow \eta\phi)$ [33]. Assuming no signal, the expected upper limit on \bar{S} is calculated for $\hat{S} = 0$.

3.6.4 Background Expectation

The expected background number

$$\hat{B} = \hat{B}_{B\bar{B}} + \hat{B}_{q\bar{q}} \quad (3.59)$$

contains the $B\bar{B}$ background number $\hat{B}_{B\bar{B}}$ and the $q\bar{q}$ background number $\hat{B}_{q\bar{q}}$. For each given set of cuts, the expected number of $B\bar{B}$ background B^0 candidates in the sideband $\hat{N}_{B\bar{B}}$ is determined from the background selection efficiency $\varepsilon_{B\bar{B}}$ and the expected number of background B decays in the data sample $\hat{N}_{B\bar{B}}^0(B^0 \rightarrow \eta\phi)$ by

$$\hat{N}_{B\bar{B}} = \varepsilon_{B\bar{B}} \hat{N}_{B\bar{B}}^0(B^0 \rightarrow \eta\phi). \quad (3.60)$$

As before, $\hat{N}_{B\bar{B}}^0(B^0 \rightarrow \eta\phi)$ comes from $B\bar{B}$ counting, in which the signal contributions are negligible. Assuming a common cross section, the expected number of $q\bar{q}$ background B^0 candidates in the sideband $\hat{N}_{q\bar{q}}$ is derived from the ratio of the integrated luminosities \mathcal{L}_{on} and \mathcal{L}_{off} of the on-peak and off-peak data sample, respectively, by evaluating

$$\hat{N}_{q\bar{q}} = \frac{\mathcal{L}_{\text{on}}}{\mathcal{L}_{\text{off}}} N_{\text{SB}} \quad (3.61)$$

in the off-peak data sample. Finally, the expected background numbers are calculated from Eq. 3.49 by

$$\hat{B}_{B\bar{B}} = R_{B\bar{B}} \hat{N}_{B\bar{B}}, \quad (3.62)$$

$$\hat{B}_{q\bar{q}} = R_{q\bar{q}} \hat{N}_{q\bar{q}}. \quad (3.63)$$

3.6.5 Cut Optimization

The cut optimization is performed by simultaneous variation of all cuts in the ranges given in Sec. 3.5. The choice of the optimization criterion determines the precision of the measured branching fraction $\mathcal{B}(B^0 \rightarrow \eta\phi)$ and depends on the expected value of the signal number S . If the signal is significant, maximum precision of \mathcal{B} is equivalent to maximum significance S/σ_S , which by Eq. 3.51 leads to the criterion

$$\frac{S^2}{S+B} \rightarrow \max. \quad (3.64)$$

If the signal is not significant, but the mean value of the background distribution can still be estimated by $\bar{B} \approx B$, the upper limit \bar{S}_ε on the mean value \bar{S} of the Poisson distribution of S at $1 - \varepsilon = 90\%$ is used instead. In Bayesian statistics, it is fitted to the relation [35]

$$\varepsilon = \frac{\sum_{n=0}^S e^{-B} \frac{B^n}{n!}}{\sum_{n=0}^S e^{-(B+\bar{S}_\varepsilon)} \frac{(B+\bar{S}_\varepsilon)^n}{n!}}. \quad (3.65)$$

Since the uncertainty on the branching fraction \mathcal{B} decreases with a decreasing upper limit \bar{B}_ε , the optimization criterion is then

$$\bar{B}_\varepsilon(B^0 \rightarrow \eta\phi) \rightarrow \min. \quad (3.66)$$

The results of an optimization for the signal criterion are given in Tab. 3.9. No significant signal is expected in either channel. The fixed cuts and those optimized for the

no-signal criterion are summarized in Tab. 3.10. The dependences of the expected upper limit on $\mathcal{B}(B^0 \rightarrow \eta\phi)$ on the varied cuts are shown in App. B. The signal selection efficiencies and expectations for signal and background numbers, numbers of signal and background B^0 candidates in the sidebands and upper limits on $\mathcal{B}(B^0 \rightarrow \eta\phi)$ under these cuts are given in Tab. 3.11. The joint distributions of m_{ES} and ΔE in the signal Monte Carlo, $B\bar{B}$ Monte Carlo, off-peak data and data sample under these cuts are shown in App. C. (*This appendix contains unblinded results.*)

	$\eta \rightarrow \gamma\gamma$	$\eta \rightarrow \pi^+\pi^-\pi^0$
\hat{S}	$< 31.73 \pm 0.70$	$< 13.14 \pm 0.37$
$\hat{B}_{B\bar{B}}$	0.15 ± 0.11	0.040 ± 0.030
$\hat{B}_{q\bar{q}}$	6.5 ± 1.4	3.10 ± 0.88
$\hat{S}^2/(\hat{S} + \hat{B})$	$< 26.3 \pm 1.2$	$< 10.61 \pm 0.67$

Table 3.9 Expected signal number \hat{S} , background numbers $\hat{B}_{B\bar{B}}$ and $\hat{B}_{q\bar{q}}$ and optimization criterion $\hat{S}^2/(\hat{S} + \hat{B})$ for signal optimized cuts in the channels $\eta \rightarrow \gamma\gamma$ and $\eta \rightarrow \pi^+\pi^-\pi^0$. Limits are given at 90% c.l.

3.6.6 Sideband Measurement

The numbers of B^0 candidates counted in the sidebands of the data sample are presented in Tab. 3.12. They agree with the expected numbers in Tab. 3.11 at 12% c.l. in the channel $\eta \rightarrow \gamma\gamma$ and 1.2% c.l. in the channel $\eta \rightarrow \pi^+\pi^-\pi^0$. Their deviations are tracked down to the influence of cuts on topological variables. Since these variables depend on the absolute energy in the center-of-mass system of the beams, they can show differences between on-peak and off-peak data. Expected and measured candidate numbers at successively applied *optimized* cuts are compared in Fig. 3.30. For the order of cuts see Sec. 3.6.1.

While the observed deviations concern the optimization result, the measurement of the branching fraction only depends on the validity of the background ratio. To cross-check the final ratios in Tab. 3.8, the sideband extrapolated background ratios defined in Eq. 3.53 are calculated under the optimized cuts in the data sample. They are found to be consistent with the final ratios within 32% c.l. The sideband extrapolated ratios and the background numbers calculated from both sets of ratios are also given in Tab. 3.12.

3.6.7 Systematic Uncertainties

Differences between the distribution shapes of the variables m_{ES} and ΔE in the signal Monte Carlo and the data sample cause differences between the signal selection efficiencies ε_S . Since the signal regions of these variables are blinded in the data sample, the differences in ε_S have to be assessed indirectly from the signal shapes of the masses that

	$\eta \rightarrow \gamma\gamma$	$\eta \rightarrow \pi^+\pi^-\pi^0$
N_{track}	≥ 3	≥ 5
$i_{K_1^\pm}$	$\geq \text{VeryLoose}$	
$i_{K_2^\pm}$		
$i_{K^\pm\pi_1^\pm}$	$\leq \text{VeryTight}$	
$i_{K^\pm\pi_2^\pm}$		
E_γ	$\geq 0 \text{ GeV}$	
$ m_{\gamma\gamma} - \bar{m}_\eta $	$\leq 0.025 \text{ GeV}/c^2$	
$ m_{\gamma\gamma} - \bar{m}_{\pi^0} $		$\leq 0.015 \text{ GeV}/c^2$
$ m_\eta - \bar{m}_\eta $		$\leq 0.01 \text{ GeV}/c^2$
$ m_\phi - \bar{m}_\phi $	$\leq 0.01 \text{ GeV}/c^2$	$\leq 0.02 \text{ GeV}/c^2$
\mathcal{F}	≤ 0.1	
$ \cos(\vartheta_\lambda \eta) $	≤ 0.9	
$ \cos(\vartheta_\lambda \pi^0) $		≤ 0.9
$ \cos(\vartheta_\lambda \phi) $	≥ 0.5	

Table 3.10 Fixed and no-signal optimized cuts on the number of tracks N_{track} , the kaon identifications i_{K^\pm} of the K^\pm and $i_{K^\pm\pi^\pm}$ of the π^\pm candidates, the energy E_γ of the photon candidates, the invariant masses $m_{\gamma\gamma}$ of the η and π^0 candidates, the composite masses m_η and m_ϕ of the η and ϕ candidates, the Fisher discriminant \mathcal{F} and the helicity angles $\vartheta_\lambda \eta$, $\vartheta_\lambda \pi^0$ and $\vartheta_\lambda \phi$ of the η , π^0 and ϕ candidates in the channels $\eta \rightarrow \gamma\gamma$ and $\eta \rightarrow \pi^+\pi^-\pi^0$.

govern the mass of the B^0 candidates. For this purpose, the signal components of the p.d.f.'s fitted to the distributions of the masses of the η and ϕ candidates in Fig. A.1 to A.5 are normalized to their reconstruction ranges and integrated within the optimized cut ranges. The statistical uncertainties of the integrals in the signal Monte Carlo and the data samples and their deviations at 32% c.l. are taken for uncertainties on ε_S . This procedure is illustrated in Fig. 3.31 for the η candidates and in Fig. 3.32 for the ϕ candidates and gives the relative uncertainties listed in Tab. 3.13.

Further uncertainties arise from the fact that the number of B^0 candidates in the side-band scaled by the ratio $R_{q\bar{q}}$ also contains $B\bar{B}$ background and signal candidates. For $N_{B\bar{B}}$ $B\bar{B}$ background and $N_{q\bar{q}}$ $q\bar{q}$ background candidates, the relative deviation of the background number is

$$\frac{\Delta B}{B} = \frac{N_{B\bar{B}}}{N_{B\bar{B}} + N_{q\bar{q}}} \left(1 - \frac{R_{B\bar{B}}}{R_{q\bar{q}}} \right). \quad (3.67)$$

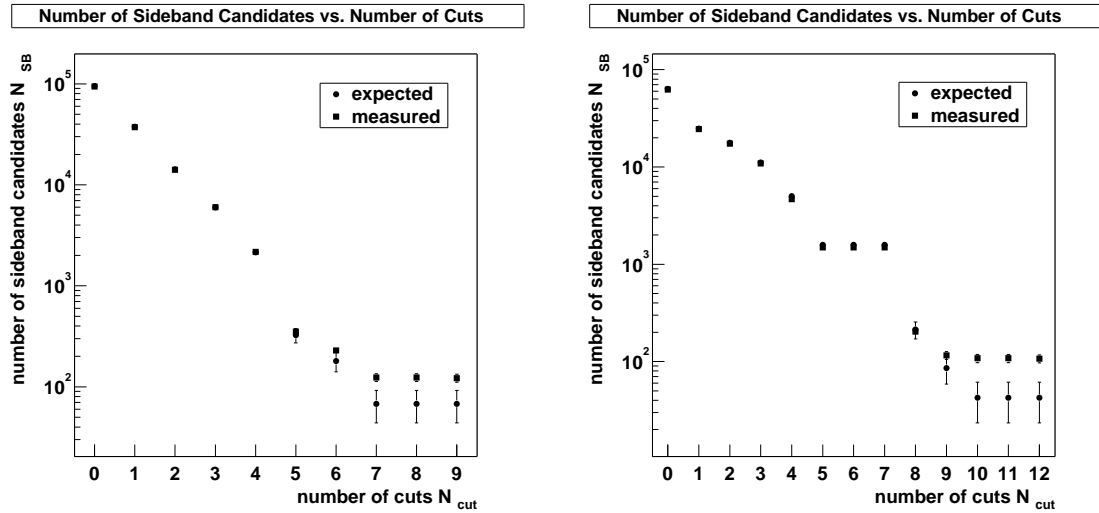


Figure 3.30 Expected and measured numbers of candidates in the sidebands of the data sample for the channels $\eta \rightarrow \gamma\gamma$ (left) and $\eta \rightarrow \pi^+\pi^-\pi^0$ (right) vs. number of cuts.

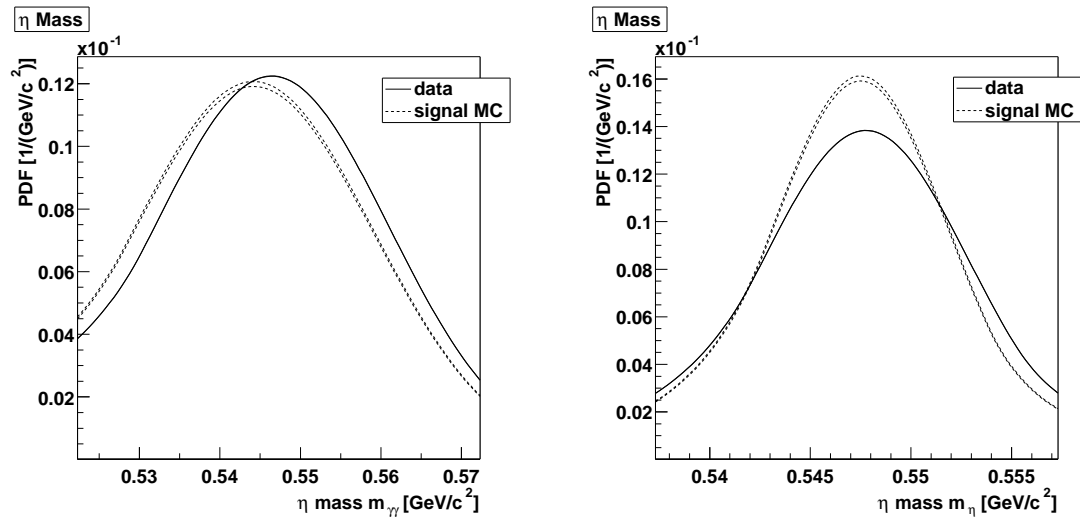


Figure 3.31 Signal components of p.d.f.'s fitted to the distributions of the invariant mass and the composite mass, respectively, of the η candidates in the signal Monte Carlo and the data sample for the channels $\eta \rightarrow \gamma\gamma$ (left) and $\eta \rightarrow \pi^+\pi^-\pi^0$ (right) in the optimized cut ranges. The error belts cover two standard deviations of the p.d.f. integrals.

	$\eta \rightarrow \gamma\gamma$	$\eta \rightarrow \pi^+\pi^-\pi^0$
ε_S	0.1624 ± 0.0020	0.1238 ± 0.0018
\hat{S}	$< 25.11 \pm 0.57$	$< 10.97 \pm 0.32$
\hat{S}_{SB}	$< 0.697 \pm 0.053$	$< 0.401 \pm 0.031$
$\hat{N}_{B\bar{B}}$	$< 1.878 \pm 0.021$	$< 1.806 \pm 0.020$
$\hat{B}_{B\bar{B}}$	$< 0.173 \pm 0.025$	$< 0.046 \pm 0.012$
$\hat{N}_{q\bar{q}}$	68 ± 24	43 ± 19
$\hat{B}_{q\bar{q}}$	2.16 ± 0.77	1.19 ± 0.54
$\hat{\mathcal{B}}_{\text{Bay}}$	$< (1.42 \pm 0.31) \times 10^{-6}$	$< (2.80 \pm 0.74) \times 10^{-6}$
$\hat{\mathcal{B}}_{\text{FC}}$	$< (1.43 \pm 0.16) \times 10^{-6}$	$< (2.84 \pm 0.37) \times 10^{-6}$

Table 3.11 Signal selection efficiencies ε_S , expected signal numbers \hat{S} and background numbers $\hat{B}_{B\bar{B}}$ and $\hat{B}_{q\bar{q}}$, expected numbers of signal B^0 candidates \hat{S}_{SB} and background B^0 candidates $\hat{N}_{B\bar{B}}$ and $\hat{N}_{q\bar{q}}$ in the sideband and expected upper limits on the branching fraction $\mathcal{B}_{\text{Bay}}(B^0 \rightarrow \eta\phi)$ in Bayesian statistics and $\mathcal{B}_{\text{FC}}(B^0 \rightarrow \eta\phi)$ in frequentist statistics for no-signal optimized cuts in the channels $\eta \rightarrow \gamma\gamma$ and $\eta \rightarrow \pi^+\pi^-\pi^0$. Limits are given at 90% c.l.

Since there are no B^0 candidates in the sidebands of the $B\bar{B}$ Monte Carlo samples, upper limits are used for the expected numbers of background candidates $\hat{N}_{B\bar{B}}$. Both $\hat{N}_{B\bar{B}}$ and $\hat{N}_{q\bar{q}}$ are taken from Tab. 3.11 and yield uncertainties below 5.1% in the channel $\eta \rightarrow \gamma\gamma$ and 0.42% in the channel $\eta \rightarrow \pi^+\pi^-\pi^0$. The large uncertainty in the channel $\eta \rightarrow \gamma\gamma$ is due to the large difference of $R_{B\bar{B}}$ and $R_{q\bar{q}}$.

To obtain the limits on the expected sideband signal number \hat{S}_{SB} that are listed in Tab. 3.11, N_{sig} is substituted by N_{SB} in Eq. 3.54. The resulting relative deviations of the background numbers

$$\frac{\Delta B}{B} = -\frac{S_{SB}}{S_{SB} + N_{SB}} \quad (3.68)$$

are smaller than 1.0% in both channels.

3.7 Maximum-Likelihood Method

The maximum-likelihood method obtains the number of signal B^0 decays in the data sample from a global multivariate maximum-likelihood fit [35]. The distribution shapes of all included variables for signal B^0 decays and $q\bar{q}$ background processes are extracted from the signal Monte Carlo and the off-peak data sample, respectively. To validate the method, it is applied to study samples composed of background shape generated “toy” B^0 candidates and different numbers of B^0 candidates from signal Monte Carlo events.

	$\eta \rightarrow \gamma\gamma$	$\eta \rightarrow \pi^+\pi^-\pi^0$
N_{SB}	122 \pm 11	107 \pm 10
B	3.88 \pm 0.39	3.01 \pm 0.33
R'	0.0243 \pm 0.0066	0.0278 \pm 0.0098
B'	2.97 \pm 0.85	3.0 \pm 1.1

Table 3.12 Measured number of candidates in the sidebands N_{SB} and background numbers B (calculated from the background ratios R in Tab. 3.8) and B' (calculated from the sideband extrapolated background ratios R') in the data sample for the channels $\eta \rightarrow \gamma\gamma$ and $\eta \rightarrow \pi^+\pi^-\pi^0$.

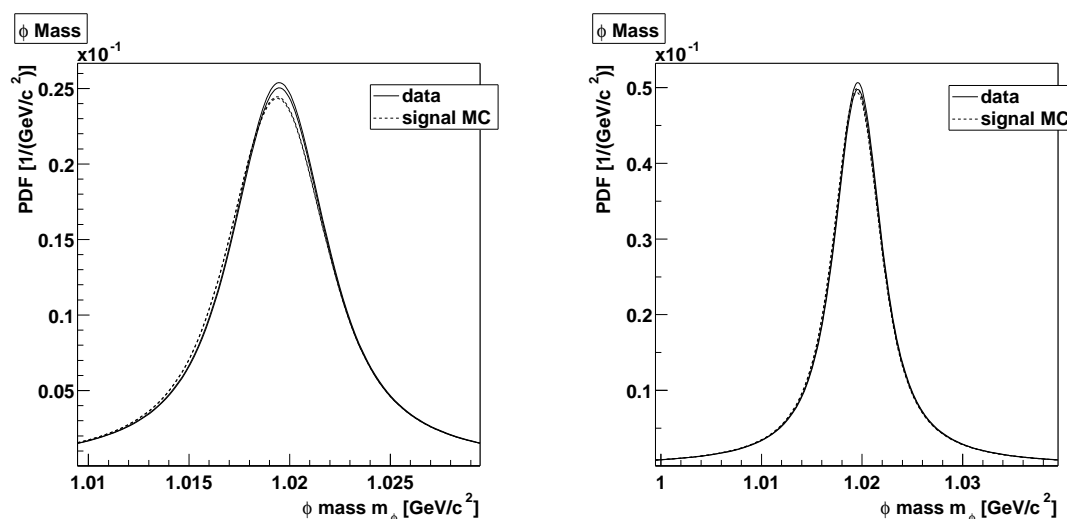


Figure 3.32 Signal components of p.d.f.'s fitted to the distributions of the composite mass of the ϕ candidates in the signal Monte Carlo and the data sample for the channels $\eta \rightarrow \gamma\gamma$ (left) and $\eta \rightarrow \pi^+\pi^-\pi^0$ (right) in the optimized cut ranges. The error belts cover two standard deviations of the p.d.f. integrals.

3.7.1 Likelihood Function

The used likelihood function has the form

$$\mathcal{L} = N! \mathcal{P}(n) \prod_{i=1}^N \sum_{j=1,2} n_j \mathcal{P}_j(\mathbf{x}_i). \quad (3.69)$$

N is the total number of candidates, n_j is the number of candidates in category j , and $\mathcal{P}_j(\mathbf{x}_i)$ is the probability density of candidate i with variable values \mathbf{x}_i in category j .

$$\mathcal{P}(n) = e^{-n} \frac{n^N}{N!} \quad (3.70)$$

		$\eta \rightarrow \gamma\gamma$	$\eta \rightarrow \pi^+\pi^-\pi^0$
$\Delta\varepsilon_S/\varepsilon_S$	$(m_{\gamma\gamma/\eta})$	1.1 %	2.5 %
	(m_ϕ)	0.74 %	1.0 %

Table 3.13 Relative systematic uncertainties $\Delta x/x$ on the signal selection efficiency $x = \varepsilon_S$ due to distribution shapes of the masses $m_{\gamma\gamma}$ and m_η , respectively, of the η candidates and m_ϕ of the ϕ candidates in the channels $\eta \rightarrow \gamma\gamma$ and $\eta \rightarrow \pi^+\pi^-\pi^0$.

is the Poisson probability of observing N candidates at an expectation of

$$n = \sum_{j=1,2} n_j \quad (3.71)$$

candidates. With $j = 1$ being the signal category and $j = 2$ being the background category, the signal yield is $S = n_1$, and the background yield is $B = n_2$. The probability densities $\mathcal{P}_j(\mathbf{x})$ are products of the p.d.f. values for

- the energy substituted mass m_{ES} ,
- energy difference ΔE ,
- the invariant mass $m_{\gamma\gamma}$ of the η candidates in the channel $\eta \rightarrow \gamma\gamma$,
- the invariant mass $m_{\gamma\gamma}$ of the π^0 candidates in the channel $\eta \rightarrow \pi^+\pi^-\pi^0$,
- the composite mass m_η of the η candidates in the channel $\eta \rightarrow \pi^+\pi^-\pi^0$,
- the composite mass m_ϕ of the ϕ candidates,
- the Fisher discriminant \mathcal{F} and
- the magnitude of the cosine of the helicity angle $|\cos(\vartheta_\lambda \phi)|$ of the ϕ candidates.

First, cuts on the number of tracks and the kaon identification of the K^\pm candidates are applied. They are chosen at the values listed in Tab. 3.10. Then S and B are fitted to the data sample. The p.d.f.'s for signal B^0 candidates, obtained from fits to the signal Monte Carlo sample, and for background B^0 candidates, obtained from fits to the off-peak data sample, are shown in App. D. The projections of the likelihood function fitted to a mixed sample of off-peak data, $B\bar{B}$ Monte Carlo and 1000 signal Monte Carlo events on the included variables are shown in App. E. (*This appendix contains unblinded results.*) As found in Sec. 3.5.4, there is no $B\bar{B}$ background in the signal Monte Carlo sample and only a small $B\bar{B}$ background component in the data sample.

In all fits to the data sample, blinded versions of S and B are supplied to the fitting algorithm. The blinding is performed by adding random constants. As a consequence, the ranges of the unblind values in the fits are unknown. To provide a coherent method for blind and unblind fits while restricting the fit range to physical values, only the magnitudes of the unblind values are used in the fit. The likelihood functions are therefore mirrored at 0.

3.7.2 Selection Efficiencies

Analogously to Sec. 3.6.2, the signal selection efficiency (Eq. 3.54)

$$\varepsilon_{\text{sel}} = \varepsilon_{\text{MC}} \frac{N_{\text{sig}}}{N_{B^0\bar{B}^0}^0} \quad (3.72)$$

is calculated from the Monte Carlo efficiency correction ε_{MC} , the number of B^0 candidates N_{sig} and the number of events $N_{B^0\bar{B}^0}^0$ in the signal Monte Carlo sample. In this method, however, N_{sig} is the number of B^0 candidates in the full variable range of the maximum-likelihood fit. The obtained efficiencies are listed in Tab. 3.14. Accordingly, the $B\bar{B}$ background selection efficiency (Eq. 3.55)

$$\varepsilon_{B\bar{B}} = \varepsilon_{\text{MC}} \frac{N_{B\bar{B}}}{2 N_{B\bar{B}}^0} \quad (3.73)$$

is obtained from the number of B^0 candidates to fit $N_{B\bar{B}}$ and the number of events $N_{B\bar{B}}^0$ in the $B\bar{B}$ Monte Carlo sample.

3.7.3 Selection Expectations

An upper limit on the expected number of B^0 candidates from signal B^0 decays in the fit \hat{N}_{sig} is determined from the signal selection efficiency ε_{sel} and the upper limit on the number of signal B^0 decays in the data sample $\hat{N}_{B^0\bar{B}^0}^0(B^0 \rightarrow \eta\phi)$ expected from the CLEO upper limit on $\mathcal{B}(B^0 \rightarrow \eta\phi)$ [33] by

$$\hat{N}_{\text{sig}} = \varepsilon_{\text{sel}} \hat{N}_{B^0\bar{B}^0}^0(B^0 \rightarrow \eta\phi). \quad (3.74)$$

The expected number of B^0 candidates from background B^0 decays in the fit $\hat{N}_{B\bar{B}}$ is determined from the $B\bar{B}$ background selection efficiency $\varepsilon_{B\bar{B}}$ and the number of background B decays in the data sample $\hat{N}_{B\bar{B}}^0(B^0 \rightarrow \eta\phi)$ expected from $B\bar{B}$ counting by

$$\hat{N}_{B\bar{B}} = \varepsilon_{B\bar{B}} \hat{N}_{B\bar{B}}^0(B^0 \rightarrow \eta\phi). \quad (3.75)$$

Assuming a common cross section, the expected number of B^0 candidates from $q\bar{q}$ background processes in the fit $\hat{N}_{q\bar{q}}$ is determined from the ratio of the integrated luminosities \mathcal{L}_{on} and \mathcal{L}_{off} of the on-peak and off-peak data sample, respectively, and the observed number of B^0 candidates to fit in the off-peak data sample N by

$$\hat{N}_{q\bar{q}} = \frac{\mathcal{L}_{\text{on}}}{\mathcal{L}_{\text{off}}} N. \quad (3.76)$$

These expectations are collected in Tab. 3.14.

3.7.4 Fit Bias and Efficiency

To account for a bias $\delta_{\text{fit}} \neq 0$ and an efficiency $\varepsilon_{\text{fit}} \neq 1$ of the maximum-likelihood fit, the signal fit yield S is parameterized as a function of the number of signal B^0 candidates to fit N_{sig} by

$$S = \varepsilon_{\text{fit}} N_{\text{sig}} + \delta_{\text{fit}}. \quad (3.77)$$

	$\eta \rightarrow \gamma\gamma$	$\eta \rightarrow \pi^+\pi^-\pi^0$
ε_{sel}	0.5039 ± 0.0035	0.4087 ± 0.0032
\hat{N}_{sig}	$< 77.9 \pm 1.6$	$< 36.23 \pm 0.96$
$\hat{N}_{B\bar{B}}$	173 ± 16	78 ± 11
$\hat{N}_{q\bar{q}}$	12197 ± 383	9054 ± 317

Table 3.14 Signal selection efficiencies ε_{sel} and expected number of B^0 candidates from signal B^0 decays \hat{N}_{sig} , $B\bar{B}$ background B^0 decays $\hat{N}_{B\bar{B}}$ and $q\bar{q}$ background processes $\hat{N}_{q\bar{q}}$ in the maximum-likelihood fit for the channels $\eta \rightarrow \gamma\gamma$ and $\eta \rightarrow \pi^+\pi^-\pi^0$. Limits are given at 90% c.l.

To use a total signal selection efficiency

$$\varepsilon_S = \varepsilon_{\text{sel}} \varepsilon_{\text{fit}} \quad (3.78)$$

in Eq. 3.1, the substitution $S \rightarrow S'$ with the bias corrected signal number

$$S' = S - \delta_{\text{fit}} \quad (3.79)$$

is applied. Since δ_{fit} and ε_{fit} are expected to depend on the total number of B^0 candidates in the fit to the data sample, but the off-peak data sample is significantly smaller than the data sample, “toy” B^0 candidates are generated from the distribution shapes of their variables in the off-peak data sample.⁹ δ_{fit} and ε_{fit} are determined from fits to study samples composed of these background B^0 candidates and signal B^0 candidates from the signal Monte Carlo sample. While the chosen numbers of background B^0 candidates correspond to the expectations given in Tab. 3.14, the numbers of signal B^0 candidates are varied between 0 and 25. To gain uncorrelated estimates, the available signal Monte Carlo events are distributed over approximately 2400 study samples such that the relative statistical uncertainties on the mean values of the signal fit yields for all numbers of signal B^0 candidates are comparable. Fig. 3.33 shows the obtained profiles which are fitted by Eq. 3.77. Deviations from the fitted parameters at 32% c.l. are averaged as systematic uncertainties on δ_{fit} . The yield distributions for separate fits with selected numbers of B^0 candidates are shown in App. F. The fitted biases and efficiencies are listed in Tab. 3.15.

3.7.5 Statistical Uncertainties

If the likelihood function \mathcal{L} in Eq. 3.69 is described by a Gaussian p.d.f., the uncertainty σ_S of the signal fit yield S corresponds to an increase of the negative logarithmic likelihood

$$-2 \ln \mathcal{L} = \frac{(n_1 - S)^2}{\sigma_S^2} \quad (3.80)$$

⁹The term “toy” refers to the fact that only values for variables in the fit are generated. Besides that, the applied accept-reject method [35] is a valid Monte Carlo algorithm.

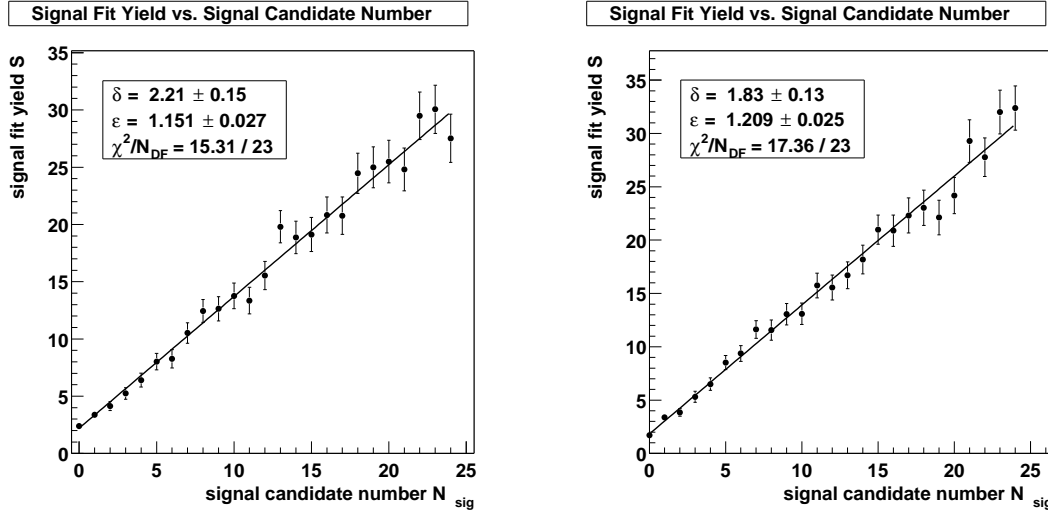


Figure 3.33 Signal fit yield vs. number of signal B^0 candidates in maximum-likelihood fits to study samples for the channels $\eta \rightarrow \gamma\gamma$ (left) and $\eta \rightarrow \pi^+\pi^-\pi^0$ (right).

	$\eta \rightarrow \gamma\gamma$	$\eta \rightarrow \pi^+\pi^-\pi^0$
δ_{fit}	2.21 ± 0.16	1.83 ± 0.14
ε_{fit}	1.151 ± 0.027	1.209 ± 0.025

Table 3.15 Signal fit bias δ_{fit} and signal fit efficiency ε_{fit} in maximum-likelihood fits to study samples for the channels $\eta \rightarrow \gamma\gamma$ (left) and $\eta \rightarrow \pi^+\pi^-\pi^0$ (right).

by $-2 \Delta \ln \mathcal{L} = 1$ from S to $S \pm \sigma_S$. While the Gaussian approximation of \mathcal{L} is safely used for significant signal yields, a Bayesian upper limit S_ε for smaller yields is calculated at $1 - \varepsilon = 90\%$ c.l. To use the bias corrected signal number S' in Eq. 3.7, the upper limit S'_ε is needed. It is calculated according to Eq. 3.5 from the normalized likelihood integral

$$1 - \varepsilon = \frac{\int_{S_\varepsilon}^{\infty} \mathcal{L}(S) dS}{\int_{\delta_{\text{fit}}}^{\infty} \mathcal{L}(S) dS} \quad (3.81)$$

and the limit condition $S'_\varepsilon = S_\varepsilon - \delta_{\text{fit}}$.

Although the signal yields of the fits to the data samples are blinded, the positions of 0 are nevertheless visible for accordingly small results. Consequently, the likelihood functions can not be used for validation of the blinded fits. On the other hand, it can be seen in Fig. 3.33 that the fit uncertainties contain both the Poisson uncertainty σ_n from Eq. 3.70 and the intrinsic fit uncertainties of the variable p.d.f.'s. Since the latter are unknown, but have a strong impact especially in the sensitive region of small results, the fit uncertainties of the blinded fits to the data samples are given at this point. They amount to $\sigma_S = 8.3$ in the channel $\eta \rightarrow \gamma\gamma$ and $\sigma_S = 4.5$ in the channel $\eta \rightarrow \pi^+\pi^-\pi^0$.

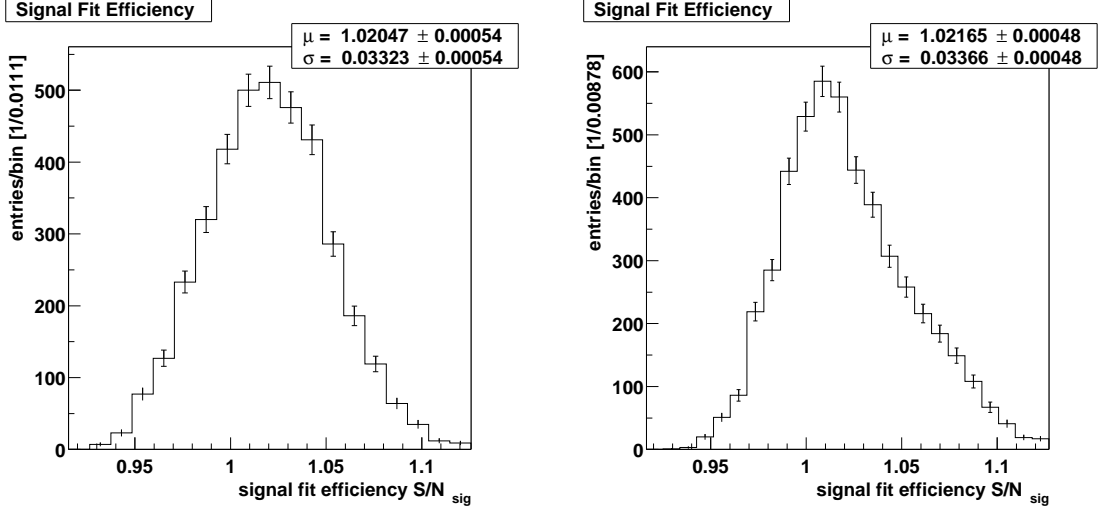


Figure 3.34 Distribution of the signal fit efficiency for variation off the p.d.f. parameters in maximum-likelihood fits to study samples for the channels $\eta \rightarrow \gamma\gamma$ (left) and $\eta \rightarrow \pi^+\pi^-\pi^0$ (right).

3.7.6 Systematic Uncertainties

Systematic uncertainties on the signal fit yields are absorbed into the signal fit efficiency. To achieve reasonable statistics while still resembling the expected signal yields, 500 signal B^0 candidates are included into study samples. First, these samples are used to assess the stability of the fit yields under varying distribution shapes. For this purpose, the correlated parameters of each p.d.f. are varied within the covariances from their fits to the off-peak data and signal Monte Carlo samples. The distributions of the fit efficiencies for simultaneous variation of all p.d.f.'s are shown in Fig. 3.34. Contributions from failed fits are removed, and the mean values $\bar{\varepsilon}_{\text{fit}}$ and standard deviations $\sigma_{\varepsilon_{\text{fit}}}$ are calculated. Relative uncertainties due to the widths of the distributions are estimated by

$$\frac{\Delta\varepsilon_{\text{fit}}}{\varepsilon_{\text{fit}}} = \frac{\sigma_{\varepsilon_{\text{fit}}}}{\bar{\varepsilon}_{\text{fit}}}. \quad (3.82)$$

Additional uncertainties due to the asymmetries of the distributions are estimated from the maximum positions $\hat{\varepsilon}_{\text{fit}}$ by

$$\frac{\Delta\varepsilon_{\text{fit}}}{\varepsilon_{\text{fit}}} = \frac{|\hat{\varepsilon}_{\text{fit}} - \bar{\varepsilon}_{\text{fit}}|}{\bar{\varepsilon}_{\text{fit}}}. \quad (3.83)$$

The resulting uncertainties are listed in Tab. 3.16.

In a second step, the validity of the signal fit yields in the presence of B^0 candidates from $B\bar{B}$ background B decays is studied. Since the p.d.f.'s for this background are not known, all B^0 candidates available in the $B\bar{B}$ Monte Carlo sample are included into a single fit. With 121 included $B\bar{B}$ background B^0 candidates, the signal fit efficiency in the channel $\eta \rightarrow \gamma\gamma$ deviates by 3.7%, while the deviation in the channel $\eta \rightarrow \pi^+\pi^-\pi^0$ with 49 added $B\bar{B}$ background B^0 candidates is 1.1%.

		$\eta \rightarrow \gamma\gamma$	$\eta \rightarrow \pi^+\pi^-\pi^0$
$\Delta\varepsilon_{\text{fit}}/\varepsilon_{\text{fit}}$	(width)	3.3 %	3.3 %
	(asymmetry)	0.0 %	1.3 %

Table 3.16 Relative systematic uncertainties $\Delta x/x$ on the signal fit efficiency $x = \varepsilon_{\text{fit}}$ due widths and asymmetries of its distributions for varied p.d.f. parameters in maximum-likelihood fits to study samples for the channels $\eta \rightarrow \gamma\gamma$ and $\eta \rightarrow \pi^+\pi^-\pi^0$.

3.8 Systematic Uncertainties

Systematic uncertainties on the measurement of the branching fraction $\mathcal{B}(B^0 \rightarrow \eta\phi)$ come from uncertainties on the variables in Eq. 3.1. Since \mathcal{B} is proportional to all variables and the variables themselves are not correlated, all relative uncertainties are added in quadrature.

Systematic uncertainties for single methods and channels have been discussed in Sec. 3.1, 3.6 and 3.7. Additional uncertainties on the signal selection efficiency $\varepsilon_{\mathcal{S}}$ come from the Monte Carlo corrections introduced in Sec. 3.4. Uncertainties on the $B\bar{B}$ counts and the channel branching fractions are taken from Sec. 3.2.

3.8.1 Efficiency Corrections

The tracking efficiency correction leaves an uncertainty of 0.8% for each `GoodTracks-Loose` track [49]. Since these uncertainties are correlated, they are multiplied by the number of tracks contributing to one B^0 candidate. In the same manner, the PID tables leave a correlated uncertainty on the corrected efficiency smaller than 1.0% for tracks in the used momentum range [50]. Since only the identification of the K^\pm candidates is used as a cut, the π^\pm candidates are not included here.

The correlated uncertainty on the reconstruction efficiency of photon candidates with smeared energies is 2.5% per candidate [51]. The correlated uncertainty on the reconstruction efficiency of non-discarded π^0 candidates is 5.0% per candidate [51]. While these uncertainties contain energy-independent contributions, there are additional energy-dependent uncertainties. To estimate their impact on this analysis, the signal Monte Carlo sample is reprocessed with dilution and correction factors randomly chosen from their Gaussian distributions. The deviation of the measured signal selection efficiency is the uncorrelated contribution to the systematic uncertainty. For the maximum-likelihood method, this includes both the efficiencies ε_{sel} and ε_{sig} .

3.8.2 Method Summary

The relative statistical and systematic uncertainties of the candidate counting and the maximum-likelihood method are summarized in Tab. 3.17 and 3.18, respectively. The common uncertainties of both methods are listed in Tab. 3.19.

		$\eta \rightarrow \gamma\gamma$	$\eta \rightarrow \pi^+\pi^-\pi^0$
σ_R/R		4.1 %	4.9 %
$\Delta R/R$		4.9 %	5.5 %
$\Delta B/B$		5.2 %	1.1 %
$\sigma_{\varepsilon_S}/\varepsilon_S$		1.2 %	1.5 %
$\Delta\varepsilon_S/\varepsilon_S$	(shapes)	1.3 %	2.7 %
	(γ)	0.66 %	3.3 %

Table 3.17 (Uncorrelated) relative statistical uncertainties σ_x/x and systematic uncertainties $\Delta x/x$ on the background ratio $x = R$, the background number $x = B$ and the signal selection efficiency $x = \varepsilon_S$ for the candidate counting method in the channels $\eta \rightarrow \gamma\gamma$ and $\eta \rightarrow \pi^+\pi^-\pi^0$.

Assuming no observed signal, the uncertainties on background ratios and background numbers for the candidate counting method correspond to uncertainties on the Bayesian upper limit on the signal number of 5.2% in the channel $\eta \rightarrow \gamma\gamma$ and 4.5% in the channel $\eta \rightarrow \pi^+\pi^-\pi^0$. Assuming no contained signal and estimating an upper limit on the signal fit yield of 7.38 from Fig. F.1, the relative uncertainty on the upper limit on the substituted signal fit yield S' of the maximum-likelihood fit in the channel $\eta \rightarrow \gamma\gamma$ is 3.0%. Assuming no contained signal and estimating an upper limit on the signal fit yield of 6.2 from Fig. F.5, the relative uncertainty on the upper limit on the substituted signal fit yield S' of the maximum-likelihood fit in the channel $\eta \rightarrow \pi^+\pi^-\pi^0$ is 3.1%. The added uncertainties for all channels and methods are given in Tab. 3.20.

3.8.3 Peaking Backgrounds

$B\bar{B}$ background that comes from *correctly* reconstructed B decays is not included in the background distributions. Instead, it will peak in the signal region. Within the kinematic range of this analysis, however, no resonances but the searched η and ϕ mesons are expected. To eliminate unrecognized contributions, a Monte Carlo sample of 11.5×10^6 $B\bar{B}$ events with exclusively charmless decays is processed. After application of the common cuts on the number of tracks and the kaon identification of the K^\pm candidates, only the reconstructed decays listed in Tab. 3.21 are found in the signal box.

The decay $B^0 \rightarrow \eta K^+ K^-$ is the non-resonant contribution to the analyzed decay chain $B^0 \rightarrow \eta\phi$, $\phi \rightarrow K^+ K^-$. While the transition amplitudes for both B^0 decays are identical except for the creation of one additional $u\bar{u}$ pair, the phase-space population of the three-body decay is very different. The squared invariant mass of the $K^+ K^-$ system is evenly distributed within the limits $[(2\bar{m}_{K^\pm})^2, (\bar{m}_{B^0} - \bar{m}_\eta)^2]$ given by the meson masses \bar{m}_{K^\pm} , \bar{m}_{B^0} and \bar{m}_η [8], and only 0.57% fall into the reconstruction range. This fraction is even further reduced by application of the selection cuts and fit ranges.

The resonance $f_0(980)$, which is simulated with a mass of $1 \text{ GeV}/c^2$ and a width of $50 \text{ MeV}/c^2$, is largely included in the reconstruction range. It has, however, an unclear

		$\eta \rightarrow \gamma\gamma$	$\eta \rightarrow \pi^+\pi^-\pi^0$
$\sigma_{\varepsilon_{\text{sel}}}/\varepsilon_{\text{sel}}$		0.69 %	0.77 %
$\Delta\varepsilon_{\text{sel}}/\varepsilon_{\text{sel}}$	(γ)	0.28 %	1.9 %
$\sigma_{\delta_{\text{fit}}}/\delta_{\text{fit}}$		7.1 %	7.4 %
$\sigma_{\varepsilon_{\text{fit}}}/\varepsilon_{\text{fit}}$		2.3 %	2.0 %
$\Delta\varepsilon_{\text{fit}}/\varepsilon_{\text{fit}}$	(p.d.f.)	3.3 %	3.4 %
	($B\bar{B}$)	3.7 %	1.1 %
	(γ)	1.6 %	0.02 %

Table 3.18 (Uncorrelated) relative statistical uncertainties σ_x/x and systematic uncertainties $\Delta x/x$ on the signal selection efficiency $x = \varepsilon_{\text{sel}}$, the signal fit bias $x = \delta_{\text{fit}}$ and the signal fit efficiency $x = \varepsilon_{\text{fit}}$ for the maximum-likelihood method in the channels $\eta \rightarrow \gamma\gamma$ and $\eta \rightarrow \pi^+\pi^-\pi^0$.

		$\eta \rightarrow \gamma\gamma$	$\eta \rightarrow \pi^+\pi^-\pi^0$
$\Delta\varepsilon_S/\varepsilon_S$	(track)	1.6 %	3.2 %
	(PID)	2.0 %	2.0 %
	(γ)	5.0 %	5.0 %
$\Delta N_{B\bar{B}}/N_{B\bar{B}}$		1.1 %	1.1 %
$\Delta\mathcal{B}_{\text{ch}}/\mathcal{B}_{\text{ch}}$		1.6 %	2.3 %

Table 3.19 (Correlated) relative systematic uncertainties $\Delta x/x$ on the signal selection efficiency $x = \varepsilon_S$, the $B\bar{B}$ counts $x = N_{B\bar{B}}$ and the channel branching fractions $x = \mathcal{B}_{\text{ch}}$ in the channels $\eta \rightarrow \gamma\gamma$ and $\eta \rightarrow \pi^+\pi^-\pi^0$.

structure and no sufficient coupling to gluons [57] to replace the ϕ meson in $B^0 \rightarrow \eta\phi$. Since it has spin $j_s = 0$, it is also suppressed by the helicity selection.

3.9 Unblinded Results

After uncovering the signal boxes and unblinding the fit yields in the data sample, the branching fractions $\mathcal{B}(B^0 \rightarrow \eta\phi)$ in the candidate counting and the maximum-likelihood method are calculated. At this point, all uncertainties estimated from the signal Monte Carlo, $B\bar{B}$ Monte Carlo and off-peak data samples are considered *systematic*, while *statistical* uncertainties are placed on the numbers of candidates in the signal boxes and sidebands and on the fit yields in the data sample. The uncovered signal boxes are

		$\eta \rightarrow \gamma\gamma$	$\eta \rightarrow \pi^+\pi^-\pi^0$
$\Delta\mathcal{B}/\mathcal{B}$	(counting)	8.1 %	9.3 %
	(likelihood)	8.8 %	8.7 %

Table 3.20 Added relative systematic uncertainties $\Delta x/x$ on the branching fraction $x = \mathcal{B}(B^0 \rightarrow \eta\phi)$ for the candidate counting and maximum-likelihood methods in the channels $\eta \rightarrow \gamma\gamma$ and $\eta \rightarrow \pi^+\pi^-\pi^0$.

	$\eta \rightarrow \gamma\gamma$	$\eta \rightarrow \pi^+\pi^-\pi^0$
$B^0 \rightarrow \eta f_0(980)$	3	2
$B^0 \rightarrow \eta K^+K^-$	3	0

Table 3.21 Number of correctly reconstructed background B^0 decays in the signal box of the charmless Monte Carlo sample for the channels $\eta \rightarrow \gamma\gamma$ and $\eta \rightarrow \pi^+\pi^-\pi^0$.

shown in App. C, and projections of the unblinded likelihood functions on the included variables are shown in App. E.

3.9.1 Evaluation

The unblinded results of the candidate counting method are presented in Tab. 3.22. After counting the number of B^0 candidates in the signal box of the data sample, the signal numbers in the channels $\eta \rightarrow \gamma\gamma$ and $\eta \rightarrow \pi^+\pi^-\pi^0$ are calculated from Eq. 3.48, using the background numbers listed in Tab. 3.12. The upper limits on the signal numbers in Bayesian statistics are fitted to the candidate numbers and background numbers by Eq. 3.65. The upper limits on the signal numbers in frequentist statistics are taken from the tables of candidate numbers and background numbers published by Feldman and Cousins [36]. To reduce the uncertainty from interpolation in the background numbers, the respective table rows are graphically approximated by smooth curves [53]. The combined signal number is obtained from adding the signal numbers in both channels. The upper limits on the combined signal number are obtained from the added candidate numbers and the added background numbers. The branching fractions and upper limits on the branching fraction $\mathcal{B}(B^0 \rightarrow \eta\phi)$ are calculated from Eq. 3.1 and 3.7, respectively. The used signal selection efficiencies are listed in Tab. 3.11. All other parameters are given in Sec. 3.1 and 3.2.

The unblinded results of the maximum-likelihood method are presented in Tab. 3.23. The signal fit yields in the channels $\eta \rightarrow \gamma\gamma$ and $\eta \rightarrow \pi^+\pi^-\pi^0$ and their statistical uncertainties are extracted from their negative logarithmic likelihoods (Eq. 3.80) as described in Sec. 3.7.5 and shown in Fig. 3.35. The bias corrected signal yields are defined by Eq. 3.79 and the biases listed in Tab. 3.15. The Bayesian upper limits on the bias corrected signal yields are extracted as described in Sec. 3.7.5 from the normalized integrals (Eq. 3.81) of the likelihood functions shown in Fig. 3.36. The combined bias corrected signal yield is obtained from adding the bias corrected signal yields in both

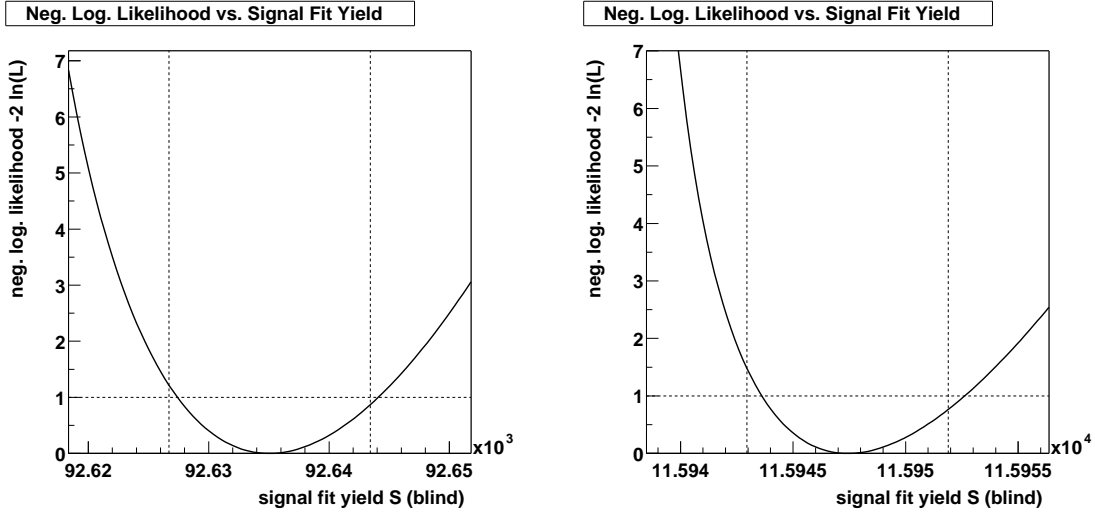


Figure 3.35 Negative logarithmic likelihood functions for the signal fit yields in the channels $\eta \rightarrow \gamma\gamma$ (left) and $\eta \rightarrow \pi^+\pi^-\pi^0$ (right). The signal yields are blinded in the maximum-likelihood fits by added random constants. Their statistical uncertainties (marked by vertical dashed lines) correspond to an increase of the negative logarithmic likelihoods by 1 (marked by horizontal dashed lines).

channels. To determine the upper limit on the combined bias corrected signal yield, the likelihood functions in Fig. 3.36 are convoluted into the likelihood function shown in Fig. 3.37. The combined bias corrected signal yield is then extracted from the normalized integral of this function and the added fit biases. The branching fractions and upper limits on the branching fraction $\mathcal{B}(B^0 \rightarrow \eta\phi)$ are calculated from Eq. 3.1 and 3.7, respectively, using the bias corrected signal yields and the signal selection efficiencies defined in Eq. 3.78. The individual signal selection and signal fit efficiencies are listed in Tab. 3.14 and 3.15, respectively. All other parameters are given in Sec. 3.1 and 3.2.

For combining the results in the channels $\eta \rightarrow \gamma\gamma$ and $\eta \rightarrow \pi^+\pi^-\pi^0$, Eq. 3.1 and 3.7 are modified by

$$S \rightarrow S_1 + S_2 \quad (3.84)$$

and

$$\varepsilon_S \mathcal{B}_{\text{ch}} \rightarrow (\varepsilon_{S_1} \mathcal{B}_{\text{ch}_1} + \varepsilon_{S_2} \mathcal{B}_{\text{ch}_2}), \quad (3.85)$$

where $S_{1,2}$ are the signal numbers, $\varepsilon_{S_{1,2}}$ are the signal selection efficiencies and $\mathcal{B}_{\text{ch}_{1,2}}$ are the branching fractions of both channels. While the signal numbers are assumed to be uncorrelated, systematic correlations between the signal selection efficiencies are obeyed throughout the calculation. The branching fractions $\mathcal{B}(B^0 \rightarrow \eta\phi)$ from all methods, channels and combined channels are compared in Fig. 3.38. The upper limits on the branching fraction $\mathcal{B}(B^0 \rightarrow \eta\phi)$ from all methods, channels and combined channels are compared in Fig. 3.39.

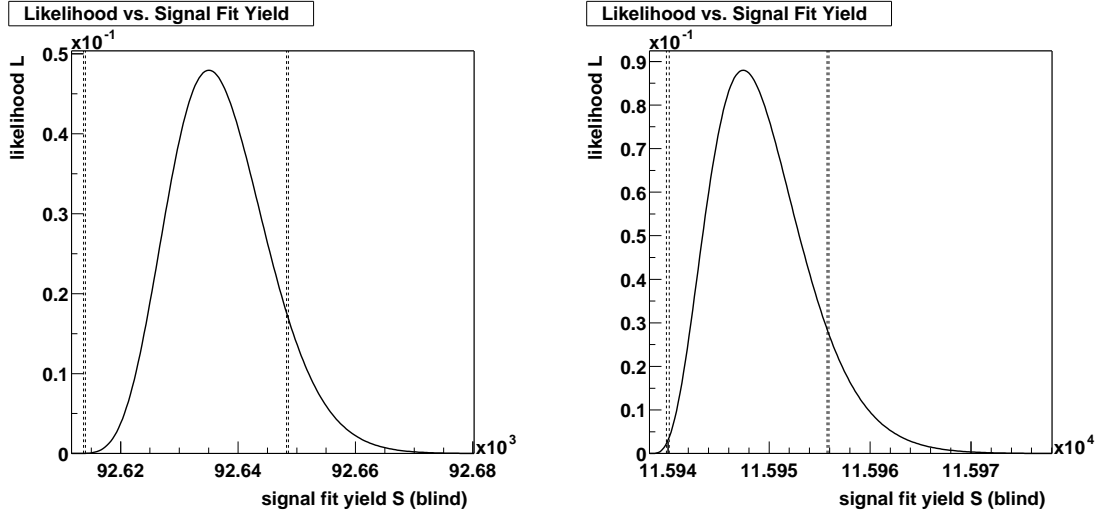


Figure 3.36 Normalized likelihood functions for the signal fit yields in the channels $\eta \rightarrow \gamma\gamma$ (left) and $\eta \rightarrow \pi^+\pi^-\pi^0$ (right). The signal yields are blinded in the maximum-likelihood fits by added random constants. Their Bayesian upper limits (marked by the dashed bands on the right) are determined by integrating the normalized likelihood functions between the fit biases (marked by the dashed bands on the left) and 90% c.l. The bands contain the uncertainties on the fit biases and the resolutions of the integration.

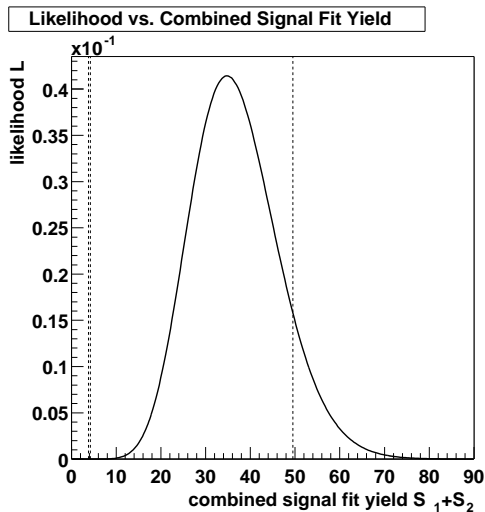


Figure 3.37 Normalized likelihood function for the combined signal yield of the channels $\eta \rightarrow \gamma\gamma$ and $\eta \rightarrow \pi^+\pi^-\pi^0$ obtained from convoluting the likelihood functions in Fig. 3.36. The Bayesian upper limit on the combined signal yield (marked by the dashed band on the right) is determined by integrating the normalized likelihood function between the added fit biases (marked by the dashed band on the left) and 90% c.l. The error bands contain the uncertainties on the fit biases and the resolutions of the convolution and the integration.

3.9.2 Conclusion

All results are dominated by their statistical uncertainties. Within these uncertainties, the branching fractions for the combined channels agree in both methods at 24% c.l. However, the uncertainty obtained from the maximum-likelihood method is 10% smaller than the uncertainty obtained from the candidate counting method. Since the signal yield of the maximum-likelihood method is nevertheless consistent with 0 at 1.0% c.l. and hence excludes this value with only three standard deviations, the signal is not considered significant. Including its systematic uncertainties, the upper limit on the branching fraction obtained from the maximum-likelihood method is

$$\mathcal{B}(B^0 \rightarrow \eta\phi) < 3.28 \times 10^{-6} \text{ (90\%)}. \quad (3.86)$$

This upper limit is consistent with all theoretical predictions in Tab. 2.1, but 64% smaller than the upper limit measured by the CLEO collaboration [33]. It is, however, 33% larger than an upper limit concurrently measured by the *BABAR* collaboration [58].

	$\eta \rightarrow \gamma\gamma$	$\eta \rightarrow \pi^+\pi^-\pi^0$	combined
N_{sig}	6 ± 2.5	2 ± 1.4	8 ± 2.8
B	$3.88 \pm 0.35 \pm 0.32$	$3.01 \pm 0.29 \pm 0.22$	$6.89 \pm 0.46 \pm 0.39$
S	$2.12 \pm 2.47 \pm 0.32$	$-1.01 \pm 1.44 \pm 0.22$	$1.11 \pm 2.86 \pm 0.39$
S_{Bay}	$< 6.87 \pm 0.37$	$< 3.53 \pm 0.10$	$< 6.76 \pm 0.38$
S_{FC}	$< 7.60 \pm 0.51$	$< 3.05 \pm 0.26$	$< 7.10 \pm 0.60$
\mathcal{B}	$(0.76 \pm 0.89 \pm 0.12) \times 10^{-6}$	$(-0.8 \pm 1.2 \pm 0.2) \times 10^{-6}$	$(0.28 \pm 0.72 \pm 0.10) \times 10^{-6}$
\mathcal{B}_{Bay}	$(< 2.46 \pm 0.21) \times 10^{-6}$	$(< 2.91 \pm 0.25) \times 10^{-6}$	$(< 1.69 \pm 0.13) \times 10^{-6}$
\mathcal{B}_{FC}	$(< 2.73 \pm 0.25) \times 10^{-6}$	$(< 2.51 \pm 0.29) \times 10^{-6}$	$(< 1.77 \pm 0.18) \times 10^{-6}$

Table 3.22 Unblinded results of the candidate counting method in the channels $\eta \rightarrow \gamma\gamma$ and $\eta \rightarrow \pi^+\pi^-\pi^0$ and for both channels combined: Number of signal B^0 candidates N_{sig} , background number B , signal number S , Bayesian upper limit S_{Bay} and Feldman-Cousins upper limit S_{FC} on the signal number, branching fraction $\mathcal{B}(B^0 \rightarrow \eta\phi)$ and Bayesian upper limit $\mathcal{B}_{\text{Bay}}(B^0 \rightarrow \eta\phi)$ and Feldman-Cousins upper limit $\mathcal{B}_{\text{FC}}(B^0 \rightarrow \eta\phi)$ on the branching fraction. The first uncertainties are statistical, the second uncertainties are systematic. The upper limits are given at 90% c.l.

	$\eta \rightarrow \gamma\gamma$	$\eta \rightarrow \pi^+\pi^-\pi^0$	combined
S	23.4 ± 8.4	9.3 ± 4.5	32.7 ± 9.5
S'	$21.2 \pm 8.4 \pm 0.2$	$7.0 \pm 4.5 \pm 0.1$	$28.7 \pm 9.5 \pm 0.2$
S'_{Bay}	$< 34.58 \pm 0.32$	$< 15.87 \pm 0.23$	$< 45.65 \pm 0.39$
\mathcal{B}	$(2.13 \pm 0.84 \pm 0.18) \times 10^{-6}$	$(1.44 \pm 0.92 \pm 0.12) \times 10^{-6}$	$(1.93 \pm 0.64 \pm 0.13) \times 10^{-6}$
\mathcal{B}_{Bay}	$(< 3.47 \pm 0.29) \times 10^{-6}$	$(< 3.26 \pm 0.27) \times 10^{-6}$	$(< 3.08 \pm 0.20) \times 10^{-6}$

Table 3.23 Unblinded results of the maximum-likelihood method in the channels $\eta \rightarrow \gamma\gamma$ and $\eta \rightarrow \pi^+\pi^-\pi^0$ and for both channels combined: Signal number S , bias corrected signal number S' , Bayesian upper limit S'_{Bay} on the bias corrected signal number, branching fraction $\mathcal{B}(B^0 \rightarrow \eta\phi)$ and Bayesian upper limit $\mathcal{B}_{\text{Bay}}(B^0 \rightarrow \eta\phi)$ on the branching fraction. The first uncertainties are statistical, the second uncertainties are systematic. The upper limits are given at 90% c.l.

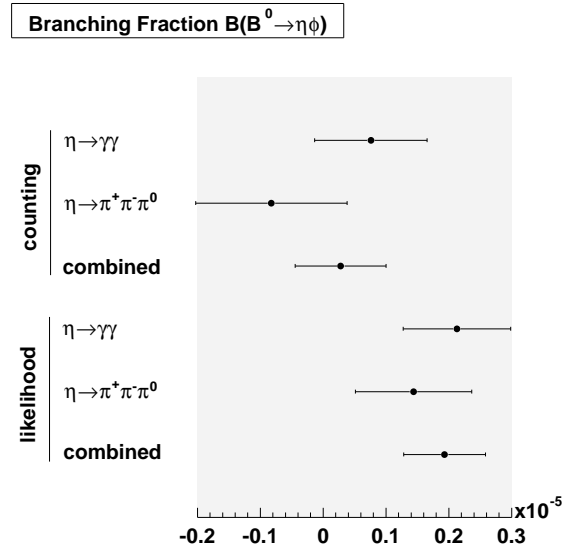


Figure 3.38 Unblinded branching fractions $\mathcal{B}(B^0 \rightarrow \eta\phi)$ from the candidate counting and the maximum-likelihood method in the channels $\eta \rightarrow \gamma\gamma$ and $\eta \rightarrow \pi^+\pi^-\pi^0$ and for both channels combined. The error bars contain statistical and systematic uncertainties.

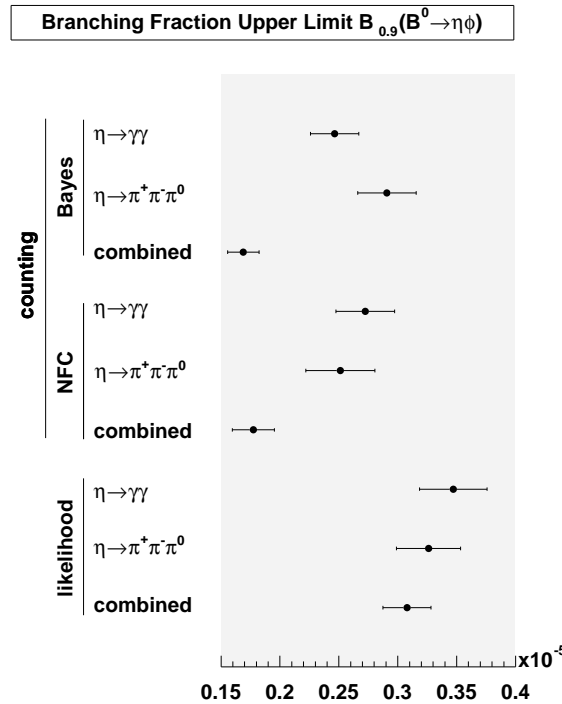


Figure 3.39 Unblinded upper limits on the branching fraction $\mathcal{B}(B^0 \rightarrow \eta\phi)$ from the candidate counting and the maximum-likelihood method in the channels $\eta \rightarrow \gamma\gamma$ and $\eta \rightarrow \pi^+\pi^-\pi^0$ and for both channels combined. The upper limits from candidate counting are calculated in Bayesian and frequentist (NFC) statistics. All upper limits are given at 90% c.l. The error bars contain systematic uncertainties.

Summary

Presented was a search for the rare hadronic B meson decay $B^0 \rightarrow \eta\phi$. It was based on the data collected in the first two years of the *BABAR* experiment. The reconstruction of data events was performed in the *BABAR* software infrastructure. ϕ mesons were reconstructed in the channel $\phi \rightarrow K^+K^-$, while η mesons were reconstructed in the channels $\eta \rightarrow \gamma\gamma$ and $\eta \rightarrow \pi^+\pi^-\pi^0$. The combined decay candidates were separated from background contributions by a two-folded approach, including a cut-based counting method and a maximum-likelihood fitting method. Both methods employed discriminating variables previously used by the ARGUS [55], CLEO [43] and Crystal Ball [56] experiments. Parameterizations for the distributions of these variables were fitted in a separate *ROOT* [53] application, utilizing imported *Roofit* [54] software packages.

In both separation methods, no significant signal contribution was found. The statistical uncertainty on the branching fraction $\mathcal{B}(B^0 \rightarrow \eta\phi)$ is therefore expressed by an upper limit. Seizable systematic uncertainties arise in the candidate counting method from

- the estimation of the number of background candidates at the final number of cuts from the numbers of background candidates at smaller numbers of cuts and
- the estimation of the selection efficiency in the data sample from the selection efficiency in the signal Monte Carlo sample.

The largest systematic uncertainties of the maximum-likelihood method come from

- the estimation of the distributions of the discriminating variables in the data sample from the distributions in the signal Monte Carlo and the off-peak data sample and
- the estimation of the efficiency and the bias of the maximum-likelihood fit to the data sample from fits to study samples generated from these distributions.

These uncertainties add less than 10% to the upper limits in both methods. The cited upper limit in the maximum-likelihood method $\mathcal{B}(B^0 \rightarrow \eta\phi) < 3.28 \times 10^{-6}$ (90%) contains the smallest statistical uncertainty. This result is consistent with recent theoretical predictions [27, 29, 32], but 64% smaller than the upper limit previously measured by the CLEO collaboration [33]. Since no theoretical prediction was excluded, this analysis supports the Standard Model of particle physics. The achieved gain in precision corresponds to the higher integrated luminosity and the improved reconstruction efficiency provided by the *BABAR* experiment.

Relying on the yield of the performed maximum-likelihood fit, an application of this method to twice the integrated luminosity is expected to obtain a significant signal contribution. An extension of the presented analysis onto the data currently available at the *BABAR* experiment (see Fig. 3.1) is thus proposed. Such an analysis could also profit from the improved Monte Carlo simulation, reducing the systematic uncertainties imposed by supplementary correction methods. As for all analyses depending on off-peak data, an increase in their integrated luminosity would distinctly contribute to the reduction of systematic uncertainties.

References

- [1] *Pep-II: An Asymmetric B Factory, Conceptual Design Report*, SLAC-R-418 (June 1993).
- [2] J. de Brunhoff, *Histoire de Babar, le petit éléphant*, Jardin des Modes (1931).
- [3] D. Griffiths, *Introduction to Elementary Particles*, Wiley & Sons (1987).
- [4] P. W. Higgs, *Phys. Rev. Lett.* **13** (1964), 508.
- [5] M. Kobayashi, T. Maskawa, *Prog. Th. Phys.* **49** (1973), 652.
- [6] L. Wolfenstein, *Phys. Rev. Lett.* **51** (1983), 1945.
- [7] BABAR Collaboration (P. F. Harrison, ed. *et al.*), *The BABAR Physics Book: Physics at an Asymmetric B Factory*, SLAC-R-504 (October 1998).
- [8] Particle Data Group (K. Hagiwara *et al.*), *Phys. Rev.* **D 66** (2002), 010001.
- [9] N. G. Deshpande, G. Eilam, *Phys. Rev.* **D 26** (1982), 2463.
- [10] BABAR Collaboration (D. Boutigny *et al.*), *BABAR: Technical Design Report*, SLAC-R-457 (March 1995).
- [11] W. R. Leo, *Techniques for Nuclear and Particle Physics Experiments*, Springer (1994).
- [12] BABAR Collaboration (B. Aubert *et al.*), *Nucl. Inst. Meth.* **A 479** (2002), 1.
- [13] P. Billoir, *Nucl. Inst. Meth.* **A 225** (1984), 352.
- [14] D. Green, *The Physics of Particle Detectors*, Cambridge (2000).
- [15] B. Stroustrup, *The C++ Programming Language*, Addison–Wesley (1986).
- [16] K. G. Wilson, W. Zimmermann, *Comm. Math. Phys.* **24** (1972), 87.
- [17] G. Buchalla, A. J. Buras, M. E. Lautenbacher, *Rev. Mod. Phys.* **68** (1996), 1125.
- [18] J. R. Ellis *et al.*, *Nucl. Phys.* **B 131** (1977), 285.
- [19] M. A. Shifman, *ITEP Lectures in Particle Physics and Field Theory*, World Scientific (1996).

- [20] D. Bortoletto, S. Stone, Phys. Rev. Lett. **65** (1990), 2951.
- [21] A. J. Buras, J. M. Gérard, R. Rückl, Nucl. Phys. **B 268** (1986), 16.
- [22] BABAR Collaboration (B. Aubert *et al.*), Phys. Rev. Lett. **93** (2004), 131801.
- [23] BABAR Collaboration (B. Aubert *et al.*), Phys. Rev. **D 69** (2004), 031102.
- [24] BABAR Collaboration (B. Aubert *et al.*), Phys. Rev. Lett. **91** (2003), 171802.
- [25] BABAR Collaboration (B. Aubert *et al.*), Phys. Rev. Lett. **91** (2003), 241801.
- [26] A. J. Buras *et al.*, Nucl. Phys. **B 370** (1992), 69.
- [27] D. Du, Z. Xing, Phys. Lett. **B 312** (1993), 199.
- [28] M. Bauer, B. Stech, M. Wirbel, Z. Phys. **C 29** (1985), 637, Z. Phys. **C 34** (1987), 103.
- [29] A. Deandrea *et al.*, Phys. Lett. **B 320** (1994), 170.
- [30] R. Casalbuoni *et al.*, Phys. Lett. **B 299** (1993), 139.
- [31] A. J. Buras *et al.*, Nucl. Phys. **B 400** (1993), 37, Nucl. Phys. **B 400** (1993), 75.
- [32] D. Du, L. Guo, Z. Phys. **C 75** (1997), 9.
- [33] CLEO Collaboration (T. Bergfeld *et al.*), Phys. Rev. Lett. **81** (1998), 272.
- [34] A. Stuart, J. K. Ord, *Kendall's Advanced Theory of Statistics (Volume 1)*, Edward Arnold (1994).
- [35] G. Cowan, *Statistical Data Analysis*, Oxford (1998).
- [36] G. J. Feldman, R. D. Cousins, Phys. Rev. **D 57** (1998), 3873.
- [37] C. Hearty, *Measurement of the Number of $\Upsilon(4S)$ Mesons Produced in Run 1 (B Counting)*, BAD¹ 134 (January 2001).
- [38] W. T. Ford, *Choice of Kinematic Variables in B Meson Reconstruction*, BAD¹ 53 (June 2000).
- [39] M. Jacob, J. C. Wick, Ann. Phys. (N.Y.) **7** (1959), 404, reprinted in **281** (2000), 774.
- [40] F. Olness, W.-K. Tung, Phys. Rev. **D 35** (1987), 833.
- [41] S. Brandt *et al.*, Phys. Lett. **12** (1964), 57.
- [42] R. A. Fisher, Ann. Eugen. **7** (1936), 179.
- [43] CLEO Collaboration (D. M. Asner *et al.*), Phys. Rev. **D 53** (1996), 1039.
- [44] G. Vasseur *et al.*, *Two-body B Meson decays to η' and ω* , BAD¹ 41 (August 2000).

- [45] BABAR Collaboration (D. Johnson, ed. *et al.*), *BABAR Software Packages Information*, The BABAR Homepage² (November 2004).
- [46] BABAR Collaboration (S. Versille, ed. *et al.*), *Cornelius User Guide*, The BABAR Homepage² (March 1997).
- [47] D. Kirkby, *Kanga Status and Plans*, BABAR Computing Review (February 2000).
- [48] G. Mancinelli, S. Spanier, *Kaon Selection at the BABAR Experiment*, BAD¹ 116 (July 2001).
- [49] M. Bona *et al.*, *Report of the Tracking Efficiency Task Force for 2001*, BAD¹ 324 (October 2002).
- [50] F. Yumiceva, *Pid Killing Status Report*, BABAR collaboration meeting (September 8, 2002).
- [51] F. Di Lodovico, *Comparison between Monte Carlo and Data of the π^0 Detection and Reconstruction Efficiency using τ 1-on-1 Decays*, BAD¹ 378 (September 2003).
- [52] D. Dujmic, *Merged π^0 Reconstruction: From Cluster Shape to Mass*, BAD¹ 514 (October 2002).
- [53] R. Brun *et al.*, *The ROOT User's Guide*, The ROOT System Home Page³ (June 2001).
- [54] D. Kirkby *et al.*, *A User's Guide to the RooFitTools Package for Unbinned Maximum Likelihood Fitting*, BAD¹ 18 (August 2001).
- [55] ARGUS Collaboration (H. Albrecht *et al.*), *Phys. Lett.* **B 185** (1987), 218.
- [56] Crystal Ball Collaboration (T. Skwarnicki *et al.*), *A Study of the Radiative Cascade Transitions Between the Υ' and Υ Resonances*, DESY-F31-86-02 (April 1986).
- [57] N. N. Achasov, *Nature of the Scalar $a_0(980)$ and $f_0(980)$ Mesons*, hep-ph/9803292 (July 2004).
- [58] BABAR Collaboration (B. Aubert *et al.*), *Phys. Rev. Lett.* **93** (2004), 181806.

¹BABAR Analysis Documents (BAD's) are available at the BABAR homepage.²

²Currently available at <http://www.slac.stanford.edu/BFR00T>.

³Currently available at <http://root.cern.ch>.

Acknowledgements

I wish to thank my thesis adviser, Prof. Dr. Bernhard Spaan of the Institut für Kern- und Teilchenphysik of the Technische Universität Dresden, for the challenging topic and his technical guidance. I am also obliged to Prof. Dr. Klaus R. Schubert for his friendly support.

I am deeply indebted to my loving wife Lavandree, who submitted to enormous privations during the composition of this thesis and who tirelessly corrected all my imperfect English.

I wish to thank my parents for their love and encouragement and for the generous moral and material support they continuously granted.

My special gratitude goes to Prof. William T. Ford, Ph.D., and Prof. James G. Smith, Ph.D., of the University of Colorado for supplying their indispensable experience to the conduct of this analysis.

I wish to thank my colleagues at the Institut für Kern- und Teilchenphysik and my collaborators at the *BABAR* experiment for the friendly working atmosphere and all the helpful advice.

This work was supported by the Bundesministerium für Bildung und Forschung (BMBF) and the Deutsche Forschungsgemeinschaft (DFG).

Appendix A

Resonance Masses

A.1 Channel $\eta \rightarrow \gamma\gamma$

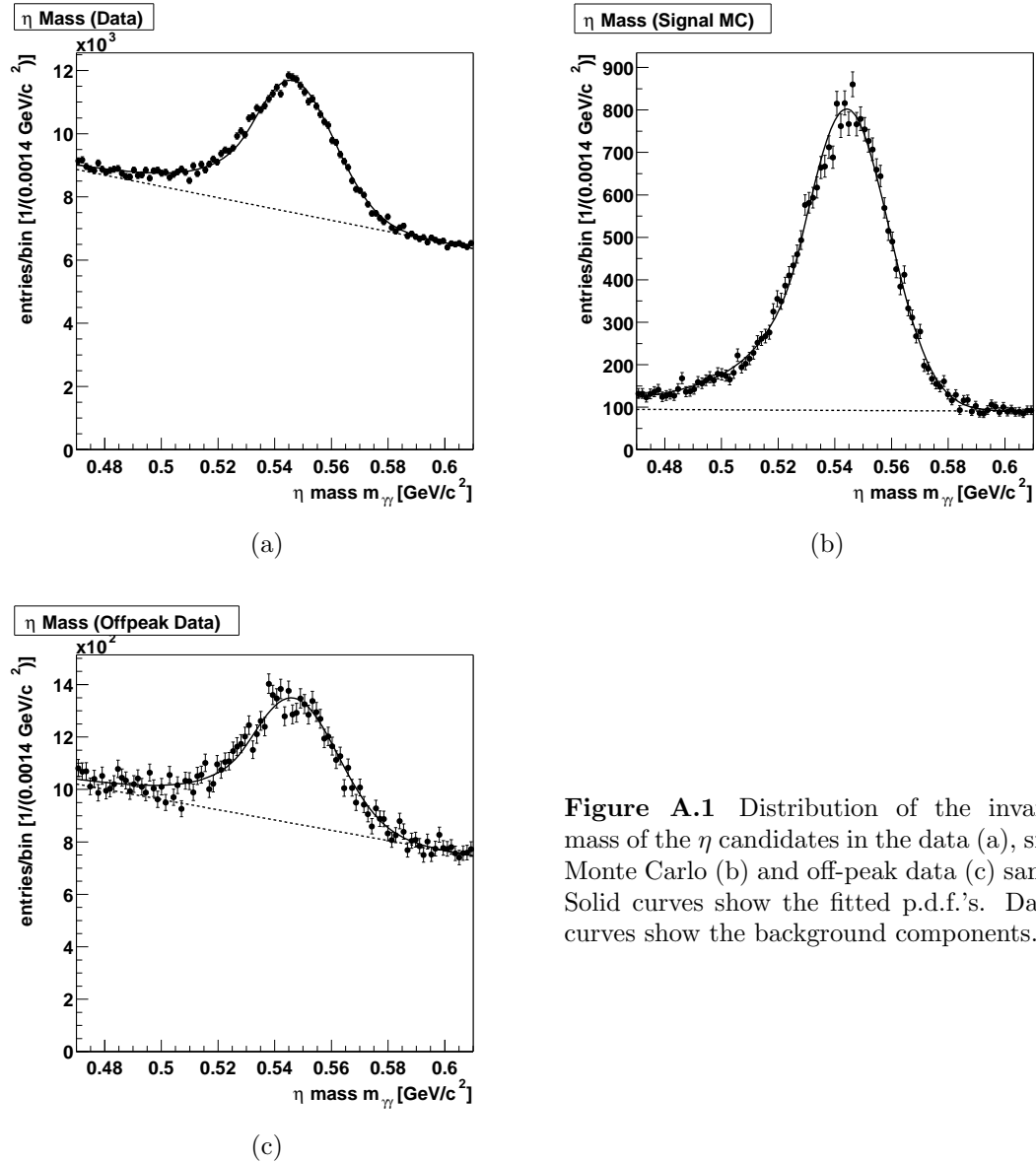


Figure A.1 Distribution of the invariant mass of the η candidates in the data (a), signal Monte Carlo (b) and off-peak data (c) sample. Solid curves show the fitted p.d.f.'s. Dashed curves show the background components.

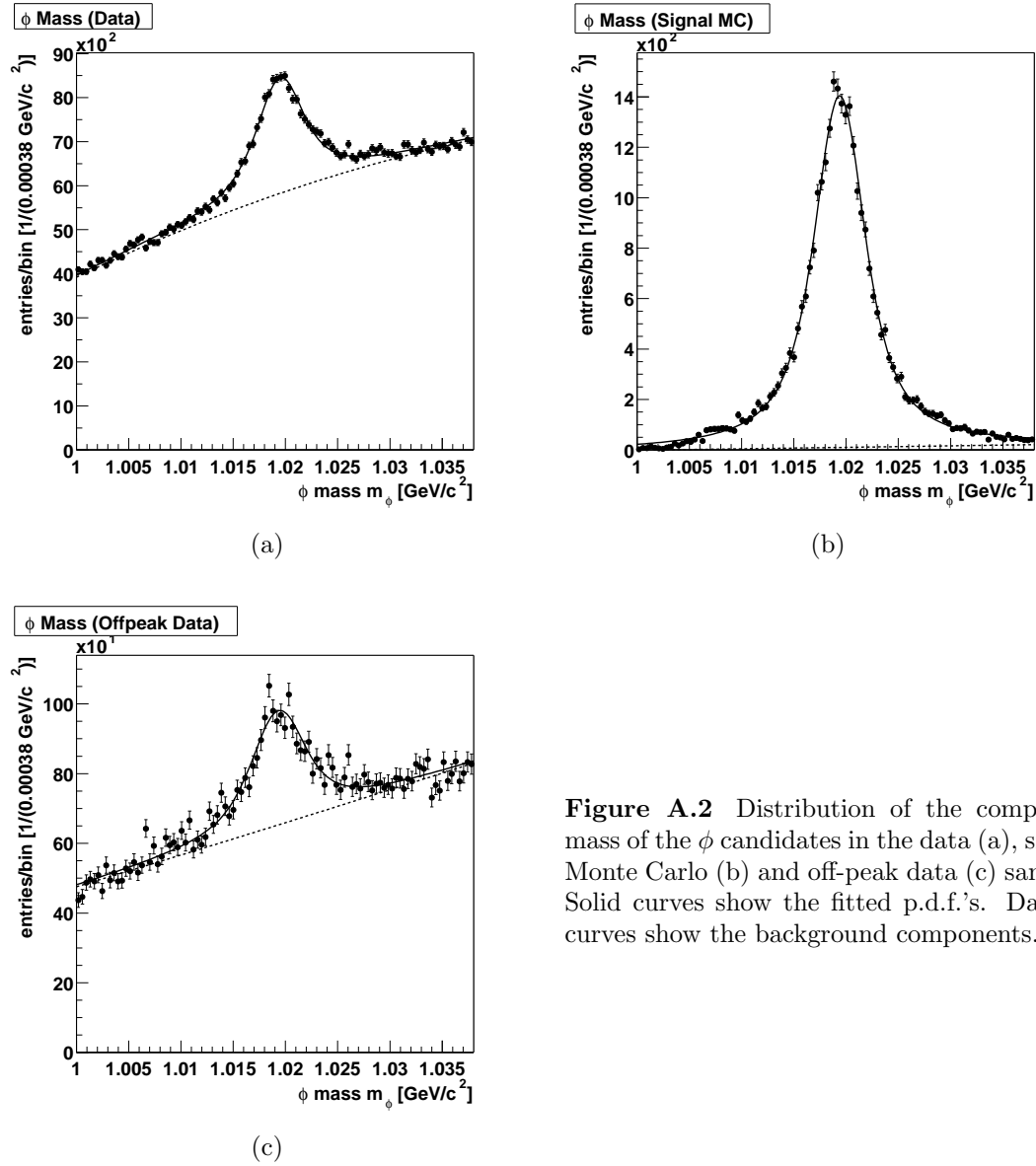


Figure A.2 Distribution of the composite mass of the ϕ candidates in the data (a), signal Monte Carlo (b) and off-peak data (c) sample. Solid curves show the fitted p.d.f.'s. Dashed curves show the background components.

	$m_{\gamma\gamma}$	m_ϕ
signal	$S = 0.6955 \pm 0.0063$ $\mu = (544.16 \pm 0.15) \text{ MeV}/c^2$ $\sigma = (14.94 \pm 0.16) \text{ MeV}/c^2$ $r = 3$ $\alpha = 1.087 \pm 0.024$ $c_0 = 1$ $c_1 = -0.30 \pm 0.26$	$S = 0.9679 \pm 0.0038$ $\mu = (1.019389 \pm 0.000022) \text{ GeV}/c^2$ $\Gamma = (4.647 \pm 0.099) \text{ MeV}/c^2$ $\sigma = (1.141 \pm 0.077) \text{ MeV}/c^2$ $c_0 = 1$ $c_1 = -9.5923 \pm 0.0025$ $c_2 = 8.5743 \pm 0.0023$
$q\bar{q}$	$S = 0.1437 \pm 0.0040$ $\mu = (546.828 \pm 0.081) \text{ MeV}/c^2$ $\sigma = (15.542 \pm 0.079) \text{ MeV}/c^2$ $r = 3$ $\alpha = 1.087$ $c_0 = 1$ $c_1 = -1.009 \pm 0.018$	$S = 0.0998 \pm 0.0032$ $\mu = (1.01931 \pm 0.00013) \text{ GeV}/c^2$ $\Gamma = 4.647 \text{ MeV}/c^2$ $\sigma = (1.38 \pm 0.23) \text{ MeV}/c^2$ $c_0 = -0.1$ $c_1 = -3.081 \pm 0.072$ $c_2 = 3.374 \pm 0.076$
data	$S = 0.13808 \pm 0.00097$ $\mu = (546.4487 \pm 0.0096) \text{ MeV}/c^2$ $\sigma = (14.574 \pm 0.018) \text{ MeV}/c^2$ $r = 3$ $\alpha = 1.087$ $c_0 = 1$ $c_1 = -1.0350 \pm 0.0058$	$S = 0.0855 \pm 0.0012$ $\mu = (1.019483 \pm 0.000038) \text{ GeV}/c^2$ $\Gamma = 4.647 \text{ MeV}/c^2$ $\sigma = (0.988 \pm 0.085) \text{ MeV}/c^2$ $c_0 = -0.1$ $c_1 = 0.188808 \pm 0.000030$ $c_2 = -0.088395 \pm 0.000032$

Table A.1 Signal fractions S and p.d.f. parameters of the invariant mass $m_{\gamma\gamma}$ of the η candidates (Eq. 3.44, Fig. A.1) and the composite mass m_ϕ of the ϕ candidates (Eq. 3.46 and 3.47, Fig. A.2) in the signal Monte Carlo, off-peak ($q\bar{q}$) data and data sample.

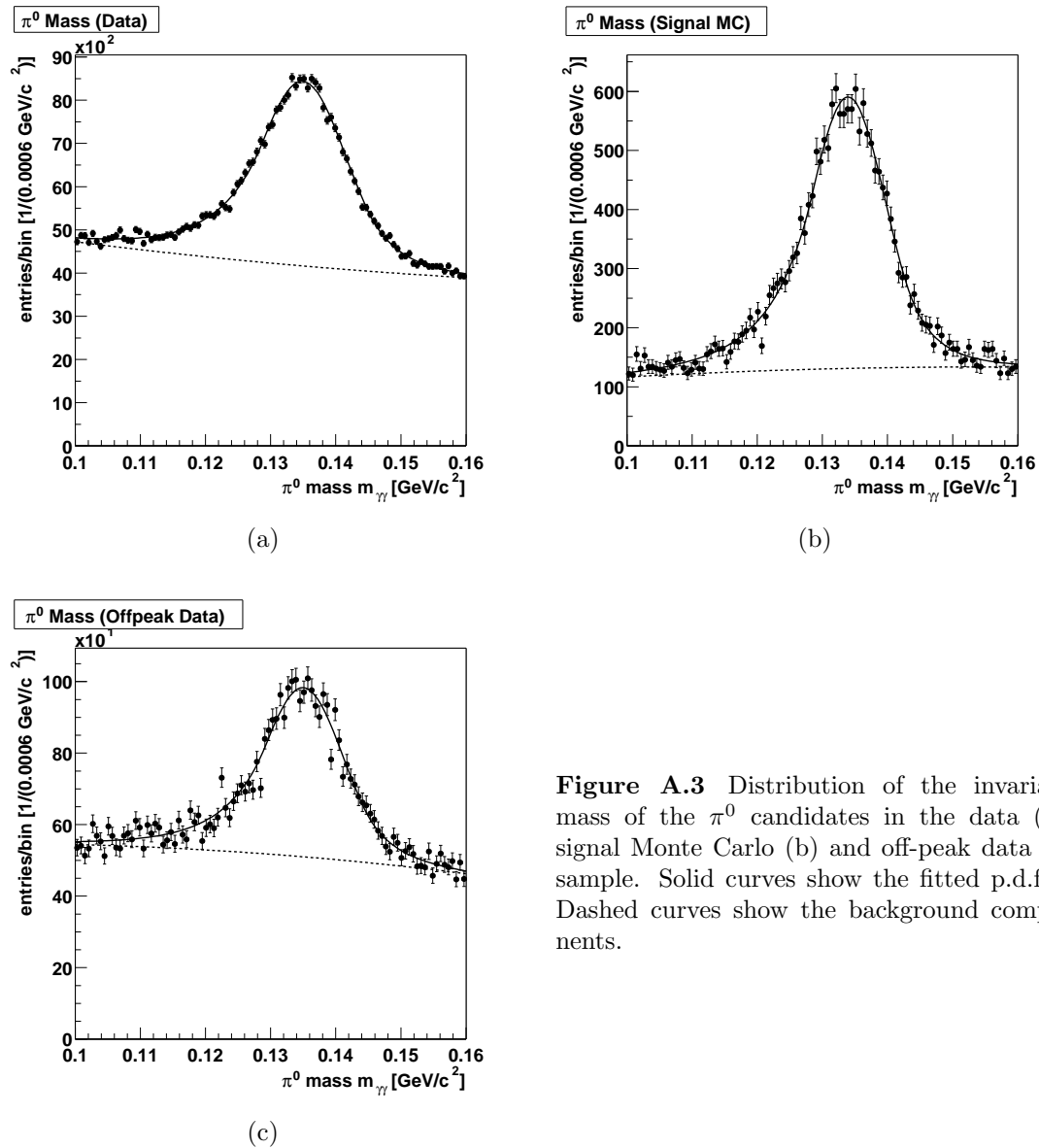
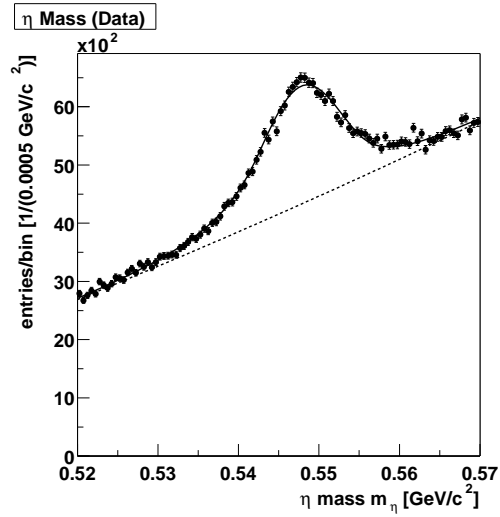
A.2 Channel $\eta \rightarrow \pi^+\pi^-\pi^0$ 

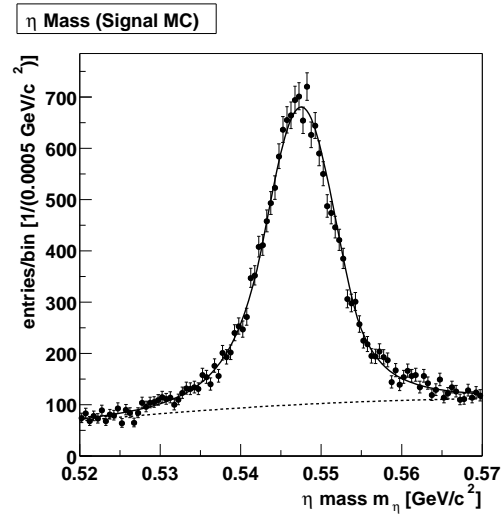
Figure A.3 Distribution of the invariant mass of the π^0 candidates in the data (a), signal Monte Carlo (b) and off-peak data (c) sample. Solid curves show the fitted p.d.f.'s. Dashed curves show the background components.

	$m_{\gamma\gamma}$
signal	$S = 0.5015 \pm 0.0078$ $\mu = (133.916 \pm 0.086) \text{ MeV}/c^2$ $\sigma = (5.85 \pm 0.10) \text{ MeV}/c^2$ $r_1 = 10$ $r_2 = 8$ $\alpha_1 = 0.930 \pm 0.030$ $\alpha_1 = -1.467 \pm 0.062$ $c_0 = -0.001$ $c_1 = 2.62 \pm 0.30$ $c_2 = -1.467 \pm 0.062$
$q\bar{q}$	$S = 0.2142 \pm 0.0056$ $\mu = (135.05 \pm 0.14) \text{ MeV}/c^2$ $\sigma = (6.15 \pm 0.21) \text{ MeV}/c^2$ $r_1 = 10$ $r_2 = 8$ $\alpha_1 = 0.930$ $\alpha_2 = -1.467$ $c_0 = 0.1$ $c_1 = 0.576 \pm 0.060$ $c_1 = -3.4 \pm 0.26$
data	$S = 0.2423 \pm 0.0016$ $\mu = (134.950 \pm 0.043) \text{ MeV}/c^2$ $\sigma = (6.667 \pm 0.060) \text{ MeV}/c^2$ $r_1 = 10$ $r_2 = 8$ $\alpha_1 = 0.930$ $\alpha_2 = -1.467$ $c_0 = 0.1$ $c_1 = -0.488 \pm 0.051$ $c_1 = 1.17 \pm 0.22$

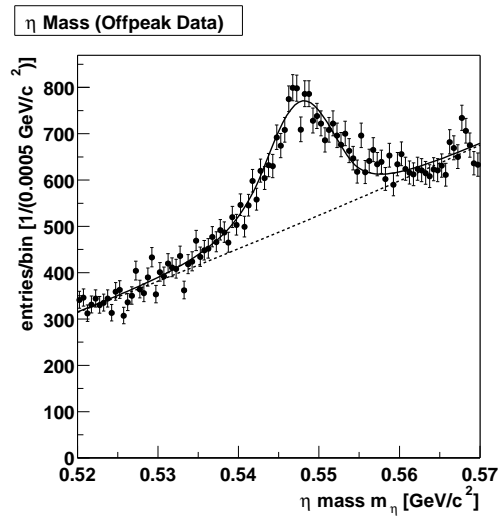
Table A.2 Signal fractions S and p.d.f. parameters for the invariant mass $m_{\gamma\gamma}$ of the π^0 candidates (Eq. 3.45, Fig. A.3) in the signal Monte Carlo, off-peak ($q\bar{q}$) data and data sample.



(a)



(b)



(c)

Figure A.4 Distribution of the composite mass of the η candidates in the data (a), signal Monte Carlo (b) and off-peak data (c) sample. Solid curves show the fitted p.d.f.'s. Dashed curves show the background components.

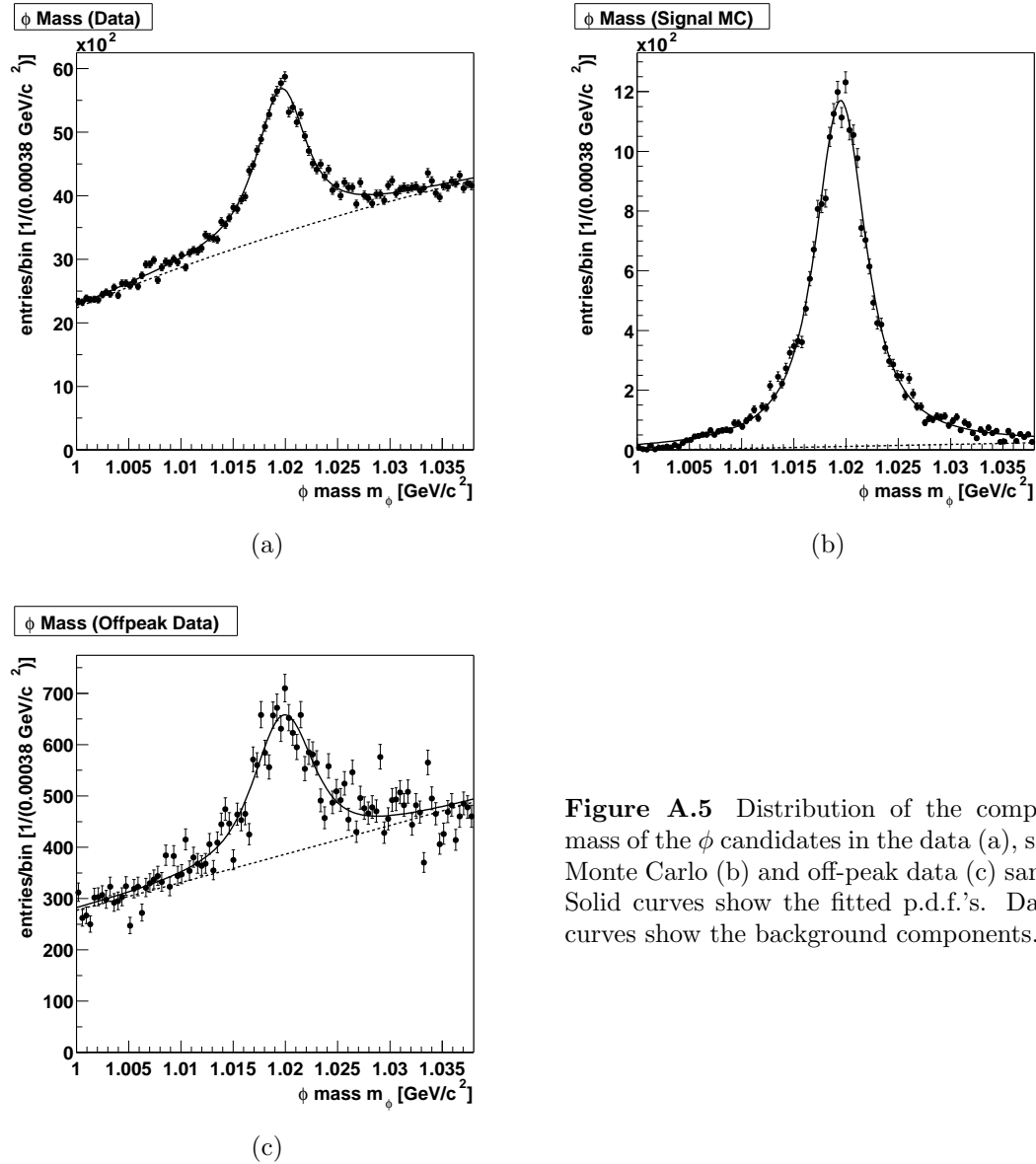


Figure A.5 Distribution of the composite mass of the ϕ candidates in the data (a), signal Monte Carlo (b) and off-peak data (c) sample. Solid curves show the fitted p.d.f.'s. Dashed curves show the background components.

	m_η	m_ϕ
signal	$S = 0.5993 \pm 0.0075$ $\mu = (547.496 \pm 0.052) \text{ MeV}/c^2$ $\sigma = (4.370 \pm 0.056) \text{ MeV}/c^2$ $r_1 = 10$ $r_2 = 3$ $\alpha_1 = 1.107 \pm 0.026$ $\alpha_2 = -1.444 \pm 0.035$ $c_0 = -1$ $c_1 = 3.5537 \pm 0.0069$ $c_2 = -3.078 \pm 0.013$	$S = 0.9556 \pm 0.0042$ $\mu = (1.019482 \pm 0.000024) \text{ GeV}/c^2$ $\Gamma = (4.80 \pm 0.10) \text{ MeV}/c^2$ $\sigma = (0.952 \pm 0.092) \text{ MeV}/c^2$ $c_0 = 1$ $c_1 = -7.6429 \pm 0.0048$ $c_2 = 6.6295 \pm 0.0048$
$q\bar{q}$	$S = 0.1155 \pm 0.0038$ $\mu = (547.636 \pm 0.029) \text{ MeV}/c^2$ $\sigma = (4.306 \pm 0.066) \text{ MeV}/c^2$ $r_1 = 10$ $r_2 = 3$ $\alpha_1 = 1.107$ $\alpha_2 = -1.444$ $c_0 = 0.01$ $c_1 = -1.951 \pm 0.064$ $c_1 = 4.12 \pm 0.14$	$S = 0.1423 \pm 0.0048$ $\mu = (1.01981 \pm 0.00011) \text{ GeV}/c^2$ $\Gamma = 4.80 \text{ MeV}/c^2$ $\sigma = (1.53 \pm 0.21) \text{ MeV}/c^2$ $c_0 = -0.1$ $c_1 = -2.383 \pm 0.015$ $c_2 = 2.632 \pm 0.016$
data	$S = 0.1223 \pm 0.0013$ $\mu = (547.761 \pm 0.044) \text{ MeV}/c^2$ $\sigma = (5.1063 \pm 0.0043) \text{ MeV}/c^2$ $r_1 = 10$ $r_2 = 3$ $\alpha_1 = 1.107$ $\alpha_2 = -1.444$ $c_0 = 0.01$ $c_1 = -4.239 \pm 0.012$ $c_1 = 9.025 \pm 0.027$	$S = 0.1218 \pm 0.0014$ $\mu = (1.019578 \pm 0.000044) \text{ GeV}/c^2$ $\Gamma = 4.80 \text{ MeV}/c^2$ $\sigma = (0.891 \pm 0.054) \text{ MeV}/c^2$ $c_0 = -0.1$ $c_1 = 0.18608 \pm 0.00035$ $c_2 = -0.08559 \pm 0.00037$

Table A.3 Signal fractions S and p.d.f. parameters for the composite masses m_η of the η candidates (Eq. 3.45, Fig. A.4) and m_ϕ of the ϕ candidates (Eq. 3.46 and 3.47, Fig. A.5) in the signal Monte Carlo, off-peak ($q\bar{q}$) data and data sample.

Appendix B

Cut Optimization

B.1 Channel $\eta \rightarrow \gamma\gamma$

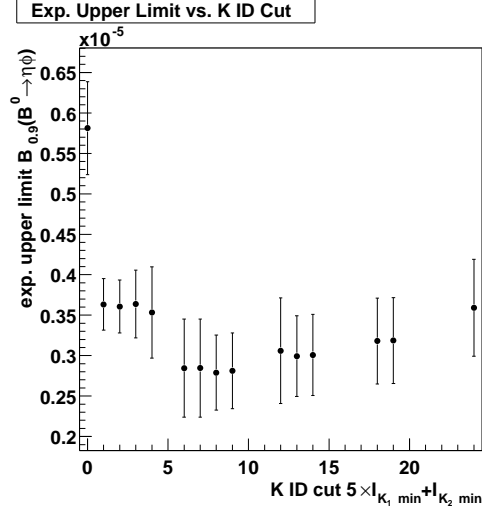


Figure B.1 Expected upper limit on the branching fraction $\hat{\mathcal{B}}_{\text{Bay}}(B^0 \rightarrow \eta\phi)$ vs. cut on the kaon identification of the K^\pm candidates.

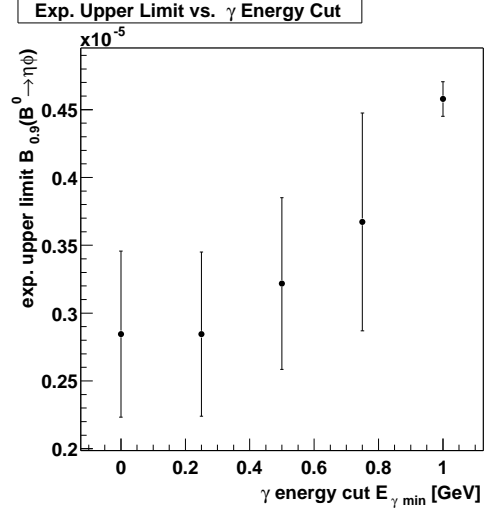


Figure B.2 Expected upper limit on the branching fraction $\hat{\mathcal{B}}_{\text{Bay}}(B^0 \rightarrow \eta\phi)$ vs. cut on the energy of the photon candidates.

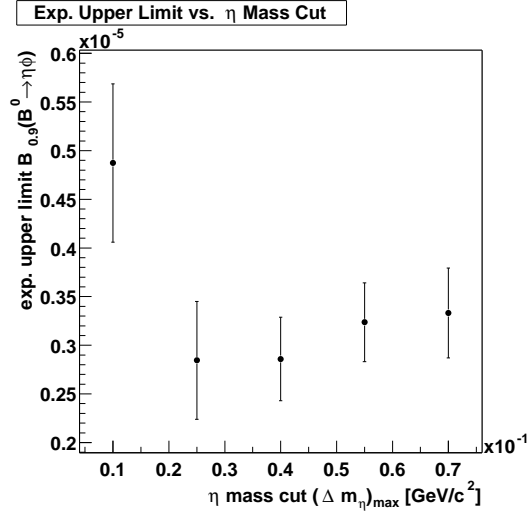


Figure B.3 Expected upper limit on the branching fraction $\hat{\mathcal{B}}_{\text{Bay}}(B^0 \rightarrow \eta\phi)$ vs. cut on the invariant mass of the η candidates.

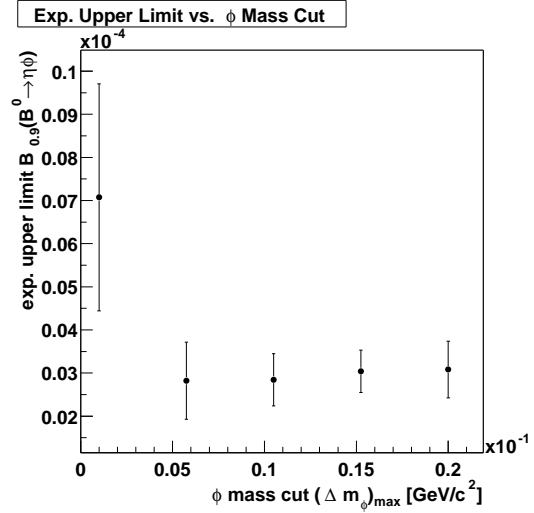


Figure B.4 Expected upper limit on the branching fraction $\hat{\mathcal{B}}_{\text{Bay}}(B^0 \rightarrow \eta\phi)$ vs. cut on the composite mass of the ϕ candidates.

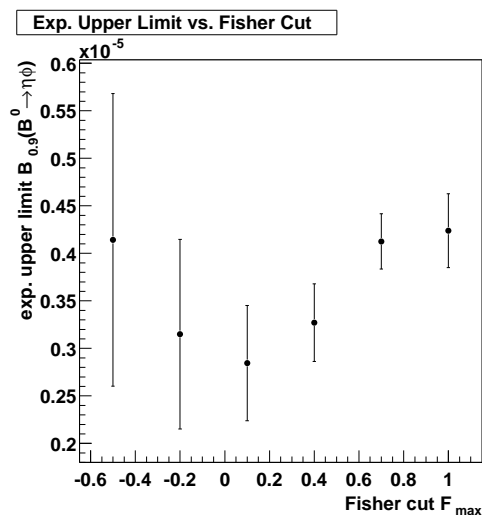


Figure B.5 Expected upper limit on the branching fraction $\hat{\mathcal{B}}_{\text{Bay}}(B^0 \rightarrow \eta\phi)$ vs. cut on the Fisher discriminant.

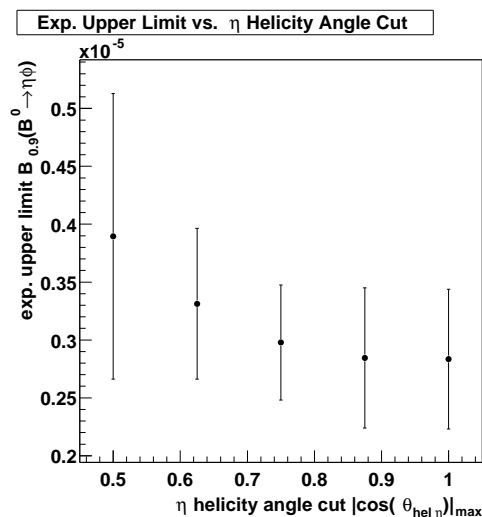


Figure B.6 Expected upper limit on the branching fraction $\hat{\mathcal{B}}_{\text{Bay}}(B^0 \rightarrow \eta\phi)$ vs. cut on the helicity angle of the η candidates.

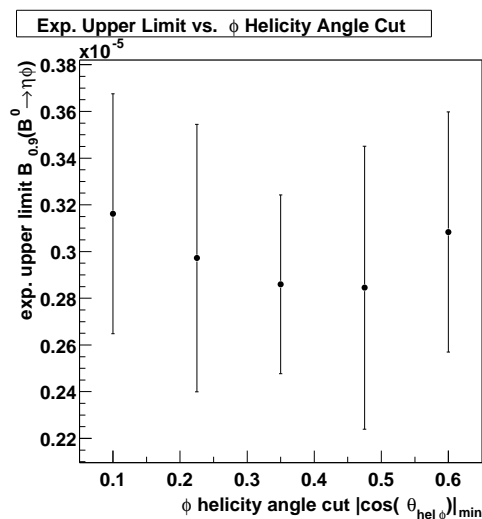


Figure B.7 Expected upper limit on the branching fraction $\hat{\mathcal{B}}_{\text{Bay}}(B^0 \rightarrow \eta\phi)$ vs. cut on the helicity angle of the ϕ candidates.

B.2 Channel $\eta \rightarrow \pi^+ \pi^- \pi^0$

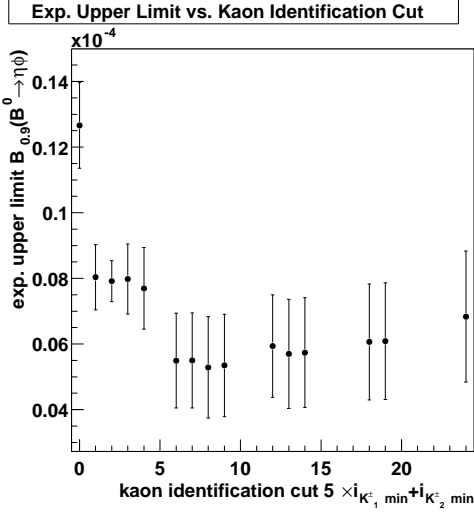


Figure B.8 Expected upper limit on the branching fraction $\hat{\mathcal{B}}_{\text{Bay}}(B^0 \rightarrow \eta\phi)$ vs. cut on the kaon identification of the K^{\pm} candidates.

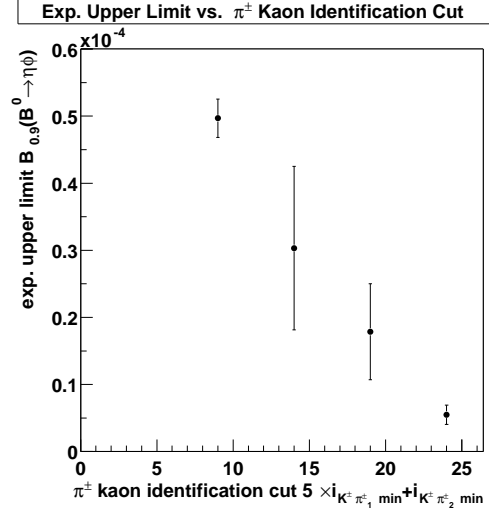


Figure B.9 Expected upper limit on the branching fraction $\hat{\mathcal{B}}_{\text{Bay}}(B^0 \rightarrow \eta\phi)$ vs. cut on the kaon identification of the π^{\pm} candidates.

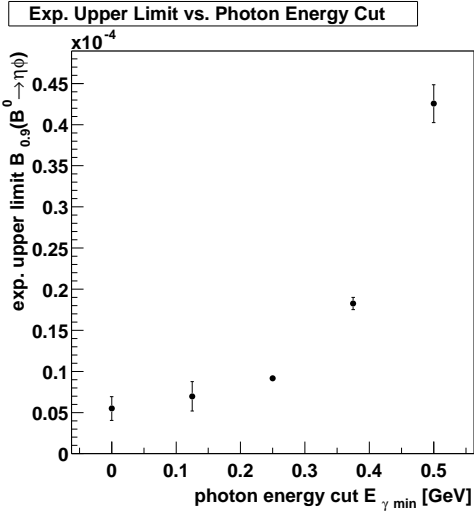


Figure B.10 Expected upper limit on the branching fraction $\hat{\mathcal{B}}_{\text{Bay}}(B^0 \rightarrow \eta\phi)$ vs. cut on the energy of the photon candidates.

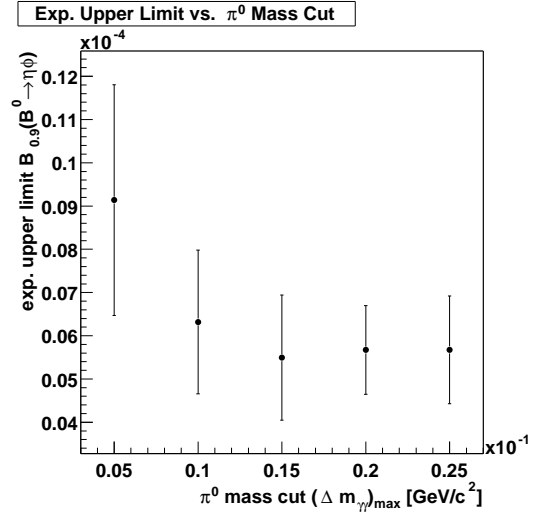


Figure B.11 Expected upper limit on the branching fraction $\hat{\mathcal{B}}_{\text{Bay}}(B^0 \rightarrow \eta\phi)$ vs. cut on the invariant mass of the π^0 candidates.

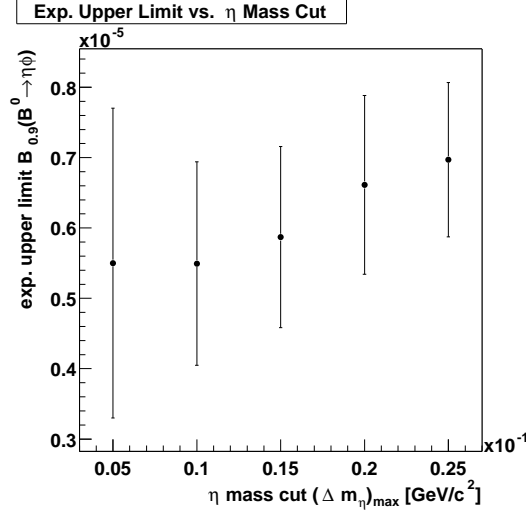


Figure B.12 Expected upper limit on the branching fraction $\hat{\mathcal{B}}_{\text{Bay}}(B^0 \rightarrow \eta\phi)$ vs. cut on the composite mass of the η candidates.

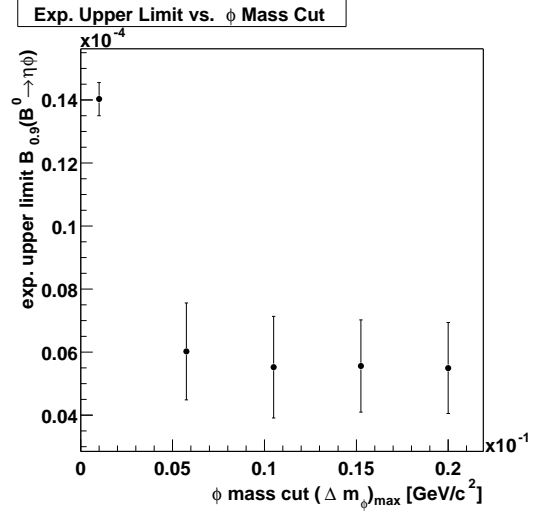


Figure B.13 Expected upper limit on the branching fraction $\hat{\mathcal{B}}_{\text{Bay}}(B^0 \rightarrow \eta\phi)$ vs. cut on the composite mass of the ϕ candidates.

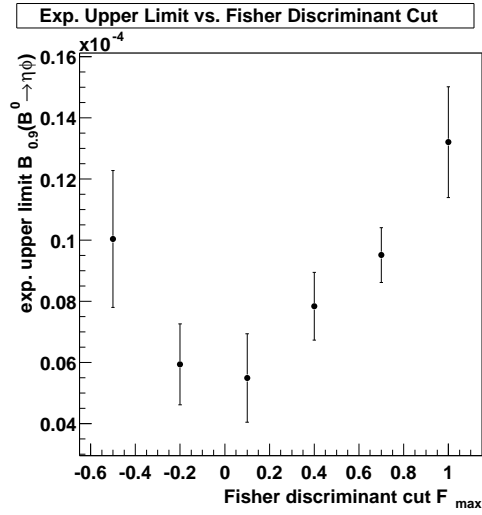


Figure B.14 Expected upper limit on the branching fraction $\hat{\mathcal{B}}_{\text{Bay}}(B^0 \rightarrow \eta\phi)$ vs. cut on the Fisher discriminant.

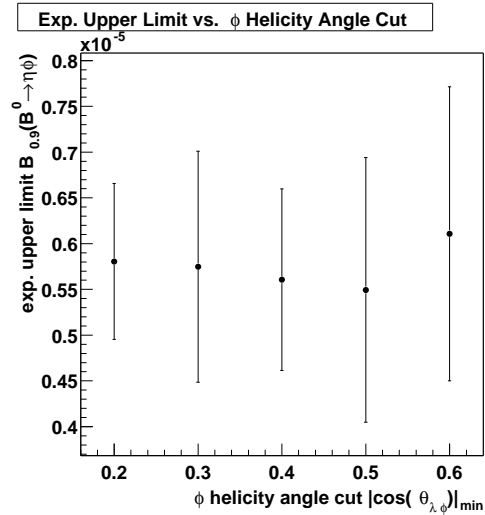


Figure B.15 Expected upper limit on the branching fraction $\hat{\mathcal{B}}_{\text{Bay}}(B^0 \rightarrow \eta\phi)$ vs. cut on the helicity angle of the ϕ candidates.

Appendix C

B^0 Masses

C.1 Channel $\eta \rightarrow \gamma\gamma$ Before Cuts

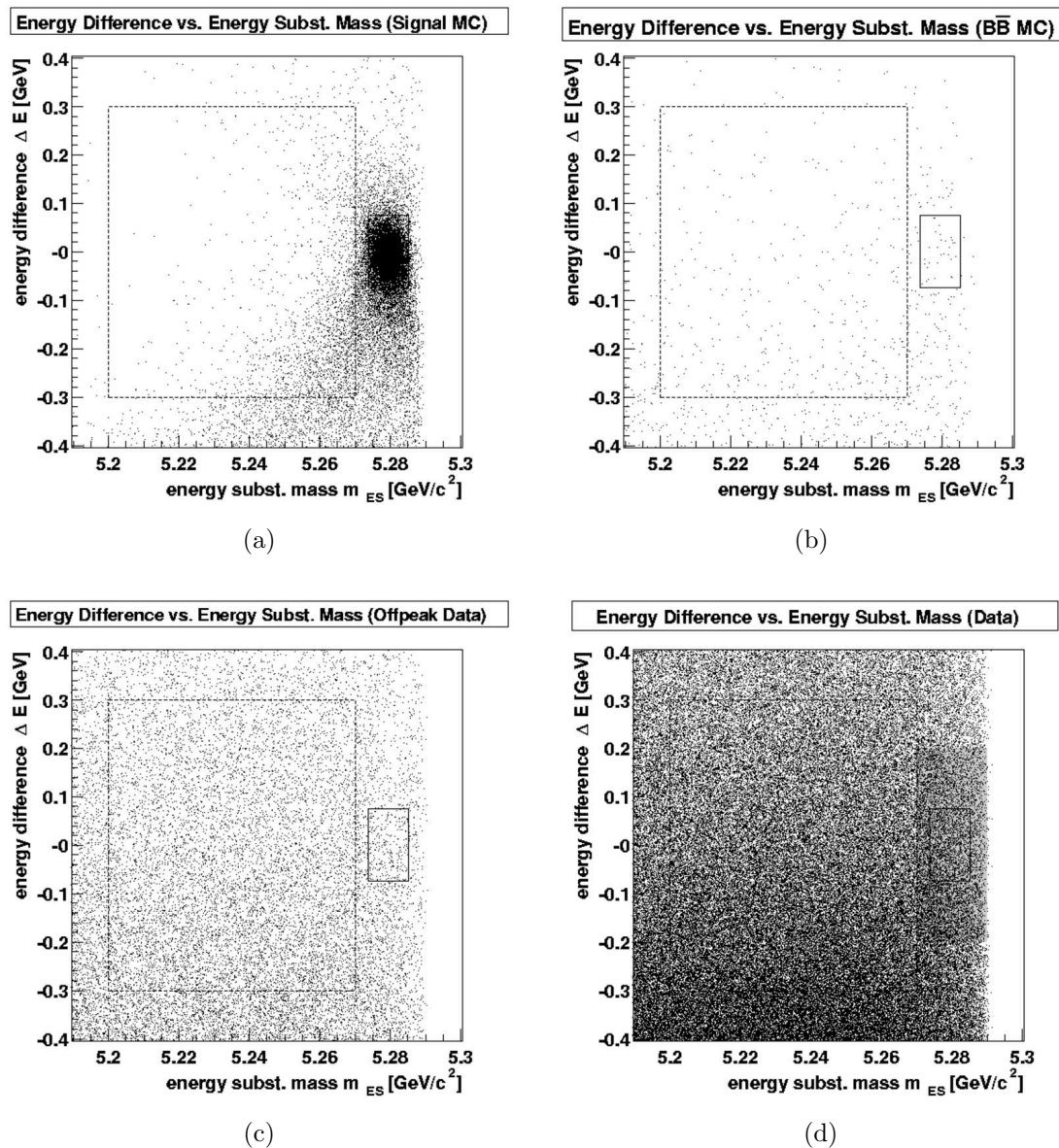


Figure C.1 Joint distribution of energy substituted mass and energy difference in the signal Monte Carlo (a), $B\bar{B}$ Monte Carlo (b), off-peak data (c) and data (d) sample. Solid lines enclose the signal box. Dashed lines enclose the sidebands. The shaded area in (d) was *blinded* in the analysis.

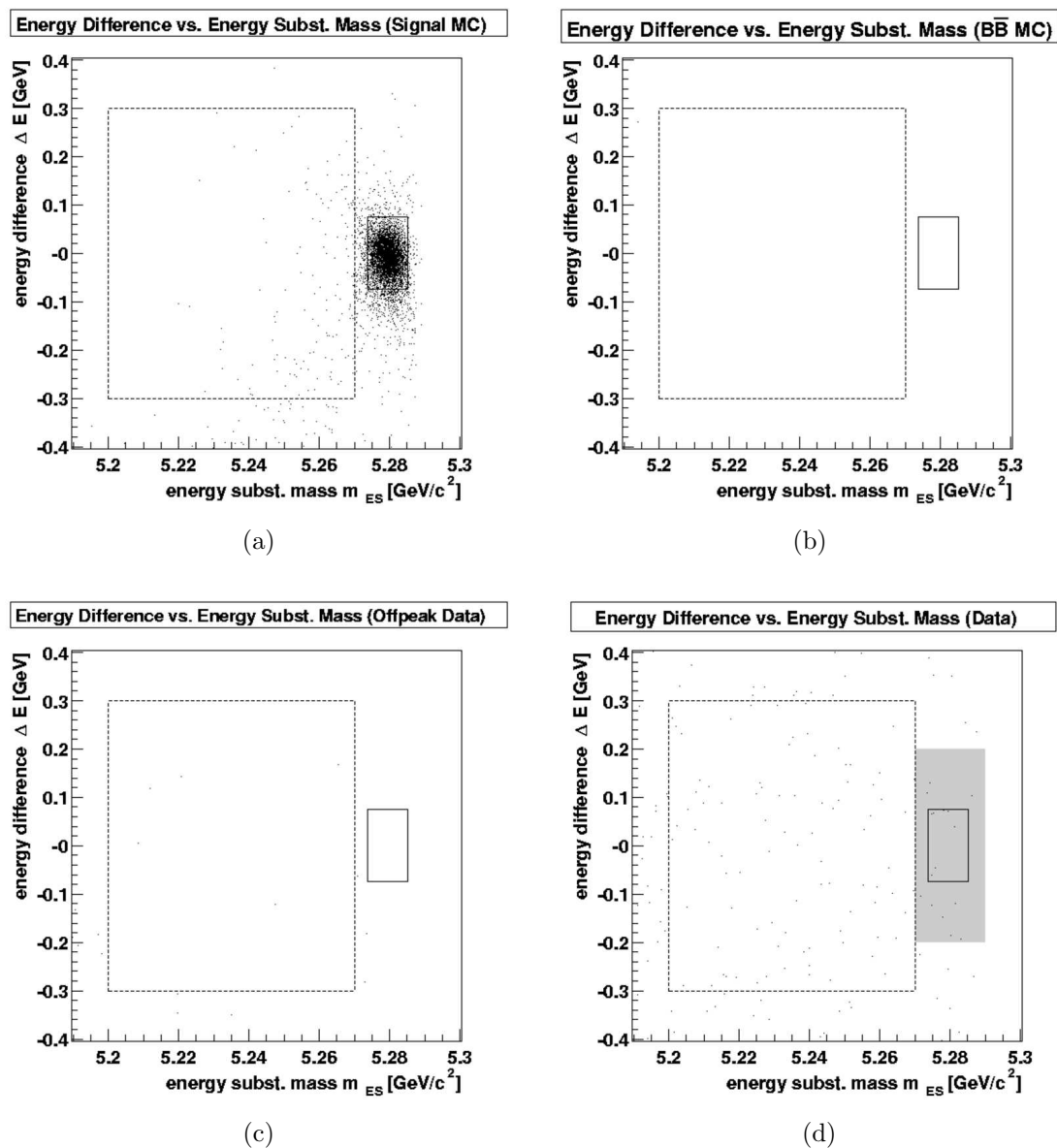
C.2 Channel $\eta \rightarrow \gamma\gamma$ After Optimized Cuts

Figure C.2 Joint distribution of energy substituted mass and energy difference in the signal Monte Carlo (a), $B\bar{B}$ Monte Carlo (b), off-peak data (c) and data (d) sample. Solid lines enclose the signal box. Dashed lines enclose the sidebands. The shaded area in (d) was *blinded* in the analysis.

C.3 Channel $\eta \rightarrow \pi^+\pi^-\pi^0$ Before Cuts

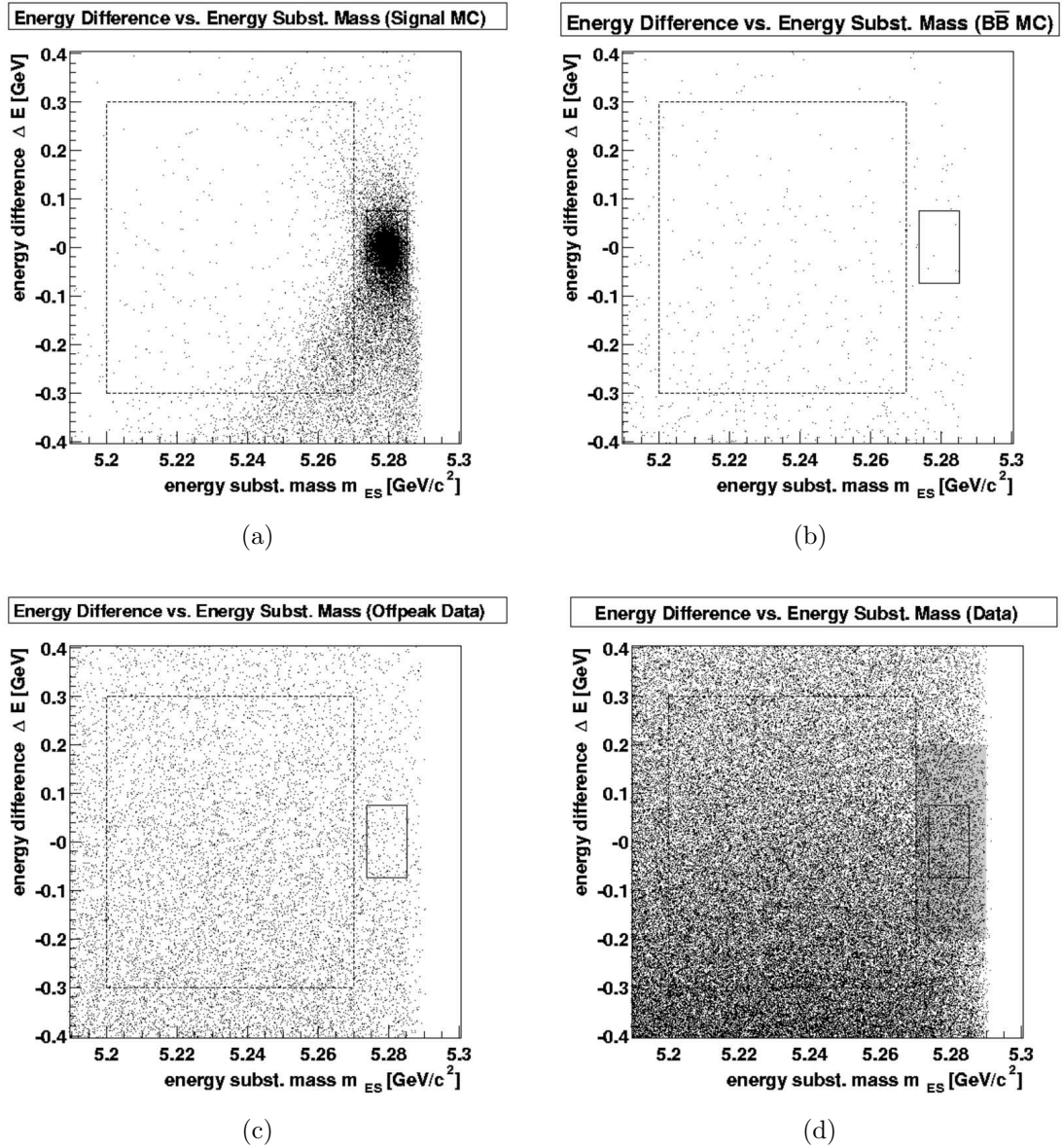


Figure C.3 Joint distribution of energy substituted mass and energy difference in the signal Monte Carlo (a), $B\bar{B}$ Monte Carlo (b), off-peak data (c) and data (d) sample. Solid lines enclose the signal box. Dashed lines enclose the sidebands. The shaded area in (d) was *blinded* in the analysis.

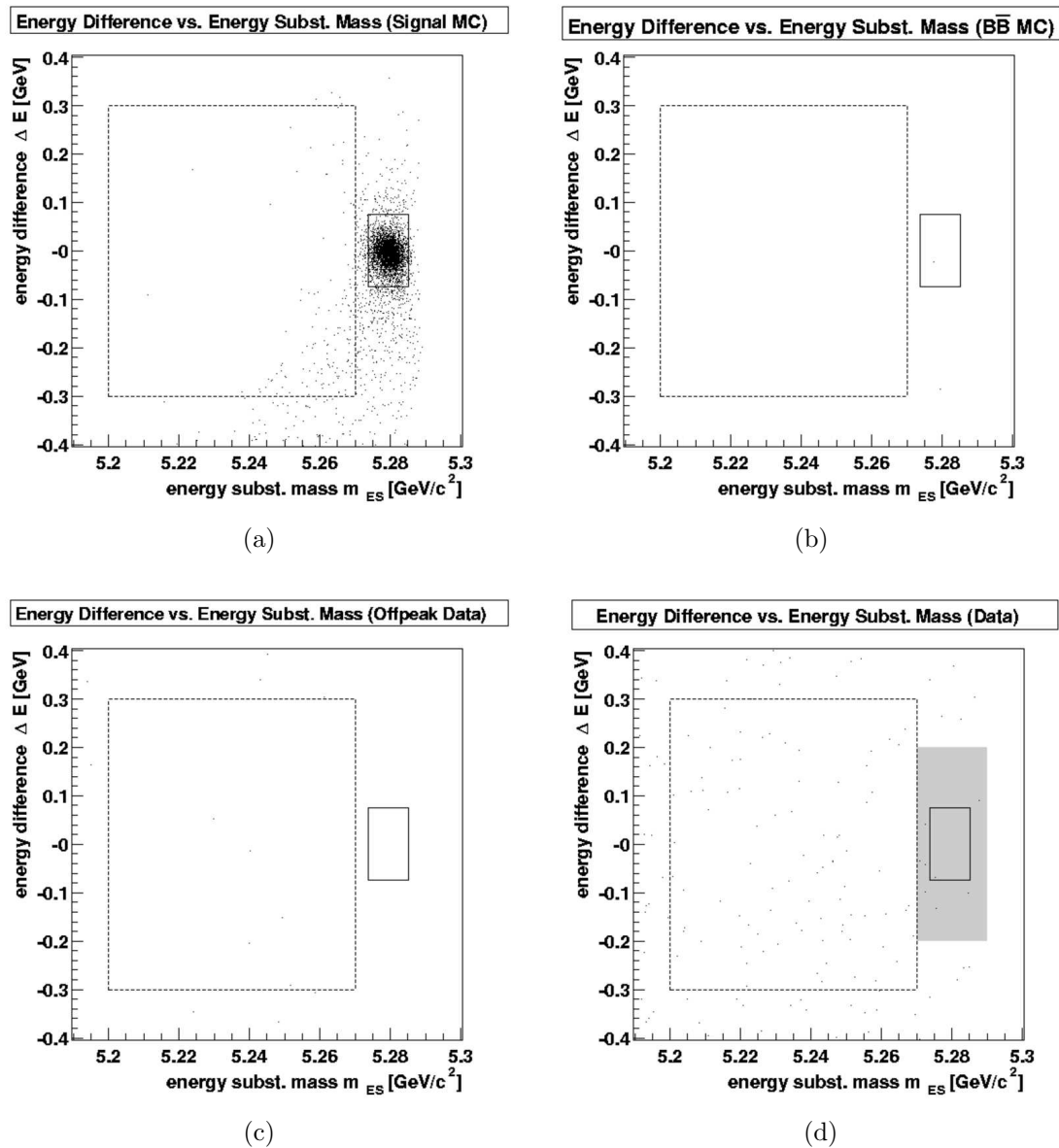
C.4 Channel $\eta \rightarrow \pi^+\pi^-\pi^0$ After Optimized Cuts

Figure C.4 Joint distribution of energy substituted mass and energy difference in the signal Monte Carlo (a), $B\bar{B}$ Monte Carlo (b), off-peak data (c) and data (d) sample. Solid lines enclose the signal box. Dashed lines enclose the sidebands. The shaded area in (d) was *blinded* in the analysis.

Appendix D

Probability Density Functions

D.1 Channel $\eta \rightarrow \gamma\gamma$

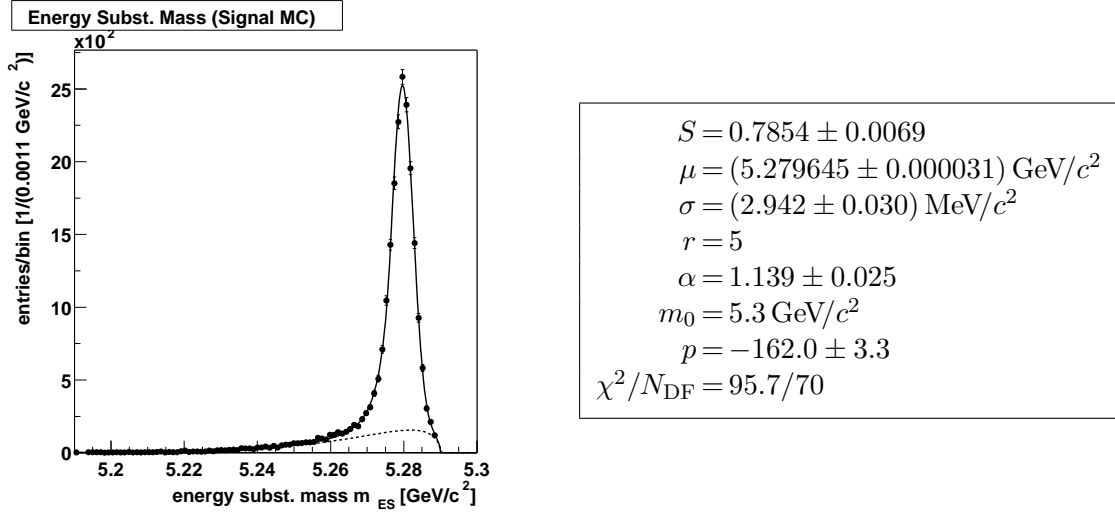


Figure D.1 Distribution, signal fraction S and p.d.f. parameters of the energy substituted mass (Eq. 3.41 and 3.44) in the signal Monte Carlo sample. The solid curve shows the fitted p.d.f. The dashed curve shows the background component.

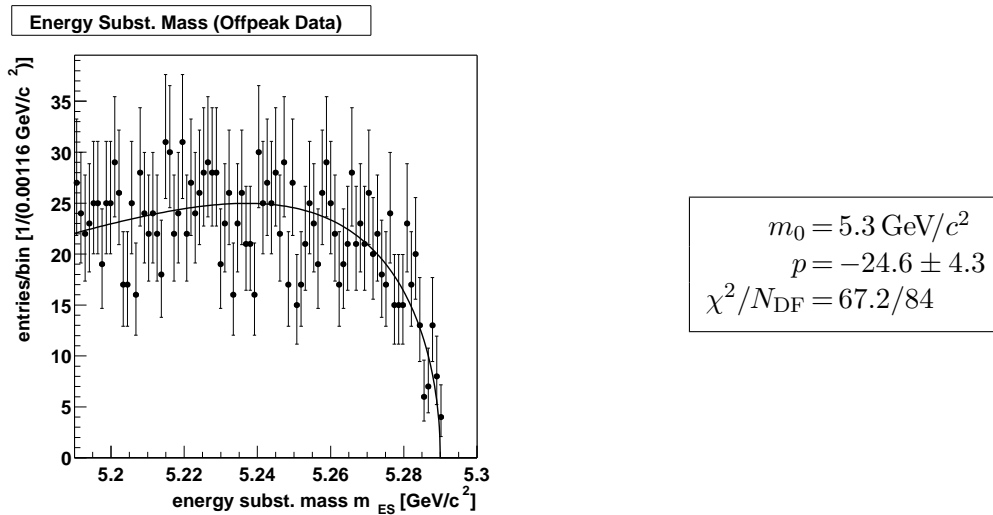


Figure D.2 Distribution and p.d.f. parameters of the energy substituted mass (Eq. 3.41) in the off-peak data sample. The curve shows the fitted p.d.f.

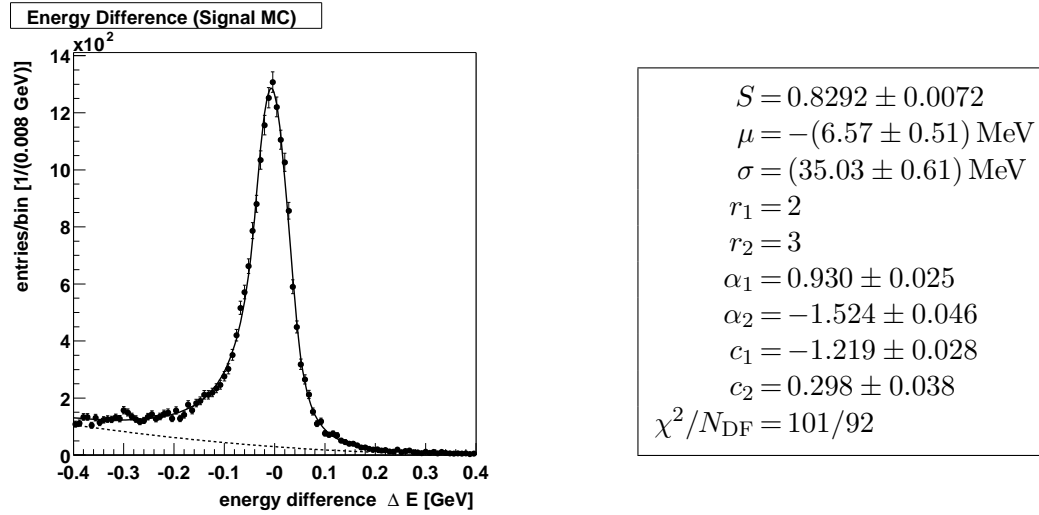


Figure D.3 Distribution, signal fraction S and p.d.f. parameters of the energy difference (Eq. 3.42 and 3.45) in the signal Monte Carlo sample. The solid curve shows the fitted p.d.f. The dashed curve shows the background component.

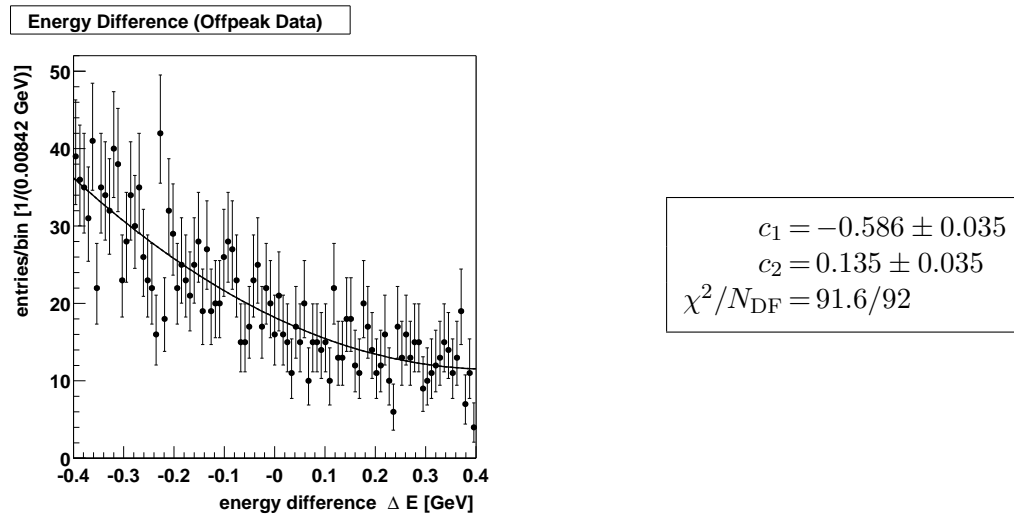


Figure D.4 Distribution and p.d.f. parameters of the energy difference (Eq. 3.42) in the off-peak data sample. The curve shows the fitted p.d.f.

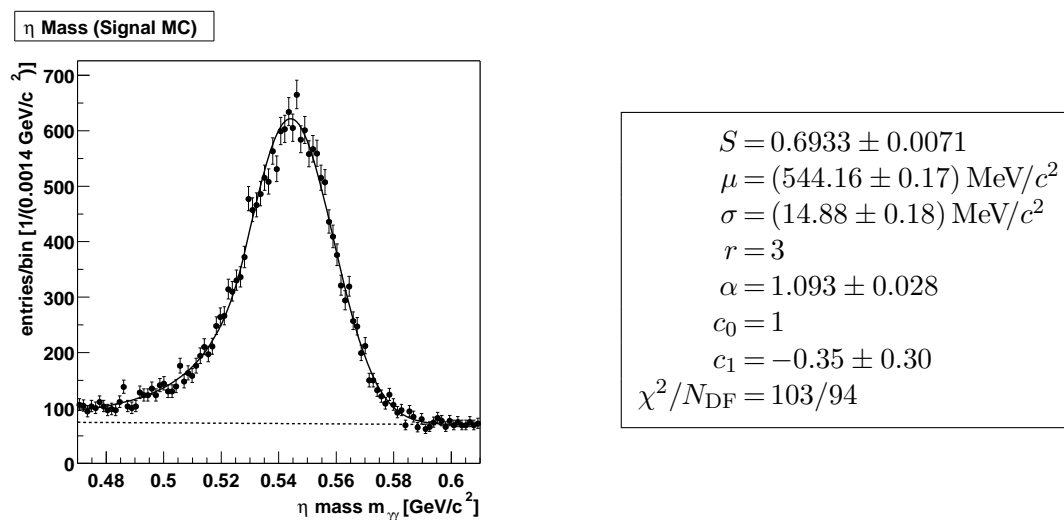


Figure D.5 Distribution, signal fraction S and p.d.f. parameters of the invariant mass of the η candidates (Eq. 3.44) in the signal Monte Carlo sample. The solid curve shows the fitted p.d.f. The dashed curve shows the background component.

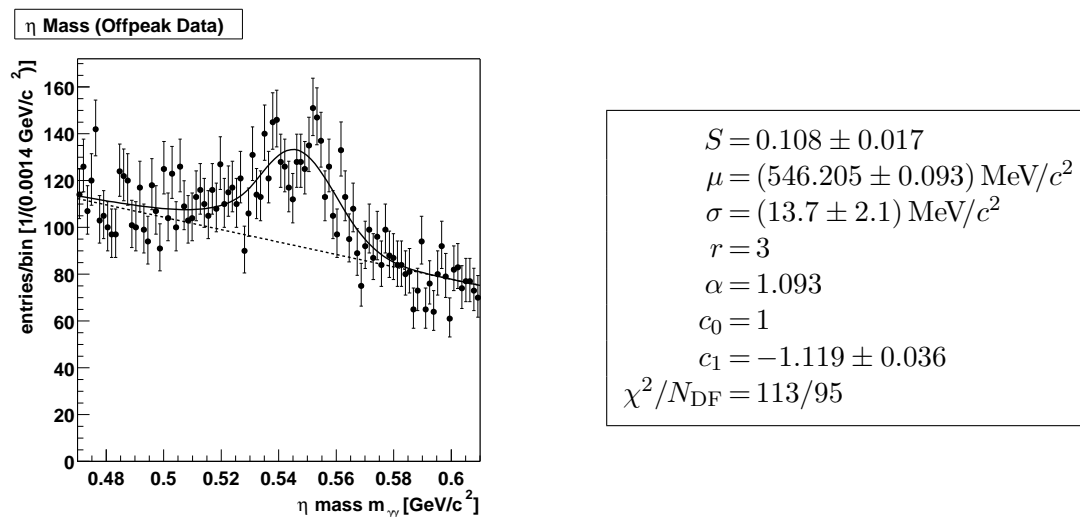


Figure D.6 Distribution, signal fraction S and p.d.f. parameters of the invariant mass of the η candidates (Eq. 3.44) in the off-peak data sample. The solid curve shows the fitted p.d.f. The dashed curve shows the background component.

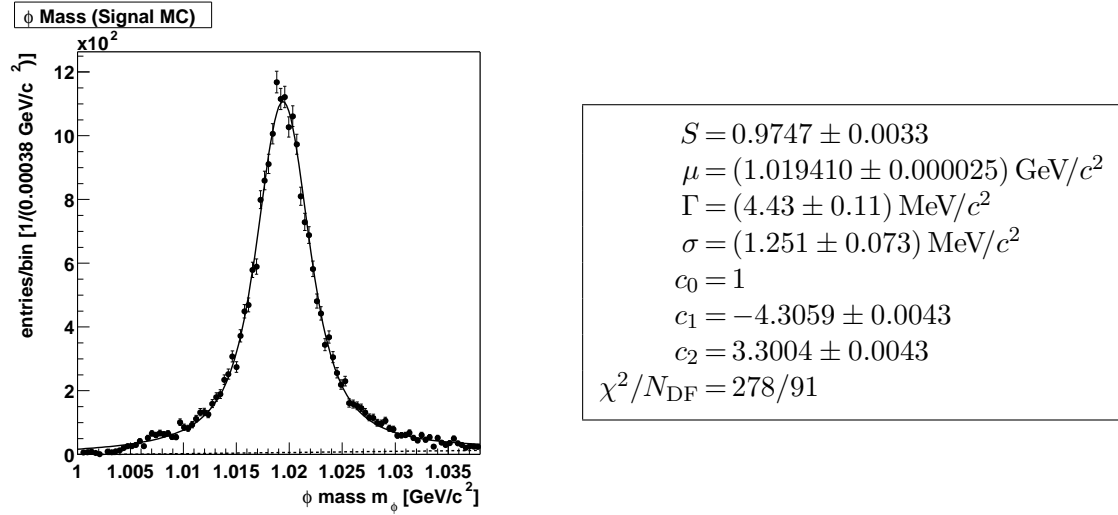


Figure D.7 Distribution, signal fraction S and p.d.f. parameters of the composite mass of the ϕ candidates (Eq. 3.46 and 3.47) in the signal Monte Carlo sample. The solid curve shows the fitted p.d.f. The dashed curve shows the background component.

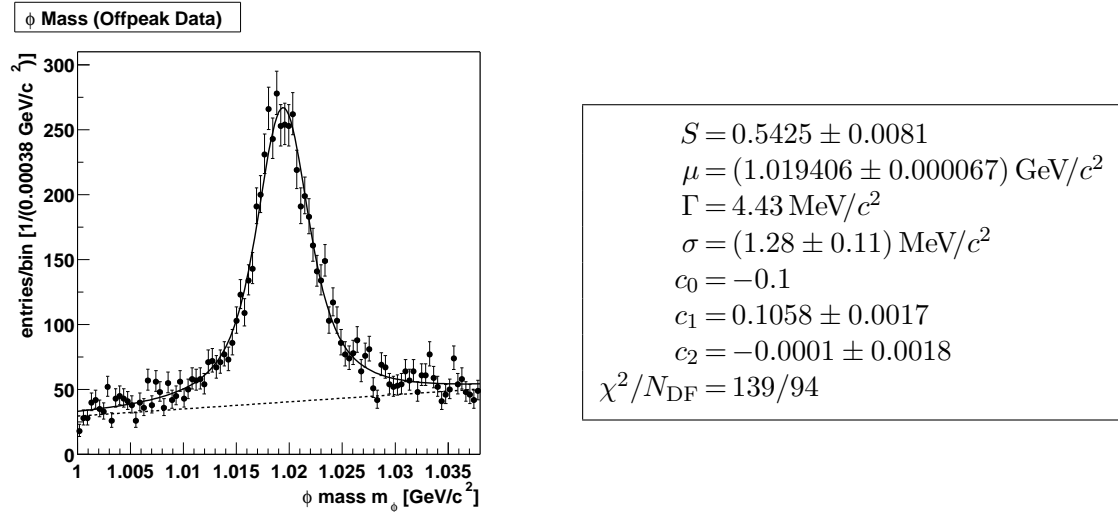


Figure D.8 Distribution, signal fraction S and p.d.f. parameters of the composite mass of the ϕ candidates (Eq. 3.46 and 3.47) in the off-peak data sample. The solid curve shows the fitted p.d.f. The dashed curve shows the background component.

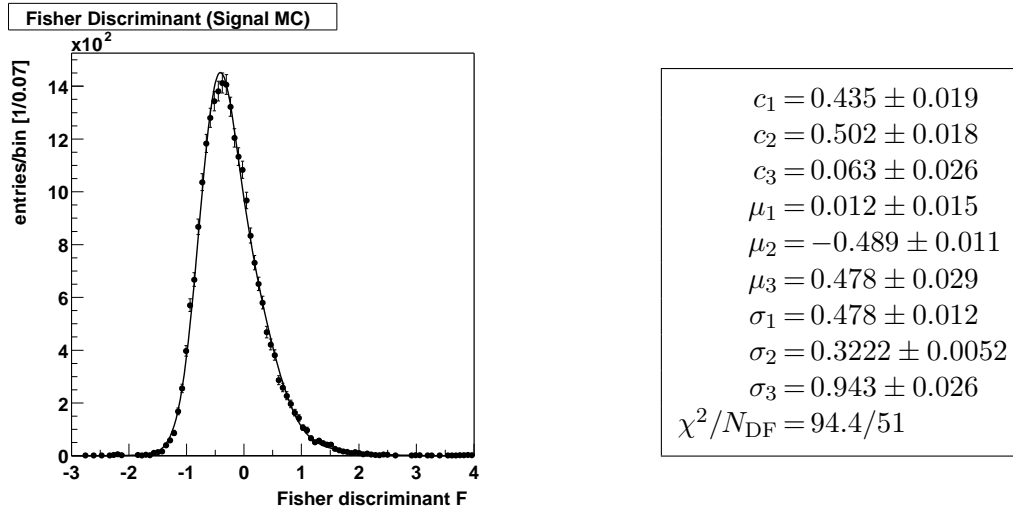


Figure D.9 Distribution and p.d.f. parameters of the Fisher discriminant (sum of three Gaussian p.d.f.'s) in the signal Monte Carlo sample. The curve shows the fitted p.d.f.

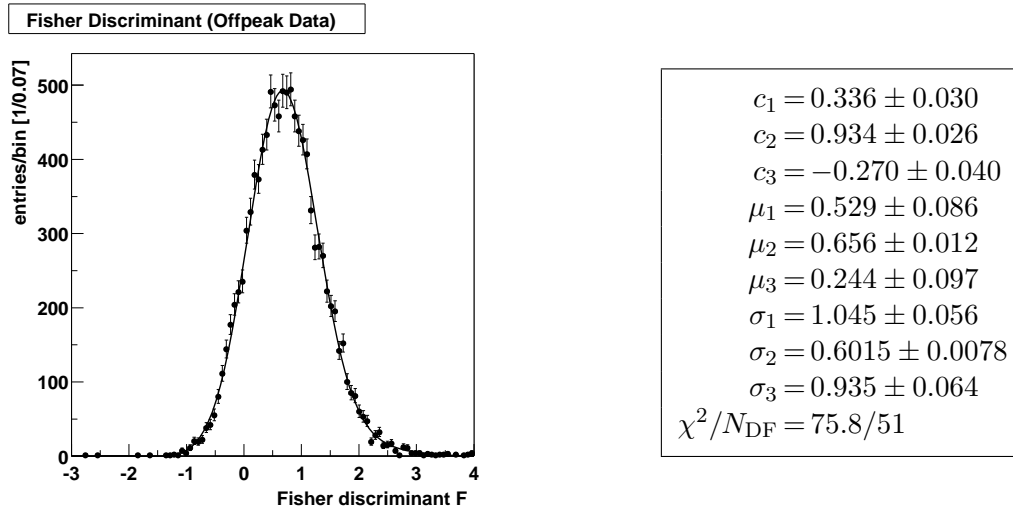


Figure D.10 Distribution and p.d.f. parameters of the Fisher discriminant (sum of three Gaussian p.d.f.'s) in the off-peak data sample. The curve shows the fitted p.d.f.

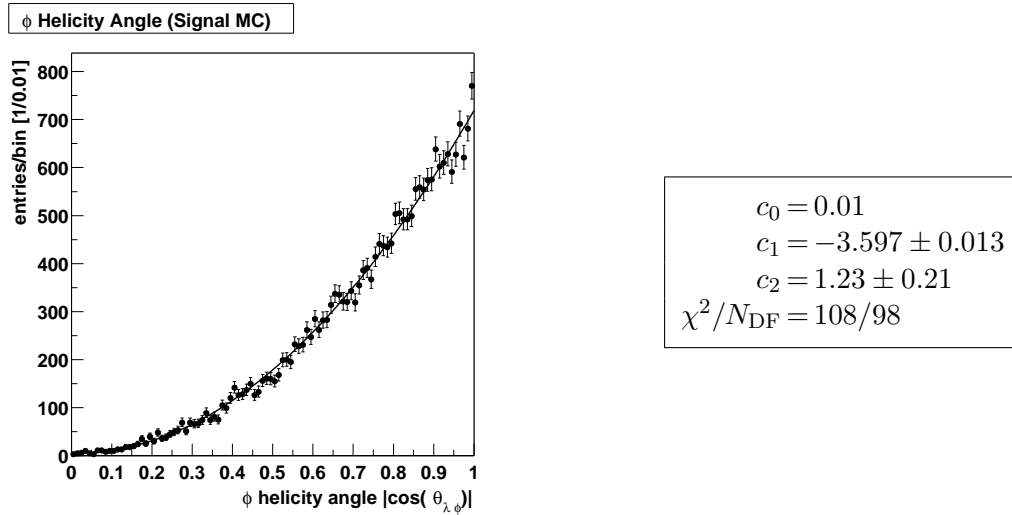


Figure D.11 Distribution and p.d.f. parameters of the magnitude of the cosine of the helicity angle of the ϕ candidates in the signal Monte Carlo sample. The curve shows the fitted p.d.f.

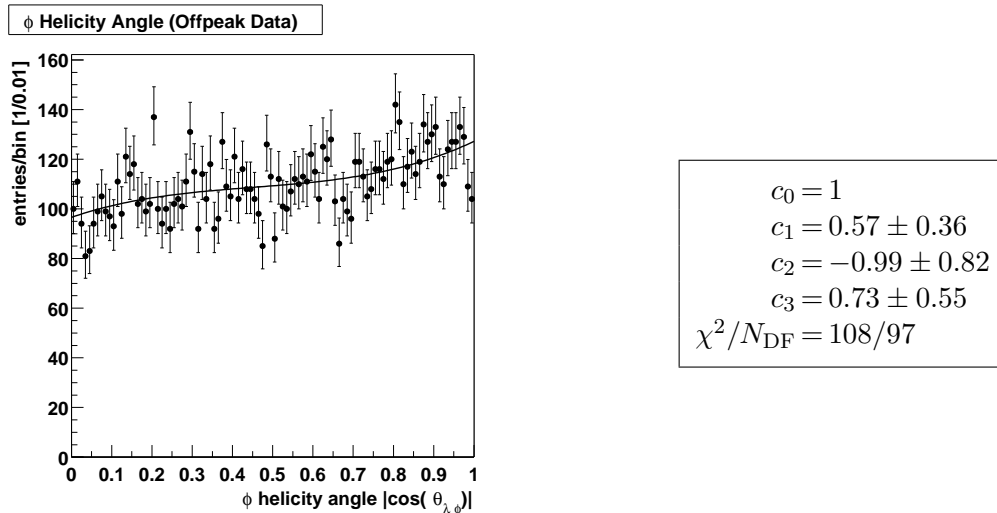


Figure D.12 Distribution and p.d.f. parameters of the magnitude of the cosine of the helicity angle of the ϕ candidates in the off-peak data sample. The curve shows the fitted p.d.f.

D.2 Channel $\eta \rightarrow \pi^+\pi^-\pi^0$

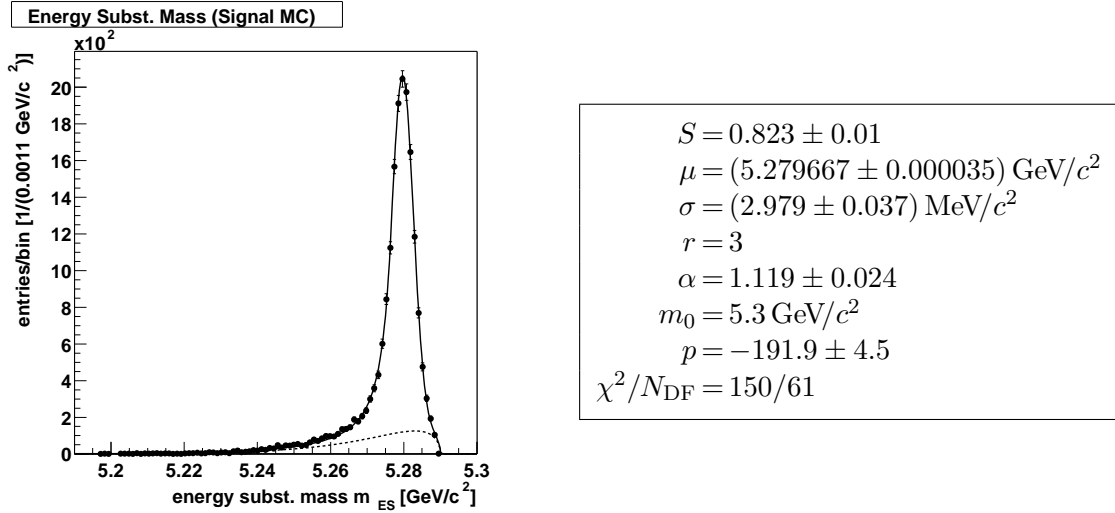


Figure D.13 Distribution, signal fraction S and p.d.f. parameters of the energy substituted mass (Eq. 3.41 and 3.44) in the signal Monte Carlo sample. The solid curve shows the fitted p.d.f. The dashed curve shows the background component.

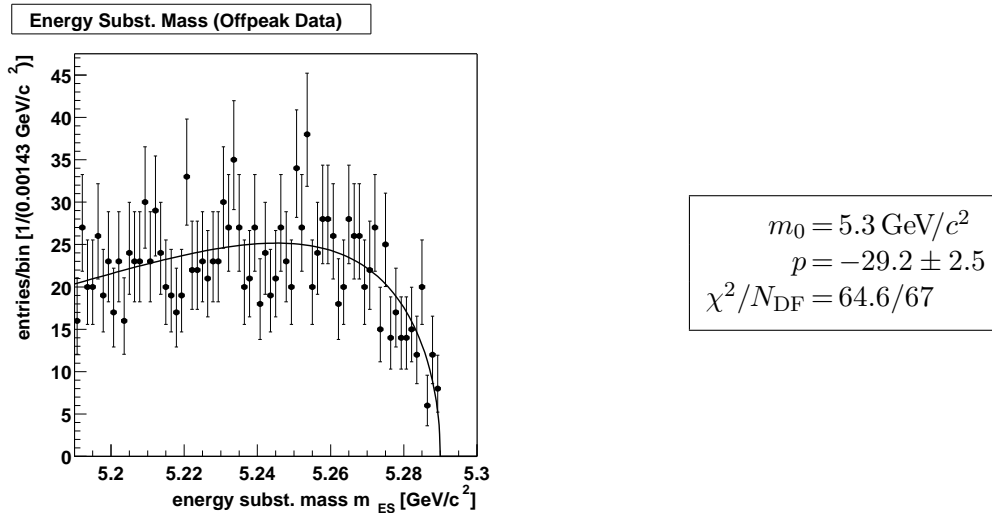


Figure D.14 Distribution and p.d.f. parameters of the energy substituted mass (Eq. 3.41) in the off-peak data sample. The curve shows the fitted p.d.f.

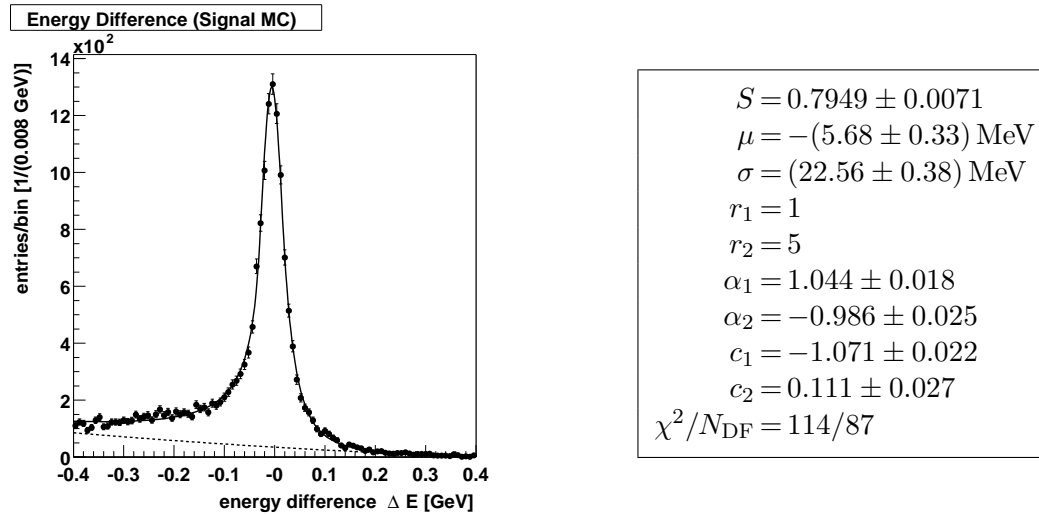


Figure D.15 Distribution, signal fraction S and p.d.f. parameters of the energy difference (Eq. 3.42 and 3.45) in the signal Monte Carlo sample. The solid curve shows the fitted p.d.f. The dashed curve shows the background component.

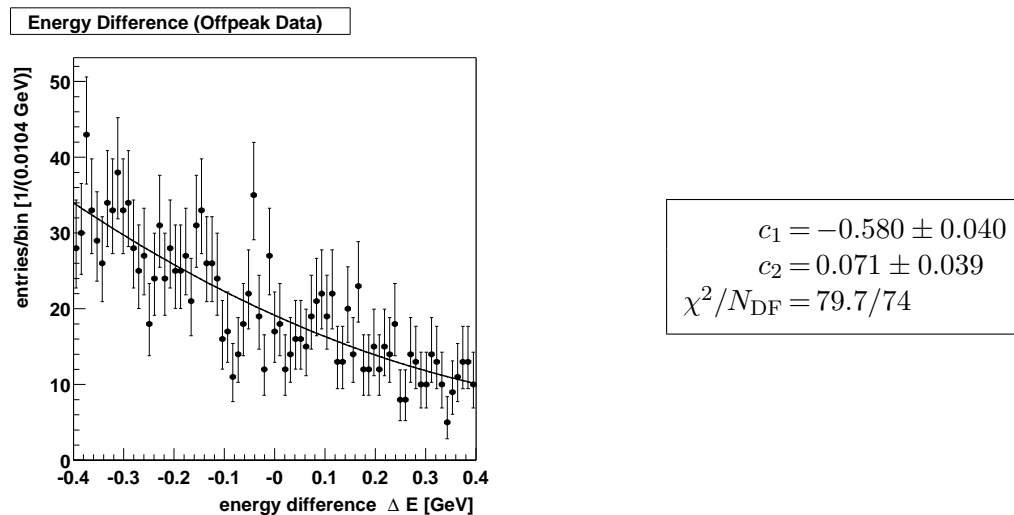


Figure D.16 Distribution and p.d.f. parameters of the energy difference (Eq. 3.42) in the off-peak data sample. The curve shows the fitted p.d.f.

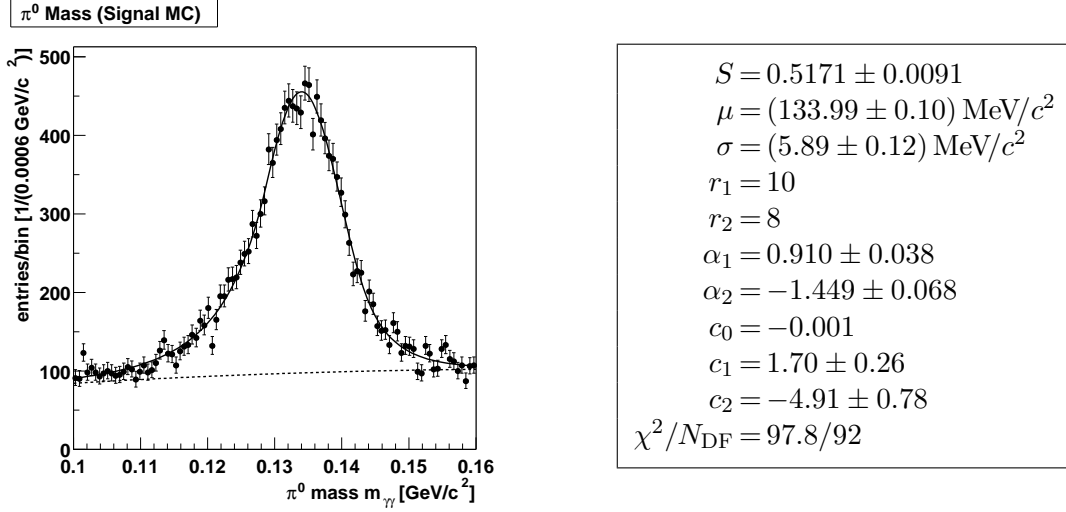


Figure D.17 Distribution, signal fraction S and p.d.f. parameters of the invariant mass of the π^0 candidates (Eq. 3.45) in the signal Monte Carlo sample. The solid curve shows the fitted p.d.f. The dashed curve shows the background component.

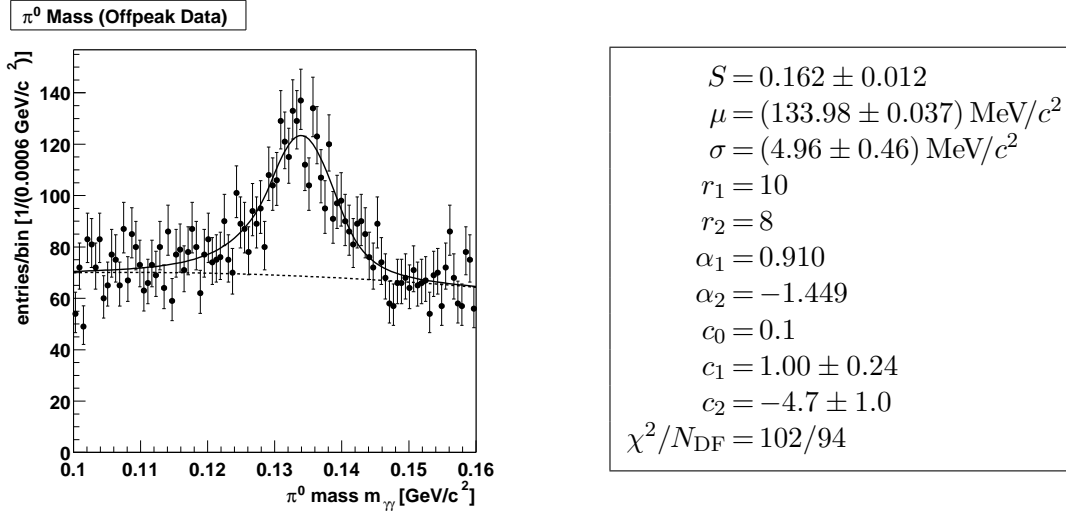


Figure D.18 Distribution, signal fraction S and p.d.f. parameters of the invariant mass of the π^0 candidates (Eq. 3.45) in the off-peak data sample. The solid curve shows the fitted p.d.f. The dashed curve shows the background component.

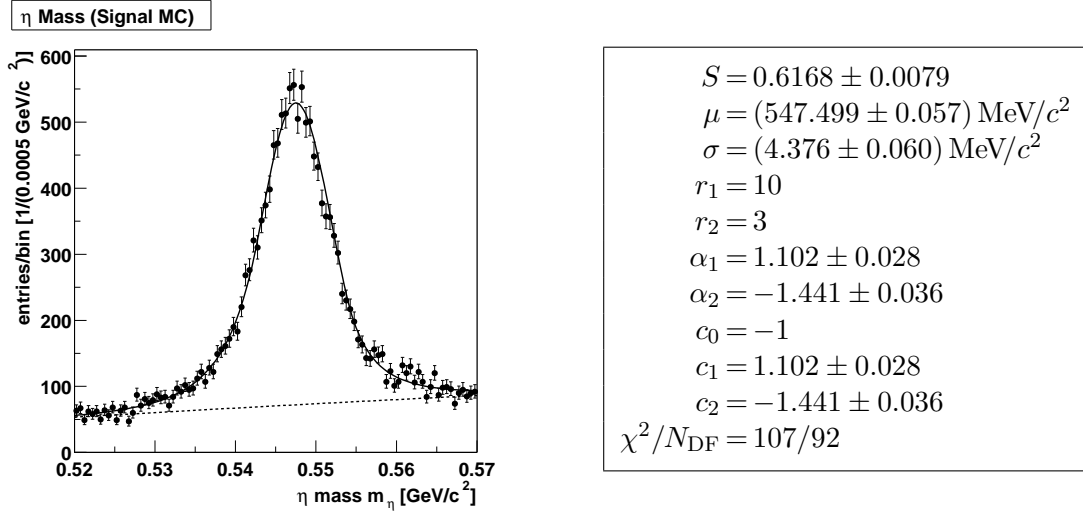


Figure D.19 Distribution, signal fraction S and p.d.f. parameters of the composite mass of the η candidates (Eq. 3.45) in the signal Monte Carlo sample. The solid curve shows the fitted p.d.f. The dashed curve shows the background component.

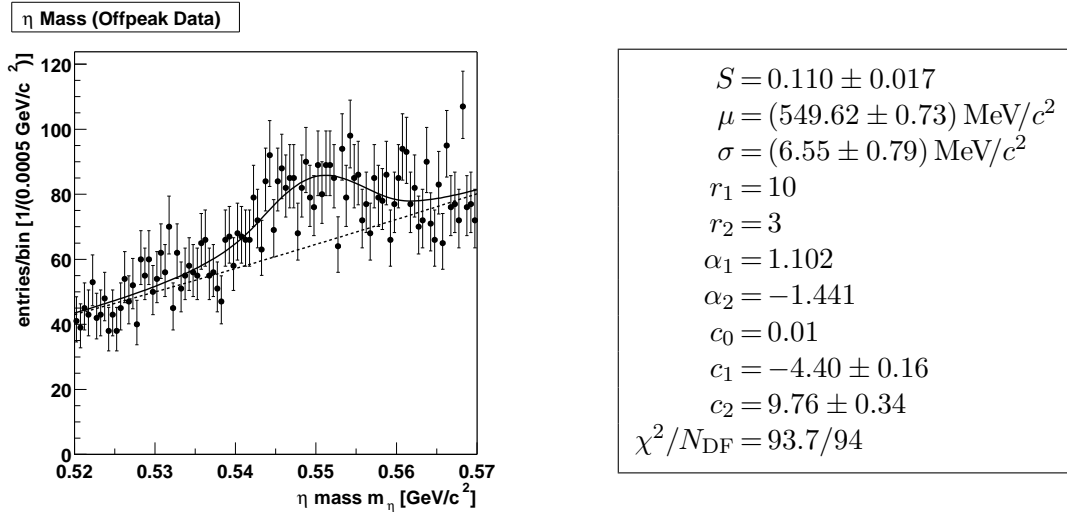


Figure D.20 Distribution, signal fraction S and p.d.f. parameters of the composite mass of the η candidates (Eq. 3.45) in the off-peak data sample. The solid curve shows the fitted p.d.f. The dashed curve shows the background component.

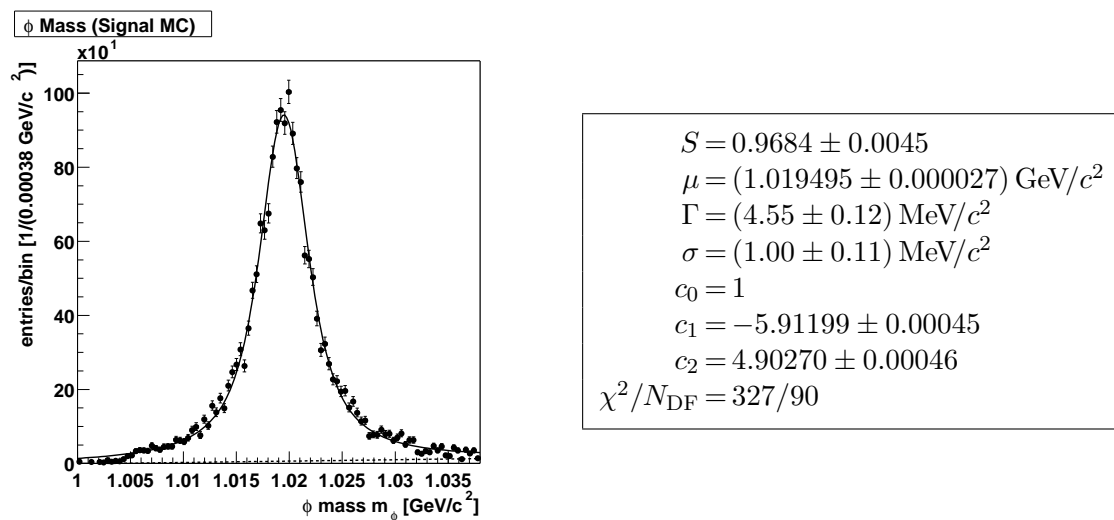


Figure D.21 Distribution, signal fraction S and p.d.f. parameters of the composite mass of the ϕ candidates (Eq. 3.46 and 3.47) in the signal Monte Carlo sample. The solid curve shows the fitted p.d.f. The dashed curve shows the background component.

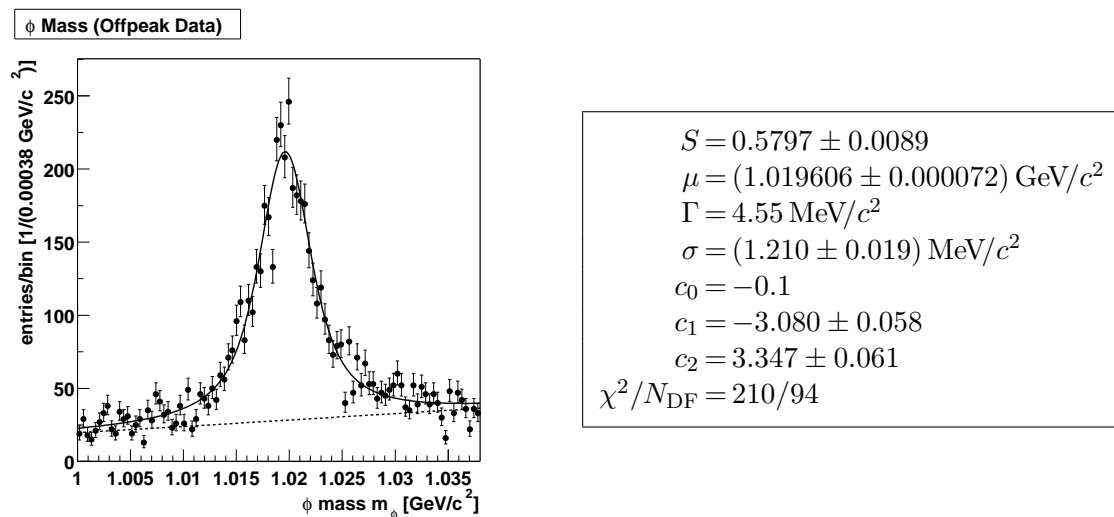


Figure D.22 Distribution, signal fraction S and p.d.f. parameters of the composite mass of the ϕ candidates (Eq. 3.46 and 3.47) in the off-peak data sample. The solid curve shows the fitted p.d.f. The dashed curve shows the background component.

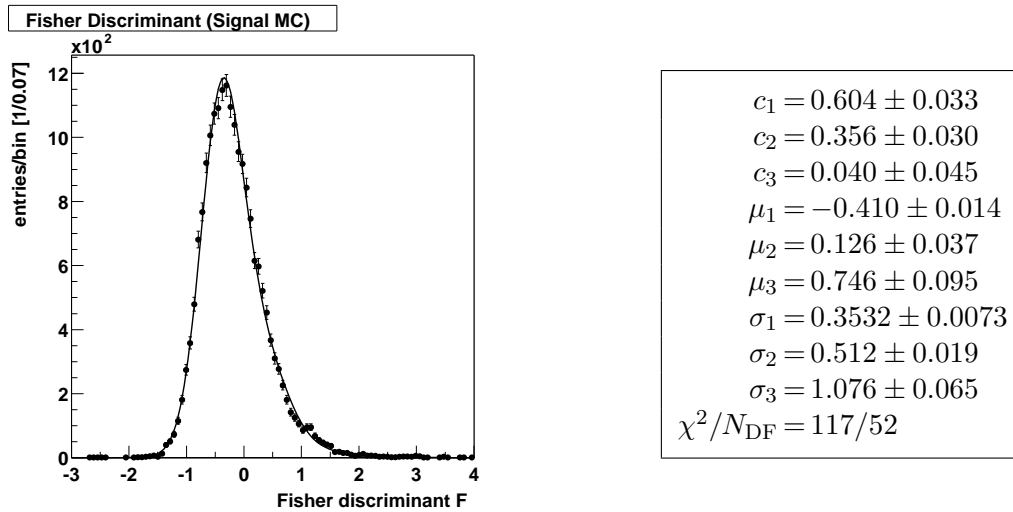


Figure D.23 Distribution and p.d.f. parameters of the Fisher discriminant (sum of three Gaussian p.d.f.'s) in the signal Monte Carlo sample. The curve shows the fitted p.d.f.

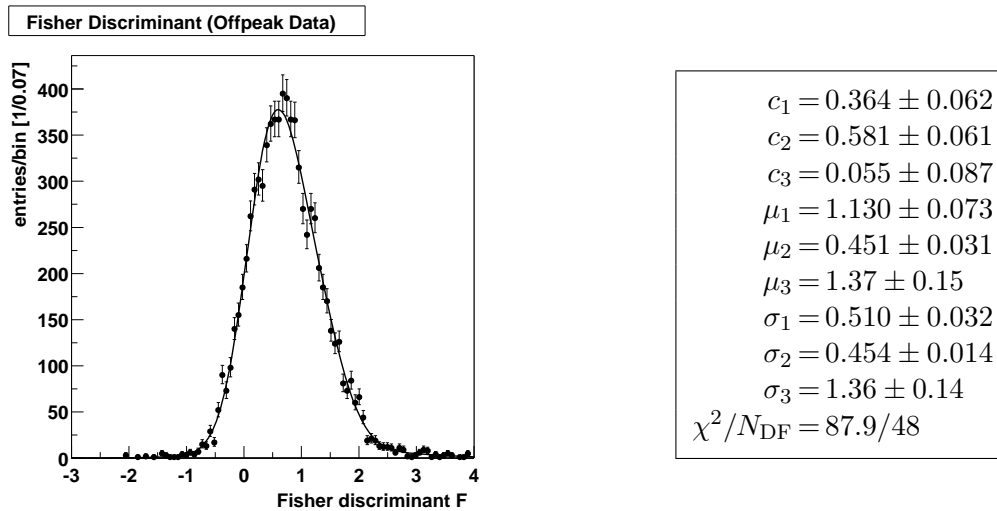


Figure D.24 Distribution and p.d.f. parameters of the Fisher discriminant (sum of three Gaussian p.d.f.'s) in the off-peak data sample. The curve shows the fitted p.d.f.

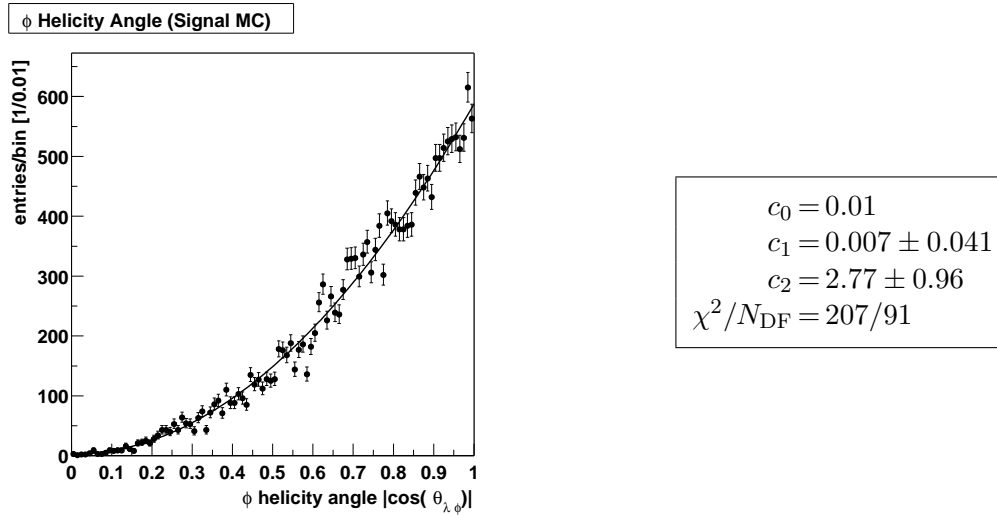


Figure D.25 Distribution and p.d.f. parameters of the magnitude of the cosine of the helicity angle of the ϕ candidates in the signal Monte Carlo sample. The curve shows the fitted p.d.f.

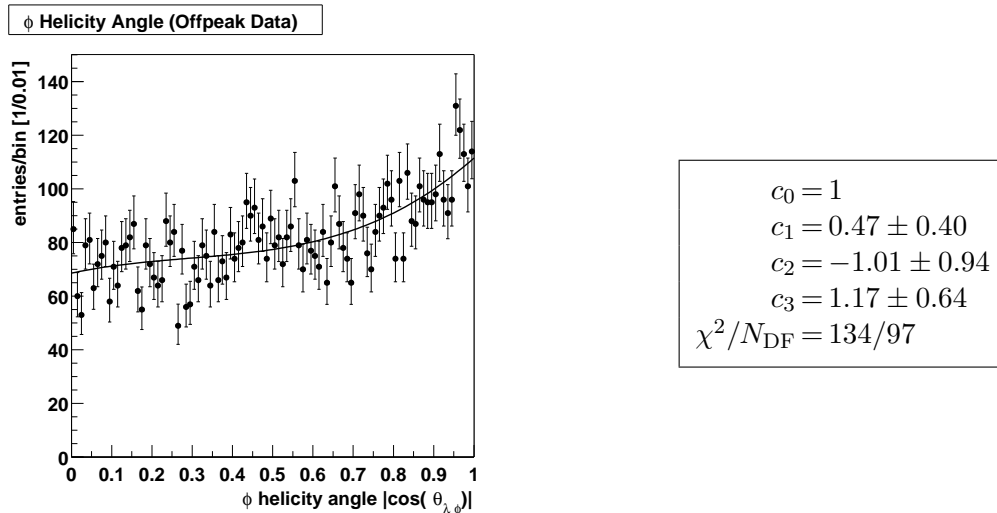


Figure D.26 Distribution and p.d.f. parameters of the magnitude of the cosine of the helicity angle of the ϕ candidates in the off-peak data sample. The curve shows the fitted p.d.f.

Appendix E

Likelihood Projections

E.1 Channel $\eta \rightarrow \gamma\gamma$

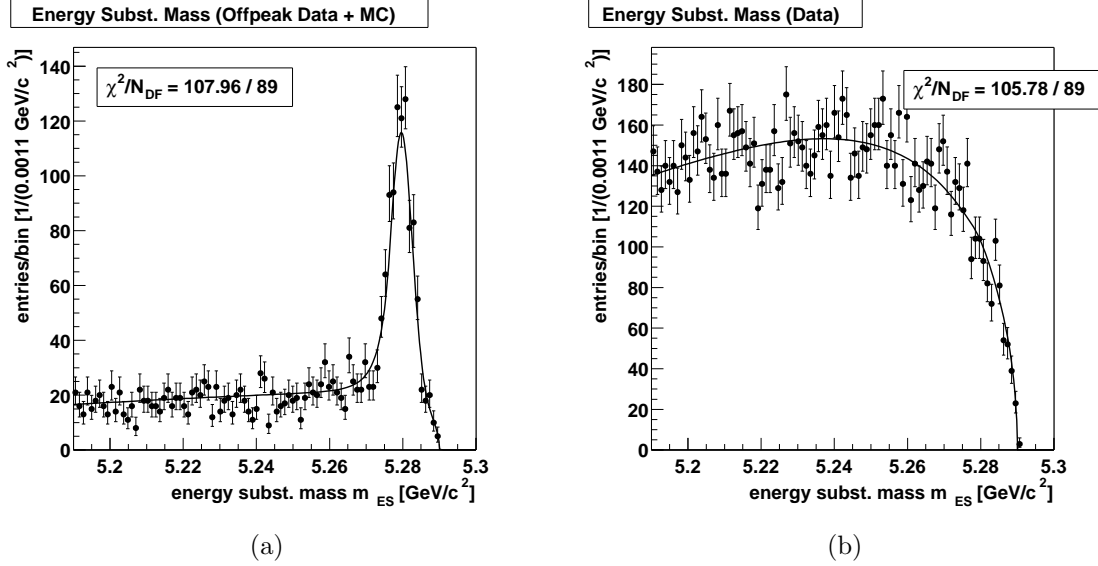


Figure E.1 Distributions of the energy substituted mass in a mixed sample of off-peak data, $B\bar{B}$ Monte Carlo and 1000 signal Monte Carlo events (a) and in the data sample (b). The solid curves show projections of the fitted likelihood functions. The distribution and the likelihood function in (b) were *blinded* in the analysis.

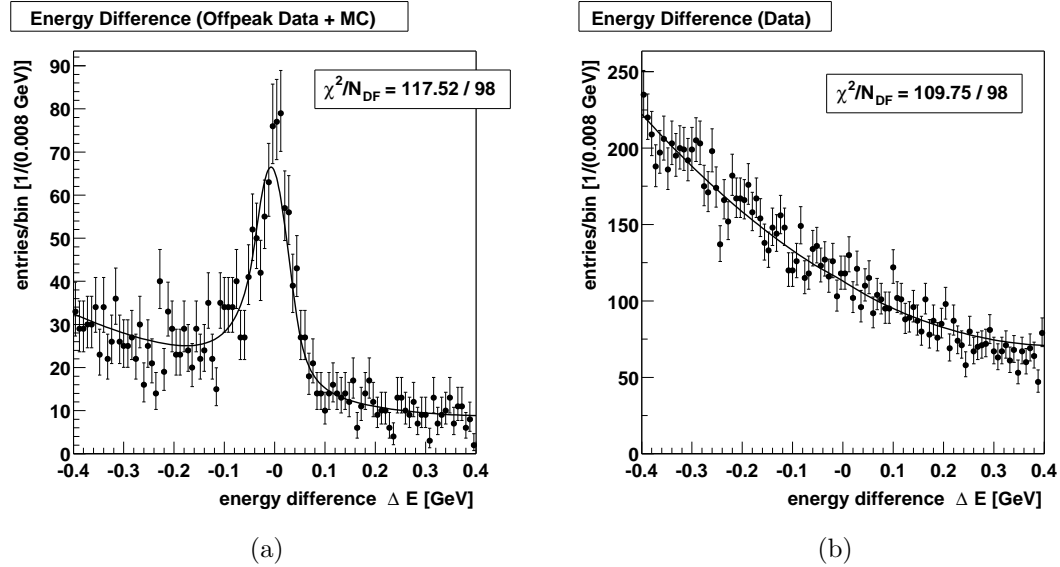


Figure E.2 Distributions of the energy difference in a mixed sample of off-peak data, $B\bar{B}$ Monte Carlo and 1000 signal Monte Carlo events (a) and in the data sample (b). The solid curves show projections of the fitted likelihood functions. The distribution and the likelihood function in (b) were *blinded* in the analysis.

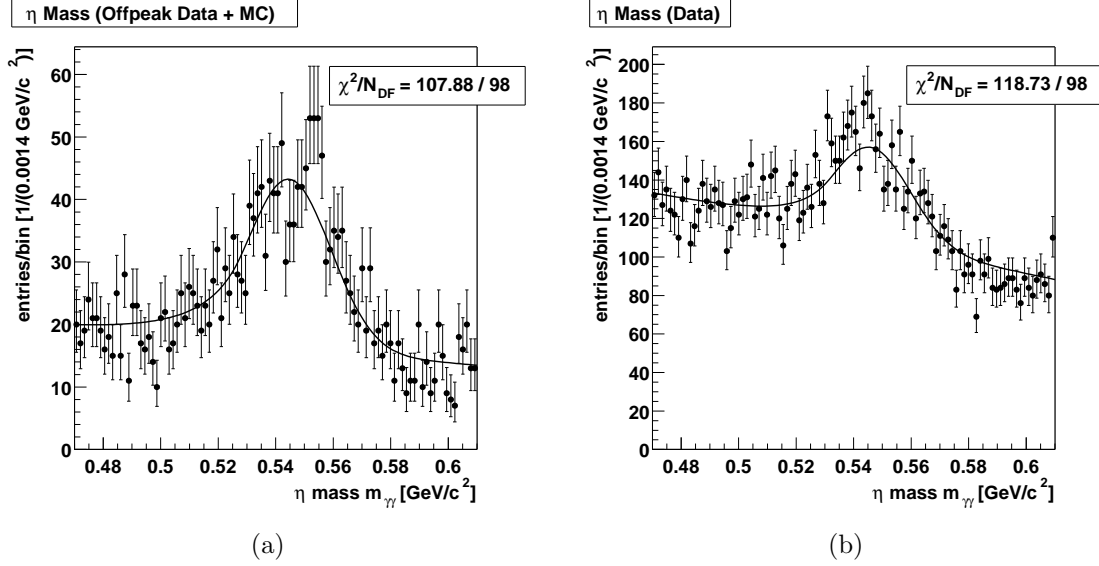


Figure E.3 Distributions of the invariant mass of the η candidates in a mixed sample of off-peak data, $B\bar{B}$ Monte Carlo and 1000 signal Monte Carlo events (a) and in the data sample (b). The solid curves show projections of the fitted likelihood functions. The distribution and the likelihood function in (b) were *blinded* in the analysis.

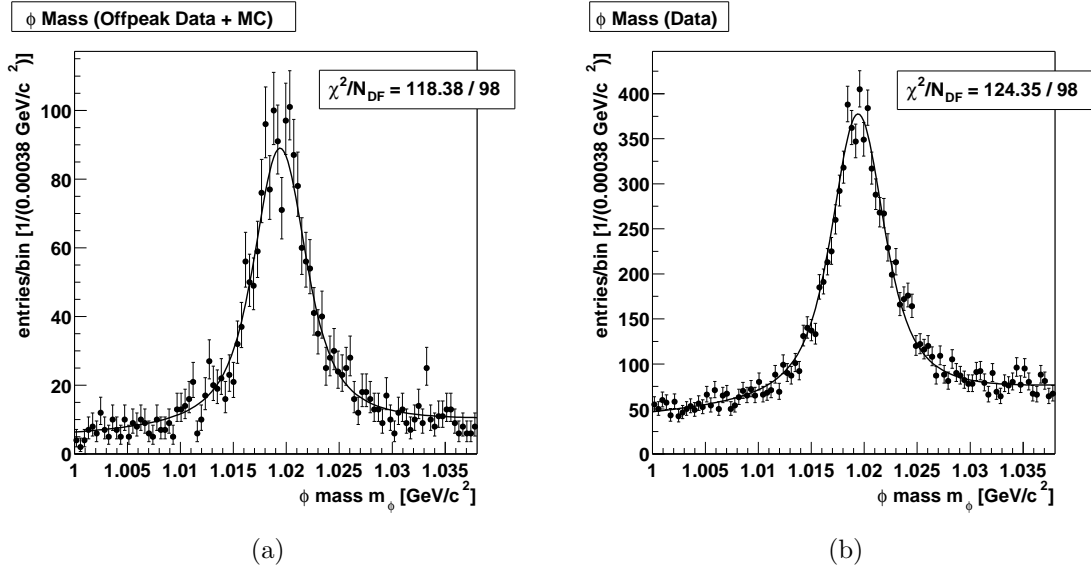


Figure E.4 Distributions of the composite mass of the ϕ candidates in a mixed sample of off-peak data, $B\bar{B}$ Monte Carlo and 1000 signal Monte Carlo events (a) and in the data sample (b). The solid curves show projections of the fitted likelihood functions. The distribution and the likelihood function in (b) were *blinded* in the analysis.

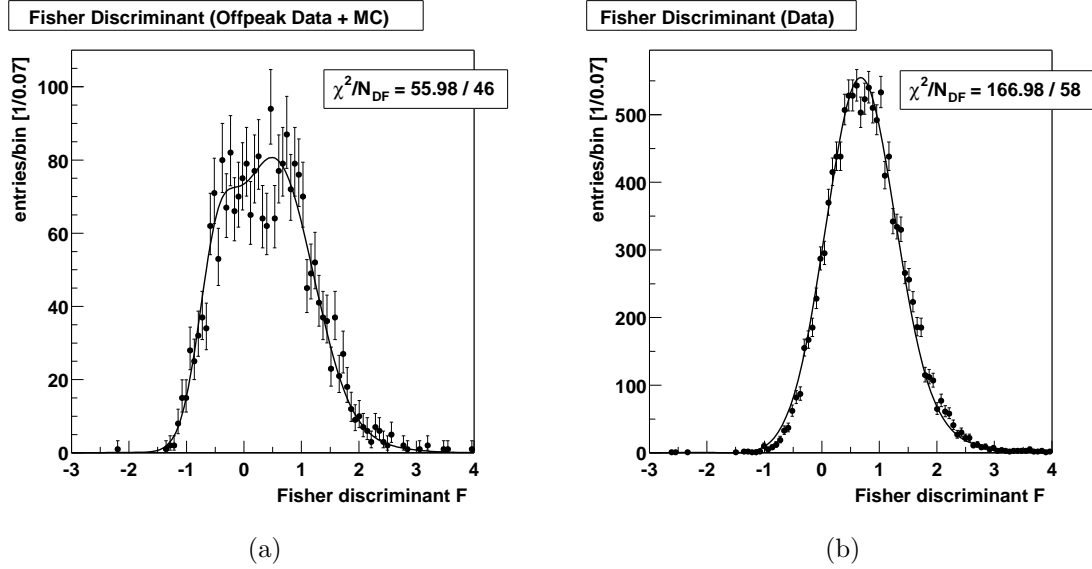


Figure E.5 Distributions of the Fisher discriminant in a mixed sample of off-peak data, $B\bar{B}$ Monte Carlo and 1000 signal Monte Carlo events (a) and in the data sample (b). The solid curves show projections of the fitted likelihood functions. The distribution and the likelihood function in (b) were *blinded* in the analysis.

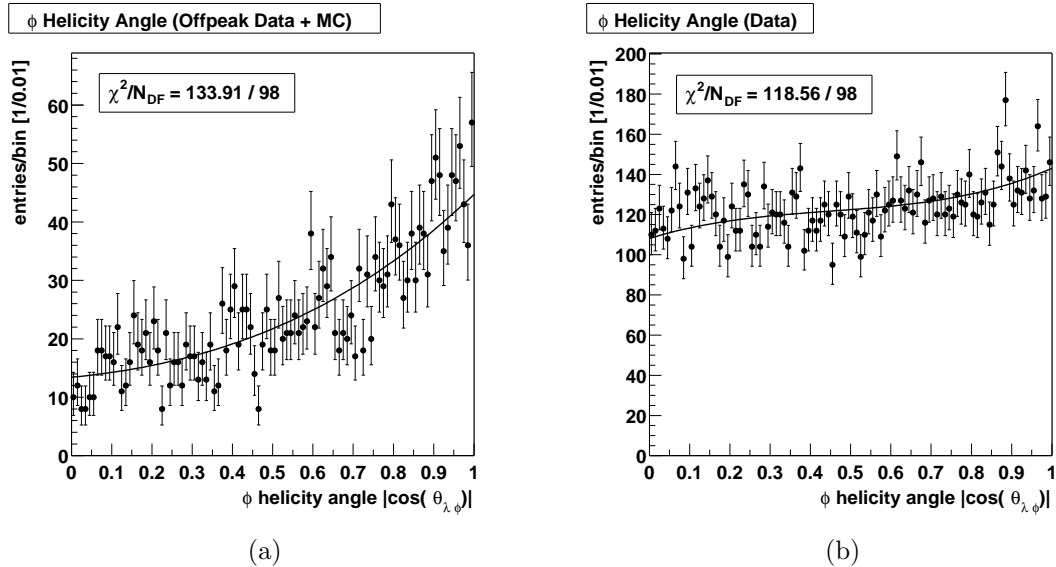


Figure E.6 Distributions of the magnitude of the cosine of the helicity angle of the ϕ candidates in a mixed sample of off-peak data, $B\bar{B}$ Monte Carlo and 1000 signal Monte Carlo events (a) and in the data sample (b). The solid curves show projections of the fitted likelihood functions. The distribution and the likelihood function in (b) were *blinded* in the analysis.

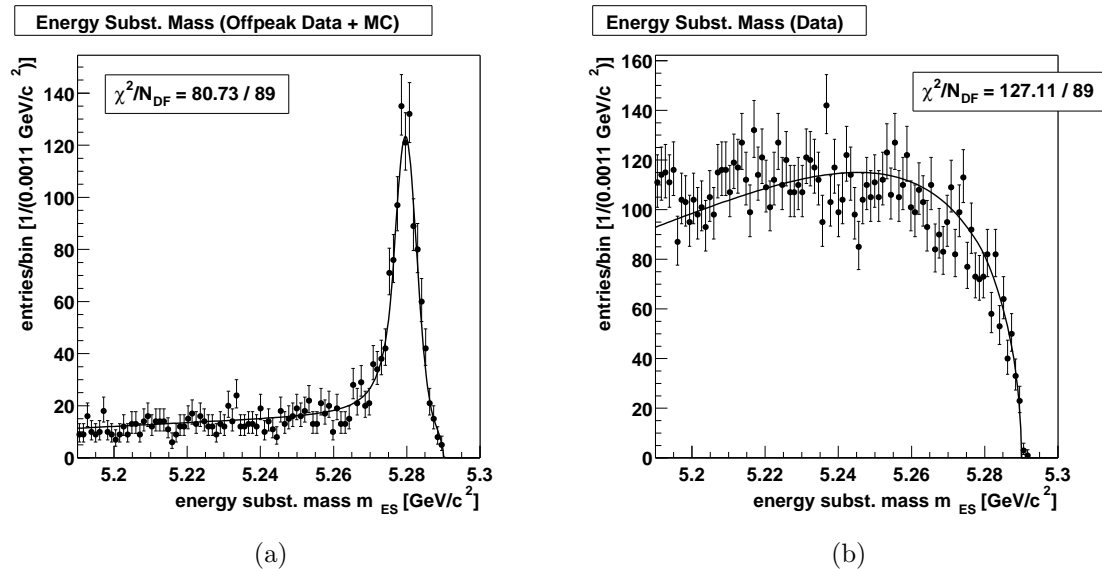
E.2 Channel $\eta \rightarrow \pi^+\pi^-\pi^0$ 

Figure E.7 Distributions of the energy substituted mass in a mixed sample of off-peak data, $B\bar{B}$ Monte Carlo and 1000 signal Monte Carlo events (a) and in the data sample (b). The solid curves show projections of the fitted likelihood functions. The distribution and the likelihood function in (b) were *blinded* in the analysis.

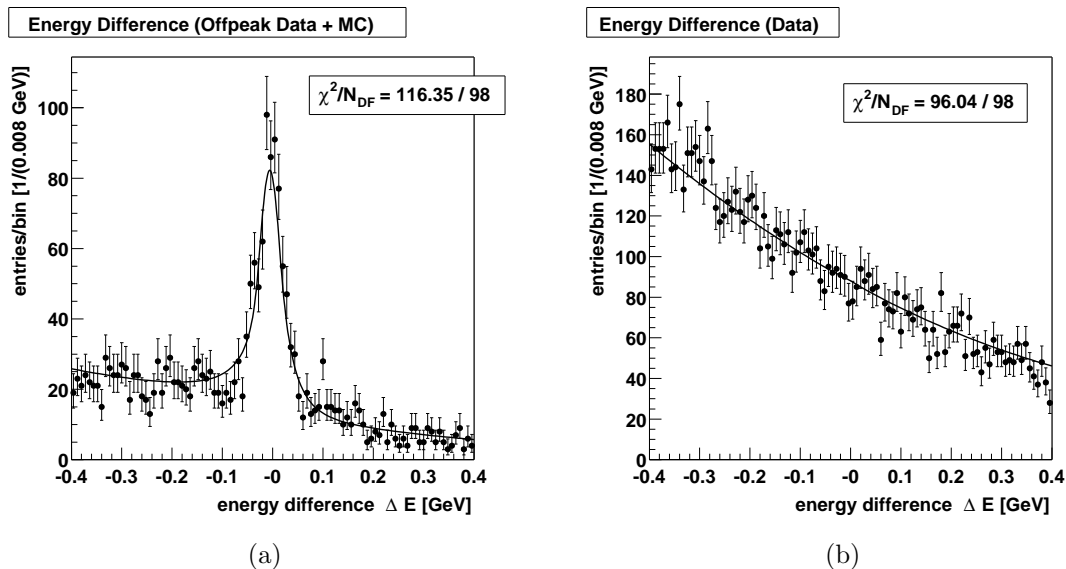


Figure E.8 Distributions of the energy substituted mass in a mixed sample of off-peak data, $B\bar{B}$ Monte Carlo and 1000 signal Monte Carlo events (a) and in the data sample (b). The solid curves show projections of the fitted likelihood functions. The distribution and the likelihood function in (b) were *blinded* in the analysis.

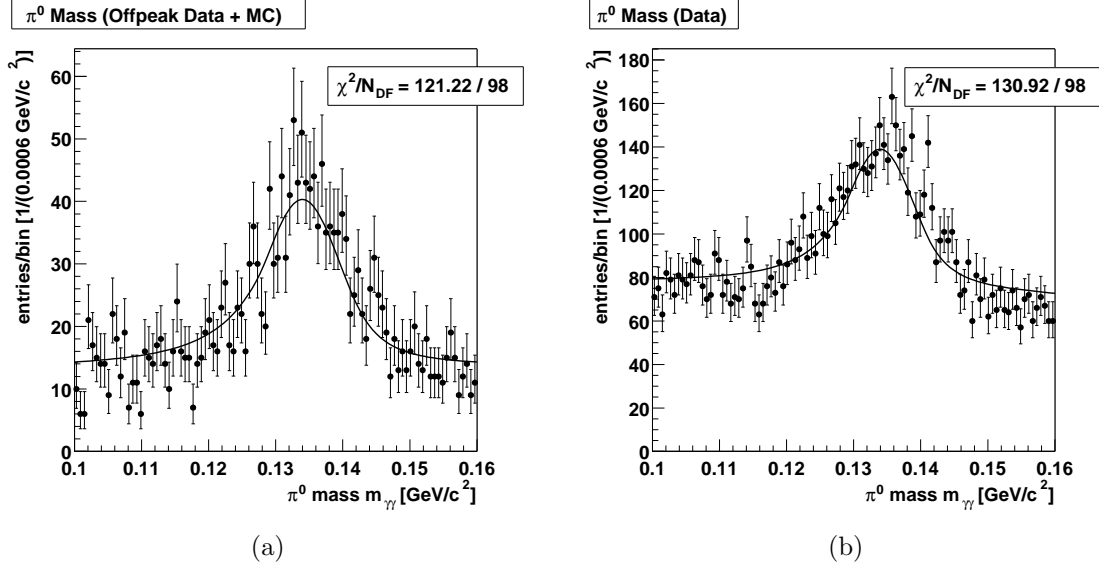


Figure E.9 Distributions of the invariant mass of the π^0 candidates in a mixed sample of off-peak data, $B\bar{B}$ Monte Carlo and 1000 signal Monte Carlo events (a) and in the data sample (b). The solid curves show projections of the fitted likelihood functions. The distribution and the likelihood function in (b) were *blinded* in the analysis.

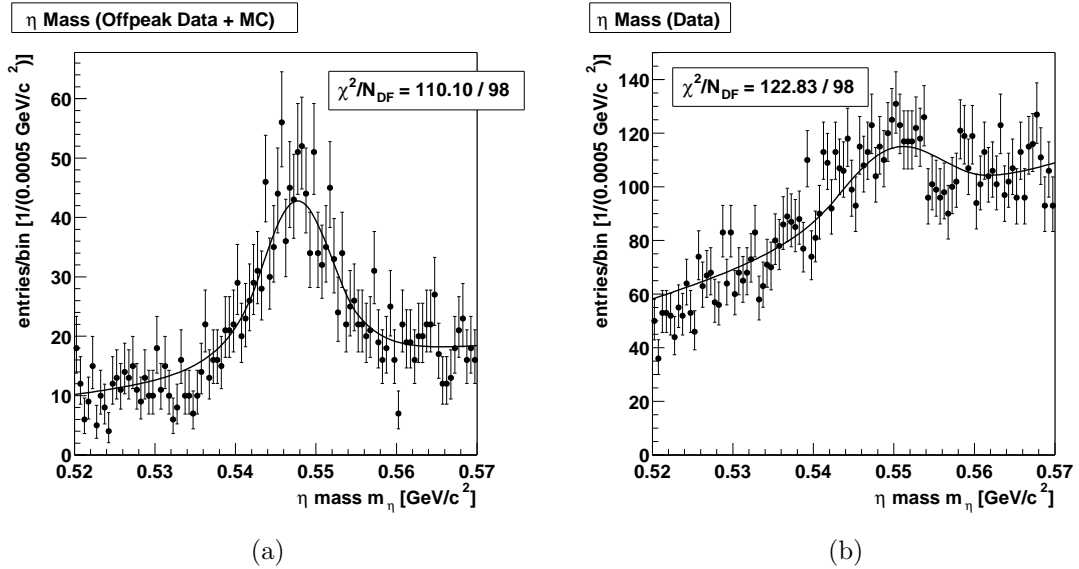


Figure E.10 Distributions of the composite mass of the η candidates in a mixed sample of off-peak data, $B\bar{B}$ Monte Carlo and 1000 signal Monte Carlo events (a) and in the data sample (b). The solid curves show projections of the fitted likelihood functions. The distribution and the likelihood function in (b) were *blinded* in the analysis.

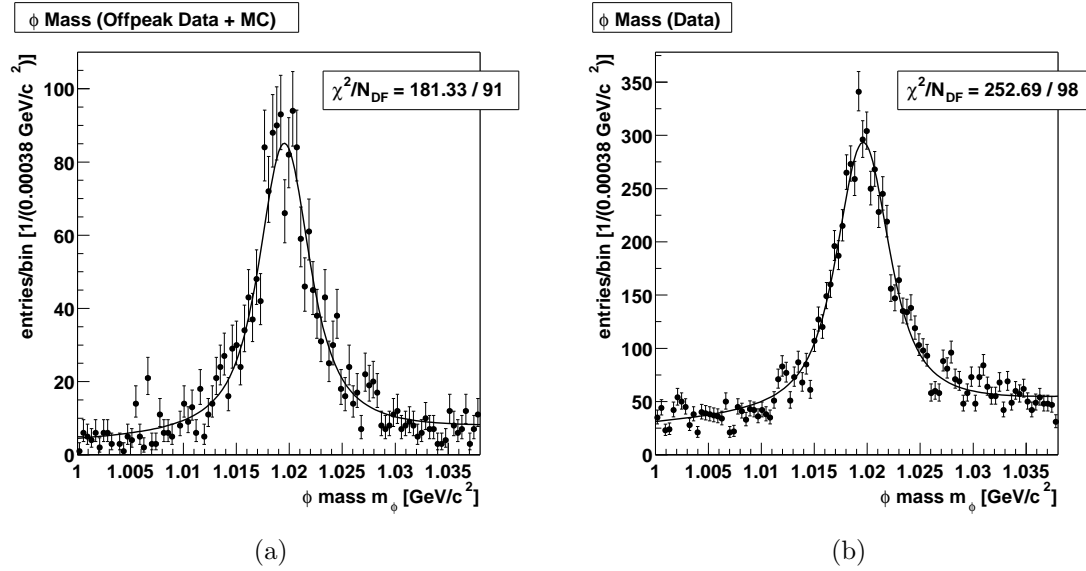


Figure E.11 Distributions of the composite mass of the ϕ candidates in a mixed sample of off-peak data, $B\bar{B}$ Monte Carlo and 1000 signal Monte Carlo events (a) and in the data sample (b). The solid curves show projections of the fitted likelihood functions. The distribution and the likelihood function in (b) were *blinded* in the analysis.

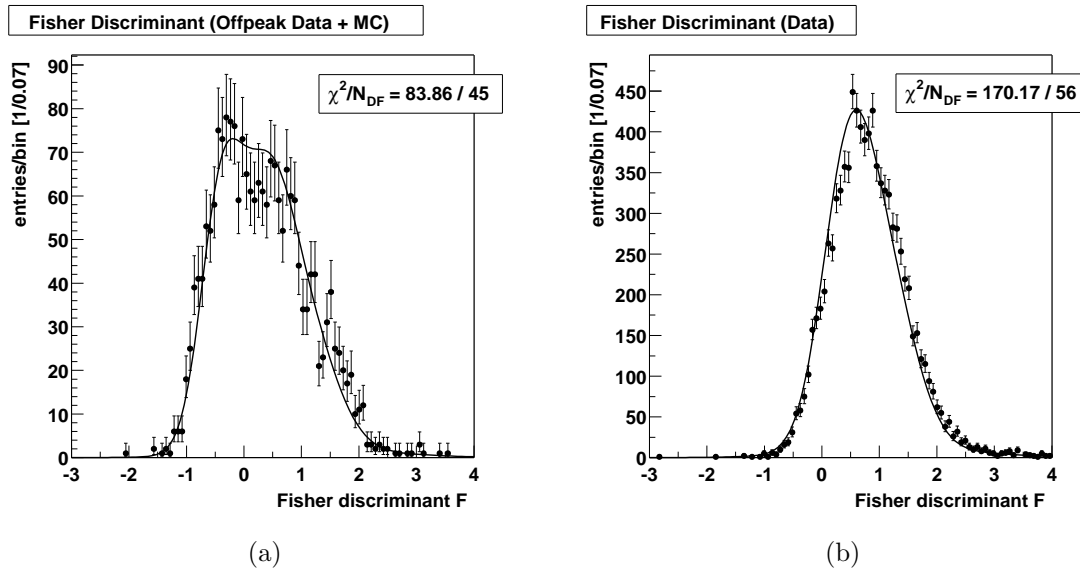


Figure E.12 Distributions of the Fisher discriminant in a mixed sample of off-peak data, $B\bar{B}$ Monte Carlo and 1000 signal Monte Carlo events (a) and in the data sample (b). The solid curves show projections of the fitted likelihood functions. The distribution and the likelihood function in (b) were *blinded* in the analysis.

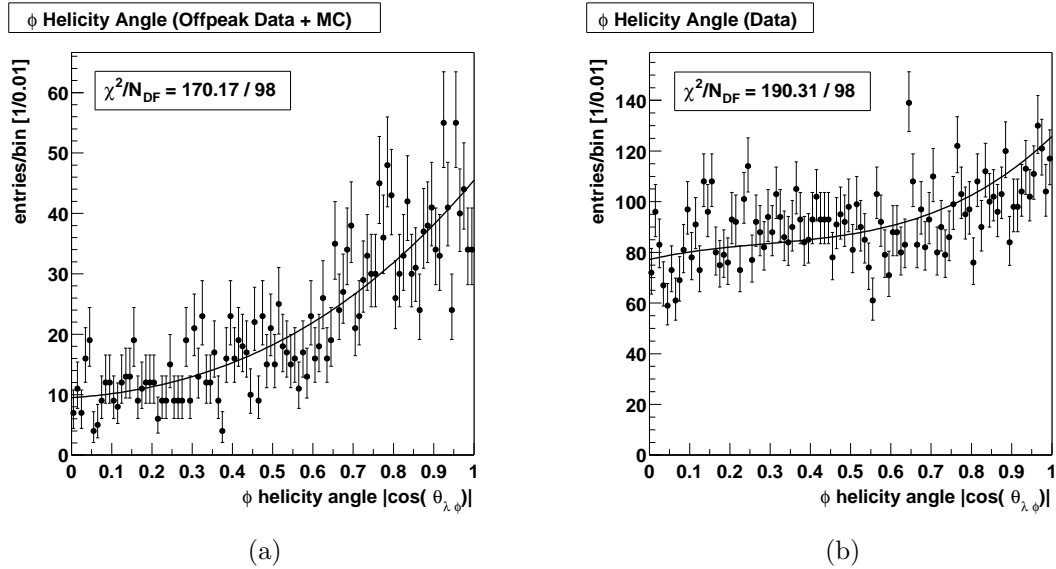


Figure E.13 Distributions of the magnitude of the cosine of the helicity angle of the ϕ candidates in a mixed sample of off-peak data, $B\bar{B}$ Monte Carlo and 1000 signal Monte Carlo events (a) and in the data sample (b). The solid curves show projections of the fitted likelihood functions. The distribution and the likelihood function in (b) were *blinded* in the analysis.

Appendix F

Yield Distributions

F.1 Channel $\eta \rightarrow \gamma\gamma$

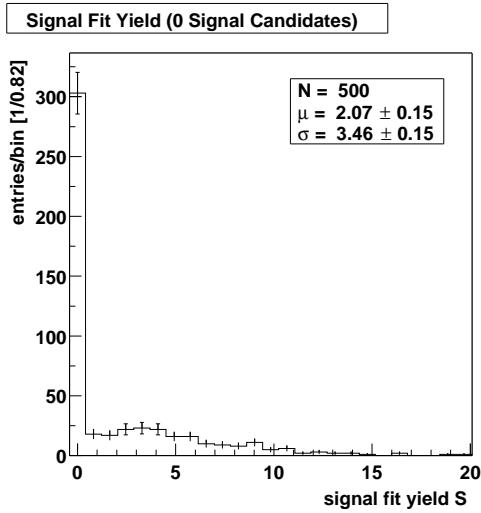


Figure F.1 Distribution of the signal yield in 500 maximum-likelihood fits to study samples with 0 signal candidates.

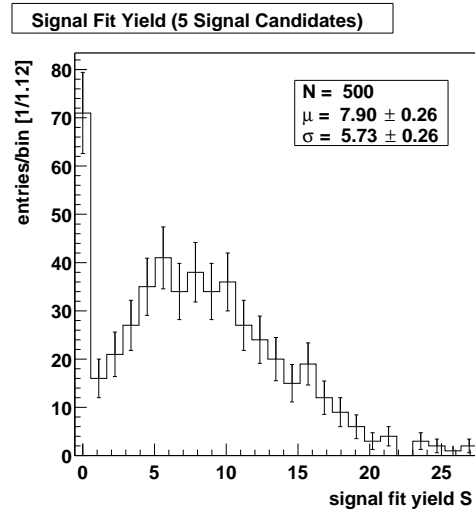


Figure F.2 Distribution of the signal yield in 500 maximum-likelihood fits to study samples with 5 signal candidates.

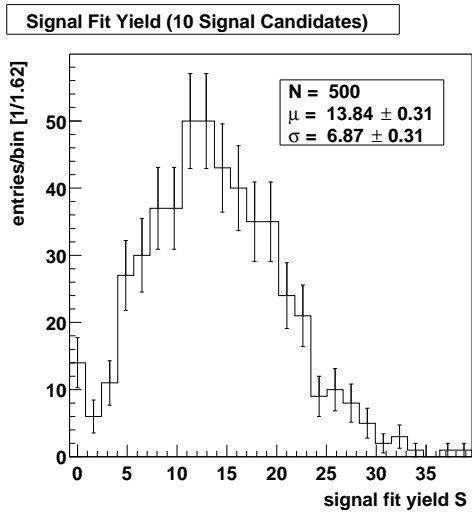


Figure F.3 Distribution of the signal yield in 500 maximum-likelihood fits to study samples with 10 signal candidates.

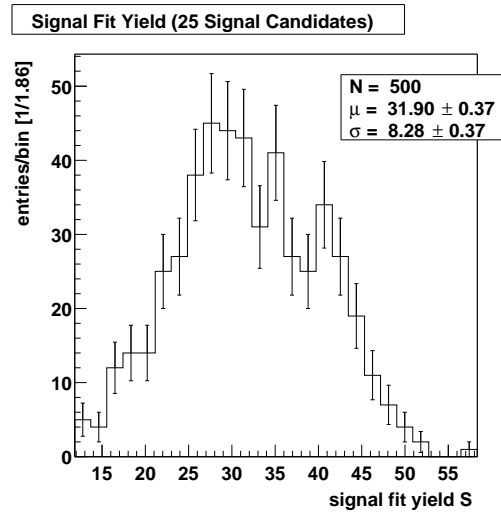


Figure F.4 Distribution of the signal yield in 500 maximum-likelihood fits to study samples with 25 signal candidates.

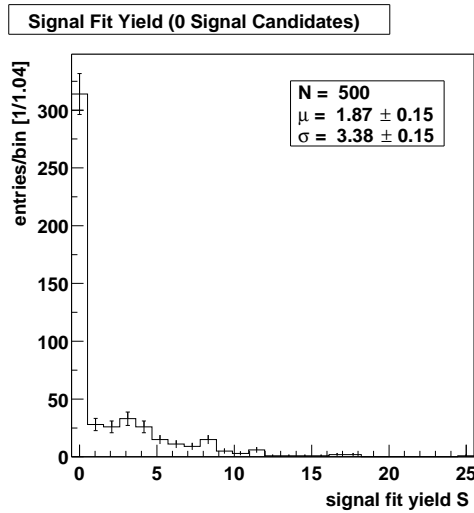
F.2 Channel $\eta \rightarrow \pi^+\pi^-\pi^0$ 

Figure F.5 Distribution of the signal yield in 500 maximum-likelihood fits to study samples with 0 signal candidates.

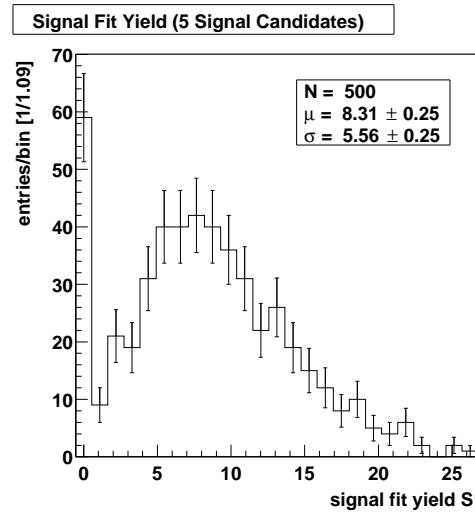


Figure F.6 Distribution of the signal yield in 500 maximum-likelihood fits to study samples with 5 signal candidates.

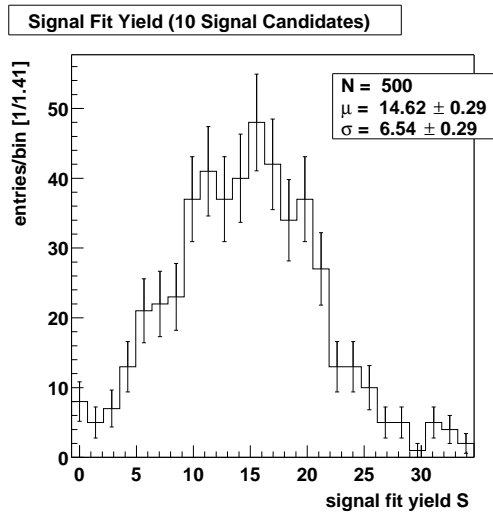


Figure F.7 Distribution of the signal yield in 500 maximum-likelihood fits to study samples with 10 signal candidates.

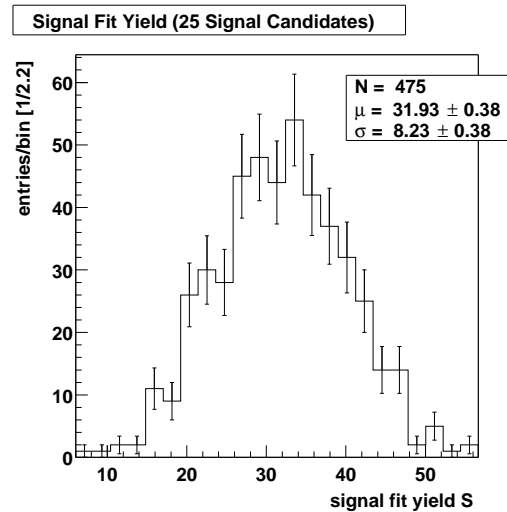


Figure F.8 Distribution of the signal yield in 500 maximum-likelihood fits to study samples with 25 signal candidates.

Erklärung

Hiermit versichere ich, daß ich die vorliegende Arbeit ohne unzulässige Hilfe Dritter und ohne Benutzung anderer als der angegebenen Hilfsmittel angefertigt und aus fremden Quellen direkt oder indirekt übernommenes Material als solches kenntlich gemacht. Die Arbeit wurde bisher weder im Inland noch im Ausland in gleicher oder ähnlicher Form einer anderen Prüfungsbehörde vorgelegt.

Diese Arbeit wurde am Institut für Kern- und Teilchenphysik der Technischen Universität Dresden unter wissenschaftlicher Betreuung von Prof. Dr. Bernhard Spaan angefertigt.

Ich erkenne die Promotionsordnung der Fakultät Mathematik und Naturwissenschaften der Technischen Universität Dresden vom 20. März 2002 gemäß Satzung vom 16. April 2003 an.

Dresden, den 29. November 2004

Stephan Otto